APPLICATIONS OF INTERNAL TRANSLATING MASS TECHNOLOGIES TO SMART WEAPONS SYSTEMS

A Dissertation
Presented to
The Academic Faculty

by

Jonathan Rogers

In Partial Fulfillment
of the Requirements for the Degree
DOCTOR OF PHILOSOPHY in the
School of AEROSPACE ENGINEERING

Georgia Institute of Technology
DECEMBER 2009

APPLICATIONS OF INTERNAL TRANSLATING MASS TECHNOLOGIES TO SMART WEAPONS SYSTEMS

Approved by:

Dr. Mark Costello, Advisor
School of Aerospace Engineering
Georgia Institute of Technology

Dr. Peter Plostins
Weapons and Materials Research Directorate
U.S. Army Research Laboratory

Dr. Olivier Bauchau
School of Aerospace Engineering
Georgia Institute of Technology

Dr. Frank Fresconi
Weapons and Materials Research Directorate
U.S. Army Research Laboratory

Dr. Eric Johnson
School of Aerospace Engineering
Georgia Institute of Technology

Date Approved: September 15, 2009

To my Mother, Father, Danny, and Bethy

ACKNOWLEDGEMENTS

Without the guidance and support of many people, this research would not have been possible. First, I would like to thank my advisor, Dr. Mark Costello, for his patience and dedication throughout my time at Georgia Tech. Dr. Costello's enthusiasm and commitment to teaching has impressed me from my first meeting with him, and it is these qualities combined with his generous and thoughtful demeanor that have allowed his students to achieve so much. Furthermore, Dr. Costello teaches his students to have professional attitudes and to be good listeners, qualities that will help them continue to learn throughout their careers.

I would also like to thank the members of my committee, Dr. Eric Johnson, Dr. Olivier Bauchau, Dr. Peter Plostins, and Dr. Frank Fresconi, for their time in helping to refine and guide this research. In addition, several people from the U.S. Army Research Lab, including Dave Hepner, Brad Davis, Gordon Brown, Dave Lyon, and Gene Cooper have been instrumental in providing substantive guidance for many of the projects described in this thesis.

Many of my fellow graduate students at Georgia Tech have provided significant support over the last three years, without whom this accomplishment would certainly not have been possible. I thank Eric Beyer, Ryan Letniak, and Michael Abraham, who have provided not only technical help, but interesting and enjoyable experiences for the past three years. I am thankful to all other members of the Costello research group, including Jack Mooney, Kyle French, Sam Zarovy, Carlos Montalvo, Jenna Stahl, Jessica Newman, Vasu Manivannan, Emily Leylek, James Wright, Luisa Fairfax, and Aaron Webb.

The values instilled in me by my family and closest friends have been key in allowing me to complete this work. John Crouse, who has taught me responsibility and patience from a young age, has provided me with encouragement and support through my years here. I thank Hillary Gerber for her kindness, generosity, and patience through these past five months. She has provided endless words of encouragement through the final stages of my time here. My brother Danny, my sister Beth, and my brother-in-law Dan have been there for me my whole life, and their endless support has enabled me to meet all of life's challenges, both in and out of school. They have provided invaluable technical help during many "homework help" phone calls, where they have proven their ability to understand subject matter from any scientific field. Finally, my mother and father have instilled in me the values that make me who I am today. Their love and generosity through good times and bad has been unending. To them I am eternally grateful.

TABLE OF CONTENTS

LIST OF TABLES

LIST OF FIGURES

LIST OF ABBREVIATIONS

6DOF	Six-Degrees of Freedom
CEP	Circular Error Probable
CG	Center of Gravity
ITM	Internal Translating Mass
MPC	Model Predictive Control
MaRV	Maneuverable Reentry Vehicle
PGM	Precision-Guided Munition
PNG	Proportional Navigation Guidance
PRIM	Partially-Restrained Internal Member
SMC	Sliding Mode Control
SLNCG	stationline mass center position referenced from rear of projectile
UAV	Unmanned Aerial Vehicle
VSS	Variable Structure System

LIST OF SYMBOLS

$\vec{a}_{P/I}$	acceleration of the projectile mass center with respect to the inertial frame
$\vec{a}_{X/I}$	acceleration of the end point of the ITM-Beam with respect to the inertial frame
A_T	magnitude of ITM-Beam displacement from center of cavity
$\vec{A}_C$	acceleration command generated by proportional navigation contoller
b	radius of electromagnetic actuators
BL	length of the ITM-Beam assembly
C	composite body center of mass
c_v	viscous damping coefficient
C_i	various aerodynamic coefficients
$\mathbb{C}_X(y)$	vector component operator that outputs a column vector comprised of the components of the generic input vector y expressed in generic frame X
D	reference diameter of projectile
DM	magnitude of magnetic dipole moment of the fixed magnet at the end of the ITM beam
$\vec{F}_C$	constraint force between the projectile body and the ITM
$\vec{F}_I$	input force exerted on the ITM by electromagnetic actuators
$\vec{F}_P$	total aerodynamic force exerted on the projectile
f_{input}	scalar value of total force applied to ITM by electromagnetic actuators
g	acceleration due to gravity (9.8 m/s^2)
$\vec{H}^P_{P/I}$	angular momentum of the projectile with respect to the inertial frame about the projectile center of mass

$\vec{H}_{T/I}^{X}$	angular momentum of the translating mass with respect to the inertial frame about point *X*
I_E	current through the electromagnetic actuators
I_T	moment of inertia matrix of the ITM or ITM-Beam
I_P	moment of inertia matrix of the projectile
$\vec{I}_{XX}, \vec{J}_{XX}, \vec{K}_{XX}$	unit vectors in the specified *XX* reference frame
k	relative permeability of iron
k_D	torsional damper coefficient
k_T	torsional spring constant
L	hinge point between ITM-Beam and projectile body
L_A	length of the electromagnetic actuators
m_P	mass of the projectile body
m_T	mass of the ITM or ITM-Beam
m	total mass of composite system
$\vec{M}_P^L$	external moments applied to projectile about the hinge point *L*
$\vec{M}_{system}^{L}$	external moments applied to the ITM-projectile system about point *L*
M_X, M_Y, M_Z	external moment components on the projectile body expressed in the projectile reference frame
N_c	Proportional Navigation gain
P	projectile center of mass
$\vec{r}_{\alpha\to\beta}$	distance vector from generic point α to another generic point β
r_1, r_2, r_3	components in the *S* frame of $\vec{r}_{P\to L}$
r_4, r_5, r_6	components in the *S* frame of $\vec{r}_{P\to X}$
p, q, r	components of $\vec{\omega}_{P/I}$ in the projectile reference frame

$\tilde{p}, \tilde{q}, \tilde{r}$	components of $\vec{\omega}_{P/I}$ in the *S* reference frame
s	position of the internal translating mass along its line of movement with respect to the center of the cavity
$\mathbb{S}_X(y)$	skew-symmetric matrix representation of generic vector *y* expressed in reference frame *X*
T_{AB}	transformation matrix from generic reference frame *A* to generic reference frame *B*
u, v, w	translational velocity components of the composite body mass center expressed in the projectile reference frame
$\vec{v}_{\alpha/\mathrm{B}}$	velocity of the generic point α with respect to a generic frame B
V	magnitude of velocity of projectile mass center
v_s	speed of the translating mass with respect to the translating mass frame
$\vec{W}_P$	weight of the projectile body
$\vec{W}_T$	weight of the ITM
X	center of the spherical mass at the end of the ITM-Beam
x_T	cavity offset from the composite body mass center
x, y, z	position vector components of the composite body mass center expressed in the inertial reference frame
X_B, Y_B, Z_B	components of total external force on composite system expressed in the projectile reference frame
$\vec{\alpha}_{\mathrm{A/B}}$	angular acceleration of the generic body A with respect to generic frame B
λ	line-of-sight angle between a vector from the projectile to the target and a vector along the projectile's axis of symmetry
γ	deflection angle of the ITM-Beam
ρ	density of air
ϕ, θ, ψ	Euler pitch, roll, and yaw angles

ϕ_T, ψ_T	Euler pitch and yaw angles representing the orientation of frame *S* with respect to frame *P*
$\vec{\omega}_{\mathrm{A/B}}$	angular velocity vector of the generic body A with respect to generic frame B
ω_{beam}	magnitude of the angular velocity of the ITM-Beam with respect to frame *S*

SUMMARY

The field of guided projectile research has continually grown over the past several decades. Guided projectiles, typically encompassing bullets, mortars, and artillery shells, incorporate some sort of guidance and control mechanism to generate trajectory alterations. This serves to increase accuracy and decrease collateral damage. Control mechanisms for smart weapons must be able to withstand extreme acceleration loads at launch while remaining simple to reduce cost and enhance reliability. Controllable internal moving masses can be incorporated into the design of smart weapons as a mechanism to directly apply control force, to actively alter static stability in flight, and to protect sensitive components within sensor packages.

This dissertation examined techniques for using internal translating masses (ITM's) for smart weapon flight control. It was first shown that oscillating a mass orthogonal to the projectile axis of symmetry generates reasonable control force in statically-stable rounds. Trade studies examined the impact of mass size, mass offset from the center of gravity, and reductions in static stability on control authority. A more detailed analysis followed in which a physical internal translating mass control mechanism was designed that minimizes force and power required using a vibrating beam as the internal moving mass. Results showed that this relatively simple mechanism provides adequate control authority while requiring low on-board power. Trade studies revealed the affect of varying beam lengths, stiffness, and damping properties. Then, the topic of static margin control through mass center modification was explored. This is accomplished by translating a mass in flight along the projectile axis of symmetry. Results showed that this system allows for greater control authority and reduced throw-off error at launch. Finally, a nonlinear sliding mode controller was designed for a projectile equipped with an internal moving mass as well as for a projectile equipped with

both an ITM and canard control mechanisms. Monte Carlo simulations that incorporated realistic uncertainty demonstrated the robust nature of the control system. These dispersion simulations examined the effect of ITM size and incorporation of a variable stability mechanism. It is shown that use of an ITM as a direct control mechanism can reduce circular error probable by nearly half, while coupling ITM control with canard control can reduce required canard area by approximately half as well. Overall, it was determined that direct ITM control generates modest control authority for practical systems. Therefore, it can be used to reduce dispersion error but not eliminate it to levels commensurate with sensor noise. Likewise, the ITM variable stability mechanism provides a limited control authority enhancement to guided projectiles controlled by other means. Thus, while the mechanism may not be useful for guided munitions that exhibit ample control authority, it provides a useful supplement to projectiles requiring slight control authority improvement.

CHAPTER 1

INTRODUCTION

Throughout the past several decades, the U.S. military has been engaged in numerous conflicts involving challenging battlefield scenarios. Combat in urban environments and against non-traditional adversaries have often exposed significant flaws in tactics and equipment that were developed for battle against a traditional large military force. These deficiencies have motivated new procurement strategies aimed at developing weapons and tactics suitable for operations in urban environments and against non-traditional foes.[1]

A key component of these new weapons systems are precision guided munitions ("smart projectiles") designed to enhance the accuracy of field artillery and other gun-launched projectiles. Precision guided munitions (PGM's) have the capability to correct trajectory errors in flight and to actively guide to designated targets using on-board control mechanisms. However, smart projectiles differ from guided missiles in that their electronics and control mechanisms must be able to withstand extreme acceleration loads associated with launch and high spin rates. Control components must be relatively inexpensive, since projectiles are typically fired in large quantities. Modern advancements in robust electronic sensors, actuators, and control systems have been the key to developing systems that meet these stringent requirements.

Precision guided munitions offer several key advantages over traditional unguided rounds, including increased combat effectiveness, improved operational flexibility, and a reduced logistical burden. Due to the increased accuracy of guided rounds, the need for high volumes of fire to hit a specific target is reduced, as is the time it takes to neutralize a target. Furthermore, because "the rules of engagement and collateral damage estimates drive the targeting decision-making process," [2] use of precision guided munitions

allows targets that have large potential for collateral damage (for instance, targets embedded in urban canyons) to be engaged with increased confidence, leading to more flexibility for field commanders. Additionally, because a single precision munition can be used in place of large volleys of unguided rounds, the logistical burden on field batteries is significantly reduced on a per-target basis.[2]

However, even though high-precision smart projectiles are useful for a wide variety of missions, the army retains the need "to saturate large areas with fire in high-intensity conflict."[3] Such missions can involve cases in which enemy location is not precisely known or "fire for effect" missions in which there is no single target to engage. In these scenarios, it may be desirable to reduce dispersion error only to a certain point in order to maintain the area fire capability of indirect fire munitions. Therefore, limited control authority systems that can significantly reduce dispersion error (but do not provide a precision strike capability) are still useful in many engagement scenarios.

Numerous smart weapons development programs have been conducted over the past several decades. While many in the areas of missiles and precision-guided bombs have been fielded, there has been only limited success in fielding smart munitions. Control engineers and designers have been challenged by the relatively small size, high spin rates and velocities, and large acceleration loads of these classes of munitions, leading to many novel control actuator designs. Some of these actuators, such as canards [4,65], ram air deflectors [5,6], and moveable noses [70,71], rely on aerodynamic effects to provide control. Others, such as gas or explosive thrusters [7,61], rely on on-board thrust mechanisms. A third class of actuator designs, inertial load mechanisms, change fundamental mass properties of the projectile leading to aerodynamically-induced control forces.[8,9] All of these mechanisms have positive and negative aspects associated with them, and the ultimate selection of a control mechanism for a smart weapon is complex and depends on the application. Furthermore, many of these control techniques are capable only of slightly altering the projectile's trajectory, often referred to as "ballistic

nudging," due to typical projectile stability characteristics and flight regimes. This limited control authority inherent in projectile configurations stands in stark contrast to missiles, which often exhibit relatively large control response.

This thesis focuses on examining the use of controllable internal moving parts for smart weapon flight control purposes, namely, as a direct control mechanism, as a means to enhance control authority, and as a means to protect the smart weapon sensor suite. While Section 1.1 provides a comprehensive overview of research performed on moving mass flight control for air vehicles, several other brief literature surveys are discussed at the beginning of Chapters 4, 5, and 6 providing background on topics related specifically to the applications discussed in those chapters.

1.1. Flight Vehicles with Moving Mass Control

Moving mass control has been applied to a wide variety of vehicles. However, for a moving mass system to provide significant control authority, movement of the internal mass must correspond to reasonably large changes in the system mass center of the air vehicle. This has restricted the use of moving mass control systems to vehicles in which a significant proportion of vehicle weight, on the order of several percent or more, can be reliably translated without prohibitive energy requirements. As a result, maneuverable reentry vehicles (MaRV's), missiles, unmanned aerial vehicles (UAV's), and gun-launched projectiles have proven suitable applications for moving mass control mechanisms.

Significant research has been conducted by several investigators exploring the use of moving mass control in reentry vehicle applications. A main advantage of moving mass control in this class of vehicles is that the control mechanism is not exposed to extreme aerodynamic loads experienced during reentry, unlike standard canard control mechanisms. In addition, extremely large drag forces act on the airframe during reentry,

leading to generation of large control moments. Petsopoulos, Regan, and Barlow [14] used an internal translating mass in a roll-control system for a fixed-trim re-entry vehicle. The controlled moving mass translated along a line perpendicular to the projectile centerline. When translated off the projectile centerline, the system mass center was laterally offset from the aerodynamic center of pressure, inducing a roll moment. In this way, the projectile could be controlled to a prescribed roll angle, and as a result of the vehicle's fixed angle of attack configuration this roll control mechanism could be used for trajectory maneuvers. Roll control autopilot equations were developed, using a linear quadratic regulator design. Furthermore, gain scheduling techniques were implemented so as to adapt the control system to the disparities in dynamic pressure experienced by re-entry vehicles throughout flight. Simulations showed that using a 2.5% mass ratio, significant roll control was possible and substantial trajectory maneuvers could be induced.

Further work was performed by Robinett, Sturgis, and Kerr [15] to investigate ITM control of both slow-spinning vehicles, exemplified by re-entry vehicles, and fast-spinning vehicles, exemplified by artillery rockets. The authors first developed equations of motion using a six-degree-of-freedom (6DOF) projectile model and a point mass ITM that could move freely in a two-dimensional plane perpendicular to the projectile's axis of symmetry. Autopilot equations were then developed to keep the mass stationary with respect to the body in a non-rolling reference frame. The authors claimed that, for slow-spinning vehicles, aerodynamic forces dominate and control moment could be effectively generated from aerodynamic drag acting at a lateral offset from the system center of mass (the same control technique considered by Petsopoulos, et al. in Reference [14]). However, for fast-spinning vehicles, inertial forces dominate and control moment could be generated by principle axis misalignment if the ITM could once again be held stationary with respect to the body in a non-rolling frame. Simulations of both fast- and slow-spinning vehicles equipped with an ITM verified that control force could be

generated to produce reasonable divert capability. Example conceptual designs for ITM mechanisms were also presented.

Menon, Sweriduk, Ohlmeyer, and Malyevac [16] considered internal translating mass control of kinetic warheads used as missile interceptors. Three orthogonal translating masses were proposed, and once again control moment was generated by a lateral offset between the aerodynamic center of pressure and the system center of mass. In exoatmospheric scenarios, control moment was generated during thrusting maneuvers by a similar lateral offset between the thrust line of action and the system mass center. A guidance and control system was developed using feedback linearization techniques. Endoatmospheric and exoatmospheric interception scenarios were considered using both non-maneuvering and weaving targets, and it was demonstrated that orthogonal ITM's, each of approximately 9% mass ratio, produced sufficient control authority to successfully intercept. The authors noted, however, that for ITM's to provide sufficient control authority within the atmosphere the airframe "must have near-neutral aerodynamic static stability characteristics."

Unmanned aerial vehicles provide a particularly suitable application for ITM control since they are often lightweight, allowing for generation of large changes in system mass center. An example of moving mass control of UAV's is provided by Beyer and Costello [69] in the design and implementation of the Hopping Rotochute. This vehicle is a small, lightweight, coaxial helicopter in the shape of a weeble-wobble.[72] The vehicle is pitched in the desired direction by creating a thrust-line offset from the vehicle center of mass. Therefore, the center of mass of the system is controlled by rotating an internal mass to a desired position on the body. A 3.4% mass was experimentally shown to provide sufficient control authority. A picture of the Hopping Rotochute with its internal moving mass highlighted is shown in Figure 1.1.

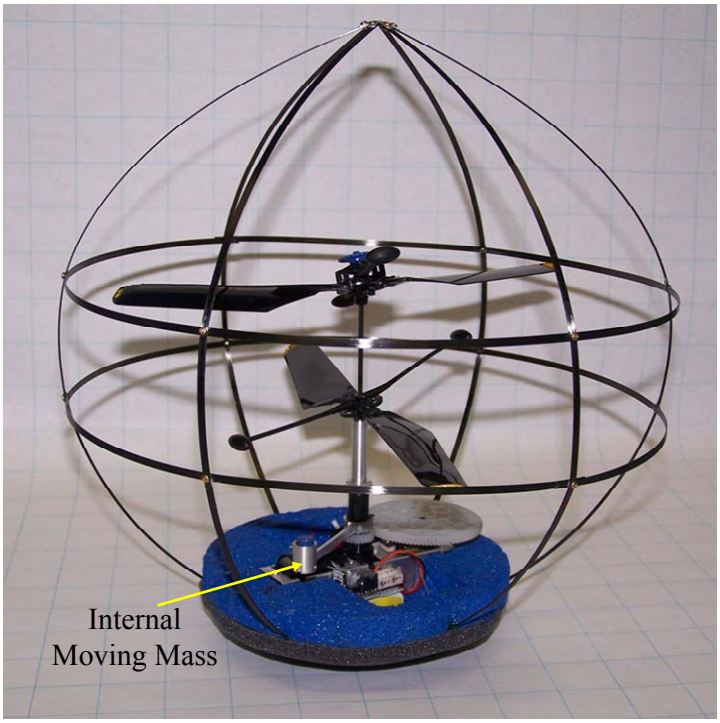

Figure 1.1: Beyer's Hopping Rotochute.

Recently, further research has attempted to incorporate moving mass control into gun-launched munitions for control purposes. Frost and Costello [8] considered a projectile wherein a disk rigidly attached in an arbitrary orientation with respect to the projectile is allowed to rotate at a constant angular velocity. Such configurations have been used in systems to precisely control projectile spin. Frost and Costello assumed known motion for the disk, and a modified linear model was developed for this configuration. This model was used to predict the affect of the rotating component on the epicyclic modes of a spin-stabilized projectile. It was found that the rotating component can alter the epicyclic dynamics substantially, even causing instability in some cases. A study on the effect of frequency and damping of these epicyclic modes was conducted by varying disk orientation, mass, location, and rotational speed.

Additional work conducted by Frost and Costello [9] investigated control authority of a round equipped with an unbalanced part that could rotate off the projectile

centerline. At some point after launch, the unbalanced part rotates to a desired roll orientation relative to the no-roll reference frame, creating a stationary mass unbalance in the two-body system. This mass unbalance creates a control moment produced by axial drag about the composite body center of mass. Frost and Costello showed that reasonable control authority could be generated for both fin-stabilized and spin-stabilized rounds, and that control authority increases linearly with the mass of the rotating part multiplied by the offset of the part from the projectile centerline. The authors found that reducing projectile stability and altering aerodynamic characteristics served to increase control authority as well.

1.2 Instability of Projectiles with Loose Internal Parts

Although extensive research has shown that moving masses in a controlled fashion leads to the potential for air vehicle flight control, it has also been shown that vehicles that contain masses allowed to vibrate or move in an uncontrolled fashion can lead to serious stability problems. Flight tests of new artillery projectiles in the 1950's resulted in the surprising discovery that very small masses moving or vibrating within a round could create significant instability. These projectiles were equipped with rotating ball fuses, sliding rings, or other internal parts that were able to vibrate or somehow move in an uncontrolled fashion within the round. Extensive research has been conducted over the past three decades in order to understand these flight instabilities.

One of the first researchers to explore these stability issues was Soper, [10] who considered a projectile containing a cylindrical mass fitted loosely within a cylindrical cavity. Although this internal mass was constrained to roll with the projectile, it could move slightly in a radial and longitudinal direction. This configuration is typical of a projectile equipped with ballast weights. Flight tests had previously shown that ballasted spin-stabilized projectiles were susceptible to continual growth in coning angle and

unusually large spin decay. Soper derived a quasi-steady state solution for the system, and showed that an unstable coning motion is obtained with this configuration. The severity of this instability was shown to be dictated by the tolerance between the cylindrical mass and the cavity as well as the frictional coefficient between the two. Reasonable parameters were shown to produce prohibitively large coning angles and a high rate of spin decay.

Shortly afterward, Murphy [11] developed a quasi-linear solution for projectiles equipped with internal masses that undergo either uncontrolled translation or uncontrolled rotation off the centerline axis of the projectile. This research was also motivated by instabilities observed during flight tests of rounds with internal moving components. Murphy's model showed that internal moving masses could decrease the damping rate of the projectile's fast-mode epicyclic motion, which in turn could cause a rapid decrease in spin rate. The results from this model reasonably matched the nature of instabilities observed during flight test.

Murphy's model provides a basis for ballistics engineers to predict under what conditions flight instabilities might occur as a result of so-called "partially-restrained internal members" (PRIM's). It assumes that the projectile undergoes decoupled slow and fast precessional modes, and in a quasi-linear fashion considers only the fast-mode as a contributor to PRIM motion. This leads to two types of resulting motion of the PRIM: precession about the PRIM's axis of symmetry and a circulatory motion of the PRIM's mass center about the projectile axis of symmetry, both at the precession frequency of the projectile. The amplitudes and phase angles of these motions are needed as inputs to the theory, so maximum physical tolerances and phase angles of 45-90 deg have traditionally been assumed when using the model.

Almost ten years after Murphy's formulation of this closed-form solution for PRIM motion, D'Amico [12] attempted to develop a more complete picture of PRIM motion via experimental methods. A hollow cylindrical ring, like that considered by

Soper [10] and Murphy [11], was attached to a freely-gimbaled gyroscope to recreate free-flight motion of a spin-stabilized projectile equipped with a PRIM. Specifically, the setup was designed to determine the phase angle between motion of the PRIM and the yaw motion of the gyroscope, which could then be used as inputs to Murphy's quasi-linear theory. Finally, D'Amico compared the motion of the gyroscope to that predicted by Murphy using experimental data as inputs. D'Amico found that when Murphy's assumptions were appropriately modeled by the experiment (namely when the motion had reached steady-state) the theoretical and experimental predictions of yaw growth matched quite well. Furthermore, experimental data showed that the use of maximum tolerances and assumed phase angles in Murphy's model resulted in over-predictions of actual PRIM-induced motion. A diagram of D'Amico's experimental setup is shown in Figure 1.2.

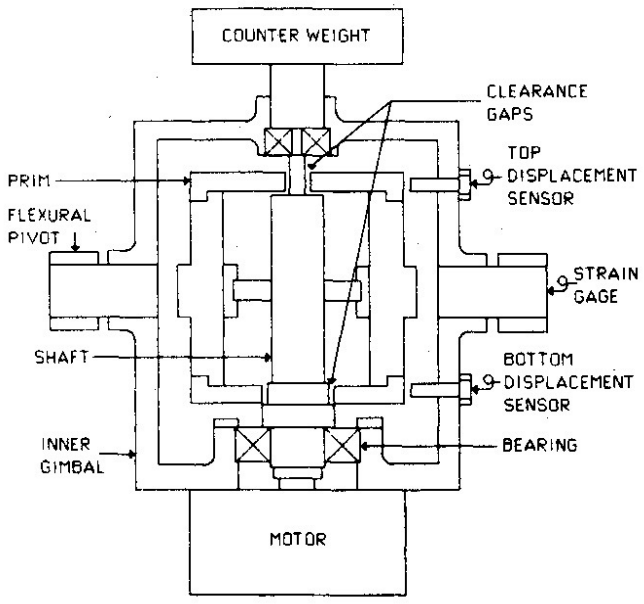

Figure 1.2: D'Amico's PRIM Experimental Setup.

Hodapp [13] continued the study of flight dynamics of projectiles with moving internal parts by considering the affect of a small offset between the projectile body mass

and the PRIM mass center. Hodapp's analysis of the dynamic equations for this system showed that, for small mass center offsets (on the order of those occurring randomly within manufacturing tolerances), slight movement could actually reduce the instability caused by the loose internal part. This stabilizing effect was confirmed through experimental tests.

1.3 Contributions of the Thesis

The contributions of this thesis involve five distinct research areas that are related in that they all involve moving mass technology applied to smart weapons. The five research areas are:

1. Control authority of a projectile equipped with a controllable internal translating mass.
2. Cantilever beam actuator design for projectile internal moving mass systems.
3. Active static margin control of projectiles using internal translating masses.
4. Sensor suite shock absorbers using internal translating masses.
5. Active control of projectiles equipped with internal moving mass actuators and combined canard-moving mass actuators.

1.4 Thesis Outline

This thesis is composed of seven chapters. A brief description of each chapter follows:

1. **Chapter 1: Introduction.** A description of the problem statement, the previous work on each topic, and the contribution of the present work are described.
2. **Chapter 2: Control Authority of a Projectile Equipped with a Controllable Internal Translating Mass.** A dynamic model of a projectile equipped with a translating mass is developed. Example simulation results are presented

demonstrating reasonable control authority. Trade studies varying system parameters are described.

3. **Chapter 3: Cantilever Beam Design of Projectile Internal Moving Mass Systems.** Another dynamic model is formulated in which the internal mass rotates on a cantilever beam within the projectile body, providing an example physical design for implementation. Example results and numerous trade studies demonstrate the advantages of this actuator design.
4. **Chapter 4: A Variable Stability Projectile Using an Internal Translating Mass.** The concept of translating a mass along the projectile's longitudinal axis during flight is discussed, exploring the impact of active static margin control. Results show that projectiles that can alter static margin control in flight require less control force than rigid projectiles to achieve the same reduction in dispersion error.
5. **Chapter 5: Sensor Suite Shock Absorbers Using an Internal Translating Mass.** A translating mass consisting of sensitive components from the electronics package within a smart weapon is considered, in which movement again takes place along the projectile's longitudinal axis. Translating mass movement occurs freely during launch and is heavily damped, aimed at providing protection against large acceleration loads. Simulation results show that, while overall acceleration loads cannot be decreased significantly, high frequency oscillations in g-loading can be considerably reduced.
6. **Chapter 6: Active Control of a Projectile Using an Internal Moving Mass.** A sliding mode guidance law is developed for an indirect fire munition using the internal moving mass control actuator and a combined canard-moving mass actuator. Dispersion simulations incorporating model uncertainty and sensor noise show the control system's effectiveness at circular error probable.

7. **Chapter 7: Conclusions and Future Work.** Conclusions from the different moving mass technologies are summarized and future work relating to several areas is proposed.

CHAPTER 2

CONTROL AUTHORITY OF A PROJECTILE USING AN INTERNAL TRANSLATING MASS

This chapter examines the trajectory alteration potential of a single internal translating mass aligned along the lateral axis of a projectile. Control authority is generated by a lateral mass center offset from the aerodynamic center of pressure. The chapter begins with a brief note on nomenclature and a description of a seven degree of freedom flight dynamic model used for trajectory predictions. A description of a flight control system to generate translating mass movement is also presented. The dynamic model is subsequently employed to predict control authority for an example projectile. Then, effects of key physical properties of the system such as internal mass size, cavity stationline location, mass oscillation amplitude, and static stability properties are examined against swerve production capability. [18,22]

2.1 Note on Nomenclature

The nomenclature used throughout this dissertation for position, velocity, angular velocity, and acceleration vectors is as follows. The nomenclature for position vectors is such that $\vec{r}_{\alpha\to\beta}$ is defined as the position vector from point α to point β. For velocity and acceleration vectors, the symbols $\vec{v}_{\alpha/Z}$ and $\vec{a}_{\alpha/Z}$ represent the velocity and acceleration vectors respectively of point α with respect to frame *Z*. Unit vectors along the *x*, *y*, and *z* axis in frame *Z* are written as $\vec{I}_Z$, $\vec{J}_Z$, and $\vec{K}_Z$ respectively. The angular velocity and angular acceleration vectors of frame *Y* with respect to frame *Z* are written as $\vec{\omega}_{Y/Z}$ and

$\vec{\alpha}_{Y/Z}$ respectively. Also, all equations in this thesis use the following shorthand notation for trigonometric sine, cosine, and tangent functions: $s_\alpha = \sin\alpha$, $c_\alpha = \cos\alpha$, $t_\alpha = \tan\alpha$.

The vector component operator shown in equation (2.1) outputs a column vector comprised of the components of an input vector in a given frame. For example, if the position vector from α to β is expressed in reference frame A as $\vec{r}_{\alpha\to\beta} = \Delta x_{\alpha\beta}\vec{I}_A + \Delta y_{\alpha\beta}\vec{J}_A + \Delta z_{\alpha\beta}\vec{K}_A$ then the vector component operator acting on this vector yields

$$\mathbb{C}_A(\vec{r}_{\alpha\to\beta}) = \begin{Bmatrix} \Delta x_{\alpha\beta} \\ \Delta y_{\alpha\beta} \\ \Delta z_{\alpha\beta} \end{Bmatrix} \tag{2.1}$$

Notice that the reference frame is denoted by the subscript on the operator.

The cross product operator shown in equation (2.2) outputs a skew symmetric matrix using the components of an input vector in the reference frame denoted in the subscript. For example, if the position vector from α to β is expressed in reference frame A as $\vec{r}_{\alpha\to\beta} = \Delta x_{\alpha\beta}\vec{I}_A + \Delta y_{\alpha\beta}\vec{J}_A + \Delta z_{\alpha\beta}\vec{K}_A$ then the cross product operator acting on $\vec{r}_{\alpha\to\beta}$ expressed in reference frame A is

$$\mathbb{S}_A(\vec{r}_{\alpha\to\beta}) = \begin{bmatrix} 0 & -\Delta z_{\alpha\beta} & \Delta y_{\alpha\beta} \\ \Delta z_{\alpha\beta} & 0 & -\Delta x_{\alpha\beta} \\ -\Delta y_{\alpha\beta} & \Delta x_{\alpha\beta} & 0 \end{bmatrix} \tag{2.2}$$

2.2 Internal Translating Mass Projectile Dynamic Model

A sketch of the basic projectile configuration is shown in Figure 2.1, while a more detailed schematic is shown in Figure 2.2. It consists of two major components, namely,

a main projectile body and an internal translating mass. The main projectile body is largely a typical projectile with the exception of an internal cavity that hosts an internal mass. The internal mass is free to translate within the main projectile cavity. An actuator inside the projectile exerts a force on the internal mass as well as the main projectile to move the mass inside the cavity to a desired location. Note that while Figures 2.1 and 2.2 show an arbitrary example artillery shell, the mechanism can be implemented on many classes of munitions.

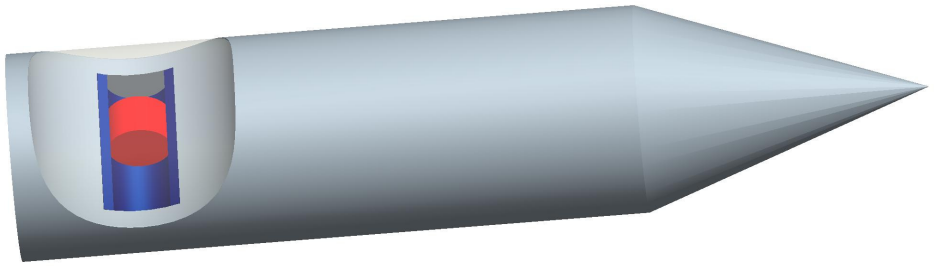

Figure 2.1: Sketch of the Translating Mass Projectile.

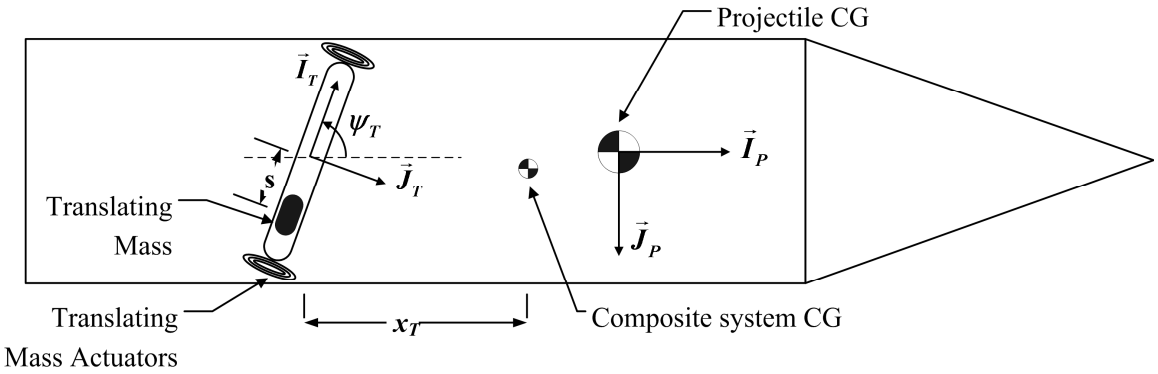

Figure 2.2: Schematic of the Translating Mass Projectile.

Three reference frames are used in development of the equations of motion for the system, namely the inertial, projectile, and translating mass reference frames. The three reference frames are related by the following two orthonormal transformation matrices.

$$\begin{Bmatrix} \vec{I}_P \\ \vec{J}_P \\ \vec{K}_P \end{Bmatrix} = \begin{bmatrix} c_\theta c_\psi & c_\theta s_\psi & -s_\theta \\ s_\phi s_\theta c_\psi - c_\phi s_\psi & s_\phi s_\theta s_\psi + c_\phi c_\psi & s_\phi c_\theta \\ c_\phi s_\theta c_\psi + s_\phi s_\psi & c_\phi s_\theta s_\psi - s_\phi c_\psi & c_\phi c_\theta \end{bmatrix} \begin{Bmatrix} \vec{I}_I \\ \vec{J}_I \\ \vec{K}_I \end{Bmatrix} = [T_{IP}] \begin{Bmatrix} \vec{I}_I \\ \vec{J}_I \\ \vec{K}_I \end{Bmatrix} \tag{2.3}$$

$$\begin{Bmatrix} \vec{I}_T \\ \vec{J}_T \\ \vec{K}_T \end{Bmatrix} = \begin{bmatrix} c_{\theta_T} c_{\psi_T} & c_{\theta_T} s_{\psi_T} & -s_{\theta_T} \\ -s_{\psi_T} & c_{\psi_T} & 0 \\ s_{\theta_T} c_{\psi_T} & s_{\theta_T} s_{\psi_T} & c_{\theta_T} \end{bmatrix} \begin{Bmatrix} \vec{I}_P \\ \vec{J}_P \\ \vec{K}_P \end{Bmatrix} = [T_{PT}] \begin{Bmatrix} \vec{I}_P \\ \vec{J}_P \\ \vec{K}_P \end{Bmatrix} \tag{2.4}$$

The inertial reference frame is referred to as the *I* frame. The projectile-fixed reference frame, the origin of which lies at the system mass center, is referred to as the *P* frame. The *T* frame, aligned with the translating mass cavity and centered at the middle of the cavity, is assumed to be fixed with respect to the *P* frame, and therefore the angles ψ_T and θ_T (the cavity pitch angle, not shown in Figure 2.2) do not change with time. A schematic of the reference frames used in the development of the dynamic model are shown in Figure 2.3.

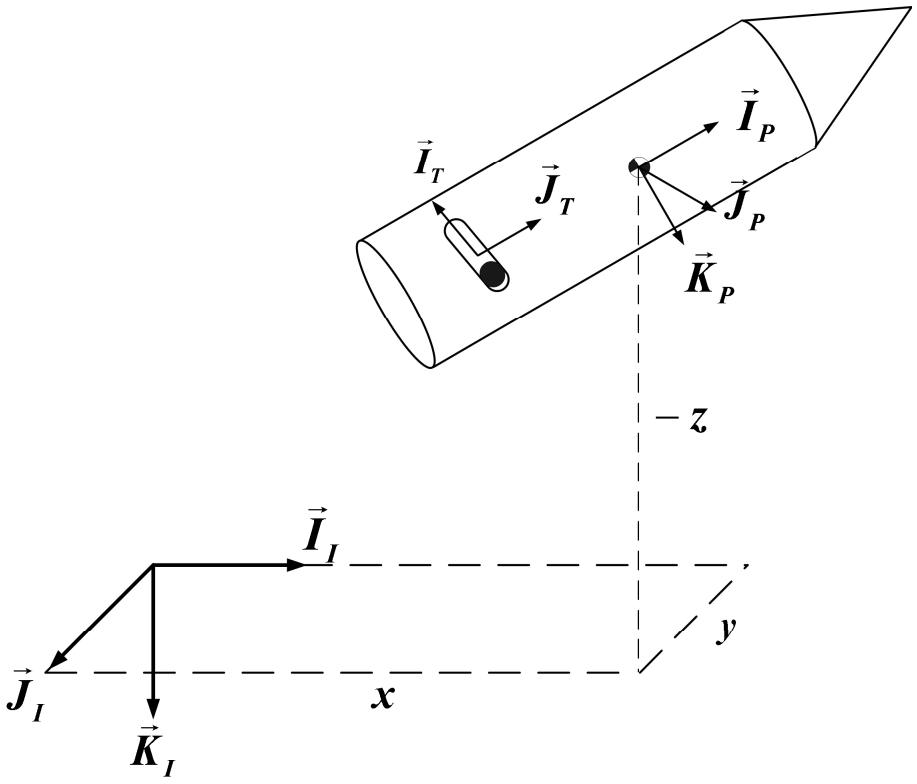

Figure 2.3: Reference Frame Schematic.

Throughout the development of the equations of motion, several different position vectors are used. The position vector of the mass center of the two-body system with respect to a ground fixed reference frame is written as,

$$\vec{r}_{O\to C} = x\vec{I}_I + y\vec{J}_I + z\vec{K}_I \tag{2.5}$$

while the position of the internal translating mass with respect to the projectile reference frame is,

$$\vec{r}_{C\to T} = \left(x_T + s(c_{\theta_T} c_{\psi_T})\right)\vec{I}_P + \left(s(c_{\theta_T} s_{\psi_T})\right)\vec{J}_P + \left(s(-s_{\theta_T})\right)\vec{K}_P \tag{2.6}$$

where x_T is the distance from the cavity center to the system center of mass along $\vec{I}_P$, and s is the position of the internal translating mass within the cavity. The mathematical model describing the motion of the internal translating mass projectile allows for 4 translational and 3 rotational rigid body degrees of freedom. The translational degrees of freedom are the three components of the composite body mass center position vector (x, y, z) and the position of the internal translating mass with respect to the projectile body (s). The rotational degrees of freedom are the Euler roll, pitch, and yaw angles (ϕ , θ, ψ) mentioned above.

2.2.1 Kinematics

The velocity of the composite body mass center can be described in the inertial reference frame or the projectile reference frame.

$$\vec{v}_{C/I} = \dot{x}\vec{I}_I + \dot{y}\vec{J}_I + \dot{z}\vec{K}_I = u\vec{I}_P + v\vec{J}_P + w\vec{K}_P \tag{2.7}$$

The translational kinematic differential equations relate these two representations of the mass center velocity components.

$$\begin{Bmatrix} \dot{x} \\ \dot{y} \\ \dot{z} \end{Bmatrix} = \begin{bmatrix} c_\theta c_\psi & s_\phi s_\theta c_\psi - c_\phi s_\psi & c_\phi s_\theta c_\psi + s_\phi s_\psi \\ c_\theta s_\psi & s_\phi s_\theta s_\psi + c_\phi c_\psi & c_\phi s_\theta s_\psi - s_\phi c_\psi \\ -s_\theta & s_\phi c_\theta & c_\phi c_\theta \end{bmatrix} \begin{Bmatrix} u \\ v \\ w \end{Bmatrix} = \left[T_{IP}\right]^T \begin{Bmatrix} u \\ v \\ w \end{Bmatrix} \tag{2.8}$$

The angular velocity of the projectile with respect to the inertial reference frame can be written in terms of appropriate Euler angle time derivatives or in terms of projectile frame angular velocity components.

$$\vec{\omega}_{P/I} = \dot{\phi}\vec{I}_P + \dot{\theta}\vec{J}_N + \dot{\psi}\vec{K}_I = p\vec{I}_P + q\vec{J}_P + r\vec{K}_p \tag{2.9}$$

The kinematic relationship between time derivatives of the Euler angles and projectile reference frame angular velocity components represents the rotational kinematic differential equations.

$$\begin{Bmatrix} \dot{\phi} \\ \dot{\theta} \\ \dot{\psi} \end{Bmatrix} = \begin{bmatrix} 1 & s_\phi t_\theta & c_\phi t_\theta \\ 0 & c_\phi & -s_\phi \\ 0 & s_\phi / c_\theta & c_\phi / c_\theta \end{bmatrix} \begin{Bmatrix} p \\ q \\ r \end{Bmatrix} \tag{2.10}$$

The final kinematic differential equation is the trivial relationship

$$\dot{s} = v_S \tag{2.11}$$

where v_s is the velocity of the translating mass with respect to the center of the cavity.

2.2.2 Dynamics

The translational dynamic equations for both the projectile and internal mass are derived through force balancing. They are given by

$$m_p \vec{a}_{P/I} = \vec{W}_P + \vec{F}_P - \vec{F}_C - \vec{F}_I - \vec{F}_F \tag{2.12}$$

$$m_T \vec{a}_{T/I} = \vec{W}_T + \vec{F}_C + \vec{F}_I + \vec{F}_F \tag{2.13}$$

The mass center definition is given by

$$m\vec{r}_{O\to C} = m_P\vec{r}_{O\to P} + m_T\vec{r}_{O\to T} \tag{2.14}$$

Taking first and second derivatives of this equation in the inertial frame leads respectively to

$$m\vec{v}_{C/I} = m_P\vec{v}_{P/I} + m_T\vec{v}_{T/I} \tag{2.15}$$

$$m\vec{a}_{C/I} = m_P\vec{a}_{P/I} + m_T\vec{a}_{T/I} \tag{2.16}$$

By adding equations (2.12) and (2.13) and noting the mass center definition in (2.16), the translational dynamics equation for the system is formed.

$$m\vec{a}_{C/I} = \vec{W}_P + \vec{W}_T + \vec{F}_P \tag{2.17}$$

Writing equation (2.17) in the projectile reference frame yields,

$$\begin{Bmatrix} \dot{u} \\ \dot{v} \\ \dot{w} \end{Bmatrix} = \begin{Bmatrix} \frac{X_B}{m} \\ \frac{Y_B}{m} \\ \frac{Z_B}{m} \end{Bmatrix} - \begin{bmatrix} 0 & -r & q \\ r & 0 & -p \\ -q & p & 0 \end{bmatrix} \begin{Bmatrix} u \\ v \\ w \end{Bmatrix} \tag{2.18}$$

where X, Y, and Z are the sum of the three forces given in equation (2.17). Another translational dynamic equation is formed from the $\vec{I}_T$ component of the translating mass equation of motion shown in equation (2.13). The well-known formula for one point moving on a rigid body yields, [26]

$$\vec{a}_{T/I} = \vec{a}_{P/I} + \vec{a}_{T/P} + (\vec{\alpha}_{P/I} \times \vec{r}_{P\to T}) + 2(\vec{\omega}_{P/I} \times \vec{v}_{T/P}) + (\vec{\omega}_{P/I} \times (\vec{\omega}_{P/I} \times \vec{r}_{P\to T})) \quad (2.19)$$

The mass center definition allows a substitution for $\vec{a}_{P/I}$, yielding

$$\vec{a}_{T/I} = \vec{a}_{C/I} + \frac{m_P}{m}\left[\vec{a}_{T/P} + (\vec{\alpha}_{P/I} \times \vec{r}_{P\to T}) + 2(\vec{\omega}_{P/I} \times \vec{v}_{T/P}) + (\vec{\omega}_{P/I} \times (\vec{\omega}_{P/I} \times \vec{r}_{P\to T}))\right] \quad (2.20)$$

Multiplying through by m_T,

$$m_T\vec{a}_{T/I} = m_T\vec{a}_{C/I} + \frac{m_P m_T}{m}\left[\vec{a}_{T/P} + (\vec{\alpha}_{P/I} \times \vec{r}_{P\to T}) + 2(\vec{\omega}_{P/I} \times \vec{v}_{T/P}) + (\vec{\omega}_{P/I} \times (\vec{\omega}_{P/I} \times \vec{r}_{P\to T}))\right] \quad (2.21)$$

The translating mass equation of motion is therefore

$$m_T\vec{a}_{C/I} + \frac{m_P m_T}{m}\left[\vec{a}_{T/P} + (\vec{\alpha}_{P/I} \times \vec{r}_{P\to T}) + 2(\vec{\omega}_{P/I} \times \vec{v}_{T/P}) + (\vec{\omega}_{P/I} \times (\vec{\omega}_{P/I} \times \vec{r}_{P\to T}))\right] = \vec{W}_T + \vec{F}_C + \vec{F}_I + \vec{F}_F \quad (2.22)$$

Extracting the $\vec{I}_T$ component of this equation is accomplished by taking the inner product of the equation with $\vec{I}_T$. Notice that the constraint force along $\vec{I}_T$ is zero since motion along this axis is permitted in the model. The following simplifications can therefore be made.

$$\vec{I}_T \bullet \vec{F}_C = 0 \quad (2.23)$$

$$\vec{I}_T \bullet (\vec{\omega}_{P/I} \times \vec{v}_{T/P}) = 0 \quad (2.24)$$

$$\vec{I}_T \bullet \vec{a}_{T/P} = \ddot{s} \quad (2.25)$$

$$\vec{I}_T \bullet \vec{F}_I = f_{Input} \tag{2.26}$$

$$\vec{I}_T \bullet \vec{F}_F = -c_V \dot{s} \tag{2.27}$$

In component form, this equation of motion is written as

$$\begin{bmatrix} A_{S1} & A_{S2} & A_{S3} \end{bmatrix} \begin{Bmatrix} \dot{u} \\ \dot{v} \\ \dot{w} \\ \ddot{s} \\ \dot{p} \\ \dot{q} \\ \dot{r} \end{Bmatrix} = \{B_S\} \tag{2.28}$$

where

$$A_{S1} = m_T \left[c_{\theta_T} c_{\psi_T}, c_{\theta_T} s_{\psi_T}, -s_{\theta_T} \right] \tag{2.29}$$

$$A_{S2} = \frac{m_P m_T}{m} \tag{2.30}$$

$$A_{S3} = -\frac{m_P m_T}{m} \left[c_{\theta_T} c_{\psi_T}, c_{\theta_T} s_{\psi_T}, -s_{\theta_T} \right] \mathbb{S}_P \left(\vec{r}_{P \to T} \right) \tag{2.31}$$

$$\begin{aligned} B_S = f_{Input} - c_V \dot{s} + \\ m_T g (-s_\theta c_{\theta_T} c_{\psi_T} + s_\phi c_\theta c_{\theta_T} s_{\psi_T} - c_\phi c_\theta s_{\theta_T}) - \\ m_T \left[c_{\theta_T} c_{\psi_T}, c_{\theta_T} s_{\psi_T}, -s_{\theta_T} \right] \mathbb{S}_P(\vec{\omega}_{P/I}) \mathbb{C}_P(\vec{v}_{C/I}) - \\ \frac{m_P m_T}{m} \left[c_{\theta_T} c_{\psi_T}, c_{\theta_T} s_{\psi_T}, -s_{\theta_T} \right] \mathbb{S}_P(\vec{\omega}_{P/I}) \mathbb{S}_P(\vec{\omega}_{P/I}) \mathbb{C}_P(\vec{r}_{P \to T}) \end{aligned} \tag{2.32}$$

Note that in equation (2.32), a viscous friction force is incorporated in the translational dynamics for the ITM using the friction coefficient c_v. This friction force accounts for both contact friction and air resistance as the ITM translates within the cavity.

The rotational dynamic equations are obtained by equating the *I* frame time rate of change of the system angular momentum about the system mass center to the total applied external moments to the system about the system mass center.

$$\frac{{}^{I}d\vec{H}^{P}_{P/I}}{dt}+\frac{{}^{I}d\vec{H}^{T}_{T/I}}{dt}+m_P\vec{r}_{C\to P}\times\vec{a}_{P/I}+m_T\vec{r}_{C\to T}\times\vec{a}_{T/I}=\vec{M}^{C} \tag{2.33}$$

Expressed in the projectile reference frame, the components of this equation are

$$A_{RR}\begin{Bmatrix}\dot{p}\\ \dot{q}\\ \dot{r}\end{Bmatrix}+A_{RS}\{\ddot{s}\}=\{B_R\} \tag{2.34}$$

where

$$A_{RR}=I_P+I_T-\frac{m_T}{m_P}m\mathbb{S}_P(\vec{r}_{C\to T})\mathbb{S}_P(\vec{r}_{C\to T}) \tag{2.35}$$

$$A_{RS}=m_T\mathbb{S}_P(\vec{r}_{C\to T})\left[T_{PT}\right]^T \tag{2.36}$$

$$\begin{aligned}B_R=&\begin{Bmatrix}M_X\\ M_Y\\ M_Z\end{Bmatrix}-\mathbb{S}_P\left(\vec{\omega}_{P/I}\right)\left(I_P+I_T-\frac{m_T}{m_P}m\mathbb{S}_P(\vec{r}_{C\to T})\mathbb{S}_P(\vec{r}_{C\to T})\right)\mathbb{C}_P\left(\vec{\omega}_{P/I}\right)-\\ &2m_T\mathbb{S}_P(\vec{r}_{C\to T})\mathbb{S}_P(\vec{\omega}_{P/I})\left[T_{PT}\right]^T\begin{Bmatrix}\dot{s}\\ 0\\ 0\end{Bmatrix}\end{aligned} \tag{2.37}$$

The dynamic equations of motion for the internal translating mass projectile are given collectively by equations (2.8), (2.10), (2.11), (2.18), (2.28), and (2.34). With a known set of initial conditions for the projectile, these 14 scalar equations are numerically integrated forward in time using a 4th order Runge-Kutta algorithm to obtain a single trajectory. [40]

2.2.3 Projectile Applied Forces and Moments

In the equations developed above, applied loads drive the motion of the projectile. Aerodynamic forces and moments calculated within the flight dynamic simulation use the PRODAS aerodynamic expansion, [27] an industry-standard aerodynamics model used extensively in ballistics and smart weapons research. The total applied force on the system is given by

$$\begin{Bmatrix} X \\ Y \\ Z \end{Bmatrix} = \begin{Bmatrix} X_P \\ Y_P \\ Z_P \end{Bmatrix} + \begin{Bmatrix} X_T \\ Y_T \\ Z_T \end{Bmatrix} \tag{2.38}$$

where the subscripts $(_P)$ and $(_T)$ denote forces on the projectile and ITM respectively. Only expressions for the applied loads on the projectile are shown. The weight force on the translating mass is similar to the projectile with obvious changes. Forces and moments can then be expanded as follows.

$$\begin{Bmatrix} X_P \\ Y_P \\ Z_P \end{Bmatrix} = \begin{Bmatrix} X_P^W \\ Y_P^W \\ Z_P^W \end{Bmatrix} + \begin{Bmatrix} X_P^A \\ Y_P^A \\ Z_P^A \end{Bmatrix} + \begin{Bmatrix} X_P^I \\ Y_P^I \\ Z_P^I \end{Bmatrix} \tag{2.39}$$

$$\begin{Bmatrix} L_P \\ M_P \\ N_P \end{Bmatrix} = \begin{Bmatrix} L_P^A \\ M_P^A \\ N_P^A \end{Bmatrix} + \begin{Bmatrix} L_P^I \\ M_P^I \\ N_P^I \end{Bmatrix} \tag{2.40}$$

In the expressions above, superscripts (^{W}), (^{A}), and (^{I}) denote forces and moments due to weight, aerodynamics, and control inputs respectively. Control forces and moments are computed within the control system, which is described later, hence expressions are not provided here. The projectile weight force expressed in the projectile reference frame is

$$\begin{Bmatrix} X_P^W \\ Y_P^W \\ Z_P^W \end{Bmatrix} = m_P g \begin{Bmatrix} -s_\theta \\ s_\phi c_\theta \\ c_\phi c_\theta \end{Bmatrix} \tag{2.41}$$

The aerodynamic forces on the projectile are split into standard steady (^{SA}) and Magnus (^{MA}) terms. The Magnus forces act at the Magnus center of pressure, which is different from the center of pressure of the steady aerodynamic forces.

$$\begin{Bmatrix} X_P^A \\ Y_P^A \\ Z_P^A \end{Bmatrix} = \begin{Bmatrix} X_P^{SA} \\ Y_P^{SA} \\ Z_P^{SA} \end{Bmatrix} + \begin{Bmatrix} X_P^{MA} \\ Y_P^{MA} \\ Z_P^{MA} \end{Bmatrix} \tag{2.42}$$

where

$$X_P^{SA} = -\frac{\pi}{8}\rho V^2 D^2 (C_{X0} + C_{X2}\varepsilon^2) \tag{2.43}$$

$$Y_P^{SA} = -\frac{\pi}{8}\rho V^2 D^2 \left[C_{NA} \frac{v}{V} \right] \tag{2.44}$$

$$Z_P^{SA} = -\frac{\pi}{8}\rho V^2 D^2 \left[C_{NA} \frac{w}{V} \right] \tag{2.45}$$

$$X_P^{MA} = 0 \tag{2.46}$$

$$Y_P^{MA} = \frac{\pi}{8}\rho V^2 D^2 \frac{pD}{2V} \left[C_{YPA} \frac{w}{V} \right] \tag{2.47}$$

$$Z_P^{MA} = -\frac{\pi}{8}\rho V^2 D^2 \frac{pD}{2V} \left[C_{YPA} \frac{v}{V} \right] \tag{2.48}$$

Equation (2.43) uses the following expression for calculation of total angle of attack:

$$\varepsilon = \frac{\sqrt{v^2 + w^2}}{\sqrt{u^2 + v^2 + w^2}} \tag{2.49}$$

The total applied body moments contain steady (^{SA}), unsteady (^{UA}), and Magnus (^{MA}) terms.

$$\begin{Bmatrix} L_P^A \\ M_P^A \\ N_P^A \end{Bmatrix} = \begin{Bmatrix} L_P^{SA} \\ M_P^{SA} \\ N_P^{SA} \end{Bmatrix} + \begin{Bmatrix} L_P^{UA} \\ M_P^{UA} \\ N_P^{UA} \end{Bmatrix} + \begin{Bmatrix} L_P^{MA} \\ M_P^{MA} \\ N_P^{MA} \end{Bmatrix} \tag{2.50}$$

The steady body aerodynamic moment is computed with a cross product between the distance vector from the center of gravity to the center of pressure and the steady body aerodynamic force vector above. Likewise, the Magnus aerodynamic moment is computed with a cross product between the distance vector from the center of mass to the center of Magnus force and the Magnus force vector.

The unsteady body aerodynamic moment provides a damping source for projectile angular motion. Expansions for the unsteady aerodynamic moment are given by

$$L_P^{UA} = \frac{\pi}{8}\rho V^2 D^3 \left[C_{LDD} + \frac{pD}{2V} C_{LP} \right] \tag{2.51}$$

$$M_P^{UA} = \frac{\pi}{8}\rho V^2 D^3 \left[\frac{qD}{2V} C_{MQ} \right] \tag{2.52}$$

$$N_P^{UA} = \frac{\pi}{8}\rho V^2 D^3 \left[\frac{rD}{2V} C_{MQ} \right] \tag{2.53}$$

A diagram showing the various forces and moments described above is shown in Figure 2.4. The aerodynamic coefficients and aerodynamic center distances are all a function of local Mach number at the center of mass of the projectile. Computationally, these Mach number dependent parameters are obtained by a table look-up scheme using linear interpolation.

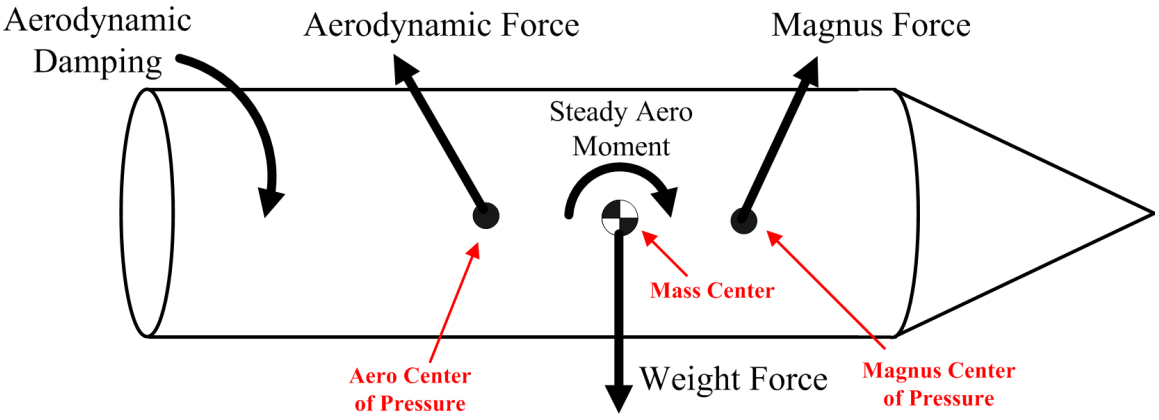

Figure 2.4: Forces and Moments on Projectile Body.

2.3 Internal Translating Mass Control System

In order to examine the capabilities of the internal translating mass control mechanism, a control law is created to move the translating mass in a prescribed manner.

The control law for the translating mass is derived using feedback linearization, [28] which assumes full state feedback. First, by solving for $\ddot{s}$, equation (2.28) is rewritten as

$$\ddot{s} = \frac{1}{A_{S2}} f_{Input} + \frac{1}{A_{S2}} b - \frac{A_{S1}}{A_{S2}} \begin{bmatrix} \dot{u} \\ \dot{v} \\ \dot{w} \end{bmatrix} - \frac{A_{S3}}{A_{S2}} \begin{bmatrix} \dot{p} \\ \dot{q} \\ \dot{r} \end{bmatrix} \tag{2.54}$$

where A_{S1}, A_{S2}, and A_{S3} are given respectively by equations (2.29), (2.30), and (2.31), and b is given by

$$\begin{aligned} b = & -c_V \dot{s} + m_T g(-s_\theta c_{\theta_T} c_{\psi_T} + s_\phi c_\theta c_{\theta_T} s_{\psi_T} - c_\phi c_\theta s_{\theta_T}) - \\ & m_T \left[c_{\theta_T} c_{\psi_T}, c_{\theta_T} s_{\psi_T}, -s_{\theta_T} \right] \mathbb{S}_P(\vec{\omega}_{P/I}) \mathbb{C}_P(\vec{v}_{C/I}) - \\ & \frac{m_P m_T}{m} \left[c_{\theta_T} c_{\psi_T}, c_{\theta_T} s_{\psi_T}, -s_{\theta_T} \right] \mathbb{S}_P(\vec{\omega}_{P/I}) \mathbb{S}_P(\vec{\omega}_{P/I}) \mathbb{C}_P(\vec{r}_{P \to T}) \end{aligned} \tag{2.55}$$

Examination of equation (2.54) leads directly to the feedback linearization control law (or inversion control) given by

$$\begin{aligned} f_{Input} = & A_{S2} \left[\ddot{s}_{com} - K_1 (\dot{s} - \dot{s}_{com}) - K_0 (s - s_{com}) \right] \\ & -b + A_{S1} \begin{bmatrix} \dot{u} \\ \dot{v} \\ \dot{w} \end{bmatrix} + A_{S3} \begin{bmatrix} \dot{p} \\ \dot{q} \\ \dot{r} \end{bmatrix} \end{aligned} \tag{2.56}$$

The commanded translating mass position s_{com} and its derivatives are generated within the simulation, and its precise form will be discussed later. Note that the feedback linearization controller is developed and used within the simulation solely to create the prescribed motion of the ITM for control authority, and does not necessarily represent a realistic control system for this mechanism. In Chapter 6, where a more realistic ITM

actuator design is proposed, the control law is changed to a simpler proportional plus derivative formulation.

2.4 Theory of Control Generation Using an Internal Translating Mass

Trajectory deflection using an internal translating mass relies on a control moment caused by aerodynamic drag acting at an offset to the system center of mass. As the translating mass moves off of the projectile centerline, the system center of mass shifts laterally off of the centerline as well. However, due to the axial symmetry of the projectiles considered, the aerodynamic center of pressure is located along the axis of symmetry of the body. This creates a yawing moment that can be used to generate trajectory control. A drawing demonstrating this control technique is shown in Figure 2.5.

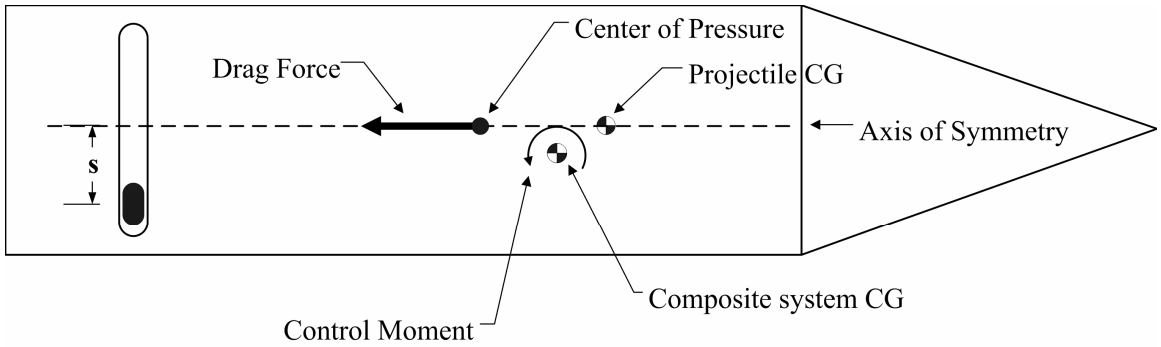

Figure 2.5: Drag Offset Control of a Projectile.

Maintaining a maneuver force in a consistent control plane in the inertial reference frame requires oscillation of the internal translating mass at the projectile roll rate in rounds that spin. Therefore, commands are sent to the ITM controller based on the projectile roll angle according to

$$s_{com} = A_T \cos(\phi + \phi_T) \tag{2.57}$$

where A_T is the ITM oscillation amplitude, or half of the ITM "stroke," and ϕ_T is the oscillation phase angle determined by the orientation of the control plane. Derivatives of equation (2.57) are determined analytically and used to compute $\dot{s}_{com}$ and $\ddot{s}_{com}$ within the simulation. Figure 2.6 shows a diagram of translating mass position, velocity ($\vec{v}$), and acceleration ($\vec{a}$) with respect to the projectile over one roll cycle.

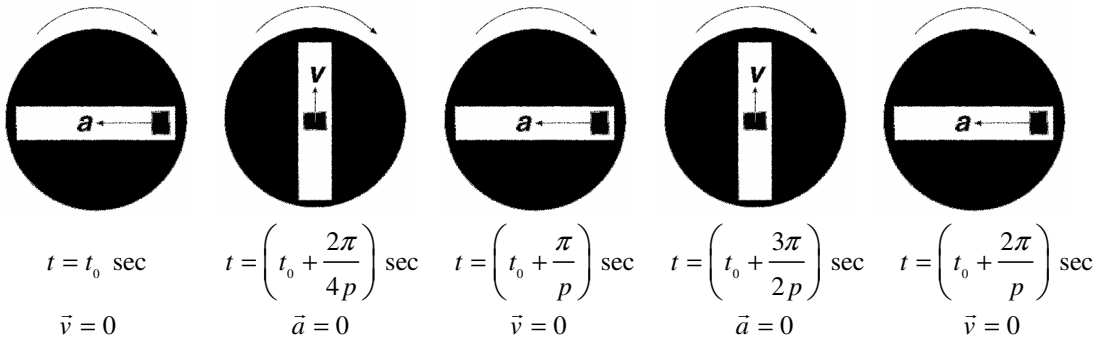

Figure 2.6: Diagram of Sinusoidal ITM Motion Over One Roll Cycle.

2.5 Example Simulation Results

Several example trajectories are shown in this section to demonstrate validity of the flight simulation as well as trajectory alteration potential of the ITM control mechanism. The projectile used to generate these example results is a fin-stabilized indirect fire projectile with a reference diameter of approximately 105 mm and a length of approximately 0.579 m. The projectile's mass, roll, and pitch inertia are 17.61 kg, 0.0377 kg-m^2, and 0.8531 kg-m^2 respectively. Stationline CG position is 0.351 m measured from the aft end of the round. For all cases in this chapter, the translating mass

Euler angles are $\psi_T = 90$ deg and $\theta_T = 0$, meaning that the ITM translates perpendicular to the projectile longitudinal axis. A drawing of the example projectile is shown in Figure 2.7.

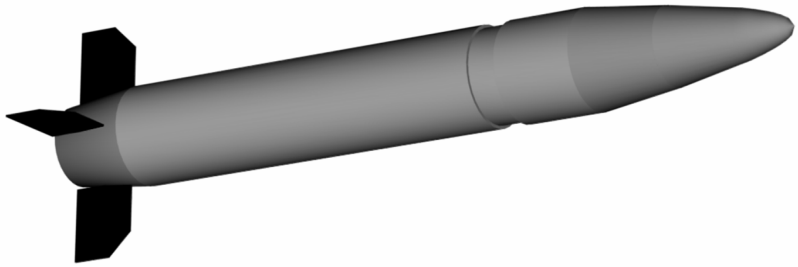

Figure 2.7: Example Indirect Fire Projectile.

Three example trajectories are shown to demonstrate model validation and control authority potential, namely a rigid 6DOF case ("Rigid 6DOF"), a translating mass projectile simulation where the ITM is held on the projectile centerline ("ITM-No Oscillation"), and a translating mass projectile simulation where the ITM is oscillated at the projectile roll rate with $\phi_T = 0$ ("ITM-Oscillation"). The rigid 6DOF case uses a previously-validated six-degree-of-freedom rigid body flight simulation. The results of the "Rigid 6DOF" case and the "ITM-No Oscillation" case are compared to show that in the case of no ITM movement, results collapse back to the rigid body case. This is taken as evidence of the validity of the flight simulation model. The "ITM-Oscillation" case demonstrates maximum control authority in the $-\vec{J}_I$ direction due to the use of $\phi_T = 0$. All initial conditions and ITM parameters for the three cases above are given in Table 2.1. Control system gains shown in Table 2.1 were tuned such that ITM tracking error from the reference signal was sufficiently small.

Table 2.1: Initial Conditions and ITM Parameters for Example Cases.

Initial Conditions	x (m)	0.0
	y (m)	0.0
	z (m)	0.0
	ϕ (deg)	90.0
	θ (deg)	2.86
	ψ (deg)	0.0
	u (m/s)	860.0
	v (m/s)	0.0
	w (m/s)	0.0
	p (rad/s)	5.0
	q (rad/s)	0.0
	r (rad/s)	0.0
ITM Parameters	m_T (kg)	0.730
	A_T (cm)	4.83
	ϕ_T (deg)	0.0
	c_v (kg/s)	0.146
ITM Control Parameters	Max Force (N)	889.8
	K_0 (nd)	10000
	K_1 (nd)	100

Figures 2.8-2.14 show time and range histories of selected projectile states. Figures 2.8 and 2.9 clearly show that the trajectories of the 6DOF case and the ITM-No Oscillation case match nearly identically, while Figure 2.9 demonstrates that the ITM mechanism is capable of generating about 30 m of trajectory deviation over approximately 5000 m range. The total velocity time history shown in Figure 2.10 is noteworthy in that, not only do all three cases match, but that the decrease in forward velocity as the flight progresses leads to noticeably less control authority at the end of flight as compared to launch, since ITM control relies on drag for its maneuver capability. This effect is

exacerbated by the fact that for fin-stabilized projectiles, static stability increases as forward velocity decreases, leading to a further loss of control authority later in flight.

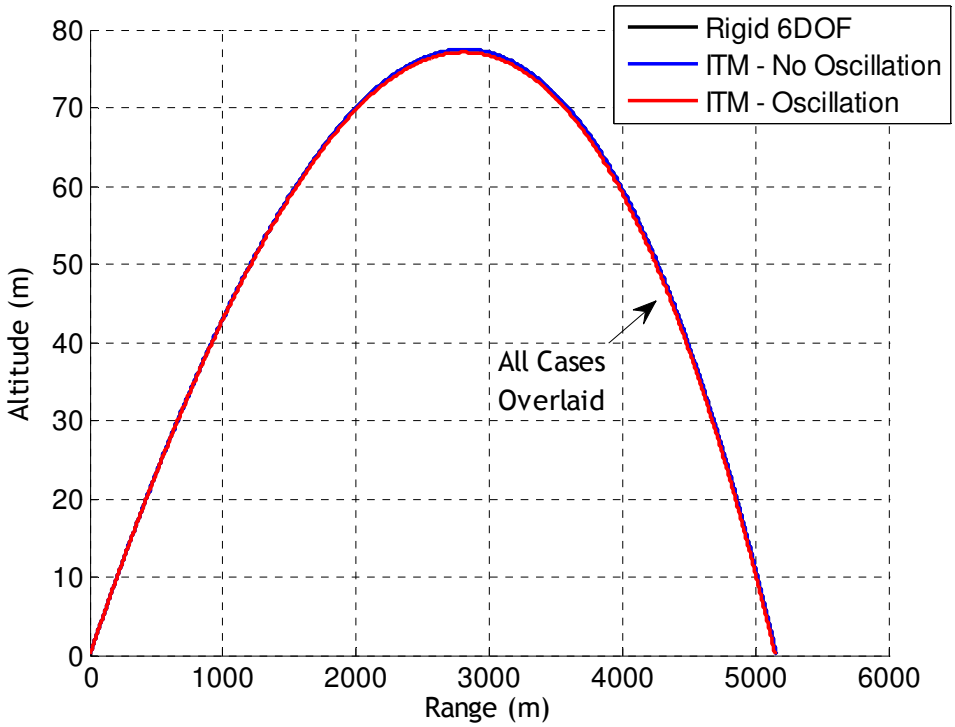

Figure 2.8: Altitude vs Range.

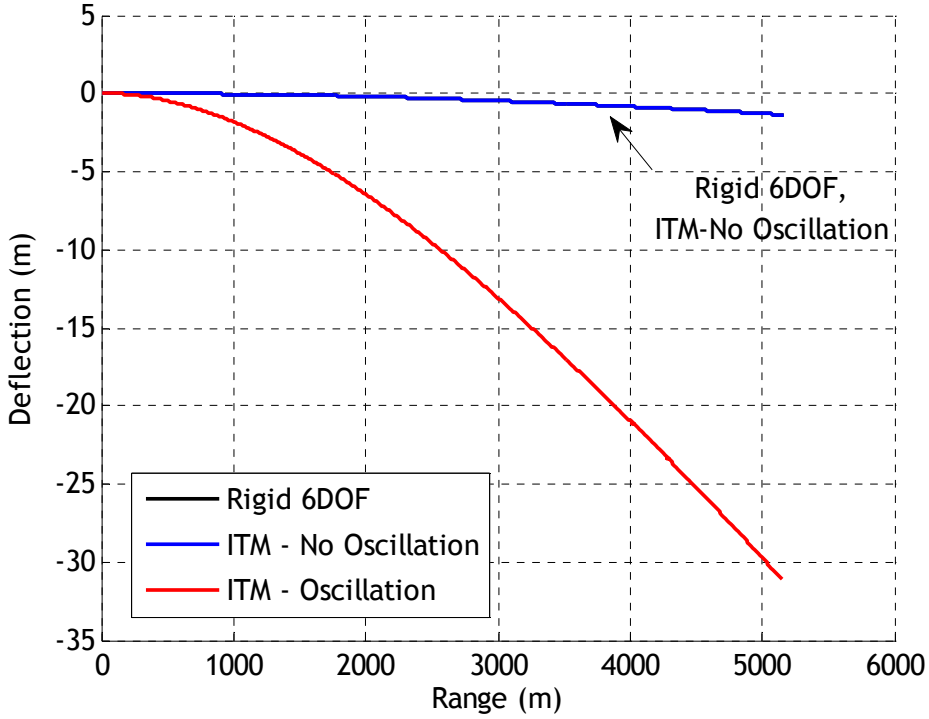

Figure 2.9: Deflection vs Range.

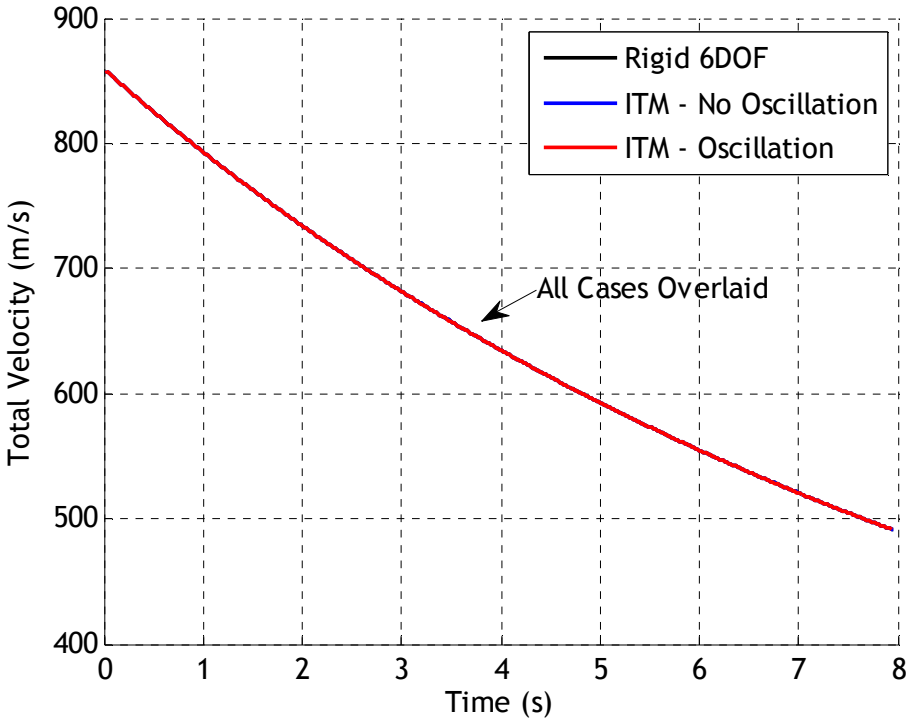

Figure 2.10: Total Velocity vs Time.

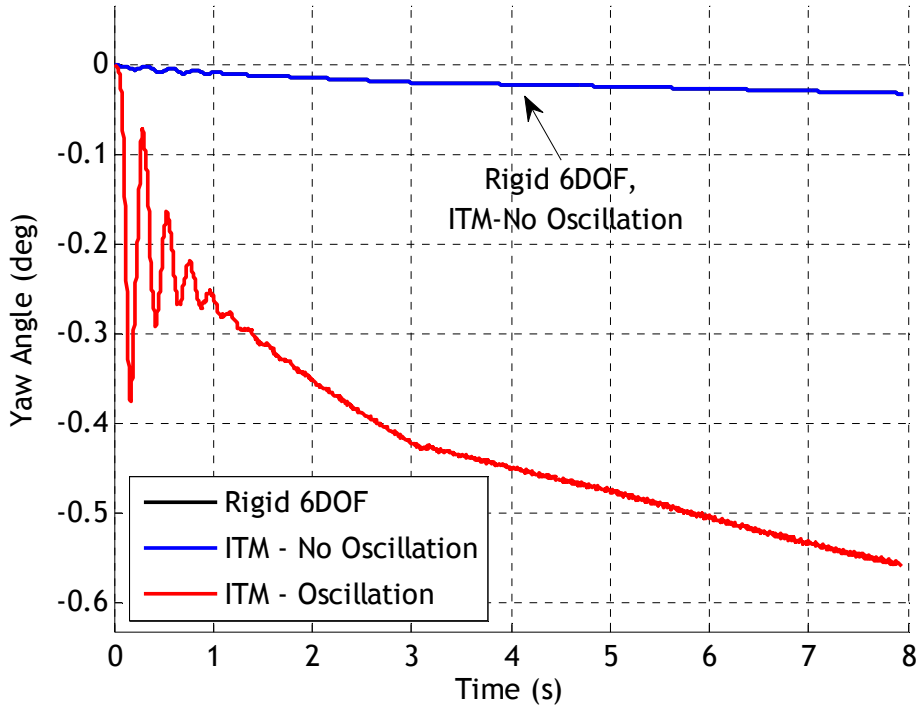

Figure 2.11: Yaw Angle (ψ) vs Time.

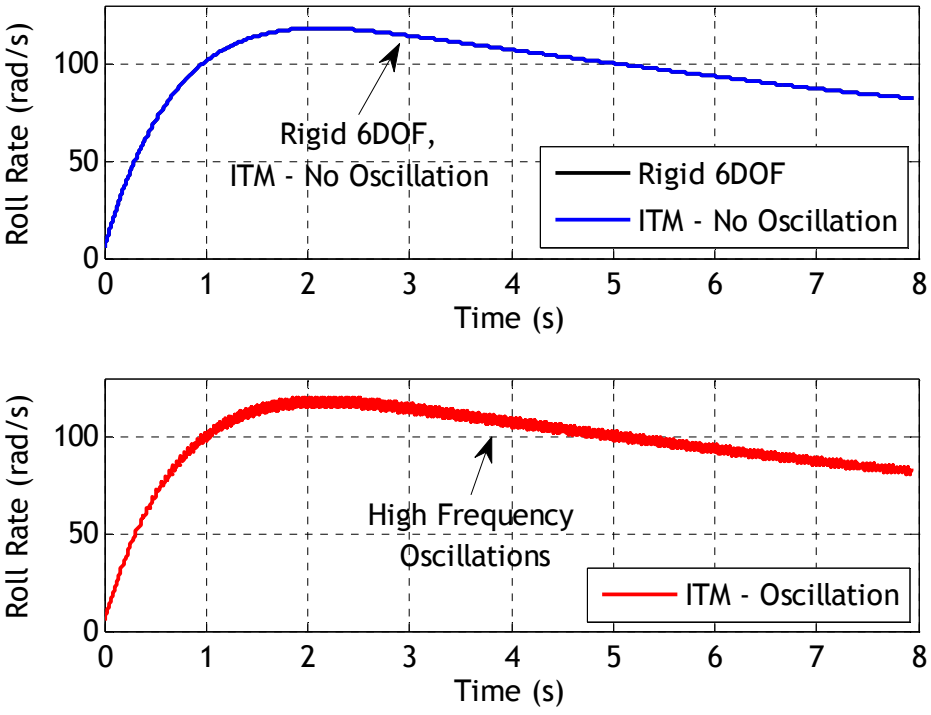

Figure 2.12: Roll Rate vs Time.

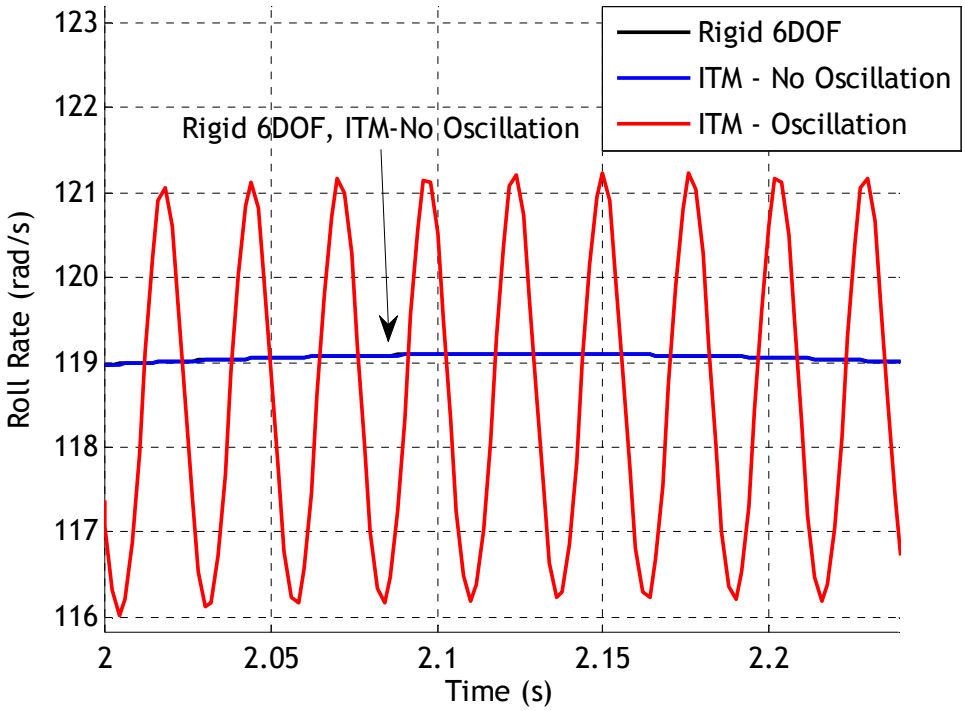

Figure 2.13: Zoom View of Roll Rate vs Time.

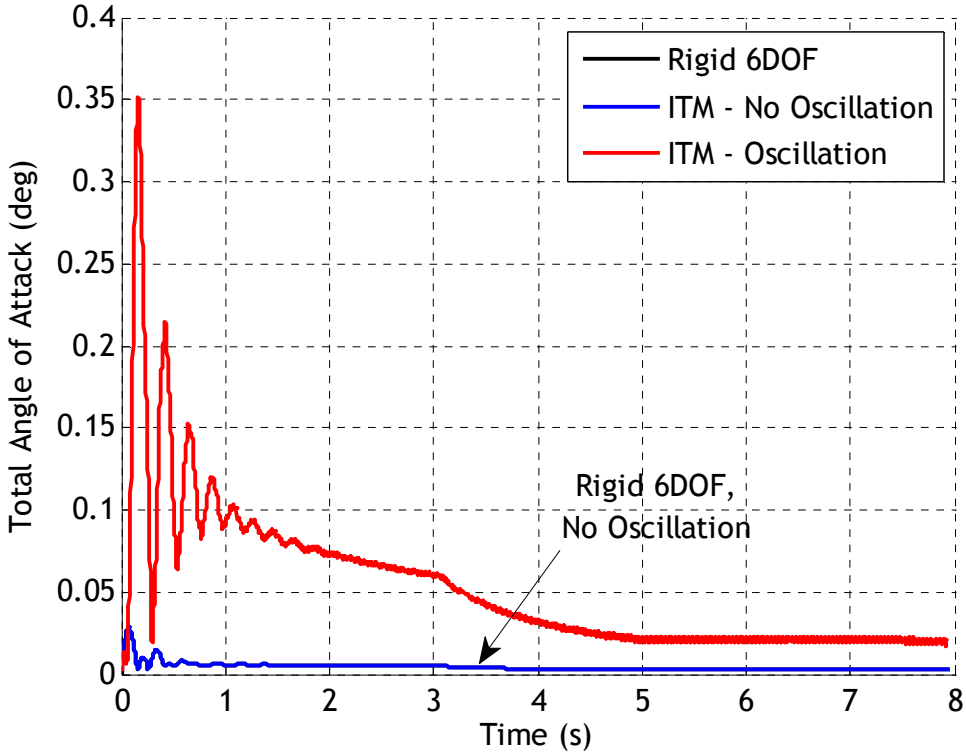

Figure 2.14: Total Angle of Attack vs Time.

The yaw angle time history shown in Figure 2.11 demonstrates this decrease in control authority as flight progresses, as the majority of trajectory deviation for the ITM-Oscillation case is established at the beginning of the trajectory. The angle of attack time history shown in Figure 2.14 confirms the decrease in control authority as flight progresses, demonstrated by the steady decrease in total angle of attack. Also note the initial large oscillations in total angle of attack caused by ITM motion just after launch before the round achieves its nominal spin rate. Roll rate time histories shown in Figures 2.12 and 2.13 demonstrate the interesting effect that when mass oscillation occurs, corresponding changes in projectile axial inertia cause oscillation in the projectile roll rate at the mass oscillation frequency. This so-called "Ice Skater" effect is corroborated by Figure 2.15, which demonstrates how roll rate changes as ITM movement occurs over half of a roll cycle for a segment of the ITM-Oscillation example case. Roll rates are highest when the ITM is centered in the cavity (i.e., $s = 0$), and lowest when ITM distance from the projectile centerline is largest. Time histories of translating mass motion for this example case are shown in Figures 2.16 and 2.17, confirming that the mass moves sinusoidally as commanded.

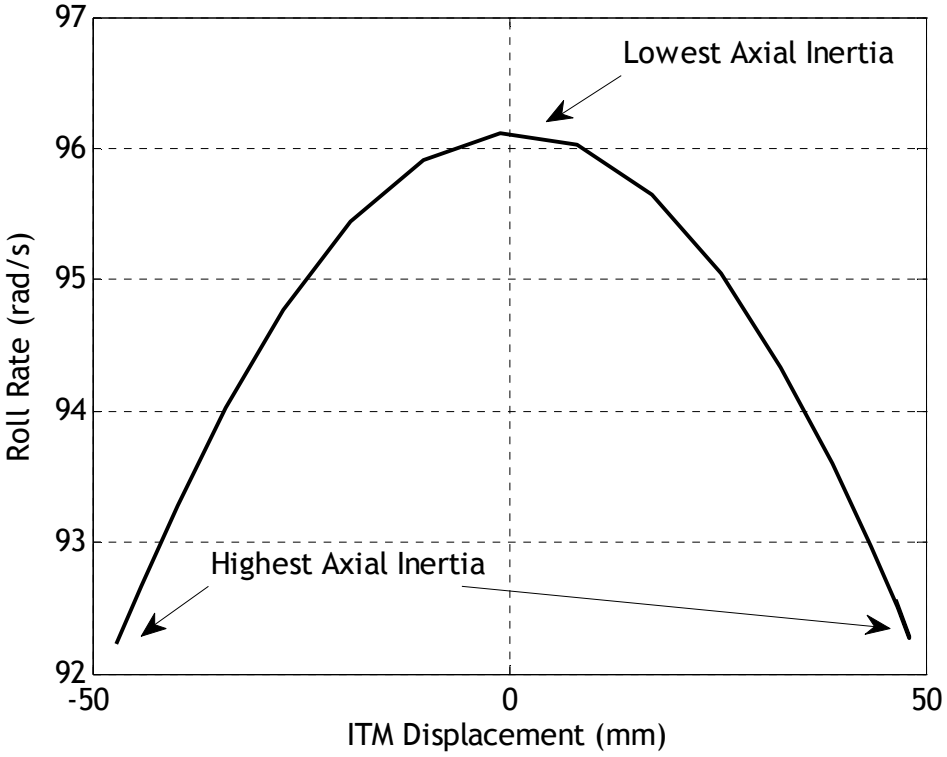

Figure 2.15: Roll Rate vs ITM Displacement for Half Roll Cycle ("Ice Skater" Effect).

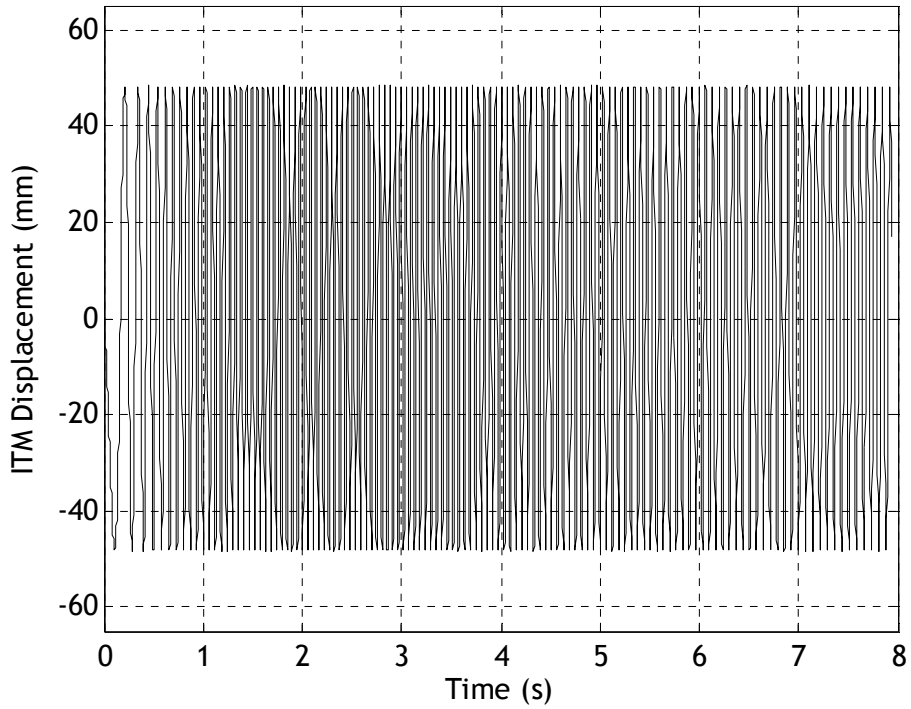

Figure 2.16: ITM Displacement vs Time.

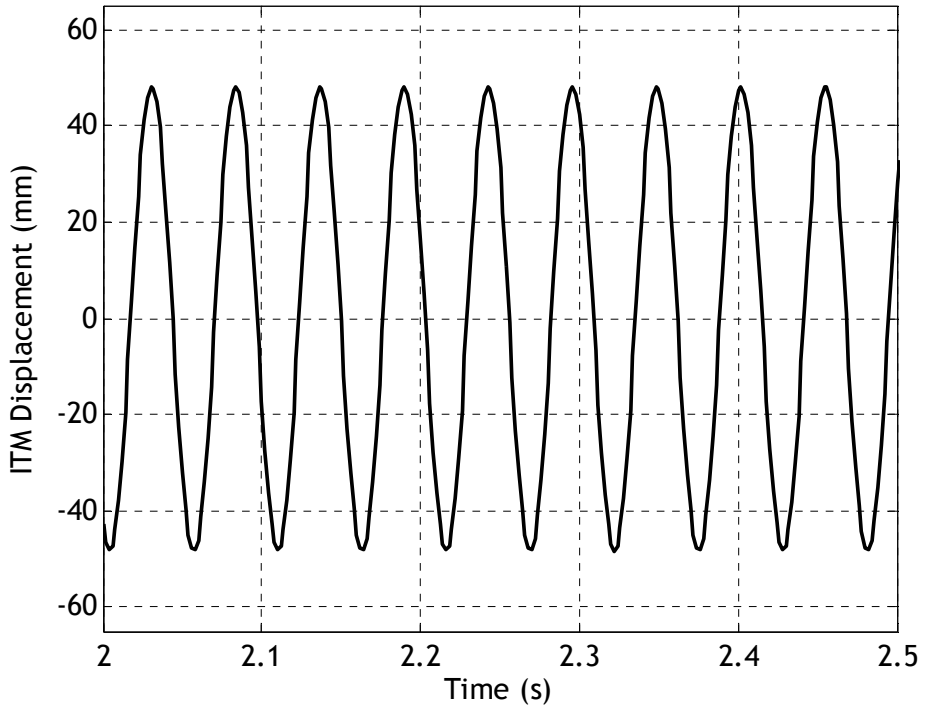

Figure 2.17: Zoom View of ITM Displacement vs Time.

Force commands output by the ITM controller for the ITM-Oscillation case are shown in Figure 2.18. The variation in amplitude of force required is driven by changes in the projectile roll rate through flight. Higher roll rates produce higher centripetal forces on the ITM, which must be counteracted by the ITM controller. Therefore, force amplitude is highest when the projectile roll rate peaks, approximately 2 sec into flight.

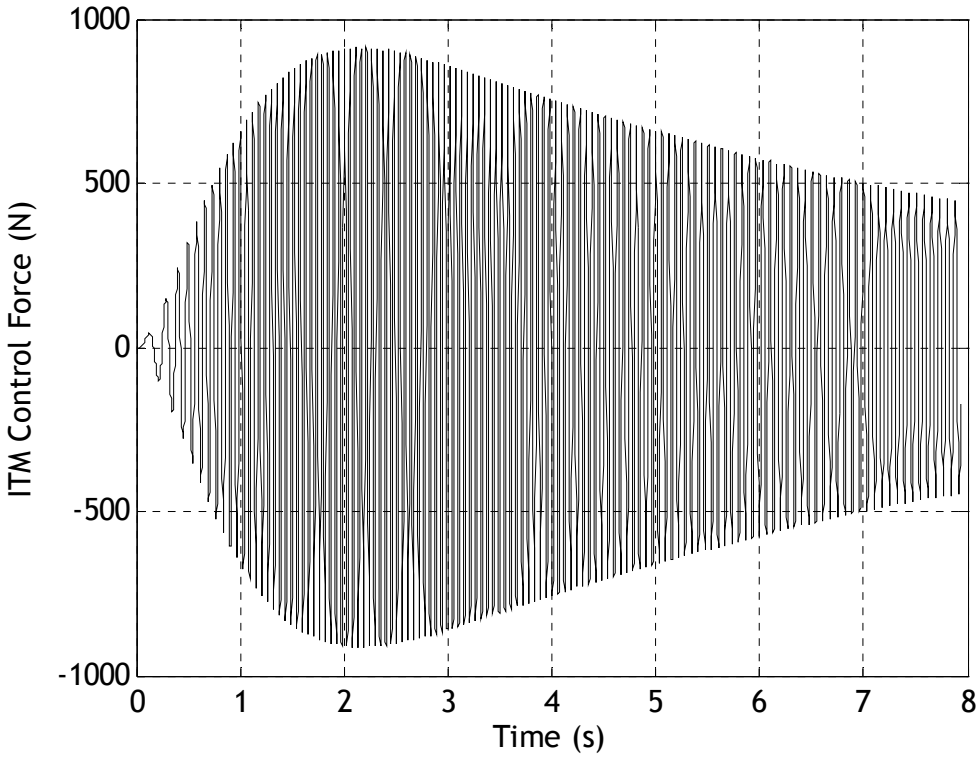

Figure 2.18: Force vs Time.

The nearly identical match between the rigid 6DOF case and the ITM-No Oscillation case provides partial evidence of model validation. Additional proof of validation is provided in Chapter 3, when a separate oscillating beam dynamic simulation is created and matched with the ITM simulation. Furthermore, reasonable control authority has been established using realistic mass and controller parameters.

2.6 Trade Studies

Trade studies are reported that explore the effects of ITM size, oscillation amplitude ("stroke"), placement with respect to the projectile center of gravity, and projectile static stability. The example projectile used for these trade studies is an 81mm mortar round, and differs from the example projectile used in Section 2.5 in order to demonstrate both the versatility of the ITM mechanism as well as its effect on different

types of munitions. The example mortar round has a reference diameter of approximately 81 mm and a length of approximately 0.54 m. The projectile's mass, roll, and pitch inertia are 4.583 kg, 0.00371 kg-m^2, and 0.04993 kg-m^2 respectively. Nominal stationline CG position is 0.282 m measured from the aft end of the round. As before, the ITM is translated orthogonal to the projectile centerline, and full control authority in the $-\vec{J}_I$ direction is commanded by setting $\theta_T = 0$. A sketch of the example mortar is shown in Figure 2.19, highlighting cavity offset and ITM stroke. A table of initial conditions for all simulations in this section is shown in Table 2.2.

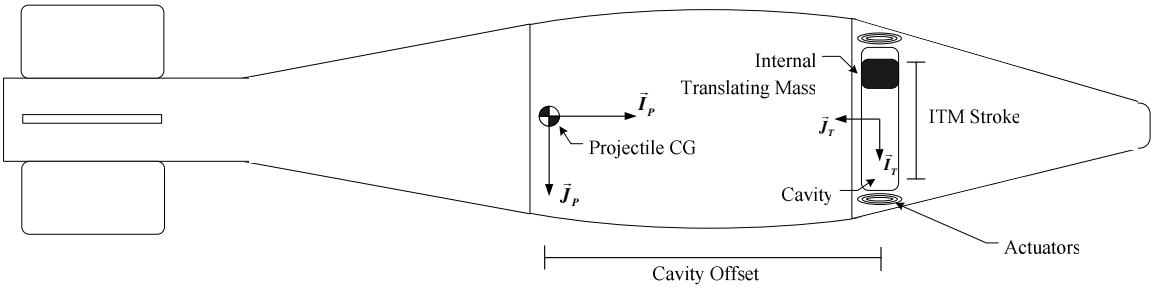

Figure 2.19: Example 81mm Mortar Projectile.

2.6.1 Static Margin Trade Study

A trade study was conducted to show that control authority using the ITM mechanism increases significantly as static margin decreases. One case was run with nominal stability characteristics (center of mass stationline of 0.282 m), termed "ITM Nominal Stability." Another case was run with reduced static stability (center of mass stationline of 0.209 m), termed "ITM Reduced Stability." For both of these cases, ITM mass size, cavity offset, and ITM stroke (as shown in Figure 2.19) were 0.125 kg, 0.167

m, and 5.08 cm respectively. Both cases were also compared with 6DOF trajectories using identical stability characteristics.

Table 2.2: Initial Conditions for Trade Study Simulations.

Initial Conditions	x (m)	0.0
	y (m)	0.0
	z (m)	0.0
	ϕ (deg)	0.0
	θ (deg)	45.8
	ψ (deg)	0.0
	u (m/s)	294.0
	v (m/s)	0.0
	w (m/s)	0.0
	p (rad/s)	0.0
	q (rad/s)	0.0
	r (rad/s)	0.0

In Figure 2.20, showing deflection versus range, it is clear that all projectiles show some deflection due to drift. Projectile drift typically increases as static stability decreases.[29] However, almost four times as much trajectory deviation is created in the reduced stability ITM-controlled round compared to the nominal stability ITM-controlled round. Total angle of attack plots shown in Figures 2.21 and 2.22 show that the ITM mechanism creates larger angle of attack oscillations in the reduced stability configuration. Furthermore, the reduced stability projectile develops a higher trim angle of sideslip (not evident in total angle of attack plots) compared to the nominal stability round. Therefore, it is concluded that reduced stability characteristics substantially increase control effectiveness of the ITM mechanism.

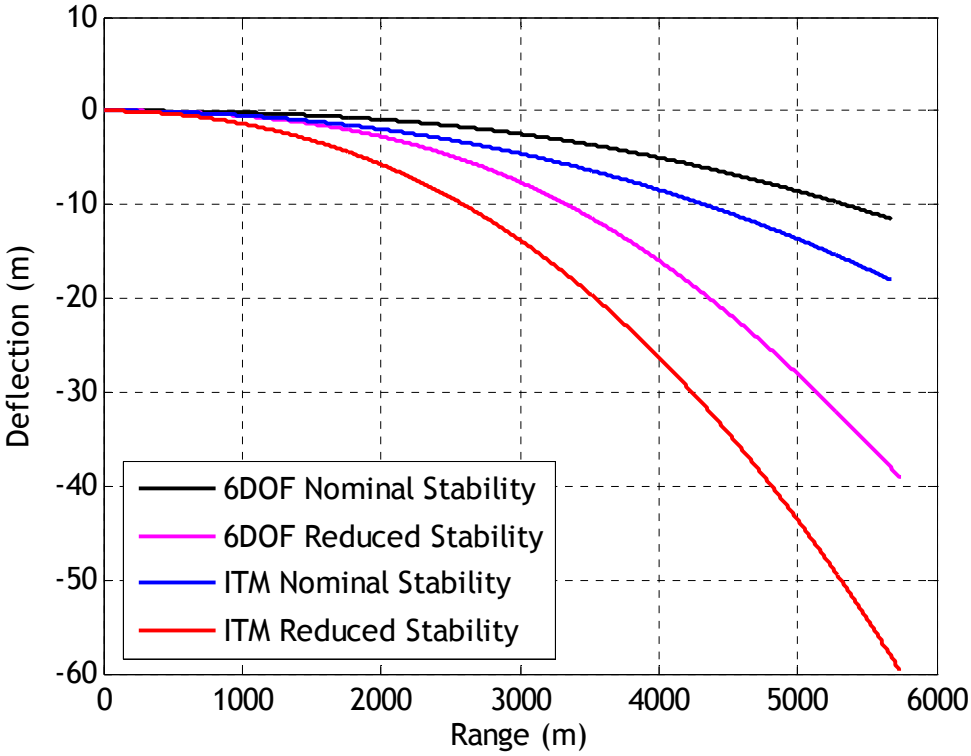

Figure 2.20: Deflection vs Range.

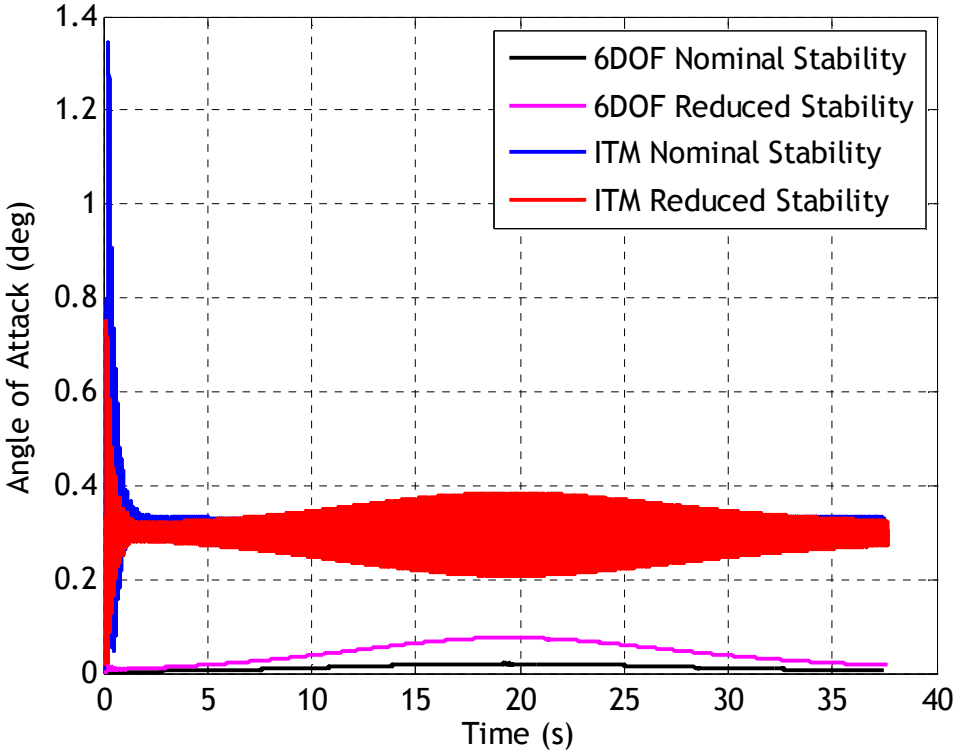

Figure 2.21: Angle of Attack vs Time.

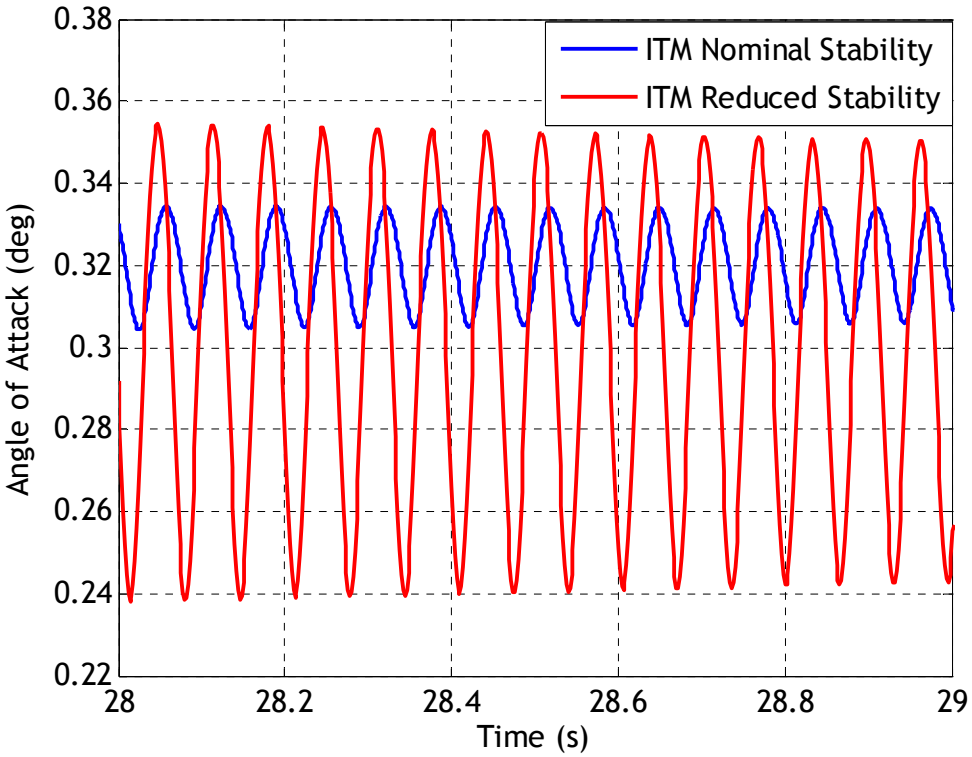

Figure 2.22: Zoom View of Angle of Attack vs Time.

2.6.2 Cavity Offset and ITM Stroke Trade Study

Another trade study was performed to examine the effect of cavity offset and ITM stroke on control authority (cavity offset and ITM stroke are clearly labeled in Figure 2.19 for reference). In this case, control authority is measured by total radial deviation, or the total distance between the impact points of the rigid round and the ITM round with identical mass properties and initial conditions. Simulations were conducted with several different cavity offsets and ITM strokes using both the nominal and reduced stability rounds described above in Section 2.6.1. Figures 2.23 and 2.24 show the results of this trade study in terms of radial deviation for various cavity offsets and ITM strokes for the nominal and reduced stability cases respectively. Also shown on the plots are the example cases from Section 2.6.1 for reference.

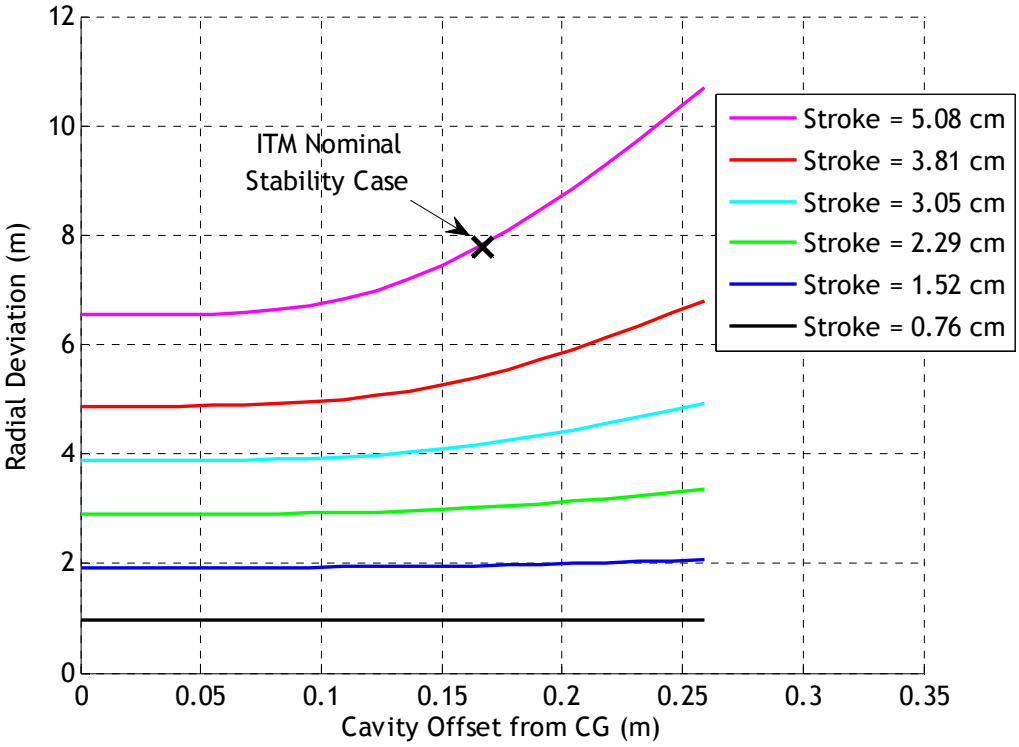

Figure 2.23: Radial Deviation vs Cavity Offset for Nominal Stability Projectile.

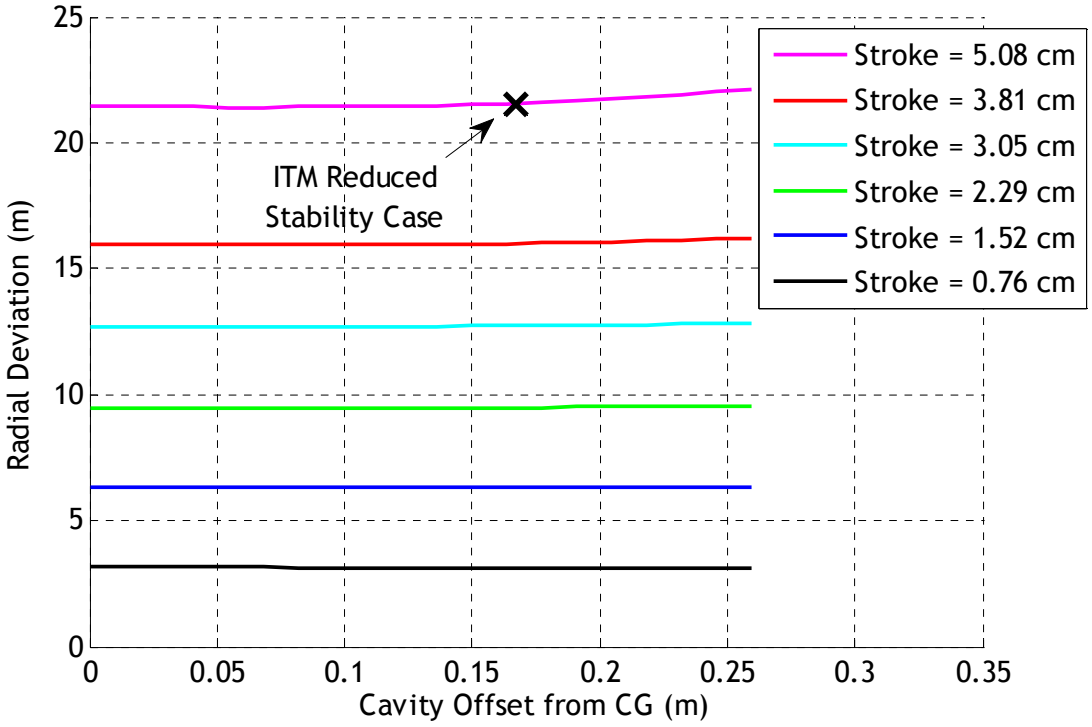

Figure 2.24: Radial Deviation vs Cavity Offset for Reduced Stability Projectile.

The results shown in Figures 2.23 and 2.24 demonstrate several interesting and somewhat predictable features. First, for most ITM strokes control authority is nearly insensitive to cavity offset. This follows from the fact that control authority is derived from a moment arm created by a lateral mass center offset, and longitudinal mass offset does not change the magnitude of this moment arm. However, ITM stroke does change the magnitude of the average lateral mass center offset, and therefore larger stroke leads to more control authority. Also, note that for larger strokes, total deviation increases somewhat with cavity offset (especially evident in Figure 2.23). This can be explained by first recognizing that reaction forces exerted by the ITM control mechanism between the projectile and the ITM are equal and opposite on both bodies. On the projectile, if this control force is exerted at an offset distance from the mass center, it will produce a corresponding moment on the projectile. This moment produces angular motion in the projectile (and corresponding angle of attack) that has a frequency of twice the roll frequency, due to the motion of the ITM being matched to the roll rate. As cavity offset grows, the magnitude of this moment grows due to the control force acting at a larger moment arm. Corresponding high angles of attack produce increased drag and subsequent decreases in range. This decrease in range leads to an increase in radial deviation from the rigid round impact point, resulting in the increasing plots for larger strokes shown in Figure 2.23. A plot of angle of attack versus angle of sideslip for various cavity offsets is shown in Figure 2.25, verifying that larger cavity offsets lead to larger angle of attack or coning motion. Note that no coning motion occurs for zero cavity offset, since the line of action of the reaction force on the projectile goes through the projectile mass center.

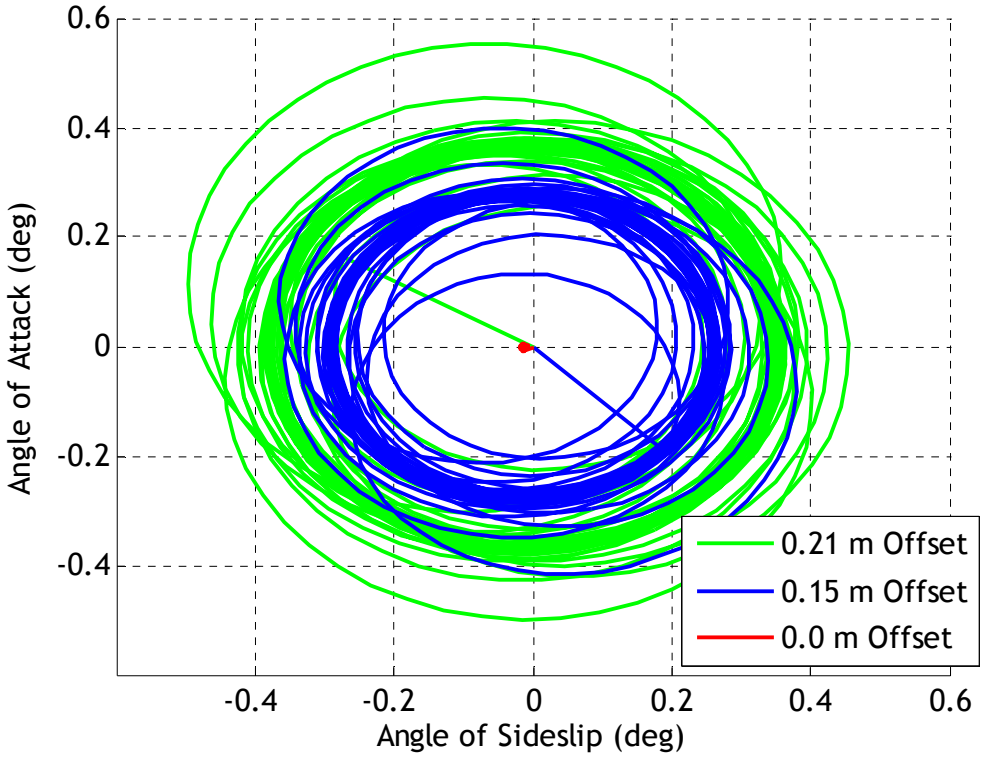

Figure 2.25: Angle of Attack vs Angle of Sideslip for Various Cavity Offsets.

2.6.3 ITM Mass and ITM Stroke Trade Study

A final trade study examined the effect of mass size on achievable radial deviation. Again, simulations were run using several different ITM strokes as well as various ITM mass sizes using both the nominal and reduced stability configurations. Figures 2.26 and 2.27 show trade study results for the nominal and reduced stability configurations respectively, with the example cases from Section 2.6.1 marked for reference. As might be expected, radial deviation increases with ITM mass size in addition to ITM stroke. This is due to the larger lateral mass center offset produced by a heavier internal translating mass.

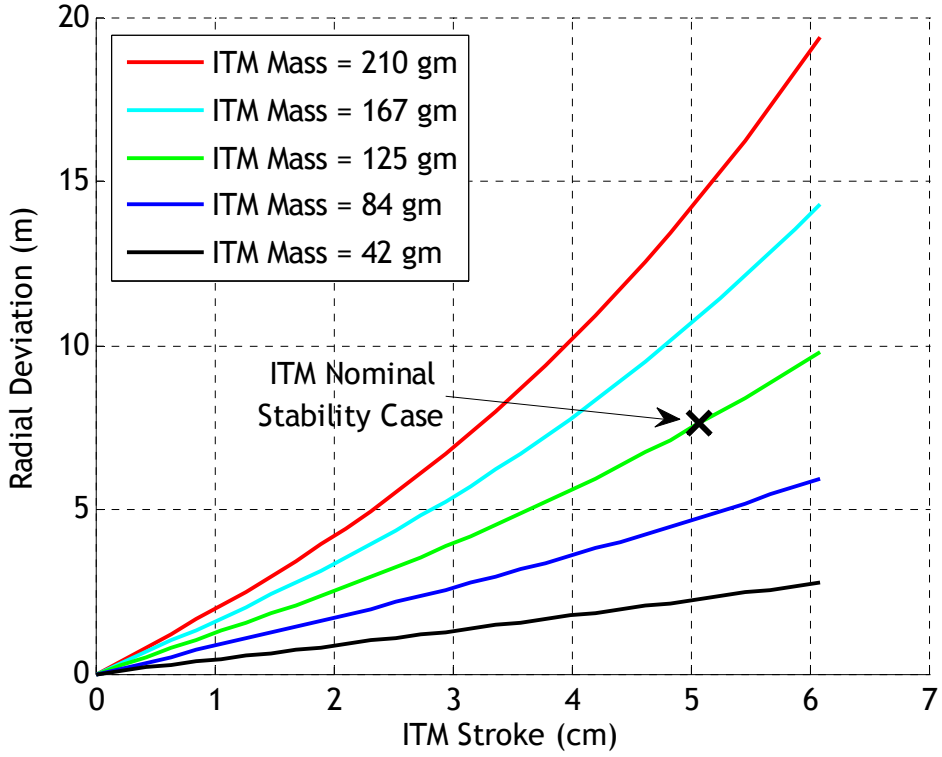

Figure 2.26: Radial Deviation vs ITM Stroke for Nominal Stability Projectile.

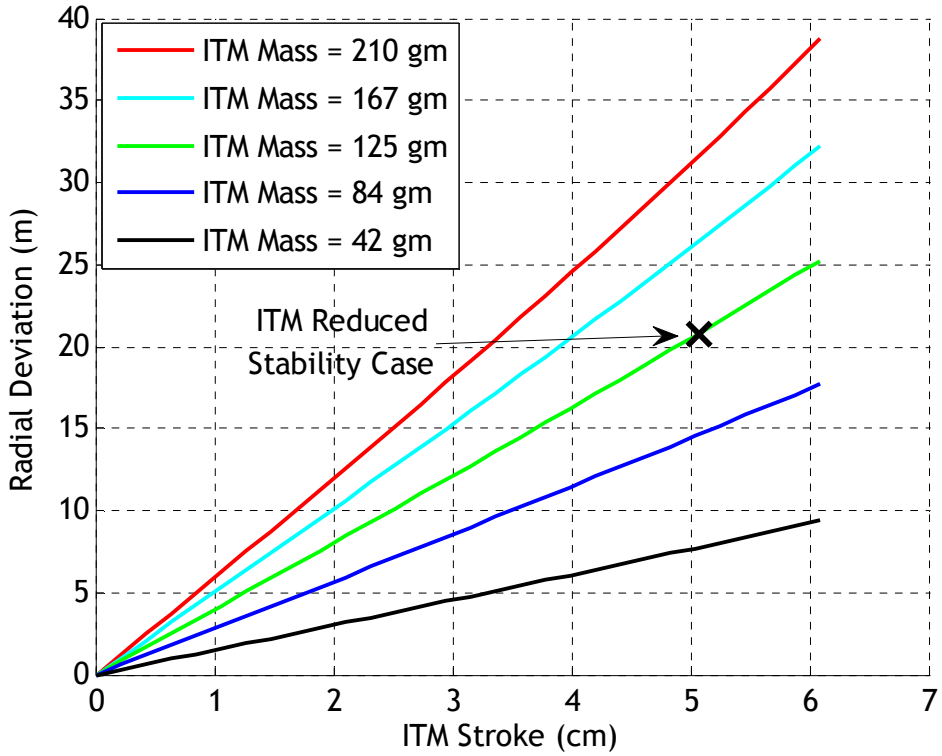

Figure 2.27: Radial Deviation vs ITM Stroke for Reduced Stability Projectile.

The trade study results shown in Sections 2.6.1-2.6.3 clearly show that the optimal mechanical configuration for the ITM mechanism includes large stroke, large mass size, and reduced projectile static stability. Large cavity offsets have negligible effect on control authority but introduce the potential for larger coning motion as the mass oscillates, producing higher drag. Therefore, placement of the cavity at or near the mass center improves flight characteristics by reducing this coning motion. However, larger masses and oscillation amplitudes significantly increase force required to move the ITM due to the required compensation for centripetal force. This design issue is the subject of Chapter 3, in which a mechanical mechanism is designed to allow for large ITM sizes and oscillation amplitudes with minimal force and power required.

CHAPTER 3

CANTILEVER BEAM DESIGN OF PROJECTILE MOVING MASS SYSTEMS

The previous chapter demonstrated that internal moving mass systems could generate reasonable control authority. However, high spin rates characteristic of many gun-launched munitions complicate the mechanical design of ITM mechanisms, since large control forces are required to overcome centripetal force experienced by the ITM. Furthermore, moving parts within the ITM control mechanism are susceptible to damage during high acceleration loading at launch. In this chapter, a mechanical design is proposed that seeks to minimize moving parts as well as actuator force and power requirements. Specifically, the translating mass is replaced by a laterally-oscillating cantilever beam powered by electromagnetic actuators. It is shown that certain choices of beam properties lead to resonant oscillations with the projectile spin frequency, leading to very low power requirements. Trade studies are performed on beam length and spring and damper constants. In addition, it is shown that active tuning of beam properties in flight can lead to further on-board power savings.[21] Finally, structural dynamics of the beam are analyzed to show that high spin accelerations at launch and continual vibration of the beam do not lead to loss of structural integrity.

3.1 Cantilever Beam Projectile Dynamic Model

The cantilever beam is a fixed-free elastic beam, with one end attached to the projectile at point *L* and the free end floating within the cavity, constrained to vibrate in the $\vec{I}_S - \vec{J}_S$ plane. The beam's first vibrational mode is the only mode considered significant to dynamic interaction with the projectile. For this reason, the cantilever

beam can be accurately modeled as a rigid, massless beam with a spherical mass (considered to be a permanent magnet) attached to the end. A torsional spring and damper are attached to the hinge point to simulate the elastic properties of the cantilever beam. This dynamically equivalent system is referred to as the ITM-Beam. A sketch of the cantilever beam design is shown in Figure 3.1, while a detailed schematic of the ITM-Beam projectile is shown in Figure 3.2. Note that γ is defined as the angle between the ITM-Beam and the centerline of the projectile. A permanent magnet is attached to the end of the beam and can swing freely about the hinge. Force is exerted on the magnet by electromagnets on both sides of the cavity to move the beam to a desired angle.

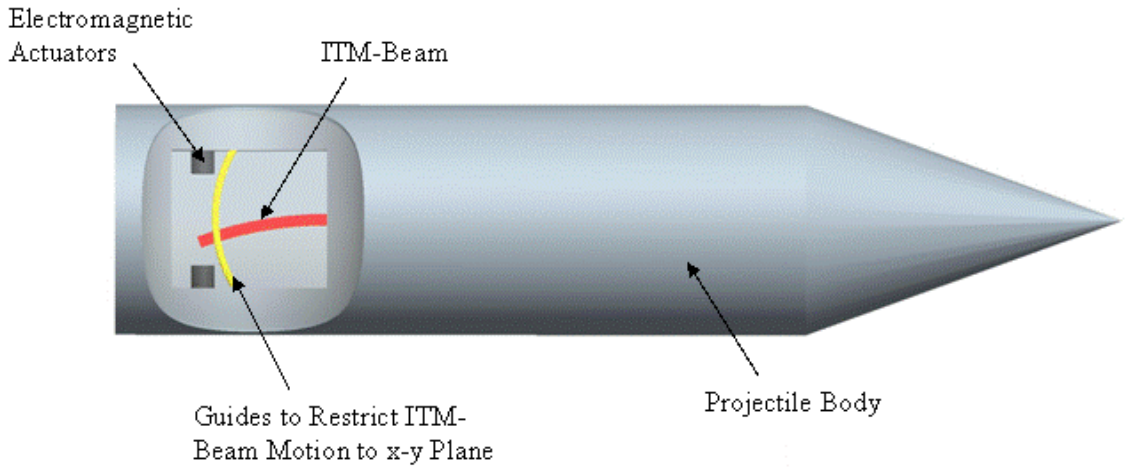

Figure 3.1: Sketch of the Cantilever Beam Projectile.

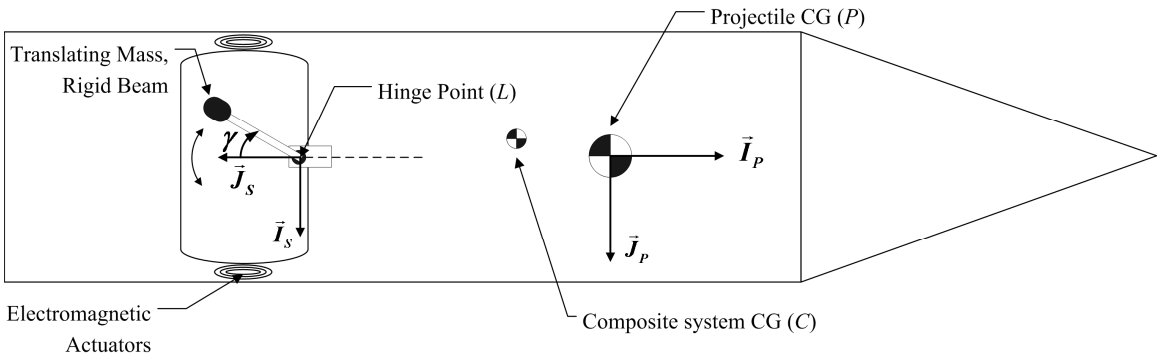

Figure 3.2: Schematic of the ITM-Beam Projectile.

Four reference frames are used in the development of the equations of motion for this system, namely the inertial, projectile, translating mass, and projectile-fixed *S* reference frames. The projectile and inertial frames are identical to those used in Chapter 2. The *S* frame is also fixed to the projectile, with its origin at the hinge point. It is defined such that the ITM-Beam oscillates about the $\vec{K}_S$ axis and $\vec{J}_S$ points to the rear of the cavity exactly equidistant from both electromagnetic actuators. Therefore, the *S* frame can be related to the *P* frame by two constant Euler angles ψ_S and θ_S such that

$$\begin{Bmatrix} \vec{I}_S \\ \vec{J}_S \\ \vec{K}_S \end{Bmatrix} = \begin{bmatrix} c_{\theta_S} c_{\psi_S} & c_{\theta_S} s_{\psi_S} & -s_{\theta_S} \\ -s_{\psi_S} & c_{\psi_S} & 0 \\ s_{\theta_S} c_{\psi_S} & s_{\theta_S} s_{\psi_S} & c_{\theta_S} \end{bmatrix} \begin{Bmatrix} \vec{I}_B \\ \vec{J}_B \\ \vec{K}_B \end{Bmatrix} \tag{3.1}$$

Throughout the rest of this chapter, fixed angles of $\psi_S = 90$ deg and $\theta_S = 0$ are used, and thus the *S* frame can be obtained by a single 90 deg rotation about the $\vec{K}_P$ axis, resulting in the orientation shown in Figure 3.2. The *T* frame is fixed to the ITM-Beam and is related to the *S* frame by the relationship

$$\begin{Bmatrix} \vec{I}_T \\ \vec{J}_T \\ \vec{K}_T \end{Bmatrix} = \begin{bmatrix} c_\gamma & s_\gamma & 0 \\ -s_\gamma & c_\gamma & 0 \\ 0 & 0 & 1 \end{bmatrix} \begin{Bmatrix} \vec{I}_S \\ \vec{J}_S \\ \vec{K}_S \end{Bmatrix} \tag{3.2}$$

Note that the *T* frame is aligned with the *S* frame when $\gamma = 0$.

3.1.1 Kinematics

The kinematic differential equations for the ITM-Beam are nearly identical to the kinematic relationships for the ITM projectile derived in Chapter 2, leading to the following position and orientation kinematic equations.

$$\begin{Bmatrix} \dot{x} \\ \dot{y} \\ \dot{z} \end{Bmatrix} = \begin{bmatrix} c_\theta c_\psi & s_\phi s_\theta c_\psi - c_\phi s_\psi & c_\phi s_\theta c_\psi + s_\phi s_\psi \\ c_\theta s_\psi & s_\phi s_\theta s_\psi + c_\phi c_\psi & c_\phi s_\theta s_\psi - s_\phi c_\psi \\ -s_\theta & s_\phi c_\theta & c_\phi c_\theta \end{bmatrix} \begin{Bmatrix} u \\ v \\ w \end{Bmatrix} = \left[T_{IP}\right]^T \begin{Bmatrix} u \\ v \\ w \end{Bmatrix} \tag{3.3}$$

$$\begin{Bmatrix} \dot{\phi} \\ \dot{\theta} \\ \dot{\psi} \end{Bmatrix} = \begin{bmatrix} 1 & s_\phi t_\theta & c_\phi t_\theta \\ 0 & c_\phi & -s_\phi \\ 0 & s_\phi / c_\theta & c_\phi / c_\theta \end{bmatrix} \begin{Bmatrix} p \\ q \\ r \end{Bmatrix} \tag{3.4}$$

The final kinematic equation relates the derivative of the ITM-Beam angle and angular velocity, and is given by

$$\dot{\gamma} = \omega_{Beam} \tag{3.5}$$

3.1.2 Dynamics

As in Chapter 2, the translational dynamic equations for the ITM-Beam projectile are derived through force balancing. Using the identical methodology as in Chapter 2, three translational dynamic equations are given by

$$\begin{Bmatrix} \dot{u} \\ \dot{v} \\ \dot{w} \end{Bmatrix} = \begin{Bmatrix} \frac{X_B}{m} \\ \frac{Y_B}{m} \\ \frac{Z_B}{m} \end{Bmatrix} - \begin{bmatrix} 0 & -r & q \\ r & 0 & -p \\ -q & p & 0 \end{bmatrix} \begin{Bmatrix} u \\ v \\ w \end{Bmatrix} \tag{3.6}$$

The rotational dynamic equations are obtained by first equating the *I* frame time rate of change of the system angular momentum about the system mass center to the total applied external moments on the system about the system mass center in the $\vec{I}_S$ and $\vec{J}_S$

directions, given by equations (3.7) and (3.8). Then, the same moment equation is used for each body separately, this time written in the $\vec{K}_S$ direction. These four equations are given by

$$\vec{I}_S \bullet \left(\frac{{}^I d\vec{H}_{B/I}^P}{dt} + \frac{{}^I d\vec{H}_{T/I}^X}{dt} + \vec{r}_{L\to P} \times m_P \vec{a}_{P/I} + \vec{r}_{L\to X} \times m_T \vec{a}_{X/I} \right) = \vec{I}_S \bullet \sum M_{System}^L \tag{3.7}$$

$$\vec{J}_S \bullet \left(\frac{{}^I d\vec{H}_{B/I}^P}{dt} + \frac{{}^I d\vec{H}_{T/I}^X}{dt} + \vec{r}_{L\to P} \times m_P \vec{a}_{P/I} + \vec{r}_{L\to X} \times m_T \vec{a}_{X/I} \right) = \vec{J}_S \bullet \sum M_{System}^L \tag{3.8}$$

$$\vec{K}_S \bullet \left(\frac{{}^I d\vec{H}_{T/I}^X}{dt} + \vec{r}_{L\to X} \times m_T \vec{a}_{X/I} \right) = -f_{Input} BLc_\gamma + \vec{K}_S \bullet \mathbb{S}\left(\vec{r}_{L\to X}\right) \mathbb{C}_S \left(\vec{W}_T\right) + k_T \gamma + k_D \dot{\gamma} \tag{3.9}$$

$$\vec{K}_S \bullet \left(\frac{{}^I d\vec{H}_{B/I}^P}{dt} + \vec{r}_{L\to P} \times m_P \vec{a}_{P/I} \right) = f_{Input} BLc_\gamma + \vec{K}_S \bullet \mathbb{S}\left(\vec{r}_{L\to P}\right) \mathbb{C}_S \left(\vec{W}_P\right) - k_T \gamma - k_D \dot{\gamma} + \vec{K}_S \bullet \mathbb{C}_S \left(\Sigma M_P^L\right) \tag{3.10}$$

where point *X* represents the center of the spherical mass at the free end of the ITM-Beam. Note that equation (3.9) equates the time rate of change of the angular momentum of the ITM-Beam to the total moment applied to the ITM-Beam. Equation (3.10) equates the time rate of change of the angular momentum of the projectile to the total moment applied to the projectile. Equations (3.7)-(3.10) were utilized so as to avoid dealing with constraint moments at the ITM-Beam hinge point.

Several intermediate expressions will be useful in deriving the rotational dynamic equations in the body-fixed *S* frame. First, note that the well-known two points fixed on a rigid body formula yields the relationship

$$\vec{a}_{X/I} = \vec{a}_{C/I} + \frac{m_P}{m} \left[\vec{\alpha}_{B/I} \times \vec{r}_{P\to L} + \vec{\alpha}_{T/I} \times \vec{r}_{L\to X} + \vec{\omega}_{B/I} \times \vec{\omega}_{B/I} \times \vec{r}_{P\to L} + \vec{\omega}_{T/I} \times \vec{\omega}_{T/I} \times \vec{r}_{L\to X} \right] \tag{3.11}$$

Equation (3.11) is used to expand $\vec{a}_{X/I}$ in terms of known quantities and state derivatives. Also, using the definition of the system center of mass it can be shown through algebraic manipulation that

$$\vec{r}_{L\to P}\times m_P\vec{a}_{P/I}+\vec{r}_{L\to X}\times m_T\vec{a}_{X/I}=\vec{r}_{L\to P}\times m\vec{a}_{C/I}+\vec{r}_{P\to X}\times m_T\vec{a}_{X/I} \tag{3.12}$$

Equation (3.12) is also used to expand the cross-product terms on the left-hand side of equations (3.7) and (3.8) in terms of known quantities and state derivatives.

Equations (3.7)-(3.10) can be expanded using the expressions in equations (3.11) and (3.12) and rearranged to form a 4×4 system of equations given by

$$\begin{bmatrix} A_{11} & A_{12} & A_{13} & A_{14} \\ A_{21} & A_{22} & A_{23} & A_{24} \\ A_{31} & A_{32} & A_{33} & A_{34} \\ A_{41} & A_{42} & A_{43} & A_{44} \end{bmatrix} \begin{bmatrix} \dot{\tilde{p}} \\ \dot{\tilde{q}} \\ \dot{\tilde{r}} \\ \ddot{\gamma} \end{bmatrix} = \begin{bmatrix} B_1 \\ B_2 \\ B_3 \\ B_4 \end{bmatrix} \tag{3.13}$$

In equation (3.13), rows 1-4 correspond to equations (3.7), (3.8), (3.9), and (3.10) respectively. The full expressions for the values of the *A* matrix and the *B* vector are lengthy and are provided in Appendix A. The set of equations given by (3.3), (3.4), (3.5), (3.6) and (3.13) constitute the equations of motion for the ITM-Beam projectile. Given a known set of initial conditions, these 14 scalar equations are numerically integrated forward in time using a fourth-order Runge-Kutta algorithm to obtain a single trajectory.

3.1.3 ITM-Beam Control System

As in Chapter 2, a feedback linearization controller is used to move the ITM-Beam in a prescribed manner. Force is exerted on the magnet at the free end of the ITM-

Beam through electromagnets. The feedback linearization (or inversion) control law is given by

$$\begin{aligned} f_{input} = \frac{-1}{BLc_{\gamma}}\left[B_{FLC} - A_{11}\dot{\tilde{p}} - A_{12}\dot{\tilde{q}} - A_{13}\dot{\tilde{r}} - A_{14}\ddot{\gamma} \right] - K_0\ddot{\gamma}_{com} \\ -K_1\left(\dot{\gamma}_{com} - \dot{\gamma}\right) - K_2\left(\gamma_{com} - \gamma\right) \end{aligned} \tag{3.14}$$

Note that B_{FLC} is defined in Appendix A and is derived from equation (3.9). Likewise, A_{11}, A_{12}, A_{13}, and A_{14}, are from equation (3.9) and provided in Appendix A. Equation (3.9) is used to compute the feedback linearization control, rather than equation (3.10), since use of equation (3.10) would require feedback of aerodynamic loads. This is complicated to physically implement and can be avoided through the use of equation (3.9) instead.

The commanded deflection angle γ_{com} is generated by synchronizing ITM-Beam movement with the projectile roll angle. This is done by setting

$$\gamma_{com} = \sin^{-1}\left(-\frac{A_T}{BL}\cos\left(\phi + \phi_T\right) \right) \tag{3.15}$$

where A_T is the magnitude of oscillation of point *X* from the cavity center and ϕ_T is a trim angle used to define the plane of control. Derivatives of equation (3.15) are computed analytically and used the control law given in equation (3.14). As in Chapter 2, this inversion controller is designed solely to generate prescribed motion of the ITM-Beam and is not meant as a practical active controller.

3.2 ITM-Beam Electromagnetic Actuator Control System

A zoom view of the ITM-Beam mechanism is shown in Figure 3.3. Two electromagnets, each at opposite ends of the cavity, exert force on the fixed magnet at the end of the ITM-Beam.

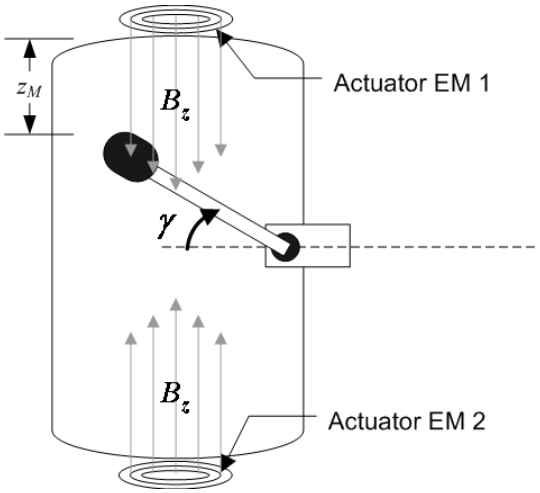

Figure 3.3: Zoom View of the ITM-Beam Mechanism.

The force exerted on a fixed magnetic dipole *DM* is given by [30]

$$\boldsymbol{f}_{input} = \boldsymbol{DM}\frac{\partial \boldsymbol{B}_z}{\partial z_M} \tag{3.16}$$

The magnetic dipole moment per unit mass is a unique property of a material, with units Joules/Tesla/kg. For example, assuming the ITM is made of magnetized iron and using an ITM-Beam mass of m_T = 0.730 kg, the dipole moment is found to be *DM* = 171.5 Joules/Tesla. The quantity $\frac{\partial \boldsymbol{B}_z}{\partial z_M}$ can be found by first recognizing that the magnetic field $\boldsymbol{B}_z$ of an iron core solenoid is given by the expression

$$B_z = \frac{I_E \mu k n}{2}\left[\frac{-z_M}{\sqrt{z_M^2 + b^2}} + \frac{z_M + L_A}{\sqrt{(z_M + L_A)^2 + b^2}}\right] \tag{3.17}$$

where I_E is the current through the electromagnet, μ is the magnetic constant ($4\pi\times10^{-7}$ N/Amp^2), z_M is the distance from the endpoint of the ITM beam to the nearest electromagnet actuator, k is the dimensionless relative permeability of iron (200 at a magnetic flux density of 0.002 W/m^2), n is the number of coils per meter, b is the radius of the solenoid, and L_A is the length of the solenoid. For all cases below, values of 3 cm, 2 cm, and 10000 were used respectively for b, L_A, and n. Taking the derivative of Equation (3.17) with respect to z_M,

$$\frac{\partial B_z}{\partial z_M} = \frac{I_E \mu k n}{2}\left[\frac{-1}{\sqrt{z_M^2 + b^2}} + \frac{z_M^2}{\left(z_M^2 + b^2\right)^{3/2}} + \frac{1}{\sqrt{(z_M + L_A)^2 + b^2}} - \frac{(z_M + L_A)^2}{\left((z_M + L_A)^2 + b^2\right)^{3/2}}\right] \tag{3.18}$$

The process of calculating current required through the mechanism is as follows. At each timestep, control force is computed using the controller above. Knowing the magnetic dipole moment and the required control force, the quantity $\frac{\partial B_z}{\partial z_M}$ is computed at each timestep using equation (3.16). Then, knowing the position of the ITM-Beam with respect to the actuators, the current required can be computed at each timestep by rearranging equation (3.18) such that

$$I_E = \frac{2}{k \mu n}\frac{\partial B_z}{\partial z_M}\left[\frac{-1}{\sqrt{z_M^2 + b^2}} + \frac{z_M^2}{\left(z_M^2 + b^2\right)^{3/2}} + \frac{1}{\sqrt{(z_M + L_A)^2 + b^2}} - \frac{(z_M + L_A)^2}{\left((z_M + L_A)^2 + b^2\right)^{3/2}}\right]^{-1} \tag{3.19}$$

Note that the electromagnet dimensions used above are comparable to dimensions for commercially-available iron-core electromagnets.

3.3 Model Validation and Example Case

An example trajectory of the ITM projectile is compared to an example trajectory of a projectile equipped with a strictly translating internal mass for model validation purposes. The translating internal mass trajectory is created using the dynamic model developed in Chapter 2. The ITM-Beam projectile ("ITM-Beam" case) and the translating mass projectile ("Translating Mass" case) use identical parameters for internal mass size, cavity offset, and oscillation amplitude. A rigid body trajectory ("Rigid 6DOF" case) is also included for comparison. All simulations use the example indirect fire fin-stabilized projectile used in Section 2.4. Initial conditions and translating mass parameters are identical to those used in the example case given in Section 2.4 and are given in Table 2.1. The ITM beam length used for the ITM-Beam simulation is 9.14 cm, and maximum ITM-Beam deflection angle is 31.6 deg. The two translating mass trajectories are generated solely to demonstrate control authority and validate the ITM-Beam simulation, and thus both controlled rounds are commanded to maximum possible deflection. Figures 3.4-3.10 show the results of each example trajectory. These results clearly demonstrate the close correlation between the ITM-Beam flight simulation model and the translating mass flight simulation model, despite significant differences in their equations of motion. Small differences in trajectories between the two models, shown in Figures 3.8, 3.9, and 3.10, are due to the small displacement of the moving mass in the longitudinal direction in the ITM-Beam case as the beam rotates, creating very small oscillations in stationline mass center position. Furthermore, both ITM models were run with the internal mass held in the center (as in Chapter 2), and both trajectories matched

the rigid results nearly exactly. The fact that these two independent models provide nearly identical results in cases of mass oscillation and in cases where the ITM rounds approximate rigid rounds offers proof of the validity of both the translating mass and the ITM-Beam simulation.

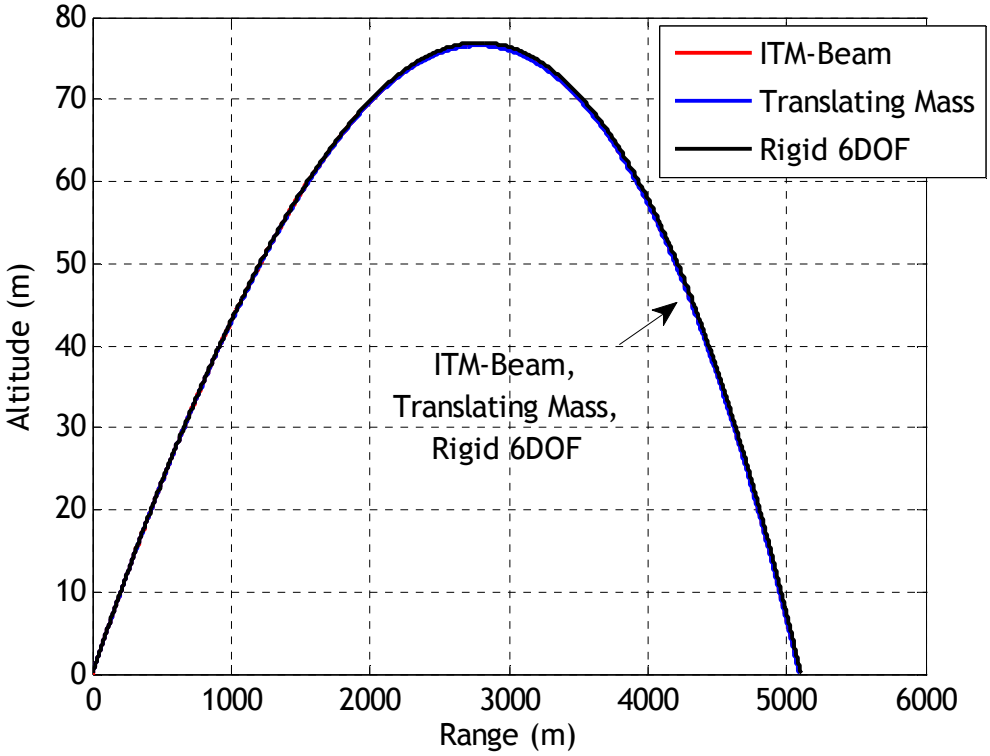

Figure 3.4: Altitude vs Range.

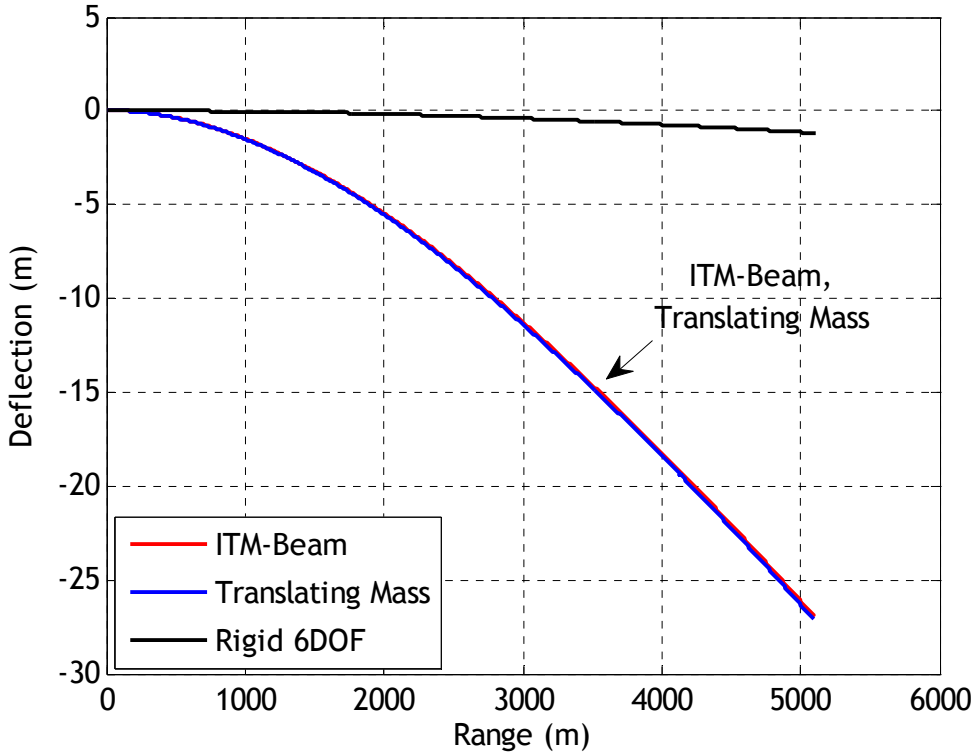

Figure 3.5: Deflection vs Range.

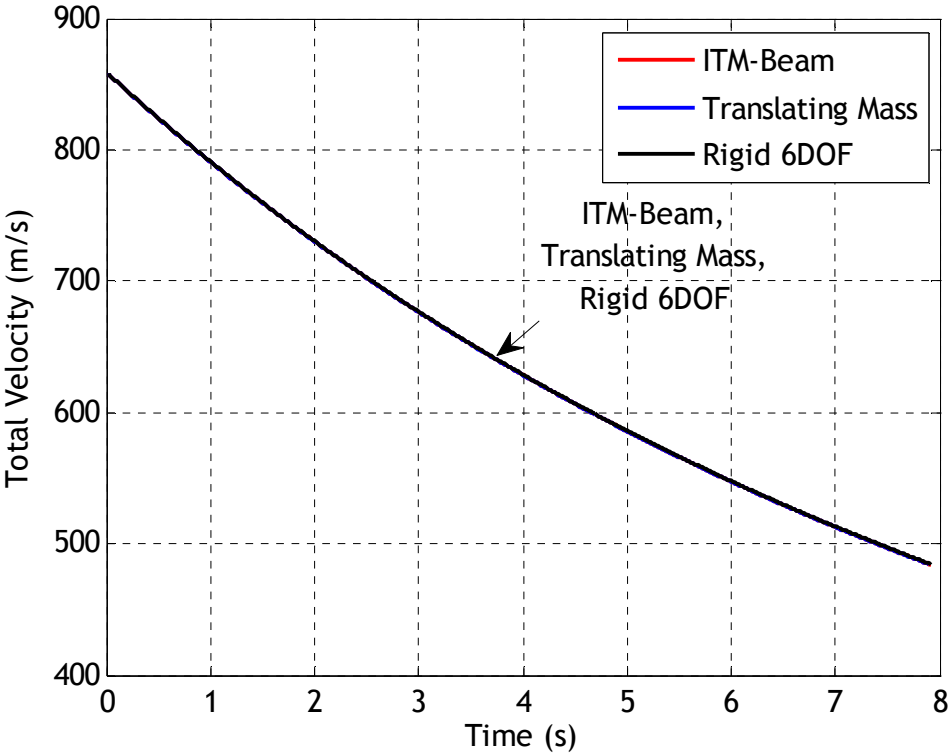

Figure 3.6: Total Velocity vs Time.

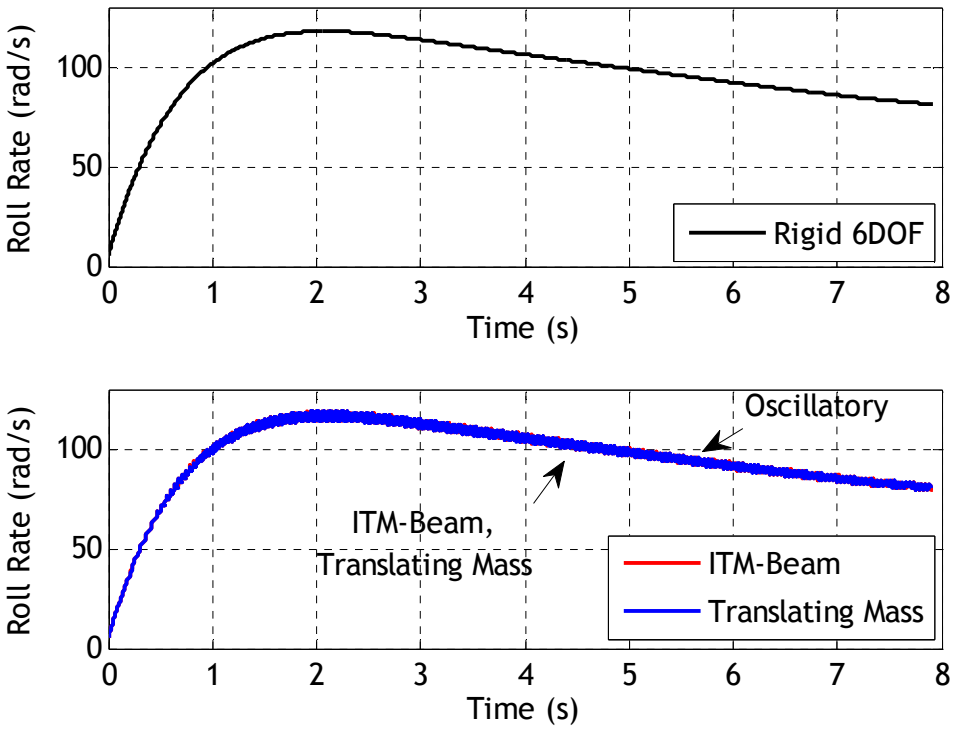

Figure 3.7: Roll Rate vs Time.

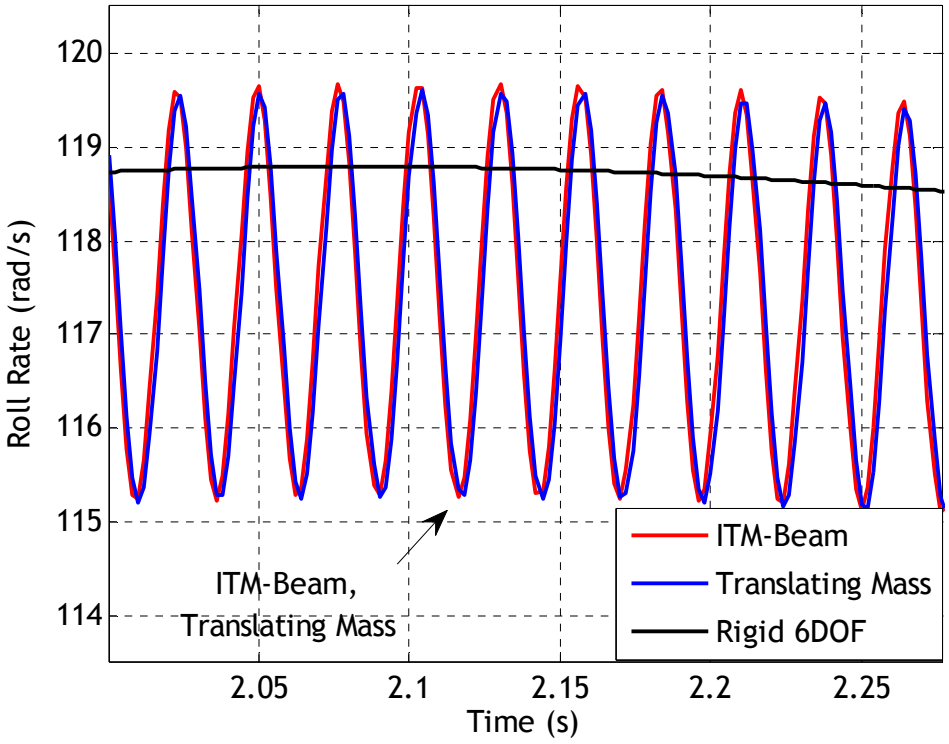

Figure 3.8: Zoom View of Roll Rate vs Time.

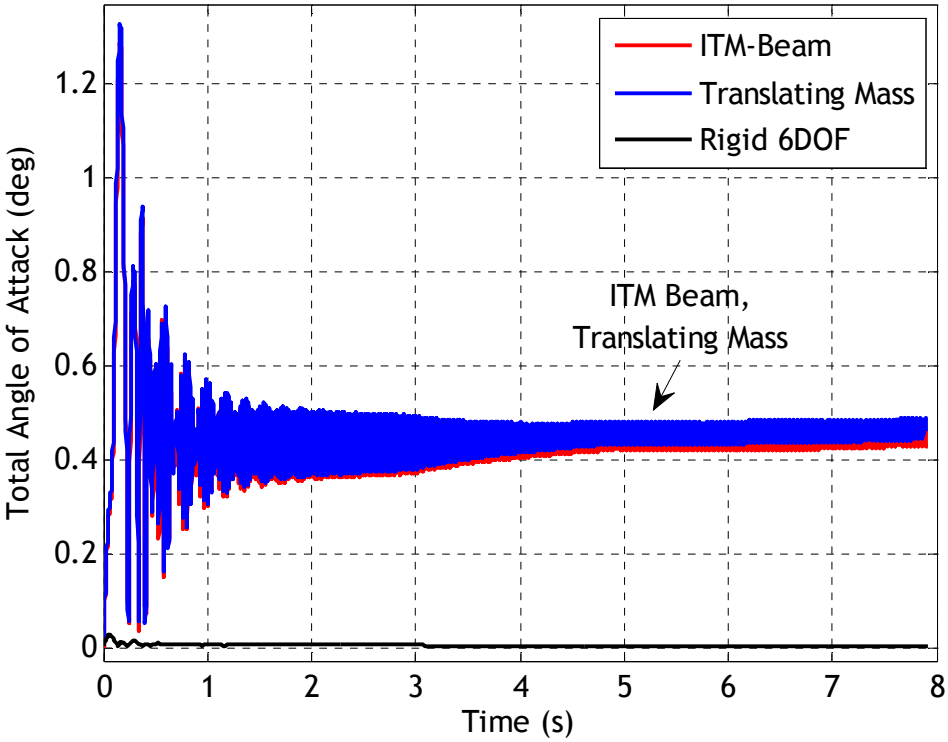

Figure 3.9: Total Angle of Attack vs Time.

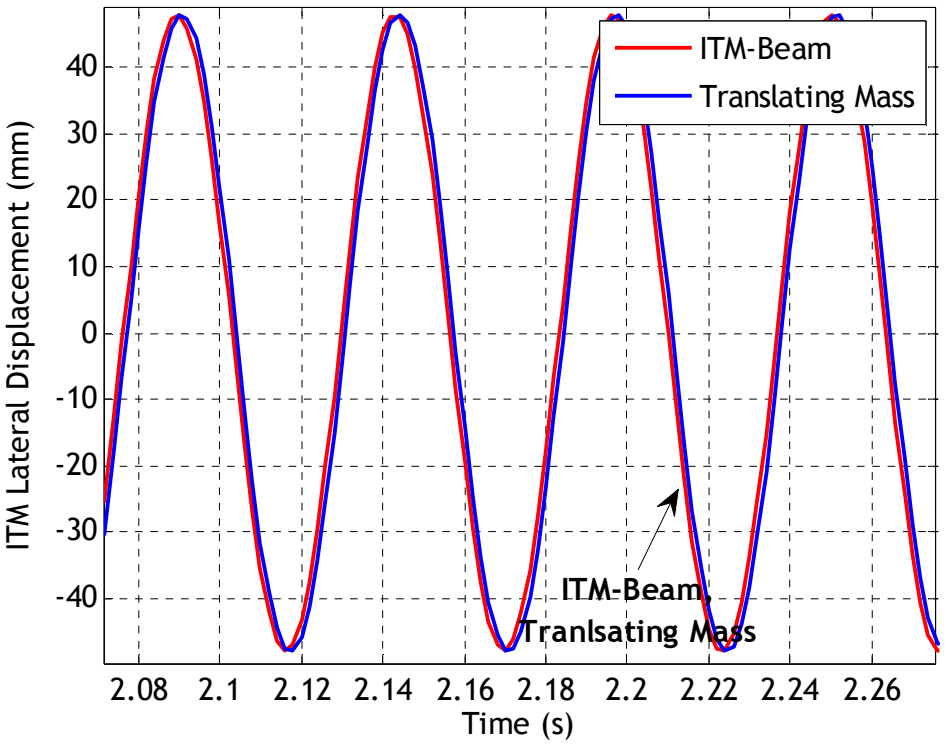

Figure 3.10: ITM Lateral Displacement vs Time.

The ITM-Beam simulation case shown above is also used to generate an example time history of current required and total battery size. Specifically, control force and ITM displacement time histories can be used to generate a time history of current required for each electromagnetic actuator. This is accomplished using the procedure outlined in equations (3.16)-(3.19). Furthermore, this current time history can be integrated to produce the total charge required for a given example flight in A-sec. This value for total charge can be used to size the battery for the ITM-Beam control system. The total charge required for the example flight shown above was 13.5 A-sec. Note that this number is relatively large since the spring and damper coefficients have not been optimized for this preliminary example case.

Figure 3.11 shows a segment of the current time history for the example ITM-Beam simulation used above. Notice that $\boldsymbol{f}_{input}$ (labeled "Force" in the plot) and the ITM-Beam lateral displacement s_x are shown on the same plot as the current time history to demonstrate the phase relationships between current, input force, and ITM-Beam displacement. When the ITM-Beam is displaced in the positive $\vec{\boldsymbol{I}}_S$ direction (s_x positive), electromagnet EM 1 shuts off and EM 2 is responsible for control. Likewise, when the ITM-Beam is displaced in the negative $\vec{\boldsymbol{I}}_S$ direction (s_x negative), electromagnet EM 2 shuts off and EM 1 is responsible for control. This scheme takes advantage of the fact that the electromagnets are much more effective when the ITM is at close range. Since current required is a nonlinear function of both distance to the ITM and control force required, the current time history is not sinusoidal like the ITM displacement time history.

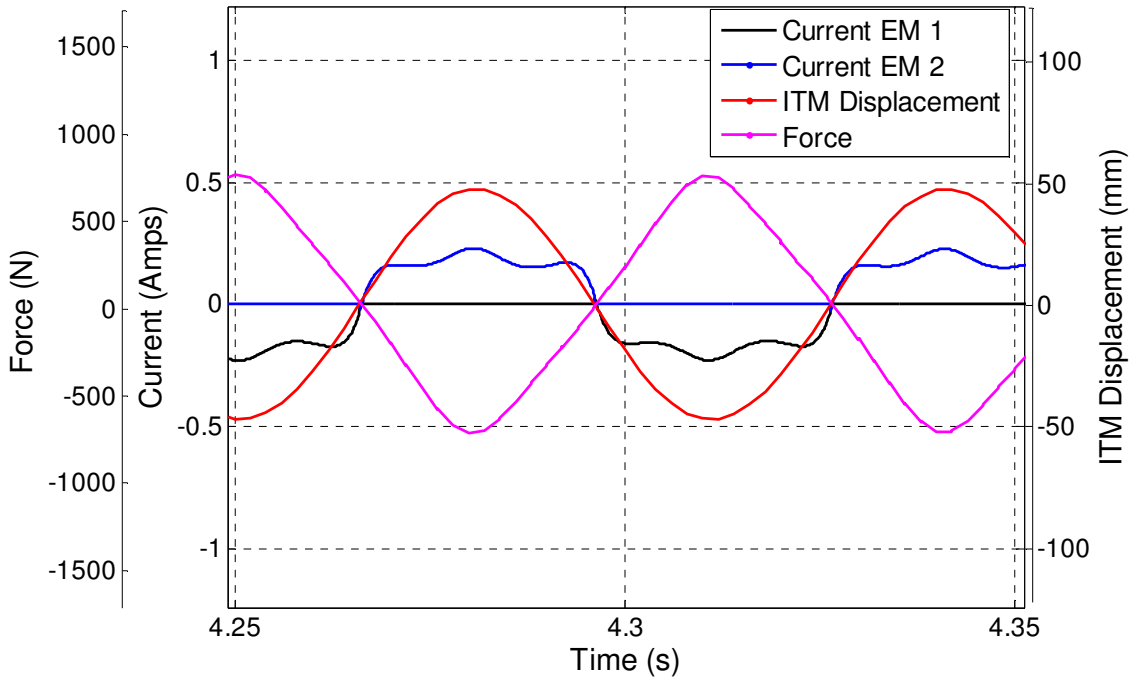

Figure 3.11: Segment of Current vs Time for ITM-Beam Actuators.

3.4 ITM-Beam Trade Studies

Several trade studies are performed to examine the effect of beam length and beam spring and damper coefficients on actuator force and power required. Section 3.4.1 discusses the ITM-Beam length trade study, while Sections 3.4.2 and 3.4.3 describe the effect of spring and damper coefficients on actuator effort over steady-state flight and full flight scenarios respectively.

3.4.1 ITM-Beam Length Trade Study

The length of the ITM-Beam has a significant impact on the force required to move the beam in a prescribed fashion. From equation (3.9), the external moment exerted on the ITM-Beam by the actuators in the $\vec{K}_S$ direction about point L is given by

$$\vec{K}_S \bullet \vec{M}^{L}_{Beam} = -f_{Input} BLc_{\gamma} \tag{3.20}$$

Therefore, the input force required to exert a given control moment on the ITM-Beam varies inversely with beam length. In addition, for a given maximum ITM displacement s_x, the maximum angular displacement $\gamma_{\max}$ varies inversely with beam length. Trade studies verified these results using example simulations with various beam lengths. The maximum ITM displacement from the projectile centerline was s_x = 47.8 mm for all cases. Figures 3.12 and 3.13 show maximum angular displacement and average force required as a function of beam length respectively. Notice that as beam length increases, maximum angular displacement and average force required both decrease. The average control force reduction with increased beam length occurs due to the increased "efficiency" of the ITM-Beam actuators (i.e., the same control moment requires less control force for a larger beam length).

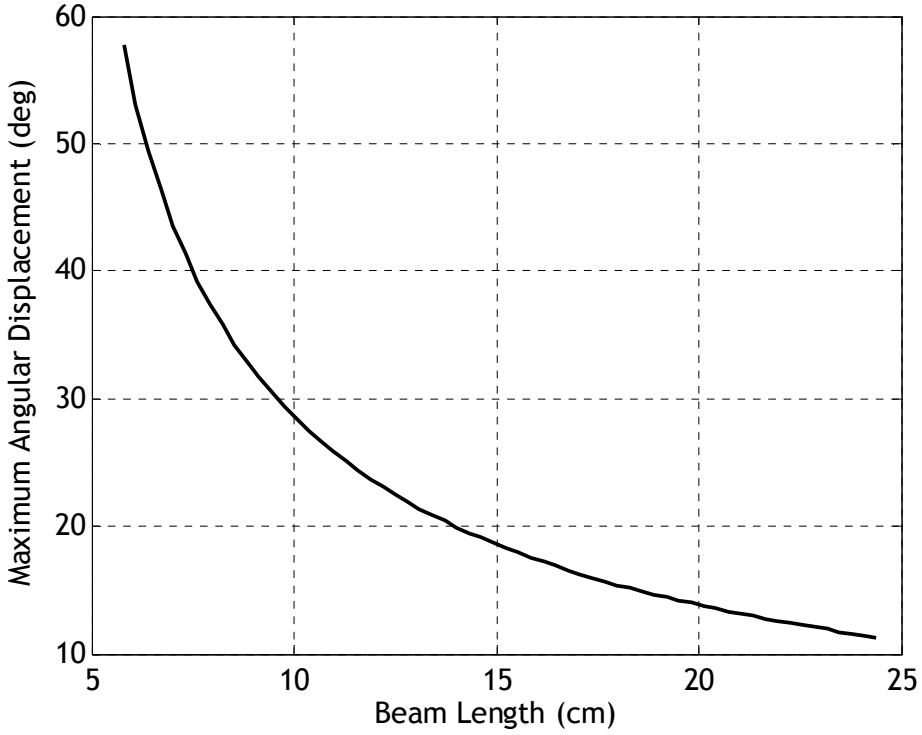

Figure 3.12: Maximum Angular Displacement vs Beam Length.

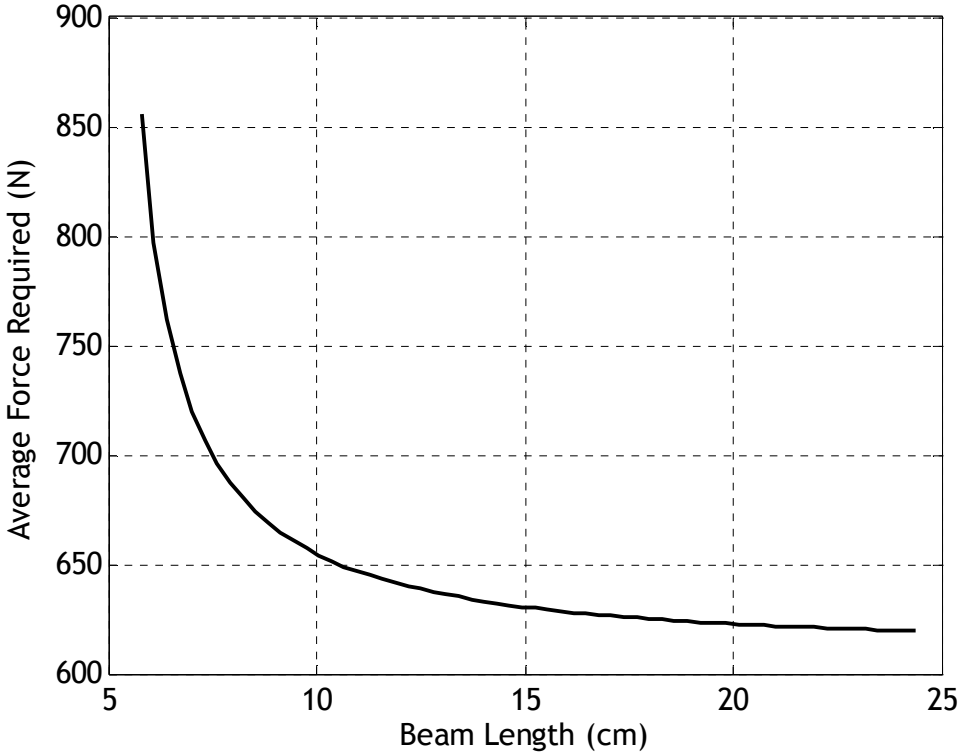

Figure 3.13: Average Force Required vs Beam Length.

3.4.2 Trade Study on Beam Elastic Properties in Steady Flight

As outlined above, the ITM-Beam dynamic model represents a fixed-free elastic beam. The rigid ITM-Beam is attached to the projectile at point *L* with a torsional spring and torsional damper to model the elastic beam's vibrational properties. A trade study examines how force and power requirements vary with different spring and damping coefficients. Once an optimum spring and damper coefficient are determined, they can be used to identify the proper elastic properties of the fixed-free beam for a prototype system.

The performance of the system is examined for a range of torsional spring constants and damping ratios for the example projectile rolling at an approximately steady-state rate of 128 rad/s. The projectile trajectory is simulated for a 2 sec flight with no gravity. This simplified flight profile is used solely to establish the correlation between spring and damper parameters and average force, average power, and total battery charge required. Figure 3.14 shows the projectile roll-rate time history for this flight profile. The high frequency oscillation of the roll rate occurs at the mass oscillation frequency due to the variation of axial inertia as the mass undergoes lateral motion (as described in Chapter 2).

Figures 3.15-3.17 show the effect of spring and damper coefficients on average force, average power, and total battery charge required. In Figure 3.15, it can be clearly seen that an optimum torsional spring constant exists, in which the spring-mass-damper system of the ITM-Beam operates near resonance with the projectile roll rate. These peaks are not as sharp as typical spring-mass-damper resonant peaks due to the fact that the projectile roll rate varies over time. Note, however, that significant reductions in force are achieved if the spring constant is placed near its optimum value and damping is lowered as much as possible. These reductions in force are mirrored by reductions in average power and total charge required, resulting in significantly smaller battery sizes.

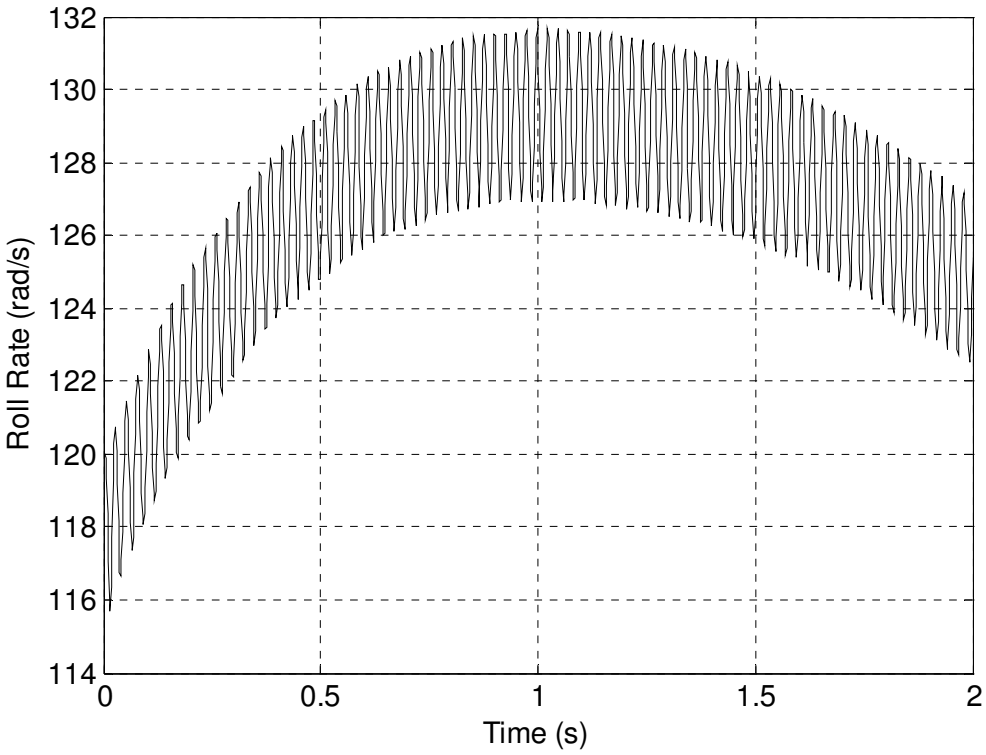

Figure 3.14: Roll Rate vs Time for Example Simulation.

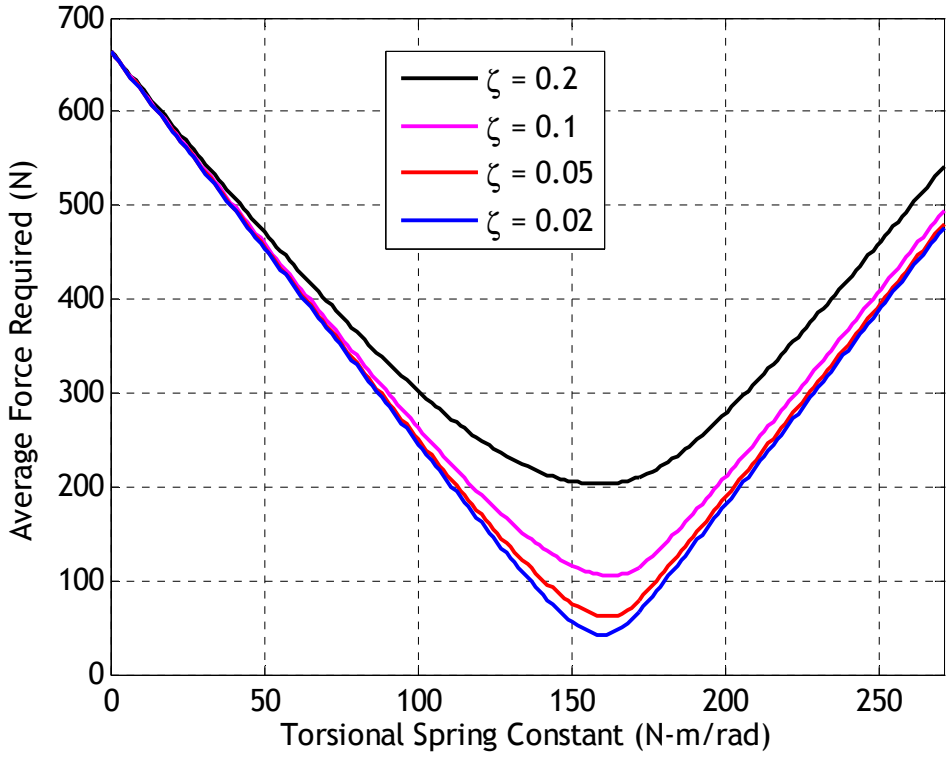

Figure 3.15: Average Force Required vs Torsional Spring Constant.

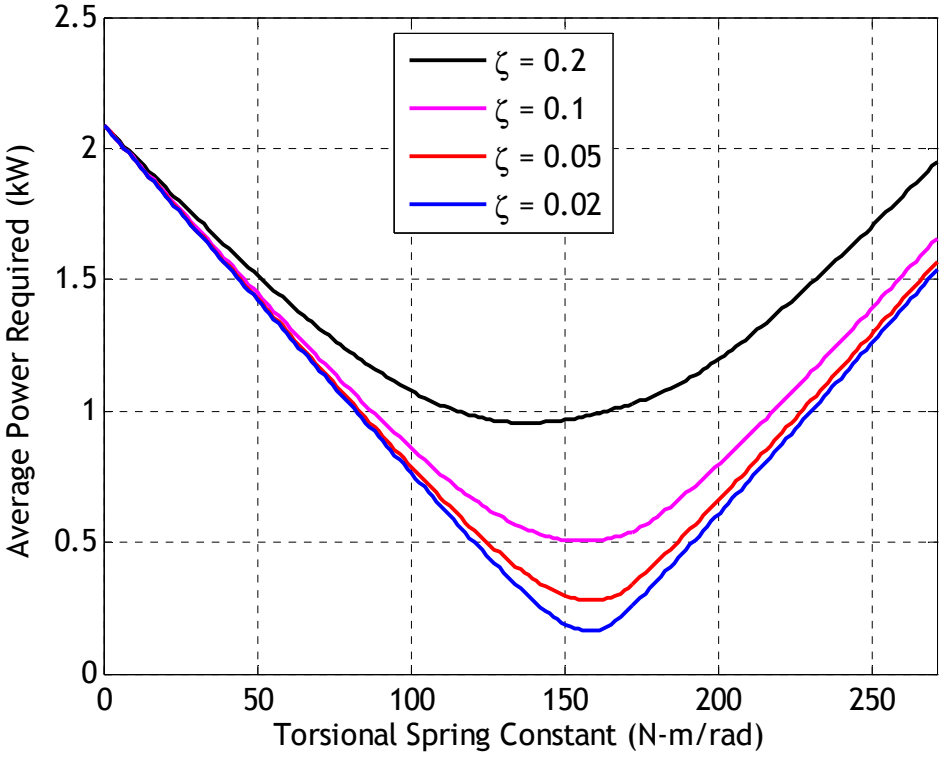

Figure 3.16: Average Power Required vs Torsional Spring Constant.

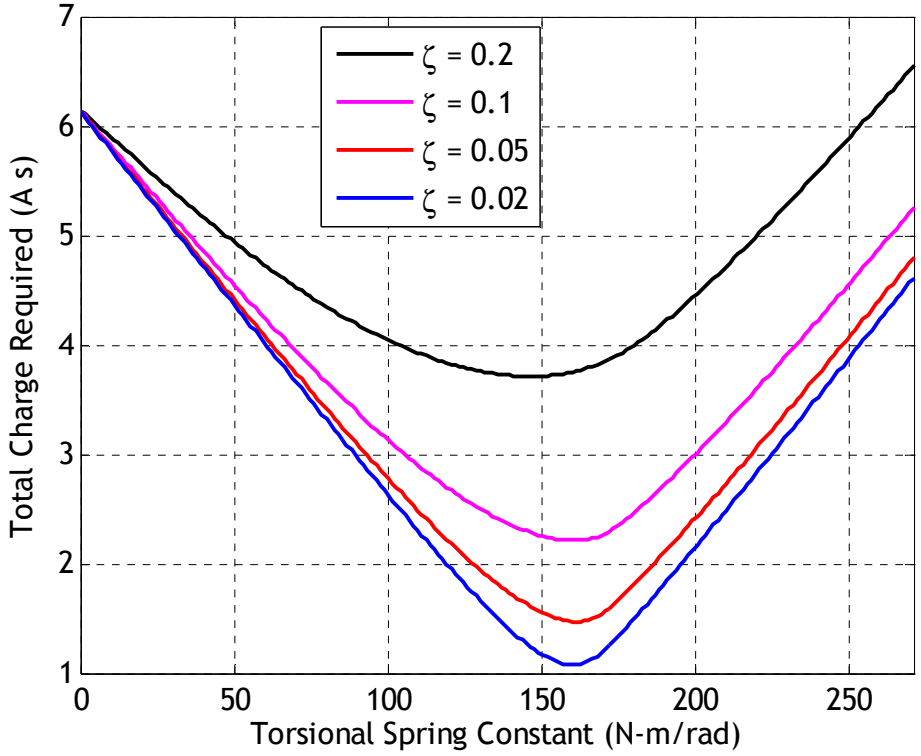

Figure 3.17: Total Charge Required vs Torsional Spring Constant.

3.4.3 Trade Study on Beam Elastic Properties for Full Flight Profile

A similar study examines the same spring-mass-damper parameters for a full flight profile of the example projectile using the same initial conditions as those used in the first example study above. Figures 3.18-3.20 show that, as in the partial flight profile case, optimal spring coefficients can be found. However, the results for the partial flight profile have a significantly sharper peak than the results for the full flight profile. This is because, as shown in Figure 3.7, roll rate of the projectile varies between 5 rad/s initially and a final value of approximately 80 rad/s. This large variation in roll rate means that the spring coefficient is only optimized for a very short period of the overall flight, and the broad peaks shown in Figures 3.18-3.20 result. To demonstrate this, Figure 3.21 shows a current time history for an example full flight trajectory using k_T = 94.9 N-m/rad and k_D = 0.068 N-m/rad/s. Note that the spring constant is optimized for the projectile roll rate approximately 1 sec into flight, and once again after spin decay occurs approximately 7 sec into the flight.

Despite the broad nature of the peaks shown in Figures 3.18-3.20, significant size and weight savings can be achieved using the proper spring constants in the form of smaller batteries. As shown in Figure 3.20, batteries with a total charge of less than 5 A-sec may be used for systems with optimal spring coefficients and low damping ratios. Furthermore, Figure 3.21 shows that reasonable maximum current levels, on the order of 150 mA, can be expected with an optimized system.

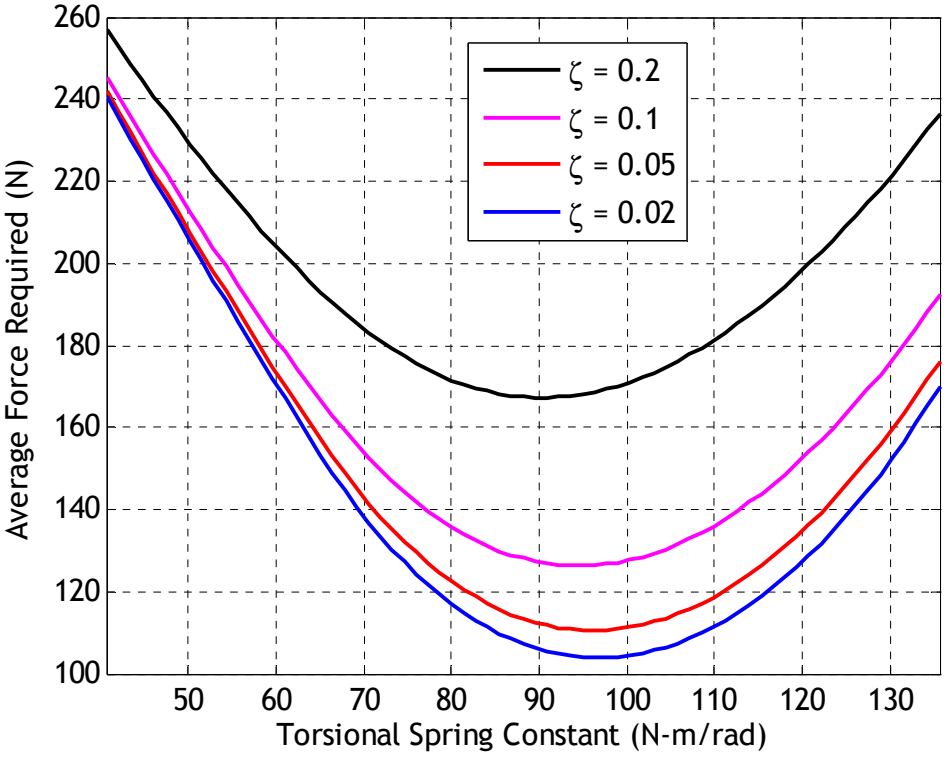

Figure 3.18: Average Force Required vs Torsional Spring Constant.

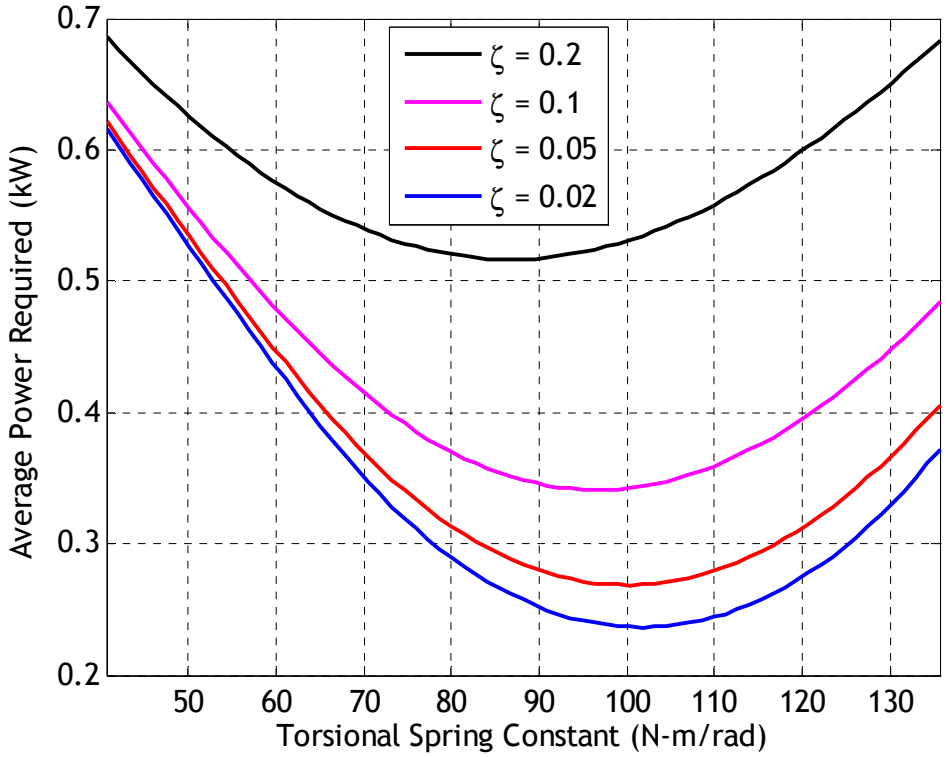

Figure 3.19: Average Power Required vs Torsional Spring Constant.

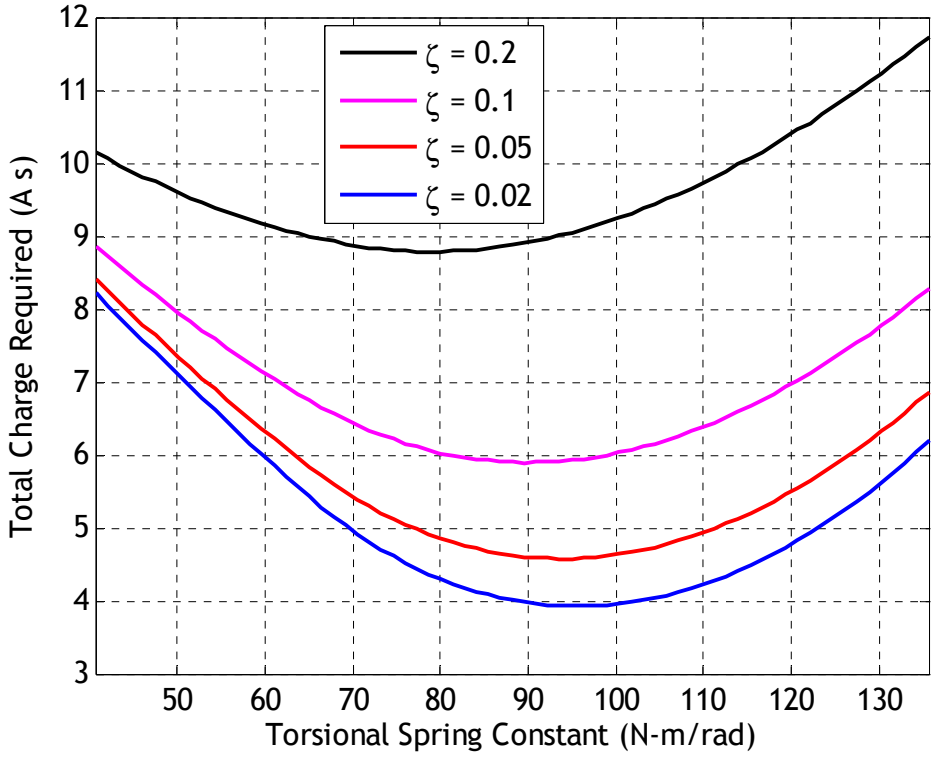

Figure 3.20: Total Charge Required vs Torsional Spring Constant.

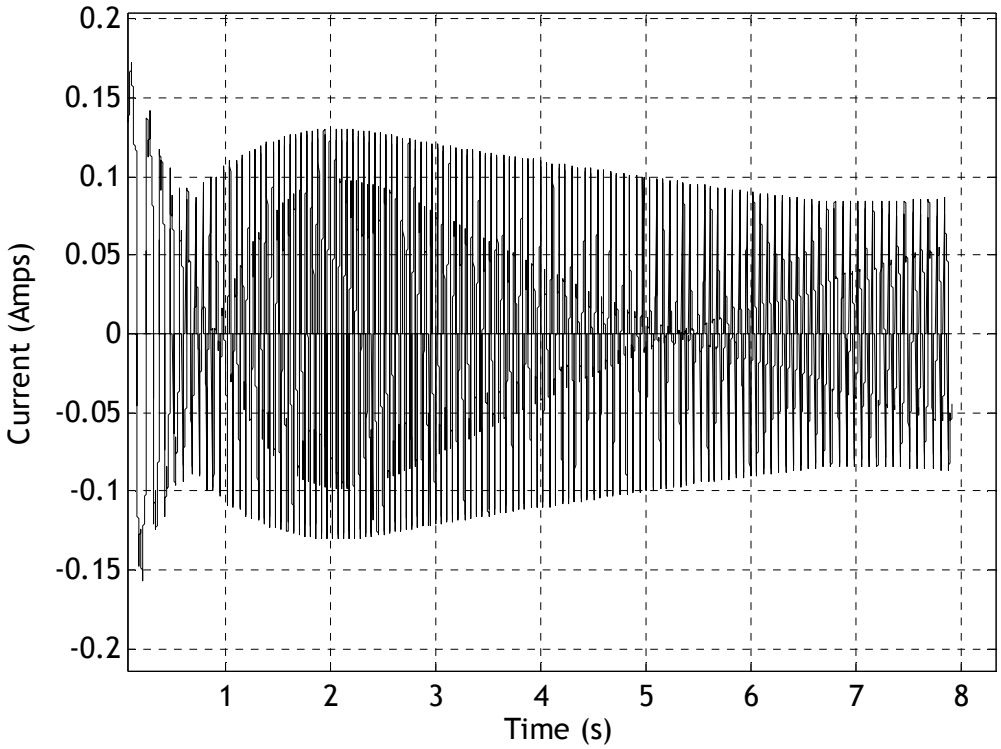

Figure 3.21: Current vs Time for Sample Case.

3.4.4 Roll Rate Feedback System

Average force levels, and therefore total charge required, can be decreased even further by actively changing the elastic properties of the beam during flight. A fixed-free cantilever beam like that used in this system has a first vibrational mode shape of

$$\boldsymbol{s}_{x} = \sin\left(\frac{\pi \boldsymbol{x}_{B}}{2\boldsymbol{BL}}\right) \tag{3.21}$$

where $\boldsymbol{x}_{B}$ is the distance along the beam. The natural frequency of the first vibrational mode is

$$\omega_{n} = \frac{\pi}{2\boldsymbol{BL}}\sqrt{\frac{\boldsymbol{E}}{\rho}} \tag{3.22}$$

where E is the modulus of elasticity of the material and ρ is the density of the beam.[31] By changing the modulus of elasticity, it is therefore possible to tune the natural frequency of the cantilever beam to a desired value. Recent investigations into smart materials, [32,33,34,35] specifically materials used in tunable vibration absorbers, have shown that various methods can be used to actively alter a material's modulus of elasticity, allowing the beam's torsional spring constant to be actively optimized during flight as the projectile roll rate changes. This would allow the ITM-Beam system to operate with the lowest possible power through the entire flight, yielding further reductions in battery size.

To investigate this, several example simulations were run. The first set simulated the projectile for the full flight using fixed optimum spring constants obtained from Figure 3.20. This produced the least possible battery charge required for the ITM-Beam system with a fixed spring constant for each damping ratio considered. The second set of

simulations included a roll-rate feedback mechanism. In these cases, at specific points throughout the flight the torsional spring and damping coefficients of the ITM-Beam were adjusted according to the current roll rate. Figure 3.22 shows how the torsional spring constant was adjusted for an example flight with $\zeta = 0.05$. Note that the curve in Figure 3.22 has the same qualitative shape as the roll rate time history shown in Figure 3.7. Table 3.1 summarizes the results of the two sets of simulations with the fixed torsional spring and variable torsional spring constants. Note that in the variable torsional spring cases, the torsional damping coefficient $\boldsymbol{k_D}$ was adjusted slightly as well so as to keep the damping ratio ζ constant. Figure 3.23 demonstrates that implementation of the roll-rate feedback system saves approximately 1 A-sec of charge for all damping ratios considered (34.4% decrease in battery size for $\zeta = 0.02$, 28.1% decrease for $\zeta = 0.05$, 20.4% for $\zeta = 0.1$, and 11.2% for $\zeta = 0.2$).

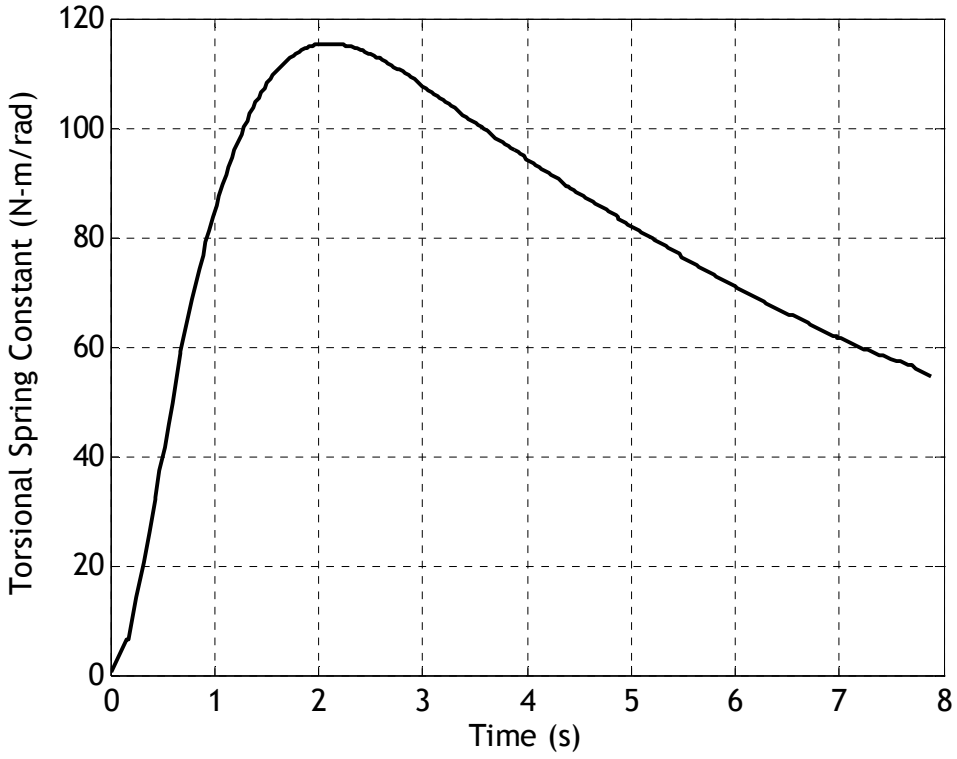

Figure 3.22: Torsional Spring Constant vs Time for Roll-Rate Feedback System, $\zeta = 0.05$.

Table 3.1: Performance Evaluation of Roll-Rate Feedback System.

Damping Ratio ζ	Optimum k_T for No Feedback Case	Charge Required (A-sec)		Percentage Decrease in Charge Required with Feedback
		No Feeback (Constant k_T)	Feedback (Variable k_T)	
0.02	71	3.924	2.576	34.4%
0.05	69	4.576	3.287	28.1%
0.1	67	5.895	4.692	20.4%
0.2	58	8.786	7.798	11.2%

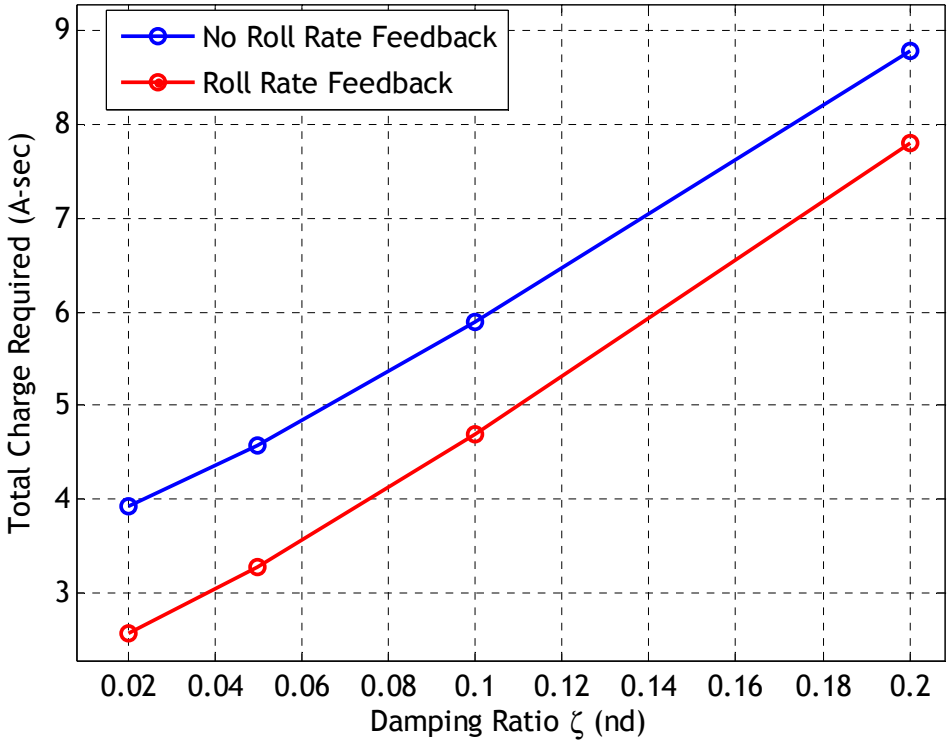

Figure 3.23: Total Charge Required vs Damping Ratio.

3.5 ITM-Beam Mechanism Structural Analysis

This section discusses several key issues associated with the flexible dynamics and structural integrity of the ITM-Beam projectile. Specifically, Section 3.5.1 explores torsional mode excitation of the ITM-Beam during projectile flight using a simplified dynamic model. In Section 3.5.2, maximum normal and shearing stresses within the ITM-Beam are calculated in order to help a designer size the beam and choose proper materials. Section 3.5.3 considers fatigue within the beam, further facilitating design of the beam's size and material makeup.

3.5.1 Torsional Mode Excitation

While the ITM-Beam is restricted to motion in the $\vec{I}_P - \vec{J}_P$ plane, it may undergo torsional motion in response to applied rolling moments. In similarly-configured dynamic systems, such as helicopter blades, these torsional modes, when coupled with bending modes, have been shown potentially to lead to instabilities. For helicopters, this phenomenon is known as pitch-flap coupling, and can be unstable for certain configurations.[49]

To analyze both the transient and steady-state behavior of the ITM-Beam, a simplified 2-degree-of-freedom model is used. The projectile body, represented as a large cylinder, is subjected to an external torque and allowed to roll freely by an angle ϕ with respect to the inertial frame. Coupled to the cylinder by a torsional spring and damper is a rectangular prism representing the ITM-Beam. The ITM-Beam is not subjected to any external torques except for the reaction moments from the hinge and damper, and rolls with respect to the projectile by an angle δ. The kinematic and dynamic equations that describe this simplified system are

$$\frac{d}{dt}\phi = \dot{\phi} \tag{3.23}$$

$$\frac{d}{dt}\delta = \dot{\delta} \tag{3.24}$$

$$\frac{d}{dt}\dot{\phi} = \frac{1}{I_B}\left(T + k\delta + d\dot{\delta}\right) \tag{3.25}$$

$$\frac{d}{dt}\dot{\delta} = \frac{1}{I_L}\left(-k\delta - d\dot{\delta} - I_L\frac{d}{dt}\dot{\phi}\right) \tag{3.26}$$

where I_B and I_T are the axial mass moments of inertia of the cylinder and beam respectively, k and d are the torsional spring and damper constants respectively, and T is the external torque applied to the cylindrical body. The cylindrical body has identical mass properties to the example projectile used in previous simulations, while the ITM-Beam's mass properties are varied in order to explore different sizing options. Furthermore, the external torque applied to the cylinder is identical to the rolling torque applied to the example projectile in flight caused by fin cant and aerodynamic spin damping. Figures 3.24 and 3.25 show schematics of the simplified system, while Figure 3.26 shows a time history of the roll torque applied to the cylinder.

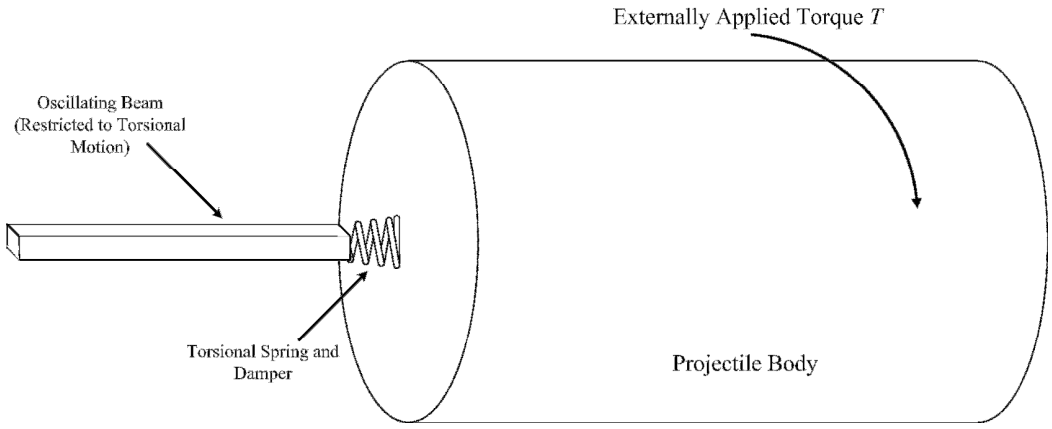

Figure 3.24: Simplified System Diagram.

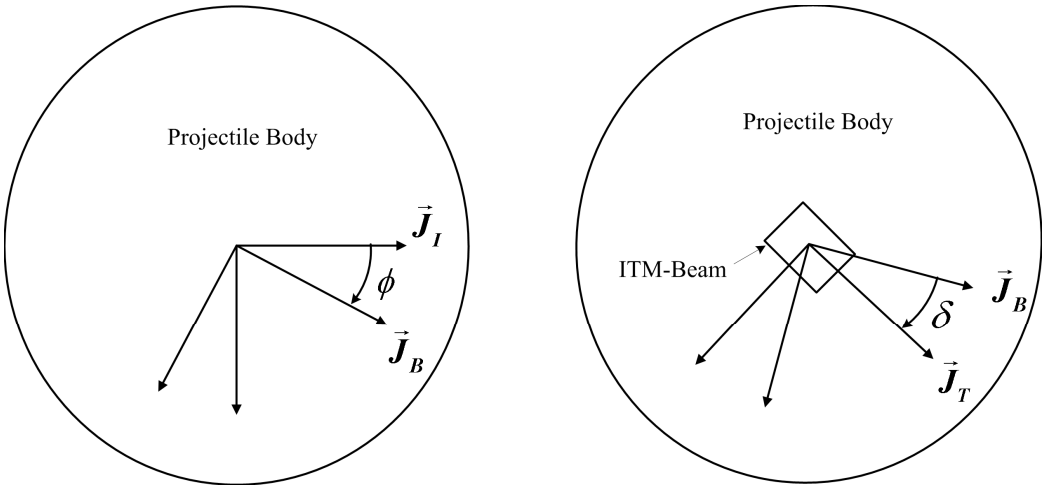

Figure 3.25: Reference Frames for Simplified System.

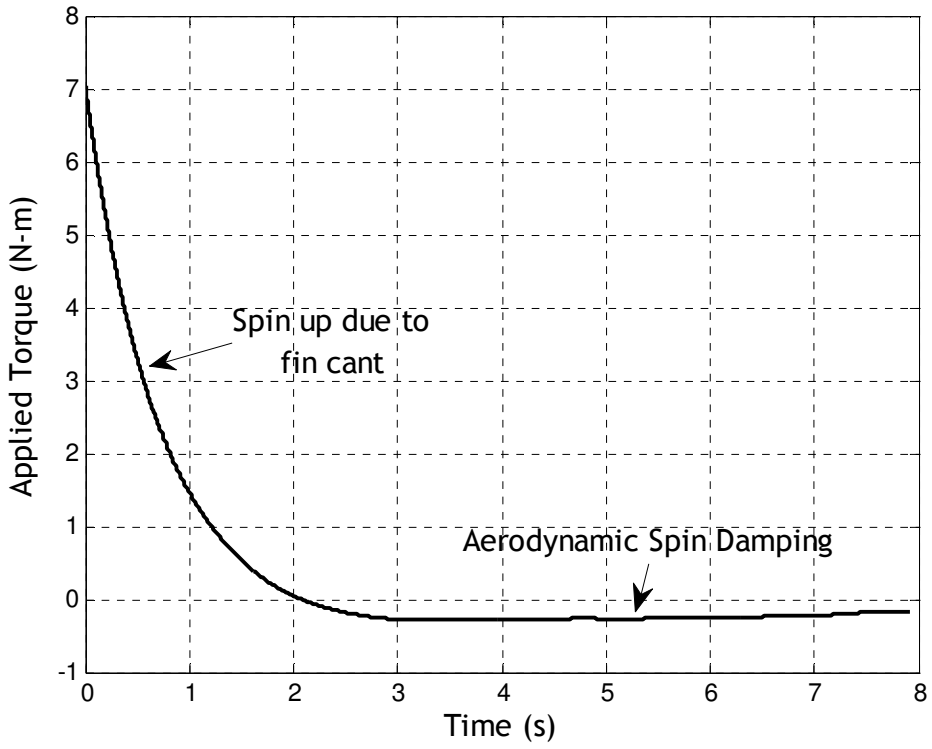

Figure 3.26: Applied Roll Torque vs Time.

The torsional spring constant for the simplified simulation represents the beam's torsional elasticity. A torque applied to the free end of a fixed-free beam is converted linearly into a rotation angle δ according to

$$\boldsymbol{T} = \boldsymbol{k}\delta \tag{3.27}$$

where $k = JG/L$ as long as the stresses within the beam fall within the elastic range. In this definition of k and equation (3.27), T is the applied torque, J is the beam's polar moment of inertia (in units of [length]^4), L is the length of the beam, and G is the shear modulus of the material. Since damping constants for such a system are likely to be small, a value of $d = 0.00014$ N-m/rad/sec was used the simulation below.

An example simulation is performed using reasonable parameters for beam size, shape and material composition. Table 3.2 provides the relevant inertial, dimensional, and material properties. Figures 3.27-3.31 show the state time histories for projectile roll angle and roll rate as well as beam roll angle and roll rate.

Table 3.2 Parameters for Example Simulation.

Cylinder Axial Mass Moment of Inertia (kg-m^2)	0.0377
Beam Axial Mass Moment of Inertia (kg-m^2)	9.8051×10^{-5}
Beam Mass (kg)	0.73
Beam Length (cm)	12.2
Beam Width (cm)	3.8
Beam Depth (cm)	1.27
Beam Area Moment of Inertia (cm^4)	5.8522
Shear Modulus *G* (N/cm^2)	3.45×10^6

Given the example set of parameters in Table 3.2, the torsional spring constant k of the beam is found to be 1.6547×10^4 N-m/rad. Therefore, the frequency of beam torsional oscillation is predicted to be

$$f_{Beam} = \frac{\sqrt{k / I_L}}{2\pi} \approx 2{,}067 \text{ Hz} \tag{3.28}$$

which matches nearly exactly with the simulated results.

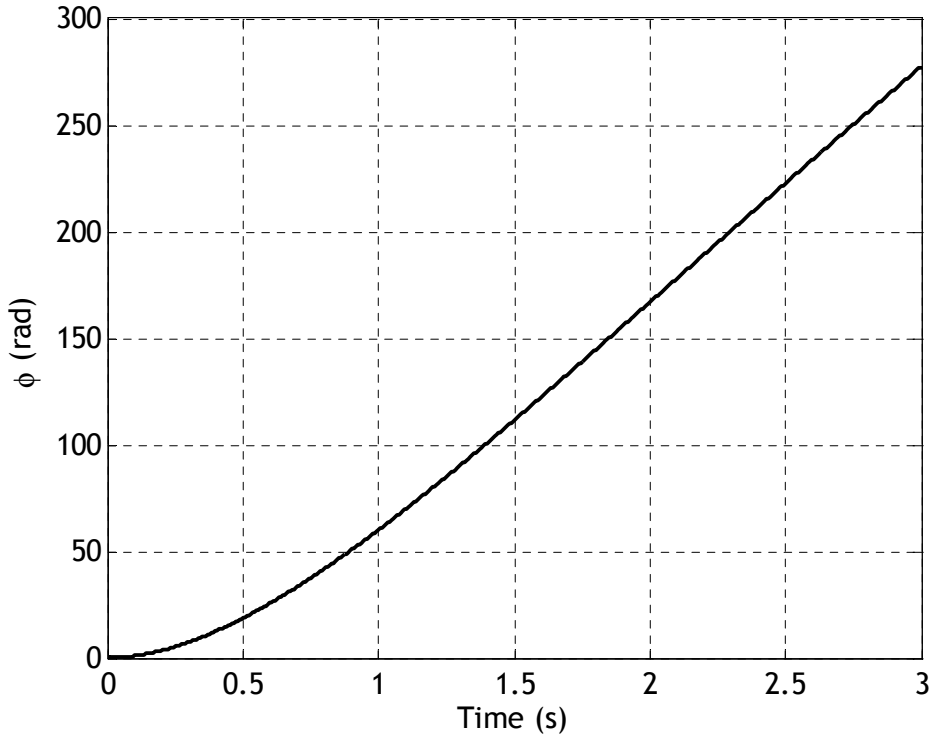

Figure 3.27: Cylinder Roll Angle (ϕ) vs Time.

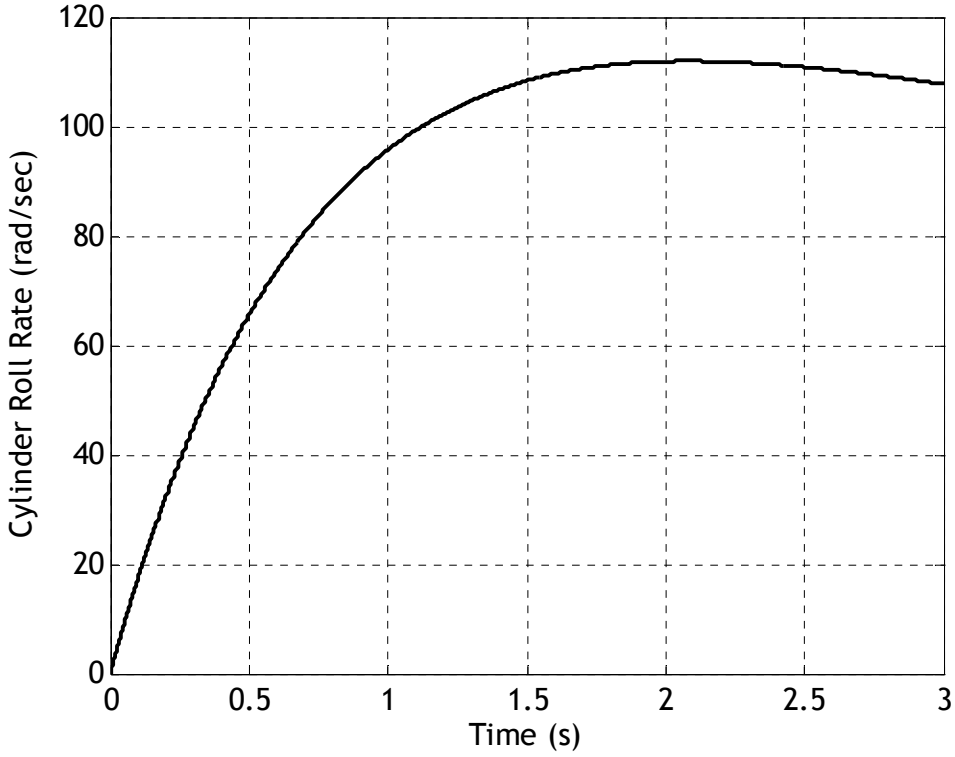

Figure 3.28: Cylinder Roll Rate vs Time.

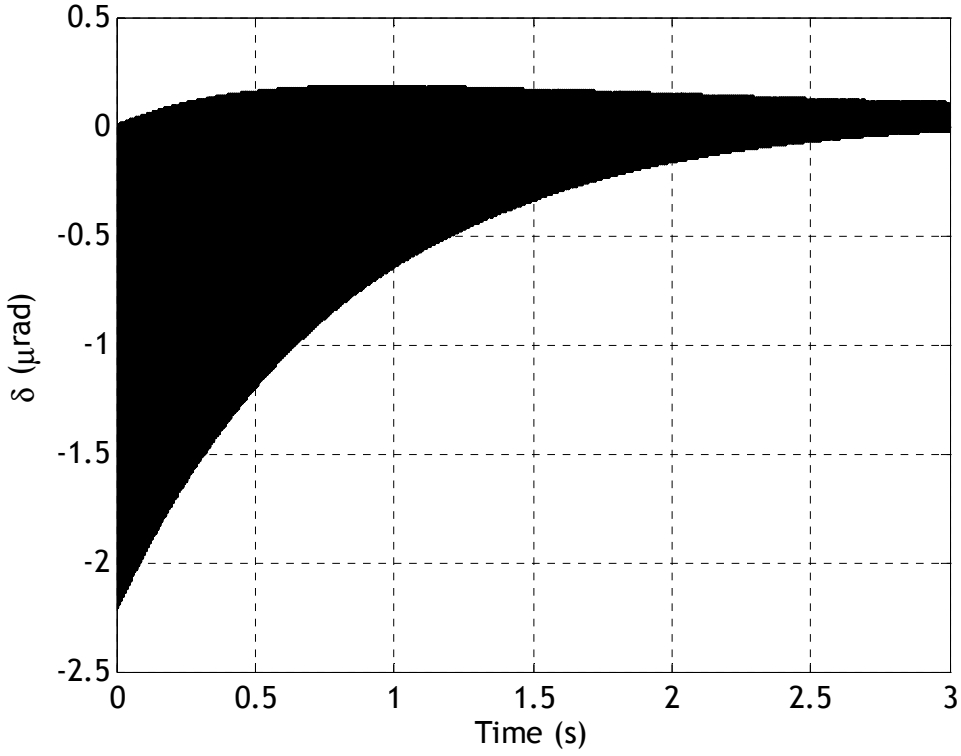

Figure 3.29: Beam Roll Angle (δ) vs Time.

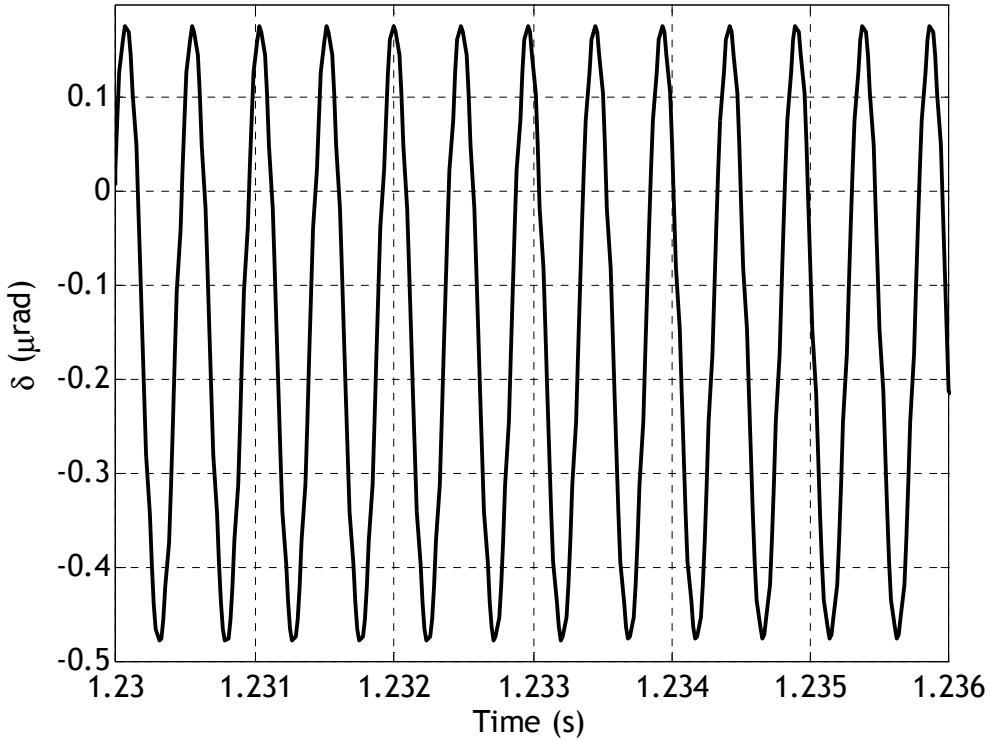

Figure 3.30: Zoom View of Beam Roll Angle (δ) vs Time.

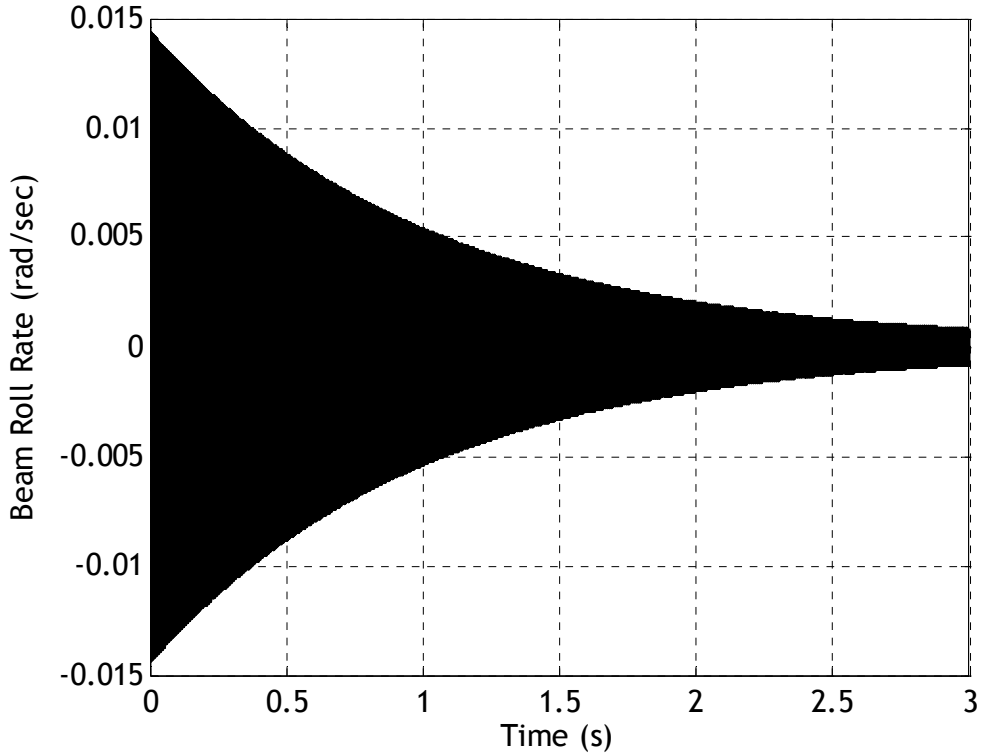

Figure 3.31: Beam Roll Rate vs Time.

Two important factors lead to the conclusion that torsional motion of the beam will have negligible impact on the flight dynamics of the projectile and the bending dynamics of the beam. First is the difference in order of magnitude between the torsional frequency of the beam, the bending frequency of the beam, the projectile roll frequency, and the epicyclic frequencies of the projectile. While the beam undergoes torsion at a frequency of roughly 2 kHz, the projectile rolls at a frequency of approximately 10-20 Hz (see Figure 3.28), with the beam bending at double the roll frequency (20-40 Hz). Epicyclic frequencies of the projectile are typically lower than the projectile roll rate. Due to the roughly three orders of magnitude difference in frequencies between the beam's torsional mode and other projectile and beam oscillation modes, it is highly unlikely that any important coupling will occur. Furthermore, the torsional mode is characterized by very small oscillation amplitudes, on the order of 10^{-6} rad, due to the relatively low external torque applied to the cylinder and very small axial inertia of the beam. These very small amplitudes lead to the conclusion that shear stress due to torsion are negligible compared to the stress induced by the bending motion of the beam.

The cause of the large frequency disparities between the beam torsional modes and the projectile roll and epicyclic modes is the roughly three orders of magnitude difference between the beam axial mass moment of inertia and the projectile axial mass moment of inertia. To demonstrate this, a trade study is conducted that measures the maximum torsional deflection of the beam for various beam moments of inertia and torsional spring constants. Figure 3.32 shows that for a wide range of spring constants and beam inertias, the beam's maximum torsional deflection is limited to milliradians. Note that the nominal case, shown in the example study above, actually lies very close to the origin in Figure 3.32.

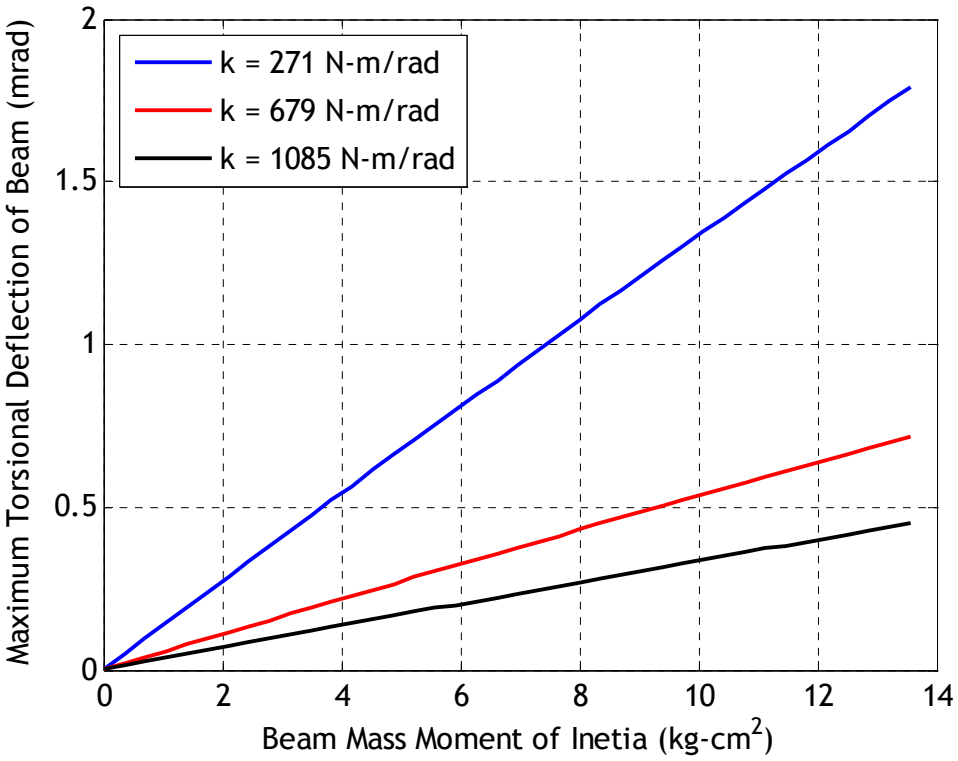

Figure 3.32: Maximum Beam Torsional Deflection vs Moment of Inertia.

The large frequency separation between projectile modes and beam torsional modes combined with the very small amplitudes associated with beam torsional motion lead to the conclusion that torsional modes of the beam will not have any significant impact on projectile flight dynamics.

3.5.2 Stress Analysis of the ITM-Beam

Both the maximum normal stress and the maximum shearing stress are computed for a rectangular ITM-Beam in order to facilitate design of the mechanism. A schematic of the simplified fixed-free beam with appropriate dimensions is shown in Figure 3.33.

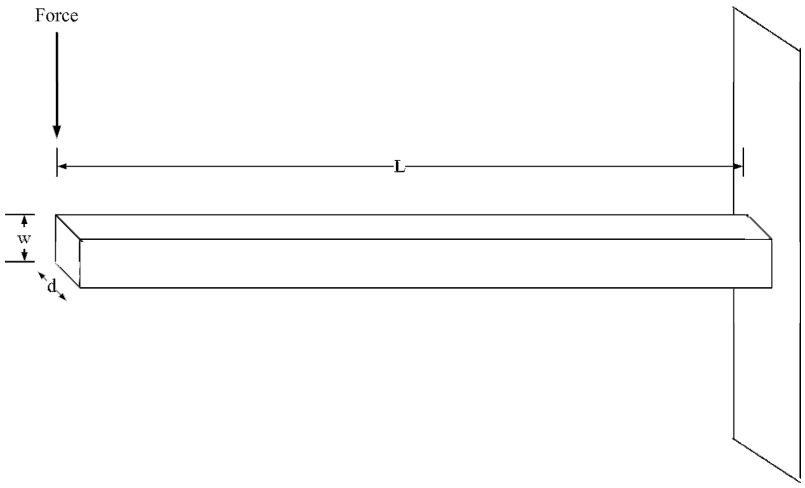

Figure 3.33: Fixed-Free ITM-Beam Configuration.

Given a fixed-free beam configuration like that used for the ITM-Beam, it can be shown that the maximum normal stress in the presence of a force at the free end of the beam occurs at the junction point of the beam to the fixed surface, at points farthest from the beam axis. The magnitude of this maximum normal stress is given by [36]

$$\left|\sigma_{\max}\right| = \frac{FLw}{2J} \tag{3.29}$$

where $\sigma_{\max}$ is the maximum normal stress, F is the force imparted on the free end of the beam, and J is the area moment of inertia of the beam. Computation of the maximum shear stress of the beam is somewhat more complicated, and cannot be solved in closed form. For a rectangular beam, the shear stress along the beam axis is computed as [36]

$$\tau_{axis} = \frac{3F}{2A} \tag{3.30}$$

where F is the force imparted on the free end of the beam and A is the area of the beam cross-section. An empirically-derived table [36] given in Table 3.3 allows the maximum and minimum shear stresses to be calculated from the shear stress along the axis. Note that beam dimensions d and w are shown in Figure 3.33.

Table 3.3: Maximum and Minimum Shear Stress Multipliers for Various Beam Depth-to-Width Ratios.

d / w	1	2	4	6
τ_{max} / τ_{axis}	1.126	1.396	1.988	2.582
τ_{min} / τ_{axis}	0.940	0.856	0.805	0.800

These multipliers can be used to compute maximum stress in the ITM-Beam based on the axial calculation given in equation (3.30). Note that equations (3.29) and (3.30) as well as Table 3.3 are only valid as long as the stresses remain within the elastic range of the material.

Equations (3.29) and (3.30) demonstrate that the maximum stresses vary linearly with the maximum force imparted on the beam. A trade study was therefore conducted to examine the maximum normal and shear stresses in the beam for various maximum force levels and various ratios of beam depth to width. Figures 3.34 and 3.35 show the results of this trade study for a beam width of 1.27 cm. Figure 3.34 shows a logarithmic plot of maximum normal stress, while Figure 3.35 shows maximum shear stress.

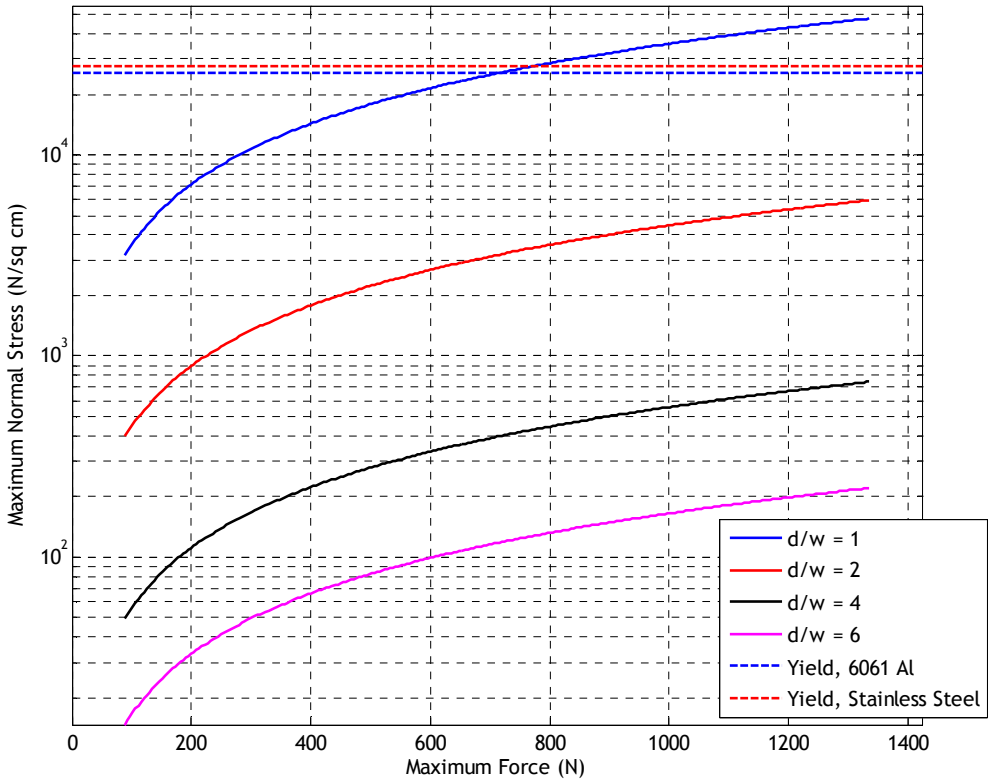

Figure 3.34: Maximum Normal Stress vs Maximum Force.

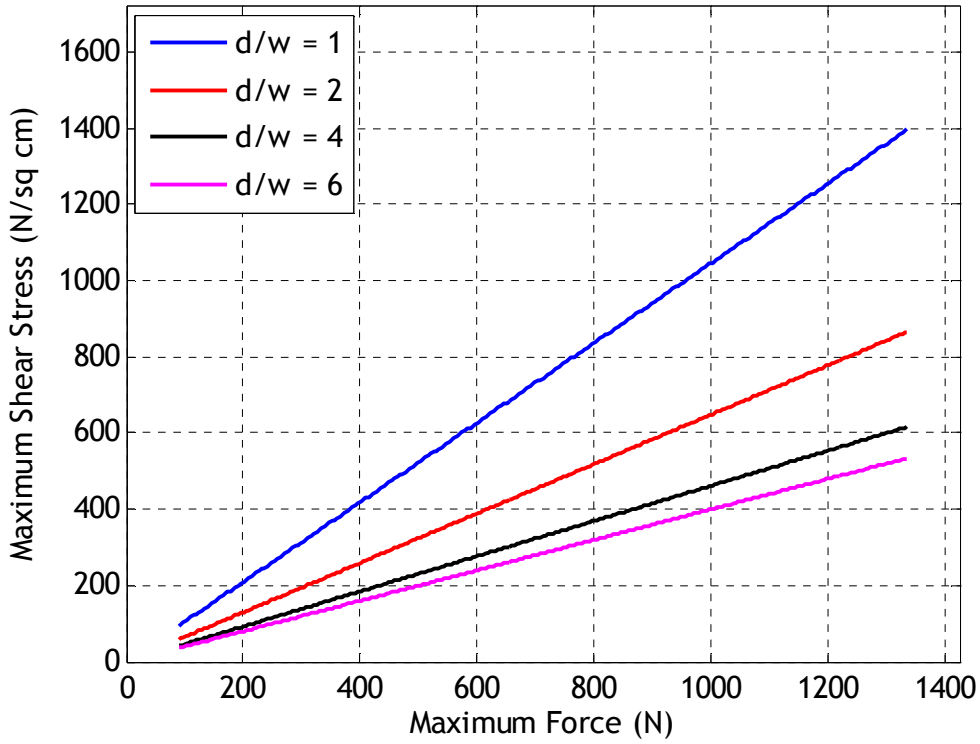

Figure 3.35: Maximum Shear Stress vs Maximum Force.

Figure 3.34 demonstrates that maximum normal stresses in rectangular beams fall well below the yield stress of typical metals such as aluminum and stainless steel. Only in the case of square beams does the maximum normal stress approach prohibitively high values. For reasonable depth-to-width ratios between 2 and 6, it is clear that composite materials with high enough yield stresses can be found to physically realize the ITM-Beam mechanism.

3.5.3 Fatigue Considerations for the ITM-Beam

Fatigue is considered by first examining the number of completely reversed cycles that are experienced by the ITM-Beam during flight and, given the maximum stress experienced by the beam, determining the probability of failure using a fatigue curve (or S-N curve). Figure 3.7 shows the roll rate profile of the example projectile. Integration of roll rate over time for a full 8 second flight reveals that the projectile undergoes approximately 124 full roll cycles. Since the ITM-Beam oscillates exactly twice every roll cycle, the ITM-Beam experiences approximately 248 total cycles during flight for the example considered here. Fatigue due to less than 1000 stress cycles is considered to be “low cycle” fatigue. In this range, most materials exhibit a failure stress of between 90% and 100% of their ultimate tensile stress, as shown in the S-N curve in Figure 3.36. Since the margin between maximum stress felt by the beam and yield (or, to be sure, ultimate) stress in several materials was shown to be so large in Section 3.5.2, it is evident that there is unlikely to be any fatigue-related failures of the ITM-Beam system.

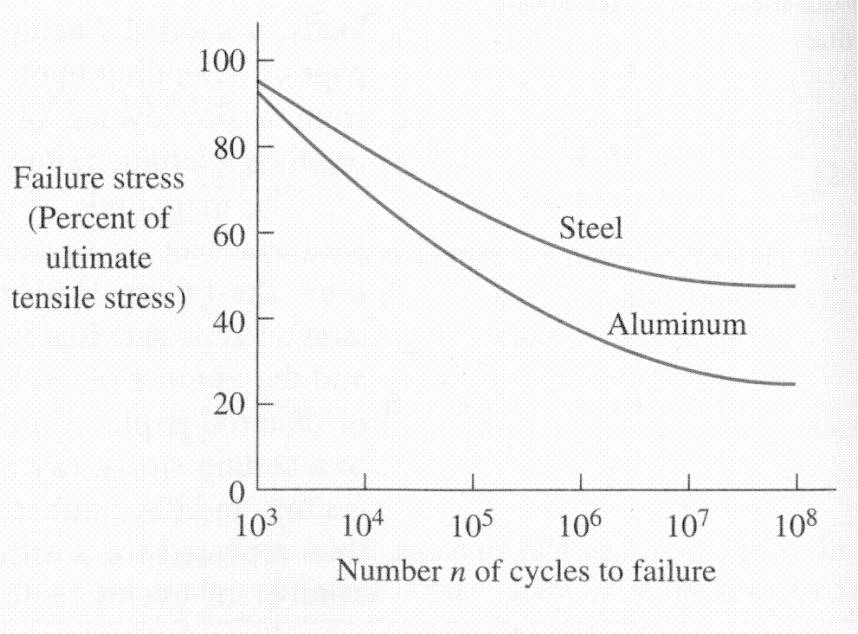

Figure 3.36: S-N Curve for Steel and Aluminum. [36]

CHAPTER 4

A VARIABLE STABILITY PROJECTILE USING AN INTERNAL TRANSLATING MASS

The previous two chapters explored the use of translating internal masses for projectile flight control purposes. In this chapter, an internal translating mass is used not to create direct control moments but rather to actively alter projectile static margin in flight. Therefore the cavity hosting the internal mass is oriented longitudinally rather than laterally within the projectile, allowing translation of the mass to alter center of gravity position along the axis of symmetry. In this so-called variable stability configuration, the ITM is translated once from the front to the aft end of the projectile, decreasing static stability after launch perturbations have dissipated allowing for greater control authority throughout the remainder of flight. Example trajectories and trade studies demonstrate the reduction in required control force provided by the variable stability mechanism. [22]

4.1 Previous Work on Static Stability and Projectile Flight Dynamics

The correlation between static margin size and projectile stability has been known for some time and utilized since the earliest days of aircraft and missile design. However, limited work has been performed to examine the effects of static margin on flight dynamics and control authority of artillery shells in particular, little of which examines the effect of actively altering the mass center location in flight.

Previous research on the effect of static margin on projectile flight dynamics have been driven by an effort to ballistically match dissimilar projectiles, resulted in investigation of the effect of mass properties on the Yaw of Repose and resulting

trajectory drift. Vaughn and Wilson [29] showed that the ratio of roll inertia to static margin is the most important factor in determining yaw of repose magnitude by developing an analytic expression for yaw of repose. Estimation of cross range drift using this expression matched closely with results from a 6DOF model. Later, Rollstin [17] continued this work by developing an analytic expression for trajectory drift that was dependent on mass center location and roll inertia, but independent of pitch or yaw inertia. This expression also closely matched results from a 6DOF model. A carefully controlled set of flight tests using the M106 munition, in which projectile mass properties were varied, also showed good correlation with Rollstin's analytic expression. The author therefore concluded that trajectory drift increases with a larger roll inertia and, for a spin-stabilized round, decreases with larger distance between the mass center and aerodynamic center.

Several researchers have investigated the benefits of varying projectile static stability in flight. Donovan [37] designed a specific mechanism for redistributing mass within a round during flight by transferring fluid between two cavities located at different stationlines along the projectile. Liquid could be transferred using pumps that take advantage of the projectile's high spin rate. The author pointed out that varying mass center location in this manner could allow flight dynamics of spin-stabilized rounds to be tuned as desired. Furthermore, a projectile could be destabilized over the target area using this mechanism, causing it to tumble and fall. A drawing of Donovan's variable stability shell is shown in Figure 4.1.

Glotz et al. [38] introduced another idea for static margin variation several years later. In their design, a rod protruding from the front of a non-spinning projectile was linked to an internal mass. Movement of the rod produced variation in aerodynamic center of pressure, while corresponding mass movement created further static margin alterations.

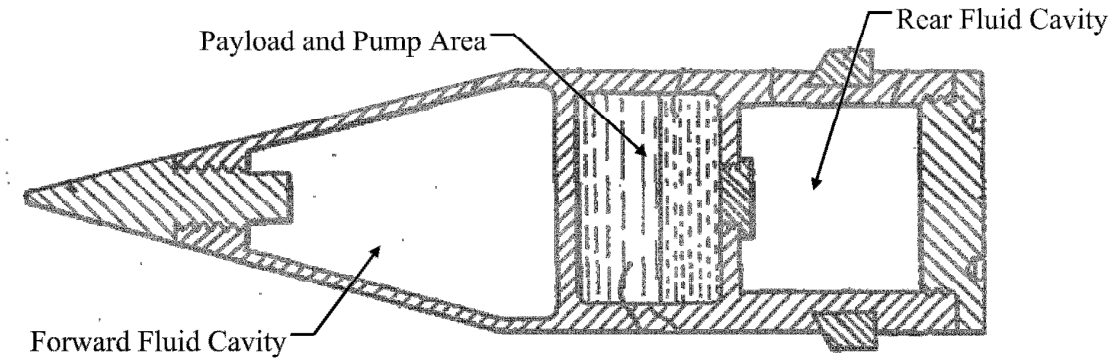

Figure 4.1: Donovan's Dual Cavity Projectile Concept.

Like Donovan, the authors pointed out that such a mechanism could be used to destabilize a projectile when desired, causing it to tumble and fall rapidly. This could occur if, for instance, the projectile missed the target during training exercises and it was highly undesirable to hit other objects on the training range. A drawing of Glotz's variable stability projectile is shown in Figure 4.2.

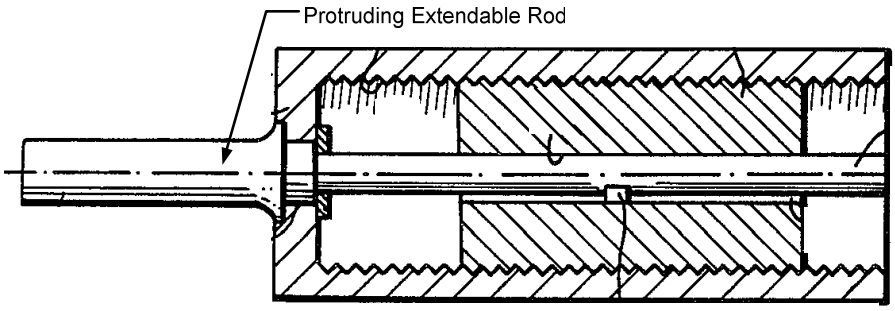

Figure 4.2: Glotz's Variable Stability Projectile.

4.2 Dynamic Model and Flight Control System

The dynamic model for the variable stability projectile is identical to the model derived in Chapter 2, with the exception that the cavity Euler angles $\psi_T = 0$ and $\theta_T = 0$. This results in a cavity aligned with the longitudinal axis of the projectile. Therefore the equations of motion remain unchanged and the flight dynamic model from Chapter 2 using these new cavity Euler angles is used to generate trajectory results. A schematic of the variable stability projectile is shown in Figure 4.3.

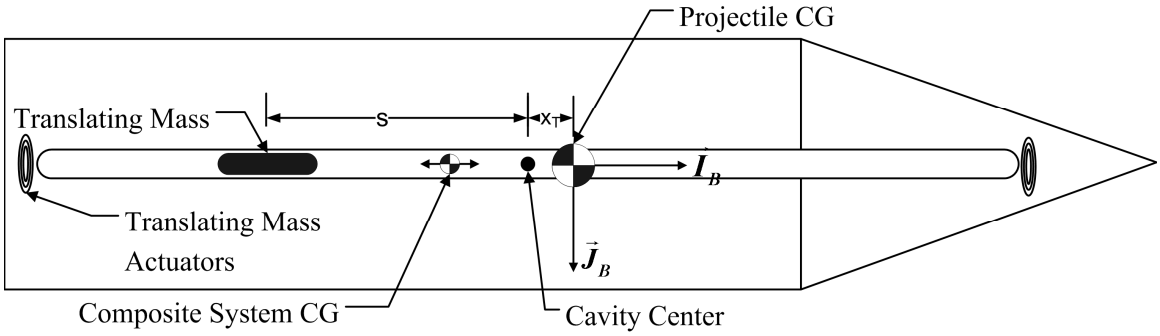

Figure 4.3: Schematic of the Variable Stability Projectile.

Translating mass position is controlled using a simple proportional plus derivative controller.

A primary goal of this chapter is to study possible reductions in required control force using a projectile incorporating the variable stability system. In order to perform a general analysis, it is assumed that an unspecified control mechanism is capable of exerting a lateral force on the projectile at some point on the body subsequently yielding an associated control moment. This control force is limited to a specific value. The control law used for trajectory guidance is Proportional Navigation Guidance (PNG), [39] a standard guidance law used in many smart weapons designs. Proportional navigation

seeks to force the line of sight angle between the projectile and the target to be constant. Therefore, the acceleration command generated by PNG can be written as

$$\vec{A}_C = N_C \vec{V}_C \dot{\lambda} \tag{4.1}$$

where $\vec{A}_C$ is the acceleration command, N_C is the PNG gain, $\vec{V}_C$ is the projectile-target closing velocity, and λ is the line-of-sight angle. Let the *L* frame denote a reference frame with unit vector $\vec{I}_L$ aligned with the line-of-sight between the projectile and the target, $\vec{J}_L$ lying in the plane formed by $\vec{I}_P$ and $\vec{J}_P$, and $\vec{K}_L$ completing the right-handed triad. Then equation (4.1) can be expressed as

$$\vec{A}_C = -N_C \vec{v}_{C/I} \times \vec{\omega}_{L/I} \tag{4.2}$$

where $\vec{v}_{C/I}$ is the velocity of the center of mass of the system with respect to the *I* frame and $\vec{\omega}_{L/I}$ is the angular velocity of the *L* frame with respect to the *I* frame. Also, noting that

$$\vec{\omega}_{L/I} = \frac{-\vec{r}_{C\to X} \times \vec{v}_{C/I}}{\left|\vec{r}_{C\to X}\right|^2} \tag{4.3}$$

where $\vec{r}_{C\to X}$ denotes the distance vector from the system mass center to the impact point, the PNG-generated acceleration command can finally be written as

$$\vec{A}_C = \frac{N_C}{\left|\vec{r}_{C\to X}\right|^2} \vec{v}_{C/I} \times \left(\vec{r}_{C\to X} \times \vec{v}_{C/I}\right) \tag{4.4}$$

All cases below use a PNG gain of 3.0.

4.3 Static Stability, Throwoff Error, and Control Force Required

Several case studies are examined first using rounds not equipped with the variable stability mechanism in order to understand the effect of CG position on uncontrolled circular error probable (CEP) for a nominal munition, as well as to determine the effect of CG position on required maximum control force. Circular error probable is defined as the radius of a circle drawn around the mean impact point that encompasses half of all dispersion impacts. Once these relationships are determined, the variable stability mechanism is introduced in a similar framework to show its ability to both decrease "throw-off" errors and to minimize control forces required to hit a given target. Throw-off errors, otherwise known as aerodynamic jump, are trajectory alterations caused by non-zero crossing velocities and roll rates at launch, and have been shown to contribute significantly to dispersion.[73] In cases where a CEP is generated, three error budgets for initial conditions are used, referred to as "Low Error," "Medium Error," and "High Error." The standard deviations for each of these error budgets, as well as the initial conditions for all simulations, are given in Table 4.1. Note that "σ" denotes standard deviation and wind azimuth is a uniform random variable between 0 and 2π.

All simulations in this chapter use the example indirect fire projectile used in Chapters 2 and 3. For all cases containing the variable stability mechanism, the length of the ITM cavity is considered to be approximately equal to the length of the round.

Table 4.1. Initial Conditions (IC's) and Error Budget Parameters.

	IC	σ - Low	σ - Medium	σ - High
x **(m)**	0.0	0.0	0.0	0.0
y **(m)**	0.0	0.0	0.0	0.0
z **(m)**	0.0	0.0	0.0	0.0
ϕ **(rad)**	0.0	0.0	0.0	0.0
θ **(rad)**	0.05	0.00015	0.00031	0.0005
ψ **(rad)**	0.0	0.00008	0.00016	0.00025
u **(m/s)**	860.8	2.44	3.20	4.57
v **(m/s)**	0.0	0.55	0.91	1.52
w **(m/s)**	0.0	0.55	0.91	1.52
p **(rad/s)**	5.0	0.8	1.5	2.0
q **(rad/s)**	0.0	0.6	1.0	1.7
r **(rad/s)**	0.0	0.6	1.0	1.7
Wind (m/s)	0.0	3.66	5.58	6.40

The first study examines the effect of CG position on uncontrolled CEP of the example projectile. Two hundred Monte Carlo cases were run for each error budget at each CG location to generate the uncontrolled CEP. Figure 4.4 shows that, as expected, CEP grows significantly as the CG moves aft (and the projectile becomes less statically stable). This is mainly due to initial throw-off error experienced by the projectile during launch. As expected, analysis of trajectory data from these dispersion simulations revealed that rounds with low stability experience significantly higher angles of attack. For reference, a mass center stationline position of 0.34 m corresponds to a static margin at launch of approximately 0.103 calibers.

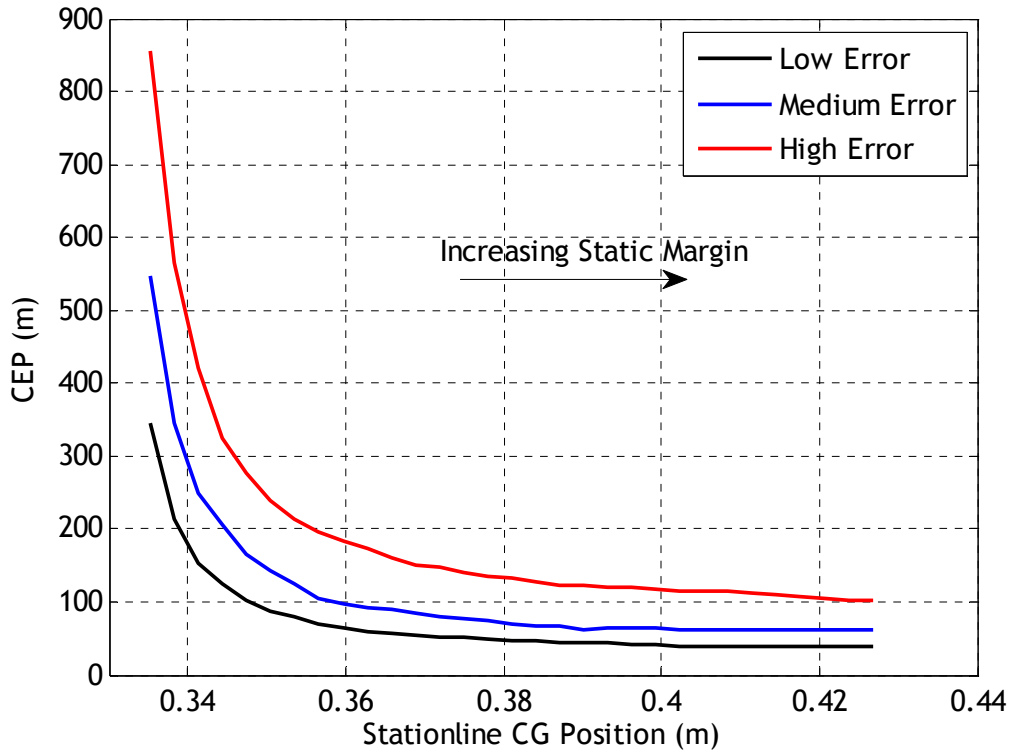

Figure 4.4: CEP vs Stationline CG Position.

At the same time, projectiles with lower stability margin (a CG further aft) respond more to control inputs than higher stability rounds. The same case was run with zero-error initial conditions for the same array of CG locations as in the first study above. Throughout the trajectory, a constant control force in the $\vec{J}_I$ direction was exerted on the projectile and the cross-range of the impact point was recorded. Figure 4.5 shows that the same amount of control force generates more cross-range in a less stable round than a more stable round.

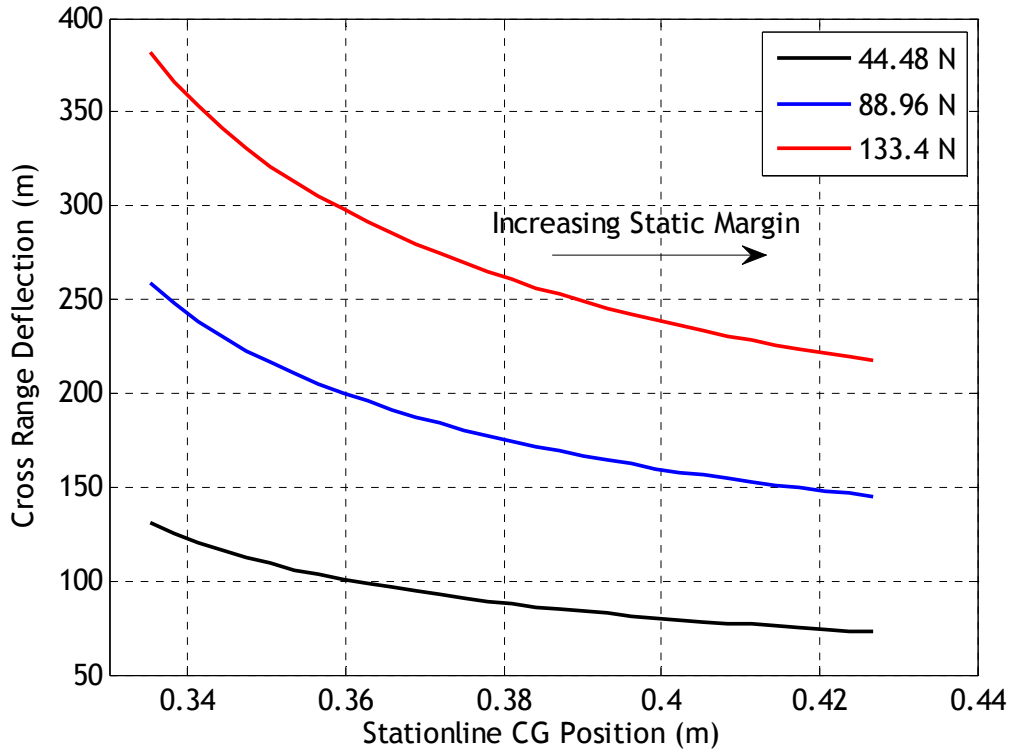

Figure 4.5: Cross Range Deflection vs Stationline CG Position.

Figures 4.4 and 4.5 demonstrate that there exists a fundamental trade-off in projectile design between a highly stable round, which requires greater control force, and a less stable round, which is more susceptible to initial throw-off error. These factors are characterized by the "controllability" effect, which refers to how responsive a round is to control force, and the "throw-off" effect, which refers to how vulnerable a round is to disturbances.

A Monte Carlo simulation using the controlled example round examines how these two effects interact and ultimately shows that there is a CG location that optimizes these two effects to produce a minimum required control force. To generate this controlled CEP simulation, a PNG control law was used to guide the example projectile to the impact point x = 4,938 m, y = -0.91 m, z = 0.0 m. A set of 200 Monte Carlo runs were completed for each CG location to generate a controlled CEP. A time history of control forces for each trajectory was collected, and then all 200 time histories were

averaged to produce a single "average force" value for each CG location. Control forces, applied 15.24 cm forward of the projectile mass center, were limited to 266.9 N in both the directions, and sensor errors were not included. The controller was activated 4 seconds into each trajectory. Figure 4.6 shows the controlled CEP for each CG location, while Figure 4.7 shows the average force required for each CG location as described above. Figure 4.6 shows that, except for marginally stable rounds that proved either too difficult to control or suffered from uncorrectable launch errors, the controller is quite effective at hitting the target. Interestingly, Figure 4.7 shows there is actually an "optimum" CG location where control force required is at a minimum. Rounds with CG positions forward of this require more effort by the controller to maneuver the round, while rounds with CG position aft of this suffer from substantial initial error and thus require more force to correct the trajectory. In this way, the "controllability" and "throw-off" effects play off one another to create an optimum CG location. These results were also verified for an example direct fire case for a fin-stablilized projectile. It is interesting to note that results from the indirect and direct fire case demonstrated that the optimum CG location varies as a function of error budget and range to target.

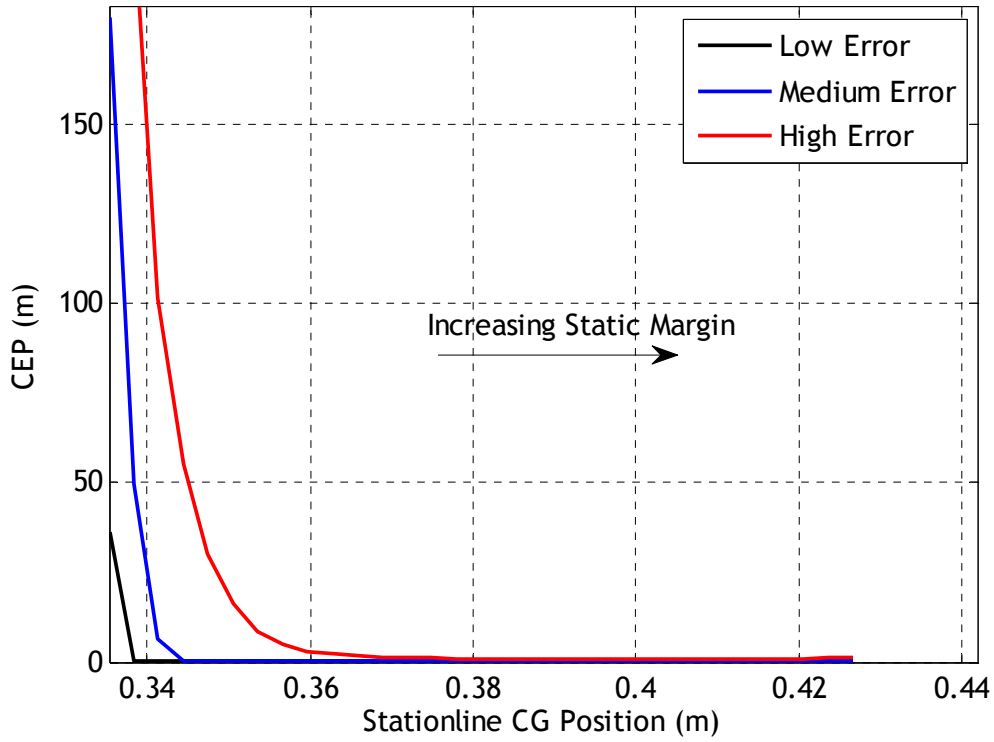

Figure 4.6: CEP vs Stationline CG Position.

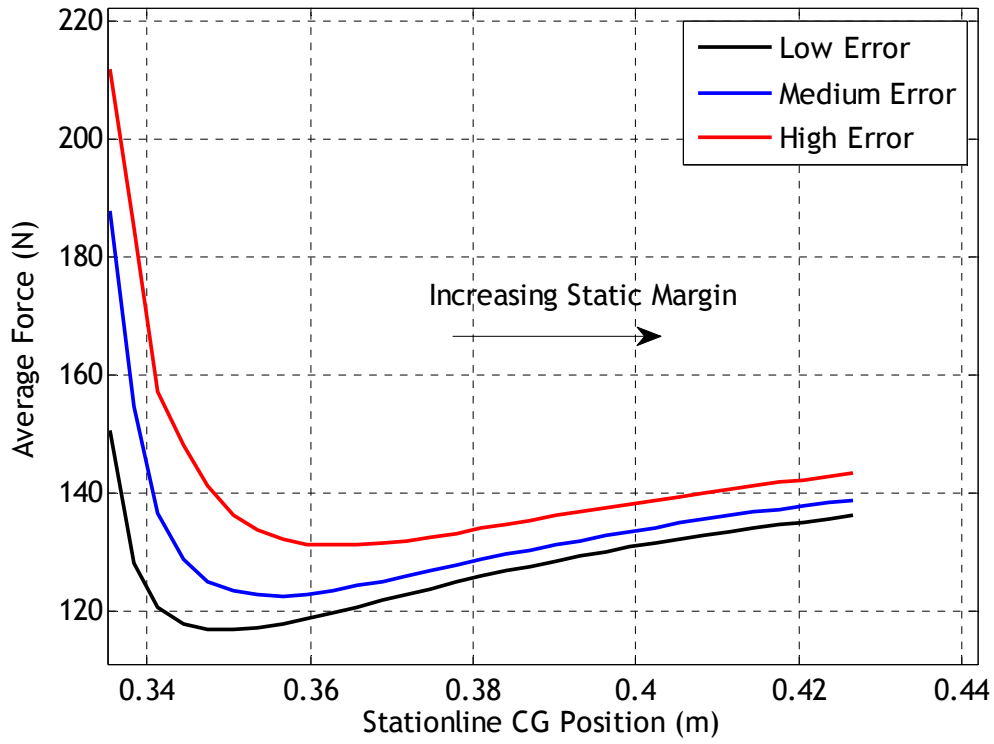

Figure 4.7: Average Force vs Stationline CG Position.

4.4 Variable Stability Example Case

Incorporating the variable stability mechanism into the example round, it can be shown that an increase in the projectile's stability for only a fraction of second beyond launch is sufficient to mitigate most throwoff error. Once initial perturbations of the round vanish, the remainder of the flight can be conducted with reduced stability with little effect on uncontrolled CEP. For comparison purposes, two projectiles were considered. The first, referred to as the "reduced stability" round, is the example projectile without the variable stability mechanism and a CG farther aft than nominal. The other, the "variable stability" round, is the example projectile with the variable stability mechanism incorporated. Uncontrolled CEP's were generated for both rounds using the "medium error" set of initial conditions given in Table 4.1. For all variable stability cases below, the mass was placed initially as far forward as possible, and then translated aft approximately 0.3 seconds into the trajectory. The experiment was designed such that with the mass in the aft position the variable stability round had identical stability characteristics to the reduced stability round. Figure 4.8 shows the static margin, defined as the distance between the total aerodynamic center of pressure and the mass center, of both the reduced and variable stability rounds for one of the above simulations using the 13% mass size. Note that the static margin of the variable stability round is initially higher, and after mass translation the stability of both projectiles are identical. Figure 4.9 shows the position of the translating mass with respect to the projectile throughout the variable stability trajectory in order to demonstrate how mass movement occurs in flight. Note that proper tuning of the proportional and derivative gains of the ITM controller results in fast response with no overshoot.

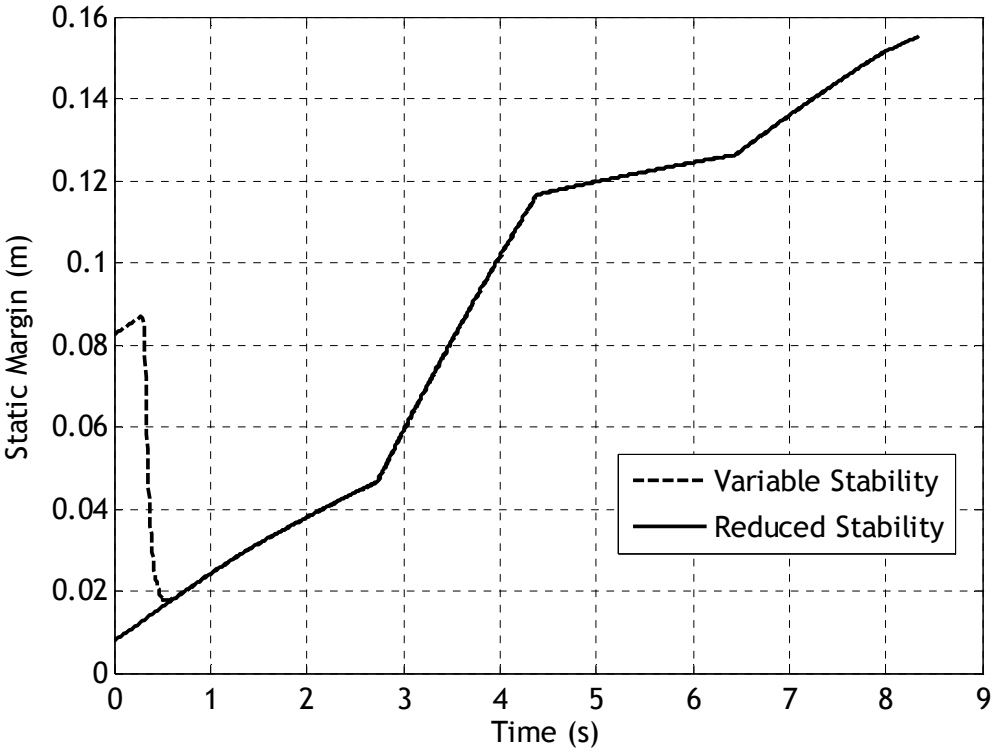

Figure 4.8: Static Margin vs Time.

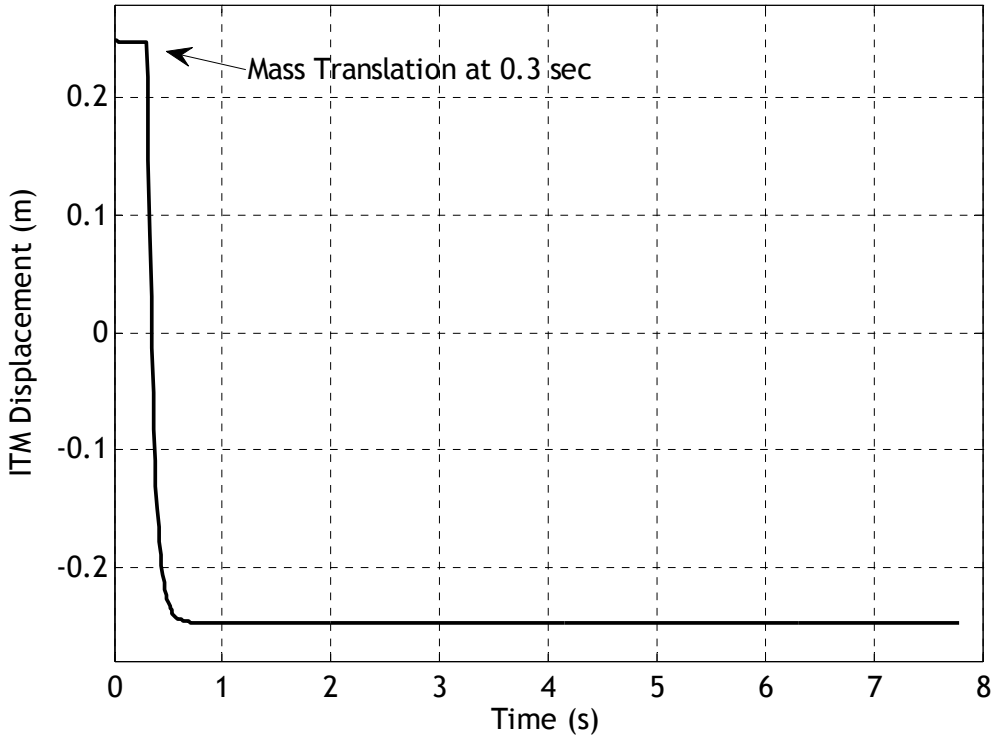

Figure 4.9: ITM Displacement vs Time.

Table 4.2 summarizes CEP results for both cases, run for two different translating mass percentages. Notice that, although the majority of the trajectory is flown at identical stability margins, the variable stability round has significantly smaller CEP than the reduced stability round. This is due to its higher initial stability, which allows initial errors (a primary cause of dispersion) to be mitigated much more effectively.

Table 4.2: CEP for Reduced and Variable Stability Rounds.

Case	ITM Percentage	Initial CG stationline (m)	Final CG stationline (m)	Impact Point Range (m)	CEP (m)
1 – Reduced	N/A	0.3667	0.3667	4,754	89.13
1 – Variable	5 %	0.3978	0.3667	4,757	55.55
2 – Reduced	N/A	0.3417	0.3417	4,913	93.32
2 - Variable	13 %	0.4164	0.3417	4,917	54.39

With the knowledge that an optimal CG location exists and that use of the internal moving mass can substantially reduce throw-off error as shown in Table 4.2, the variable stability mechanism can be implemented in a controlled round to increase control authority. In a round with a given available control force, this is equivalent to greater control authority. To demonstrate this, the variable stability mechanism is implemented in the example projectile along with the PNG guidance system with control force limits of 111.2 N in both the $\vec{J}_P$ and $\vec{K}_P$ directions. The cavity is approximately 12% of the total projectile volume and the translating mass is 8% of the total projectile mass. Two rigid projectiles, equivalent in mass to the variable stability round, are also used for comparison purposes. The first has a CG location equal to the variable stability round's CG location before mass translation, while the second has a CG location equal to that of the variable stability round after mass translation. The rigid round with the forward CG location is called "Highly Stable," while the round with the aft CG location is called

"Reduced Stability." The projectile equipped with the variable stability mechanism is referred to as "Variable Stability."

To compare the highly stable, the reduced stability, and the variable stability rounds, the target was placed at x = 4,755 m, y = -76.2 m, z = 0.0 m. The controller was turned on 4.0 seconds into the flight, representing a reasonable amount of time for sensor systems and other electronics to be powered on and initialized after launch. Randomly generated initial conditions were used: x = 0.0 m, y = 0.0 m, z = 0.0 m, ϕ = 0.0 rad, θ = 0.0499 rad, ψ = 0.0 rad, u = 860.91 m/s, v = 1.658 m/s, w = 1.089 m/s, p = 5.26 rad/s, q = -0.18 rad/s, r = 0.72 rad/s, wind magnitude = 3.29 m/s, wind azimuth = 5.12 rad. Figures 4.10, 4.11, and 4.12 show trajectory outputs, while Figure 4.13 shows time histories of the magnitude of the control forces for all three rounds. The reduced stability round misses the target by almost 200 m due to the large throwoff error, as can be clearly seen in Figure 4.11. The highly stable round misses the target by approximately 20 m, since there is insufficient control authority with the given force limit to achieve the commanded cross range. However, the variable stability projectile hits the target nearly exactly due to its small initial throwoff and its relatively large control authority. Figure 4.13 confirms this, as the controller for both the highly stable and the reduced stability rounds are saturated through the entire trajectory, while the controller for the variable stability round is out of saturation for a significant portion of the flight. The term "saturation" is used here to mean that the controller is using the maximum control force available to it, which oscillates between the maximum available in one direction (111.2 N) and the magnitude of the maximum available in both directions (157.3 N) as the projectile rolls. Therefore, as seen in Figure 4.13, for the variable stability case the controller does not require all available control for the variable stability case, while for the other cases it does. Furthermore, the average force required is 140.6 N for the highly stable round, 149.9 N for the reduced stability round, and 129.0 N for the variable stability round.

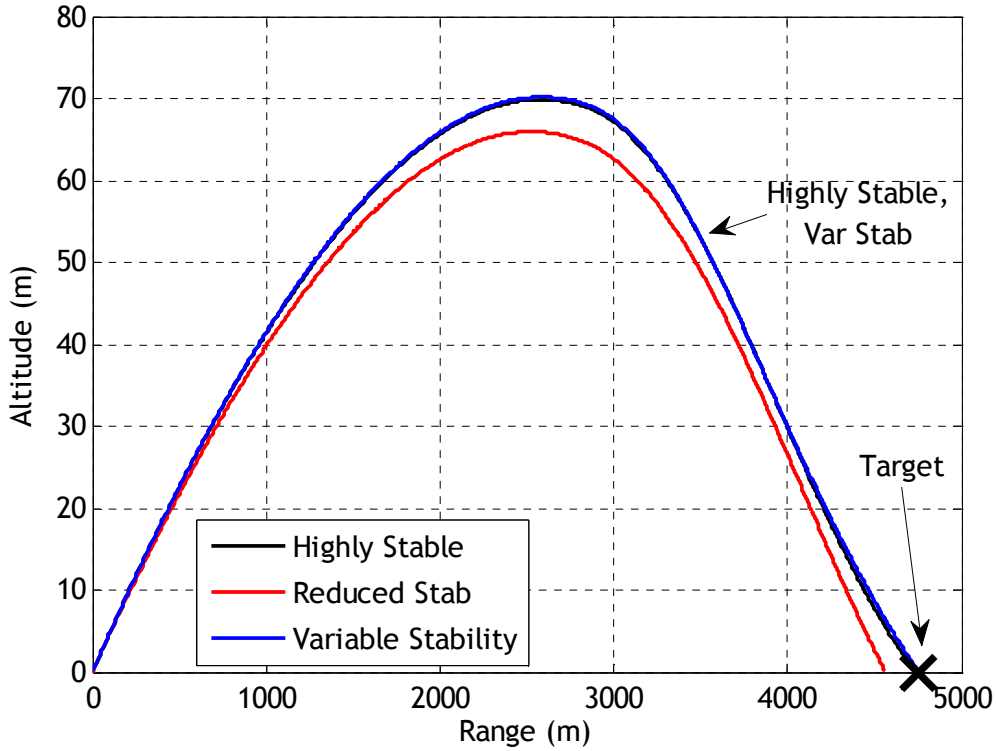

Figure 4.10: Altitude vs Range.

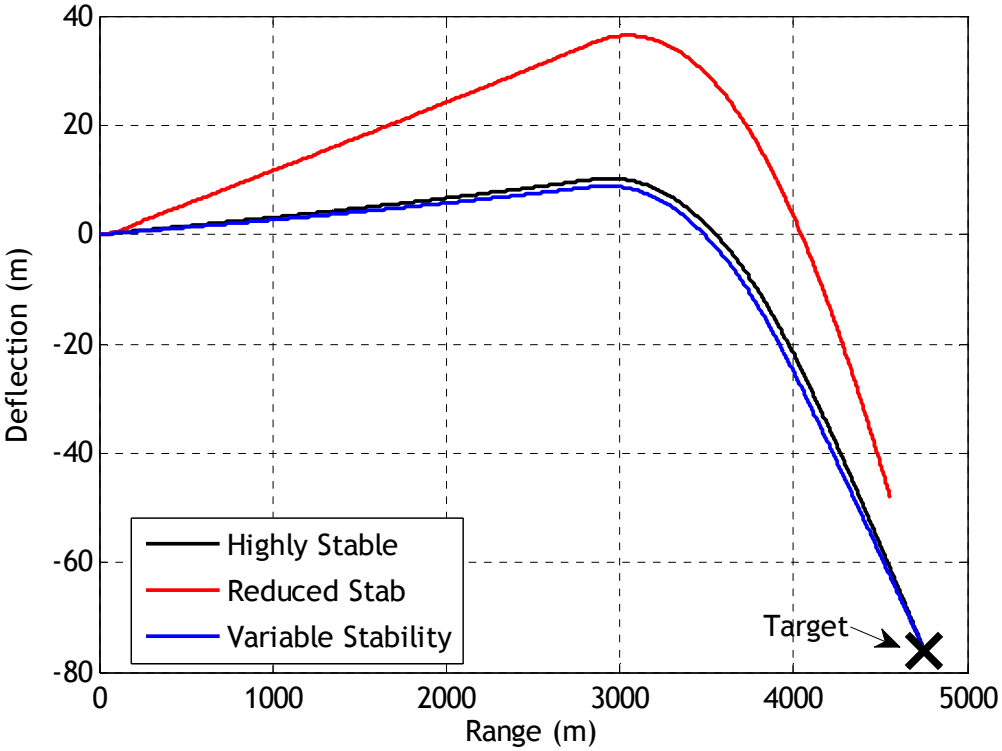

Figure 4.11: Deflection vs Range.

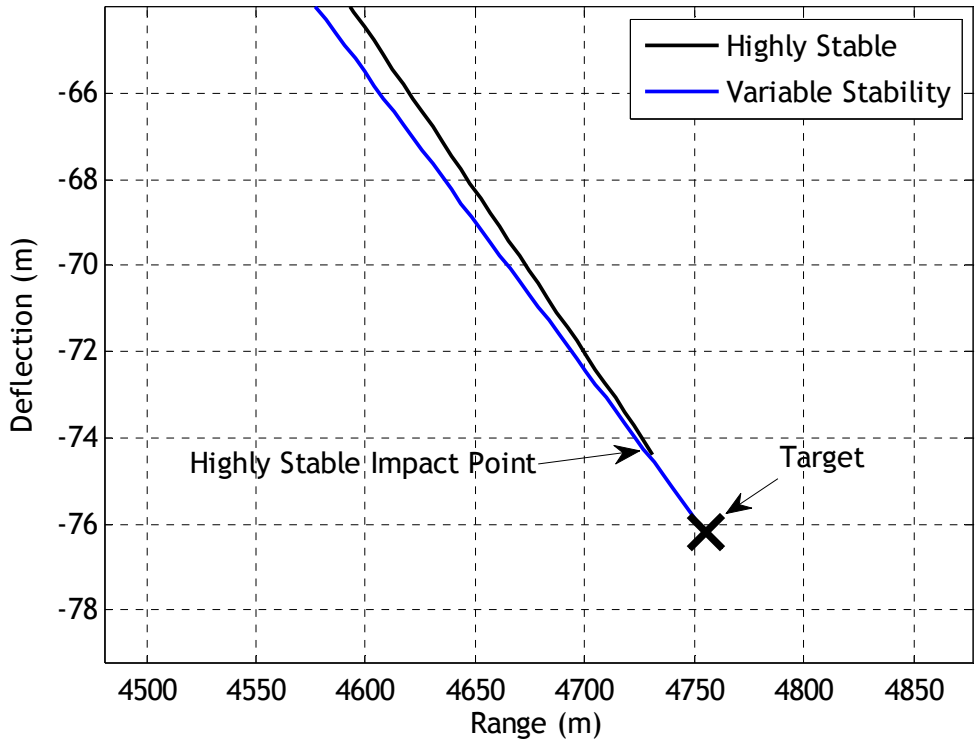

Figure 4.12: Zoom View Deflection vs Range.

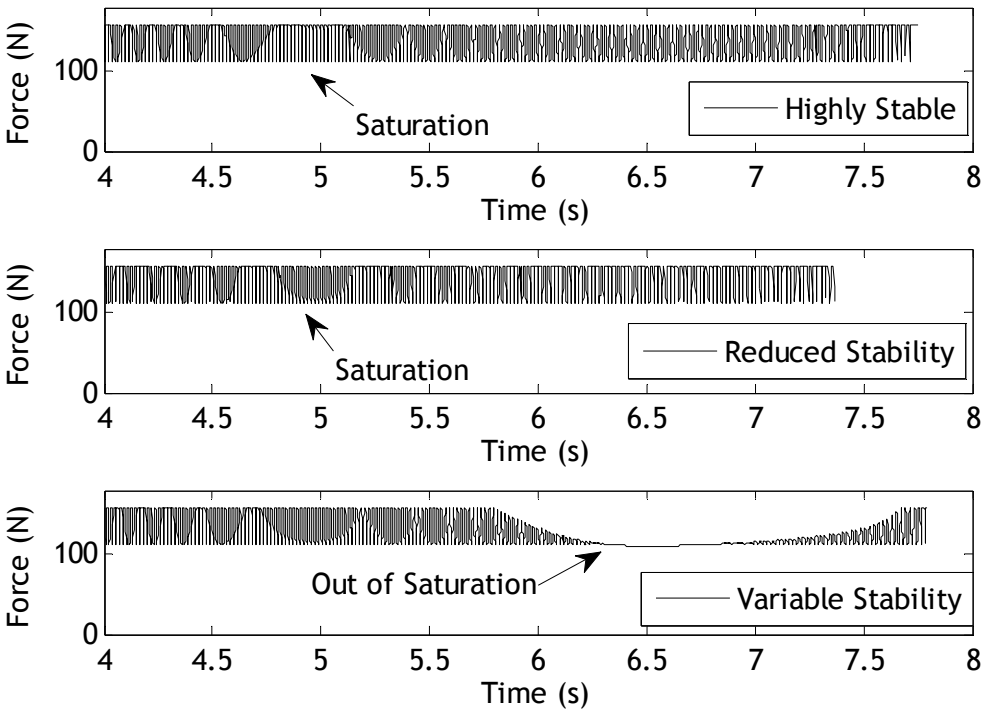

Figure 4.13: Force vs Time For Each Projectile.

Note that the average force required for the projectile equipped with the variable stability mechanism is almost 10% less than that required for the highly stable round, and almost 17% less than that required for the reduced stability round, neither of which were able to achieve the desired divert distance.

4.5 Dispersion Simulations

The benefit of the variable stability mechanism can be further explored by comparing dispersion of the highly stable, reduced stability, and the variable stability rounds. Figures 4.14-4.17 show the controlled CEP as a function of maximum maneuver control force for various internal mass sizes. Table 4.3 shows the change in mass center stationline affected by mass translation in the variable stability round. In all cases the mass center stationline after mass translation ("Aft CG Stationline") is the same, since an attempt was made to keep a static margin of at least 2/10 caliber throughout the entire flight. CEP's were generated using the "High Error" budget with the example projectile, and control force was exerted 4.0 seconds after launch. The 95% mass case (meaning that 95% of the system mass consists of the internal translating mass) may be realized as a hollow aeroshell within which nearly the entire mass of the projectile may be translated. Also, note that as mass percentage is increased, there is a corresponding change in total pitch moment of inertia. Moments of inertia of the rigid projectiles were therefore changed in each different mass percentage case in order to match the variable stability mass properties with the rigid projectile mass properties. In Figures 4.14-4.17, the controlled CEP at zero maximum maneuver control force (equivalent to uncontrolled CEP, since no force can be exerted by the controller) for the highly stable and variable stability rounds are nearly identical, demonstrating that both rounds exhibit the same response to initial perturbations. This further proves that mass translation after initial perturbations dissipate has little effect on the trajectory if no control force is exerted.

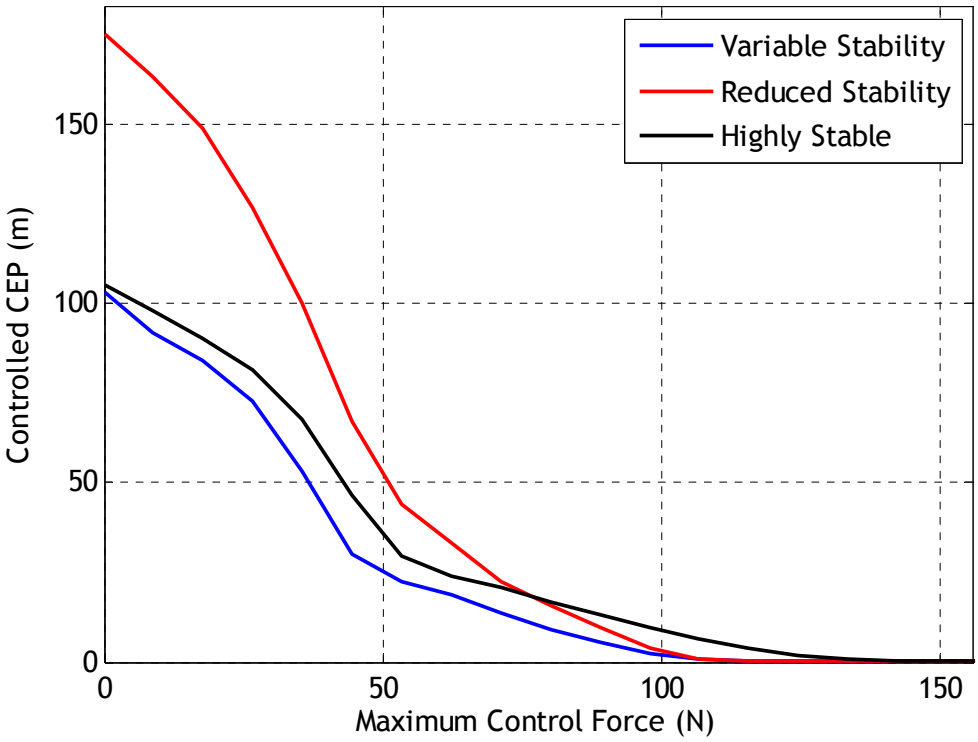

Figure 4.14: Controlled CEP vs Maximum Control Force, 10% ITM.

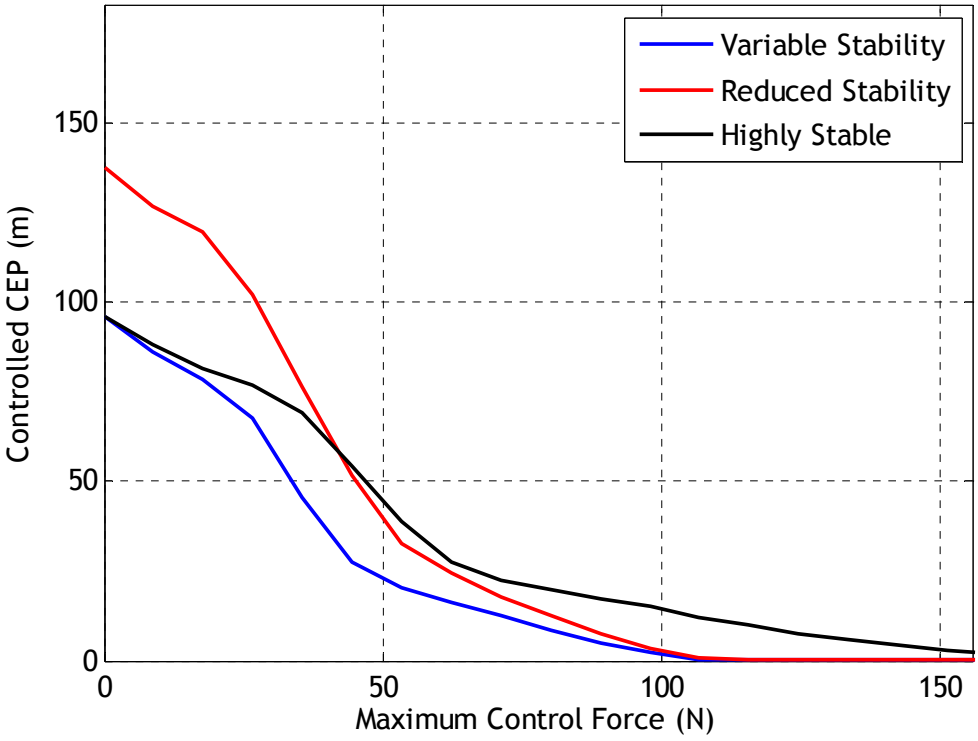

Figure 4.15: CEP vs Maximum Control Force, 30% ITM.

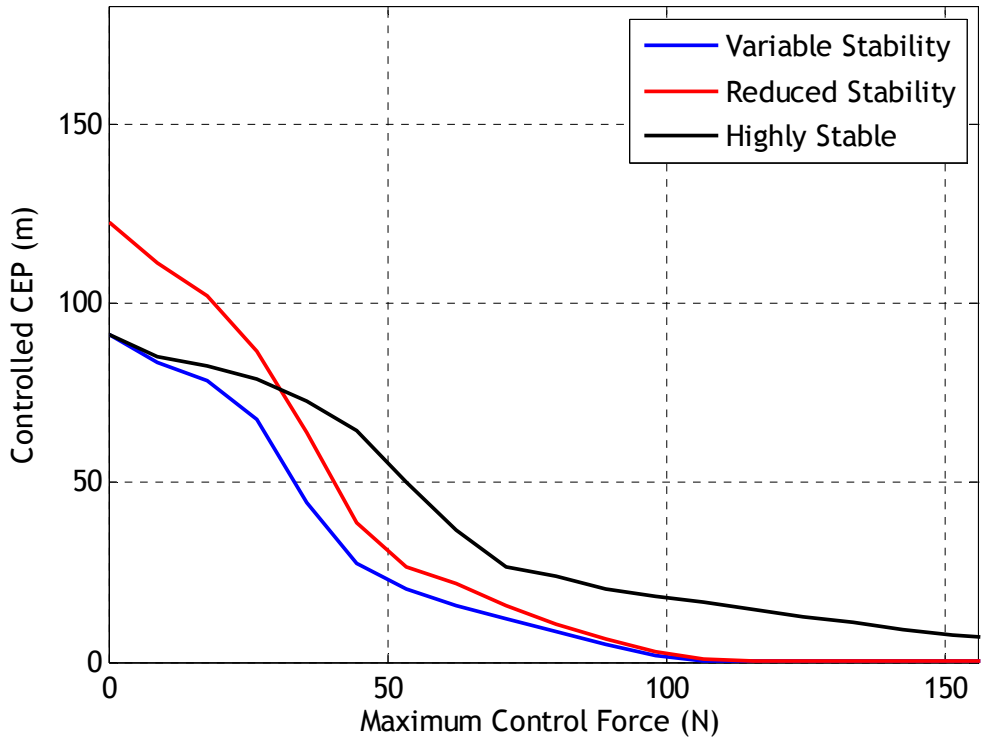

Figure 4.16: CEP vs Maximum Control Force, 65% ITM.

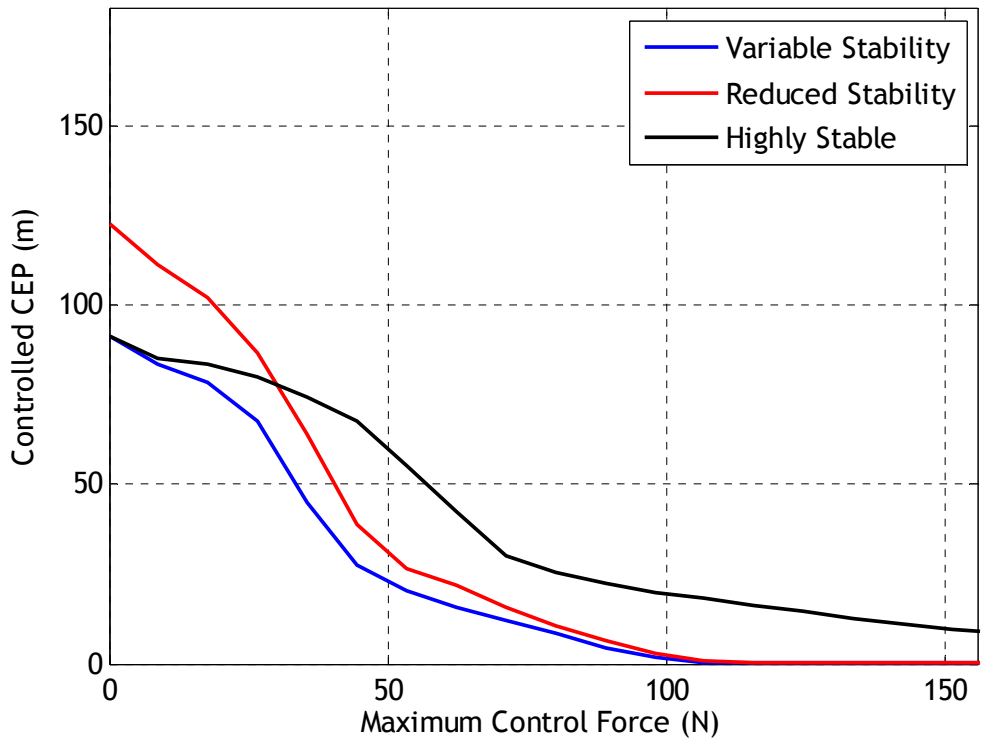

Figure 4.17: CEP vs Maximum Control Force, 95% ITM.

Table 4.3: Mass Center Position for Various Translating Mass Percentages.

Mass Percentage	Forward CG Stationline (m)	Aft CG Stationline (m)	Change in SLNCG (m)
10%	0.4144	0.3579	0.0547
30%	0.5235	0.3579	0.1639
65%	0.7147	0.3579	0.3550
95%	0.8786	0.3579	0.5190

As Figures 4.14-4.17 show, the variable stability mechanism shows better overall performance in reducing CEP for a given maximum force level than equivalent rigid rounds. The reduced stability round shows less dispersion as mass percentage increases due to the corresponding decrease in pitch moment of inertia (reducing the effect of initial perturbations). The highly stable round actually shows more dispersion as mass percentage increases, even though the round is more stable throughout the flight. This is because, as described above and in Figure 4.7, the disadvantage of reduced control authority outweighs the benefit of increased stability at these mass center locations.

Figure 4.18 shows the same variable stability CEP curves as in Figures 4.14-4.17 for each mass percentage, and establishes an important design benchmark for implementation of the variable stability mechanism. It is clear that at some mass percentage between 10% and 30%, further increases in mass percentage produce little to no benefit in reducing dispersion for a given maximum maneuver control force. First, it should be noted that all cases had the same mass center position after mass translation as described above, and therefore exhibited the same control authority during controlled portions of flight. The cases differed only in their initial mass center position, with the 95% case being the most stable at launch and the 10% case being the least stable. However, at some point further increases in projectile stability have little effect on reducing launch perturbations, and therefore little difference is seen between the 30%,

65%, and 95% cases. Thus in this case a mass percentage of between 20% and 30% would probably be sufficient to provide the maximum benefit that the variable stability mechanism has to offer in terms of reducing dispersion and increasing control effectiveness. Note, however, that the performance increase due to various mass sizes is likely to be projectile-specific.

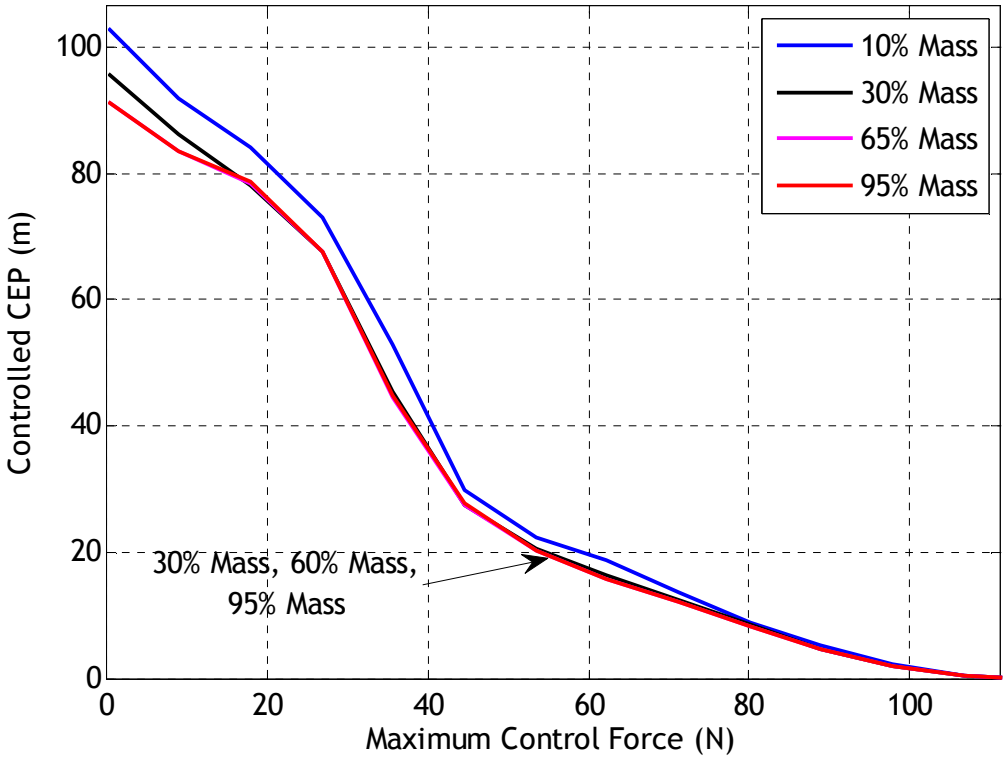

Figure 4.18: CEP vs Maximum Control Force, Variable Stability Cases.

Figures 4.19 and 4.20, based on the results above, demonstrate a further trade-off when considering mass size. Figure 4.19 shows that for low maximum force levels (0-45 N) the percentage decrease in CEP resulting from the variable stability mechanism when compared to the highly stable round is quite steep with respect to force level, and there is a local maximum for all mass sizes around 45-67 N. Also, note that the 95% mass case

shows the most improvement in percentage decrease in CEP compared to the highly stable round. However, Figure 4.20 demonstrates that the variable stability mechanism shows relatively constant percentage decreases in CEP over all force levels compared to the reduced stability round for each mass size, and the 10% mass case now shows the greatest improvement. Therefore, the high mass percentage case's improvements over the highly stable round must be tempered by the low mass percentage case's improvements over the reduced stability round, and a mass percentage in between the two extremes would provide the best trade-off.

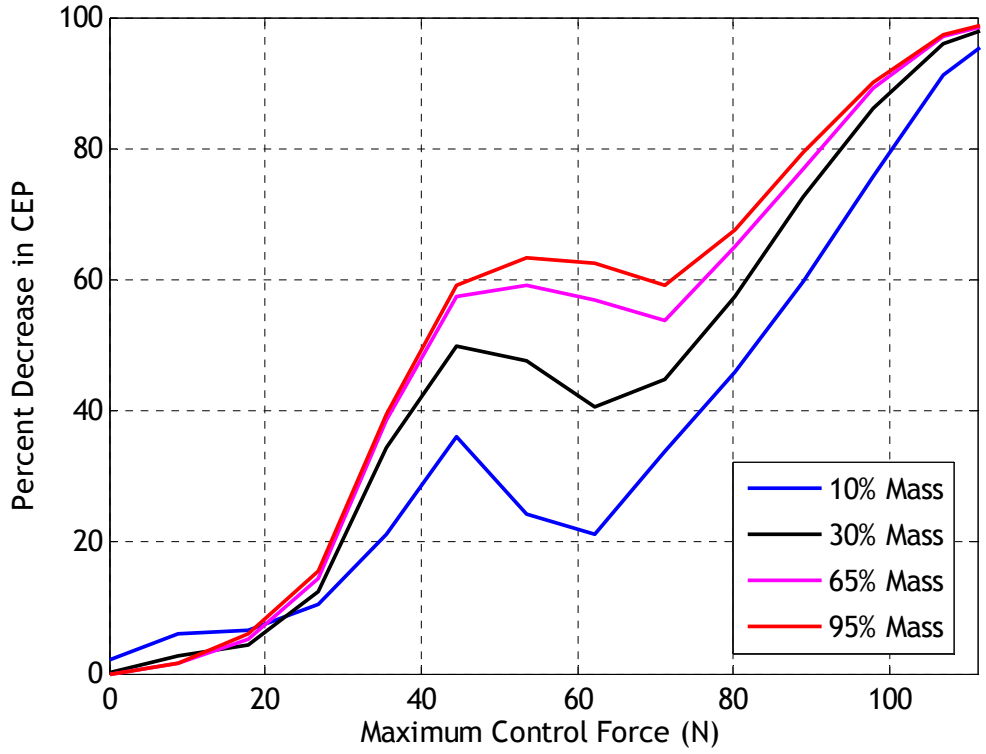

Figure 4.19: Percent Decrease in CEP Compared to Highly Stable Projectile.

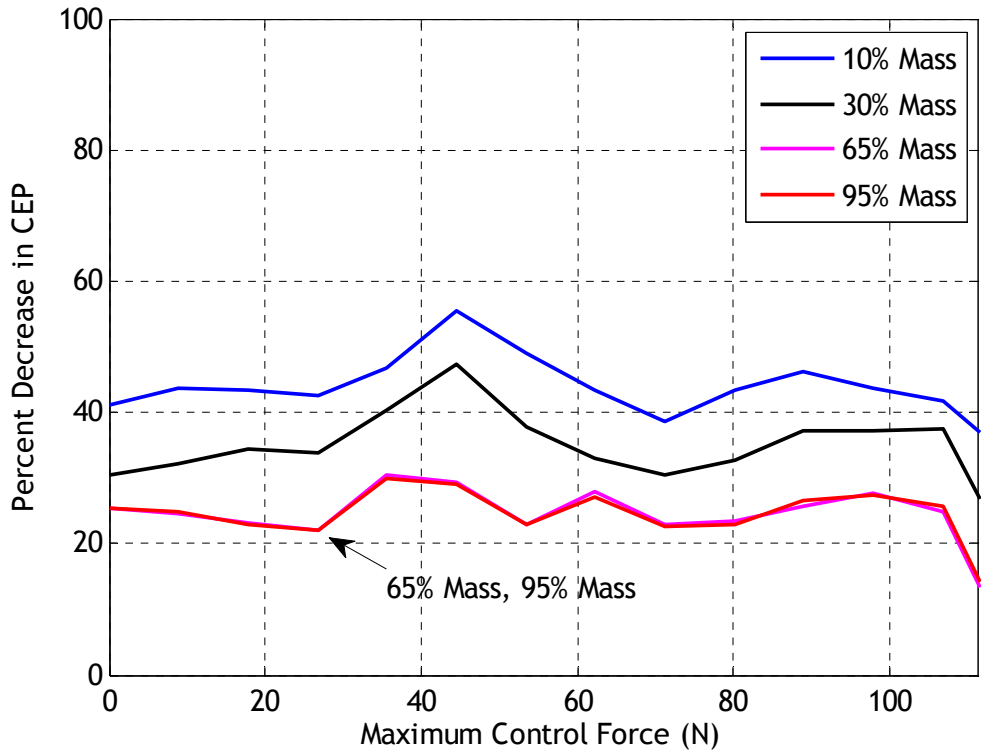

Figure 4.20: Percent Decrease in CEP Compared to Reduced Stability Projectile.

4.6 Conclusion

The variable stability mechanism has been developed to reduce required control forces for smart munitions, which often suffer from a lack of control authority. The results presented above demonstrate that a one-time shift in the mass center location in flight enables optimization of projectile flight characteristics by reducing throw-off error and increasing control authority. Active control of a projectile's center of gravity position using the variable stability mechanism lets the designer have the "best of both worlds," that is a projectile with low susceptibility to initial throw-off errors and high control authority throughout controlled portions of flight. Trade studies performed using a 7 degree of freedom flight dynamic model showed that projectiles equipped with a variable stability mechanism exhibit lower dispersion for a given maximum maneuver control force due to decreased initial errors and increased control authority. Increases in

translating mass size resulted in less dispersion, although at some point no benefit was obtained by further increasing mass percentage. Flight dynamic and control improvements must be tempered by the fact that the control mechanism adds complexity, but probably more importantly claims space on the round that is in high demand.

CHAPTER 5

SENSOR SUITE SHOCK ABSORBERS USING AN INTERNAL TRANSLATING MASS

This chapter explores the use of translating mass technology configured as a shock absorbing damper for sensitive electronics components within a smart weapon. In this configuration, the translating mass is composed of sensors and other electronic components susceptible to disturbance or damage from high acceleration loads experienced by a projectile during launch. The translating mass is allowed to move freely during launch along the longitudinal axis of the body, providing some reduction in acceleration magnitude and significant protection against high-frequency structural vibrations typically experienced just after muzzle exit. First, an example simulation using a typical interior ballistic pressure-time curve demonstrates shock absorber operation in a launch environment. Then, trade studies are performed to examine the effect of various cavity lengths, damping coefficients, and mass sizes on shock absorber performance. In addition, actual launch acceleration data from an example artillery shell is used to simulate acceleration loads, capturing shock absorber response to high-frequency acceleration oscillations. Results show that although a passive shock absorber cannot significantly reduce the magnitude of launch acceleration using reasonable cavity lengths, it can effectively isolate the electronics package from harmful high-frequency acceleration oscillations after launch.

5.1 Sensor Suite Performance in Projectile Launch Environments

The physical environment associated with the launching of projectiles is extremely harsh. Design of electronics suites able to withstand this environment has been

one of the most difficult technical issues associated with smart weapons development. In an article recently published by NDIA's *National Defense*, retired Army Col. Frank Hartline claims that "the biggest challenge for cannon-launched, precision-guided munitions has been getting sensitive guidance technology safely out of the very difficult environment of a gun barrel."[50] This environment incorporates extreme temperatures and pressures in addition to large axial and angular accelerations. Table 5.1 outlines baseline launch and flight survivability requirements for tank, artillery, mortar, and missile projectiles used for initial weapon design by the U.S. military. Note specifically the extremely high acceleration loads experienced at launch by tank, artillery, and mortar projectiles as compared to missiles. Additionally, as clearly shown in the table, operational environments during launch are far more severe than during flight, and can be viewed as the driving factor behind survivability requirements of the on-board electronics package. [51]

Table 5.1: Munition Launch and Flight Survivability Requirements. [51]

Launch Conditions	**Units**	**Tank (120mm)**	**Artillery (155mm)**	**Mortar (4.2")**	**Missile**
Chamber Pressure	ksi	80	60	15	
Max Axial Launch Accel.	g's	100K	20K	10K	500
Max Radial Launch Accel.	g's	10K	2K	1K	50
Angular Rotation In-Bore (Twist)	rev/cal	0	1/20	1/20	0
Motor Propellant Temp	K	3000	3000	3000	3000
Time In-Bore	ms	7-10	10-20	5	
Flight Conditions					
Base Pressure	psi	20	20	20	20
Max Axial Flight Accel. (Drag)	g's	-5	-10	-5	-20
Max Radial Flight Accel.	g's	0.50	0.50	1.00	2.00
Angle of Attack	degrees	±5	±15	±15	±15
Structural Vibrations	KHz	10	10	10	20
Roll Rate	Hz	0-60	100-300	0-130	0-60
Yaw/Pitch Rate	Hz	0-10	0-40	0-40	0-10
Time In-Flight	s	10	200	30	1000

Over the past decade significant advancements have been made in developing sensor suites that can withstand extreme shock loads endured at launch. Many of these sensor packages incorporate Micro-Electromechancal Systems (MEMS) due to their small packaging and robust construction. In fact, numerous MEMS accelerometers and rate sensors are available commercially that can withstand tens of thousands of g's, [45] [51] and shock-hardening of MEMS sensors continues to be a very active research area. [46,47] The Army Research Laboratory's (ARL's) Diagnostic Instrumentation Fuze (DFUZE) is an example of an integrated sensor suite comprised of these shock-hardened sensors, and has been used with great success in many projectile flight test programs over the past decade. [43,44]

However, although many sensor packages have been developed to withstand high launch accelerations, problems remain due to vibration and resonance phenomena. Gun-launched munitions experience structural ringing effects just after muzzle exit due to the sudden release of friction between the projectile and the barrel. Likewise, missiles during powered flight experience high-frequency vibrations characteristic during thrust provided by a rocket motor. Testing of MEMS accelerometers during ARL's DFUZE development program revealed that certain models exhibited large bias errors and intermittent operation after exposure to high-frequency acceleration loads produced by a shock table, similar in nature to the structural ringing experienced by gun-launched projectiles.[42] These high-frequency oscillations have also been problematic for MEMS rate sensors, which contain small proof masses that are susceptible to resonant vibration if excited at their natural frequency. Many times, vibrations experienced by gun-launched projectiles after muzzle exit and by missiles during thrusting maneuvers contain these resonant frequencies, resulting in severely decreased performance and unreliable readings from rate sensors.[41,51]

One interesting example of this is outlined by Harkins, et al. [41] in a study of telemetry data from a sensor package on-board a gun-launched model of a spacecraft.

Just after muzzle exit, “rate sensors required time to ‘recover’ from launch shocks before giving accurate output, in this case approximately 0.2 sec.” This recovery time was due to severe vibrations experienced by the proof mass within the rate sensors. During this interval, a magnetometer-based method was used instead to estimate the model’s angular rates and attitude history. Interestingly, due to the high-drag shape of the model, this short interval after launch proved critical to analysis of the air vehicle’s flight dynamics, and therefore rate sensor information would have been very beneficial to post-flight analysis if it could have been reliably obtained.

Another example of the detrimental effect of vibration on rate sensors is described by Brown [51] in a study of the effects of harsh launch and flight environments on MEMS devices. In this case, telemetry from a 2.75 inch powered rocket is collected. During the thrusting phase (for approximately 1.0 second into flight), high-frequency oscillation is experienced due to the nature of solid rocket motor combustion. This can be clearly seen in the accelerometer readings shown in Figure 5.1. This high-frequency vibration can cause “erroneous angular rate measurements depending on the relative amplitudes of vibration at the resonant frequency of the MEMS ARS [angular rate sensor].”

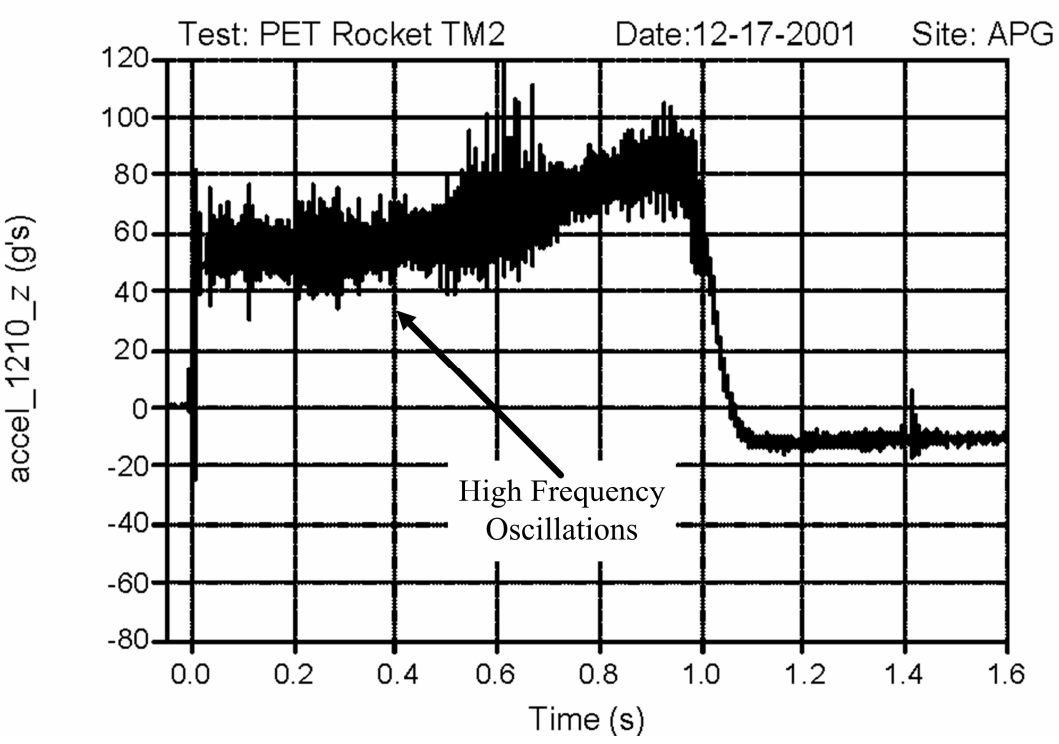

Figure 5.1: Accelerometer Output for a Powered Rocket in Flight. [51]

Both examples highlighted above motivate the need to develop vibration isolation technology for smart weapons sensor suites. While a simple method to mitigate this resonant phenomenon would be to place the natural frequency of the MEMS proof mass far outside the range of typical projectile vibration frequencies, mechanical isolation of the complete sensor suite serves the dual purpose of dampening these particular harmful oscillations while reducing overall shock and vibration loads on all sensors. Reducing these vibrations becomes especially important when using sensor feedback for control systems, since high frequency content in sensor outputs typically results in reduced control system performance. Furthermore, if structural ringing continues for a significant duration after launch, reliable sensor information may be unobtainable until later in flight. Many control mechanisms (such as the ITM mechanism) perform best early in flight, and therefore delays in control activation can cause critical control performance degradations.

5.2 Model Description and Example Simulation

A diagram of the sensor suite shock absorber placed within an example projectile is shown in Figure 5.2. The mechanism can be physically realized quite simply, for example by placing the sensitive electronics package within a cavity filled with damping fluid. Choice of fluid viscosity and shaping of the electronics package would serve to implement the desired damping characteristics of the system.

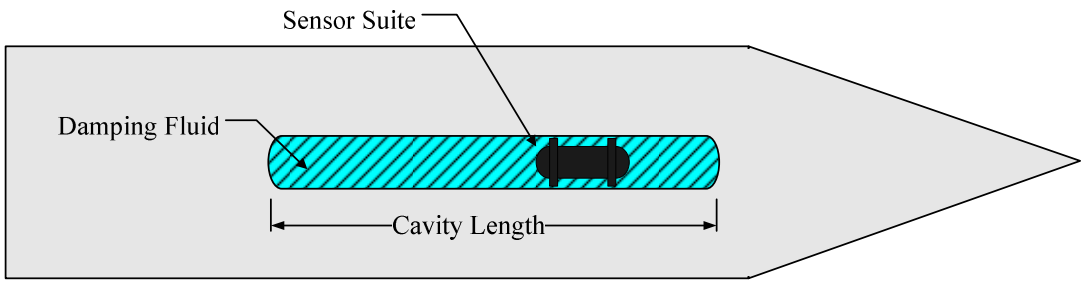

Figure 5.2: Projectile with Sensor Suite Shock Absorber.

In order to examine the capabilities of the shock absorber mechanism, a pressure-time curve is generated using a simplified interior ballistic model derived in detail in Reference [48]. The development of this model is not included here, since its sole purpose is to generate a pressure-time curve typical during launch of a large caliber artillery shell (the type of round considered for analysis in this chapter). This pressure-time curve is then used directly to generate a force on the base of the projectile, creating a simple model of projectile acceleration during launch. Furthermore, a corresponding roll torque time history is also created and used as an input into the rotational dynamic equations. The example projectile used for all simulations in this chapter is a 155 mm spin-stabilized projectile with a mass of 43.00 kg, axial inertia of 0.1472 kg-m^2, and longitudinal inertia of 1.893 kg-m^2. Projectile length is approximately 0.914 m, and nominal velocity and spin rate at muzzle exit are 826.0 m/s and 1674.1 rad/sec respectively. A drawing of the example projectile is shown in Figure 5.3. Parameters of

the interior ballistic model are adjusted appropriately so as to generate a realistic curve that results in proper muzzle exit velocity and spin rate for this type of munition. The pressure-time curve used for all simulations in Sections 5.2 and 5.3 is shown in Figure 5.4, and the roll torque time history is shown in Figure 5.5.

Figure 5.3: Example 155 mm Spin-Stabilized Projectile.

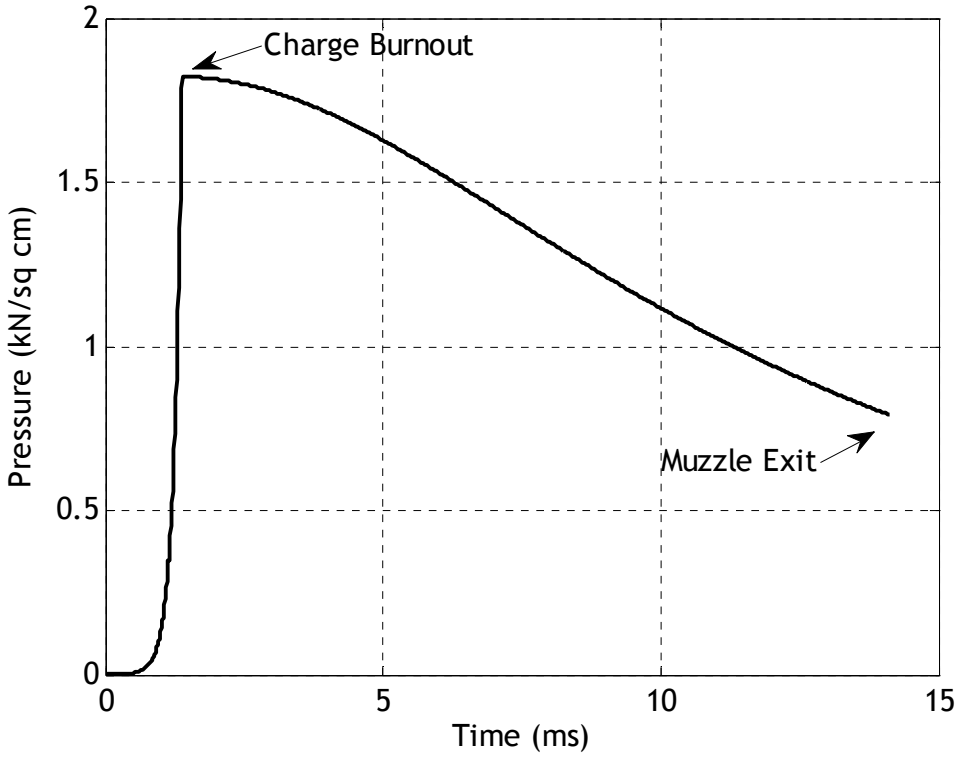

Figure 5.4: Pressure vs Time Curve for Shock Absorber Simulations.

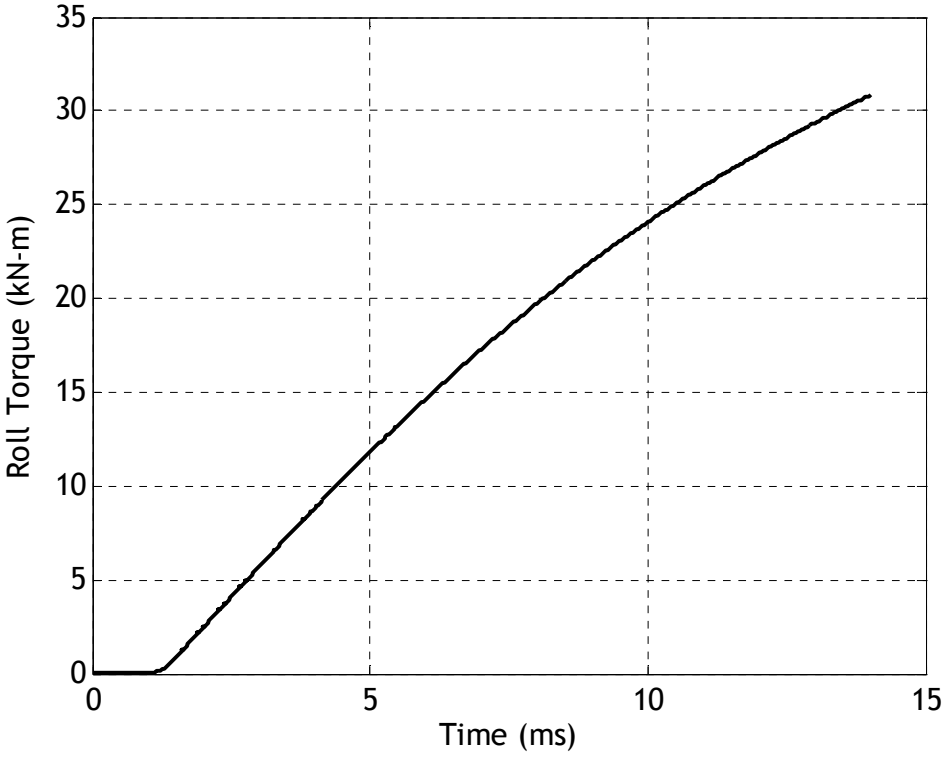

Figure 5.5: Roll Torque vs Time for Shock Absorber Simulation.

An example simulation is presented to demonstrate projectile response to the input pressure and roll torque profiles as well as to show the shock reduction capabilities of the ITM shock absorber mechanism. Cavity length is 0.914 m, mass size is 0.730 kg, and the damping coefficient of the fluid in the cavity is 671 N/m/s. Mass size is determined by assuming that the ITM consists of three 200 g MEMS sensors and 130 g of additional packaging.[63] For all cases in this chapter, the projectile starts from rest and the ITM is placed at the front of the cavity. The given pressure and torque profiles are then applied, and the simulation transitions from the interior ballistic model to the translating mass flight dynamic simulation (as derived in Chapter 2) at muzzle exit. Lateral motion of the projectile center of mass and lateral pitch rates within the gun barrel are not considered in this simple model. Projectile position, velocity, and roll rate

responses are shown in Figures 5.6-5.8. ITM displacement and velocity time histories are shown in Figures 5.9 and 5.10.

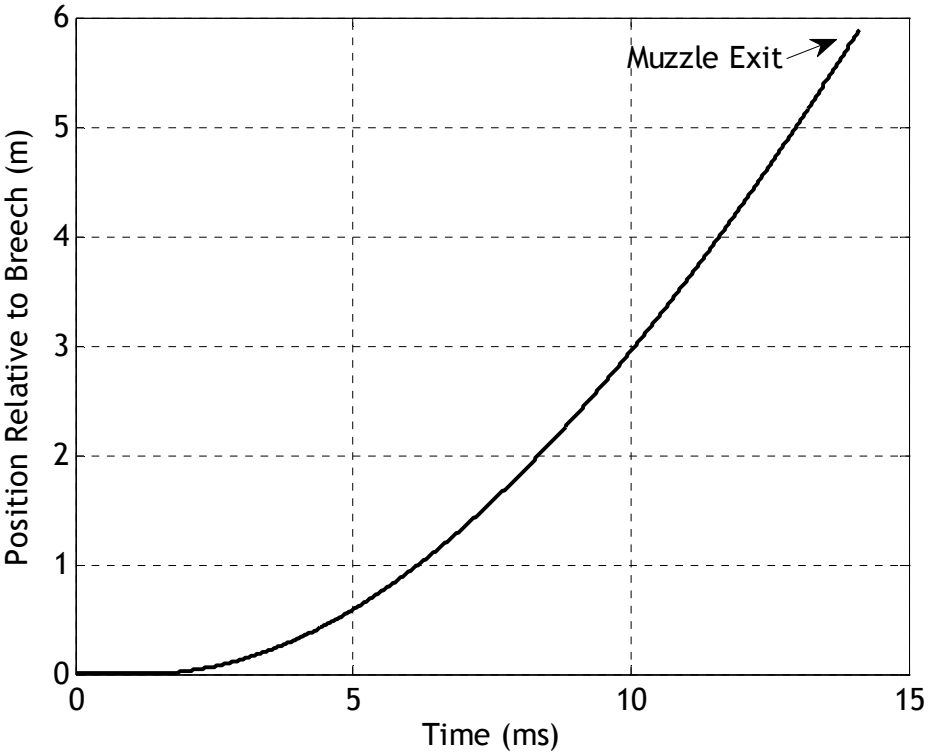

Figure 5.6: Projectile Position Relative to Breech vs Time.

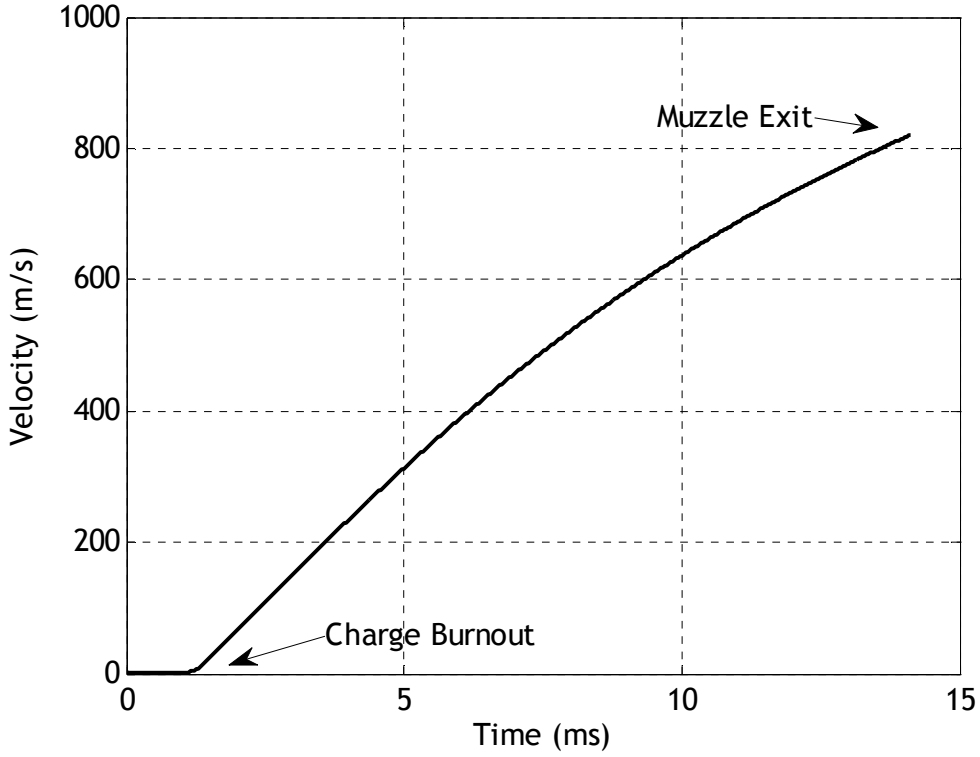

Figure 5.7: Projectile Velocity Along $\vec{I}_P$ vs Time.

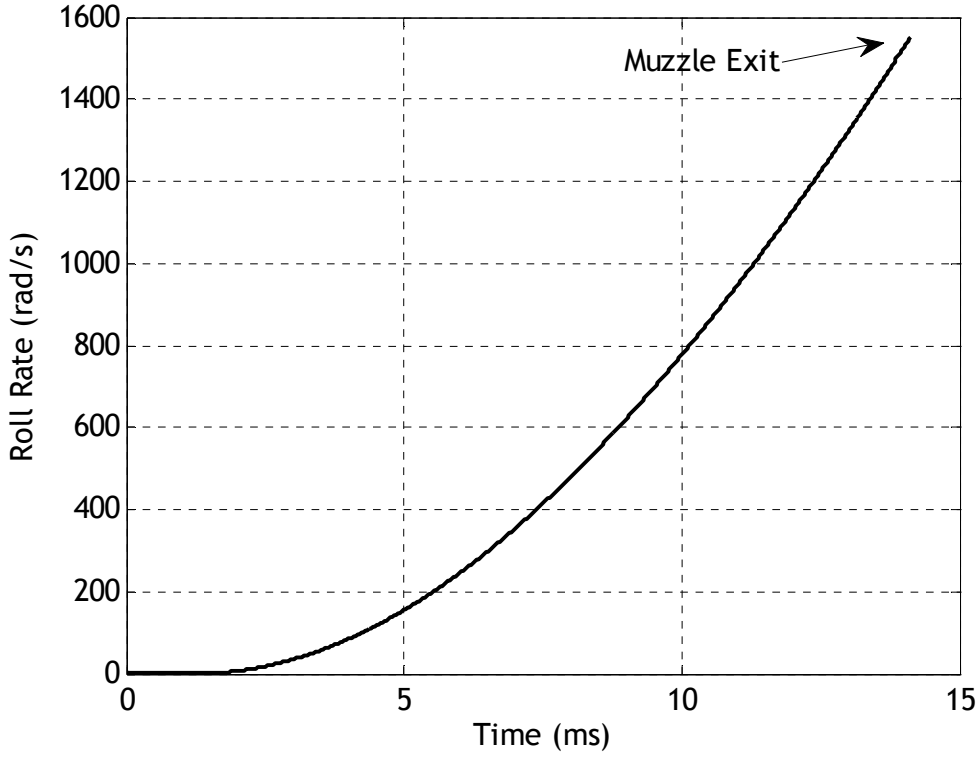

Figure 5.8: Roll Rate vs Time.

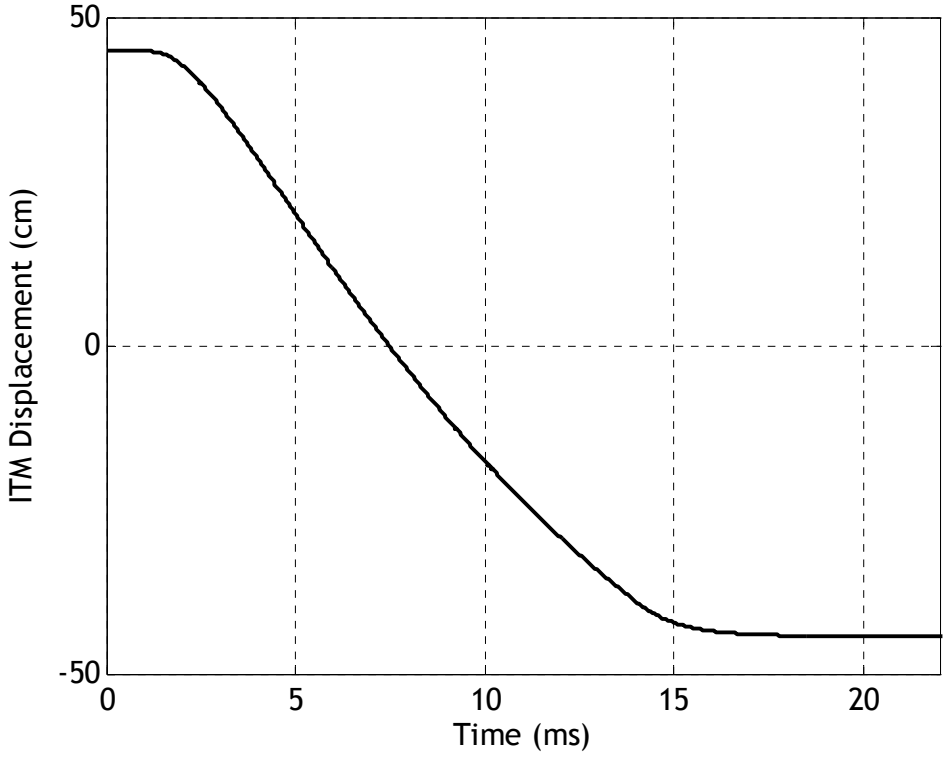

Figure 5.9: ITM Displacement vs Time.

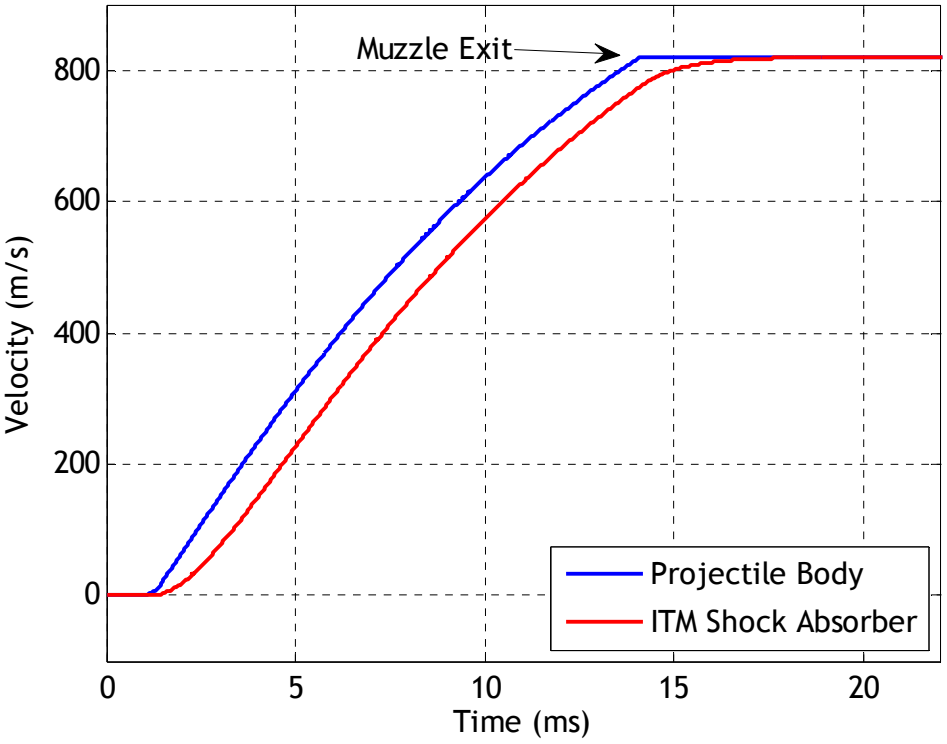

Figure 5.10: Projectile and ITM Velocity vs Time.

Figures 5.9 and 5.10 show that the ITM shock absorber demonstrates responses typical of a first-order damper, as expected. Transition from the front to the rear of the cavity occurs during projectile acceleration within the barrel and continues for a short time after muzzle exit, resulting from an acceleration impulse of longer duration but lower magnitude. The acceleration loads experienced by the projectile and the ITM shock absorber are shown in Figure 5.11. Note the mild reduction (approximately 10%) in peak acceleration experienced by the ITM shock absorber.

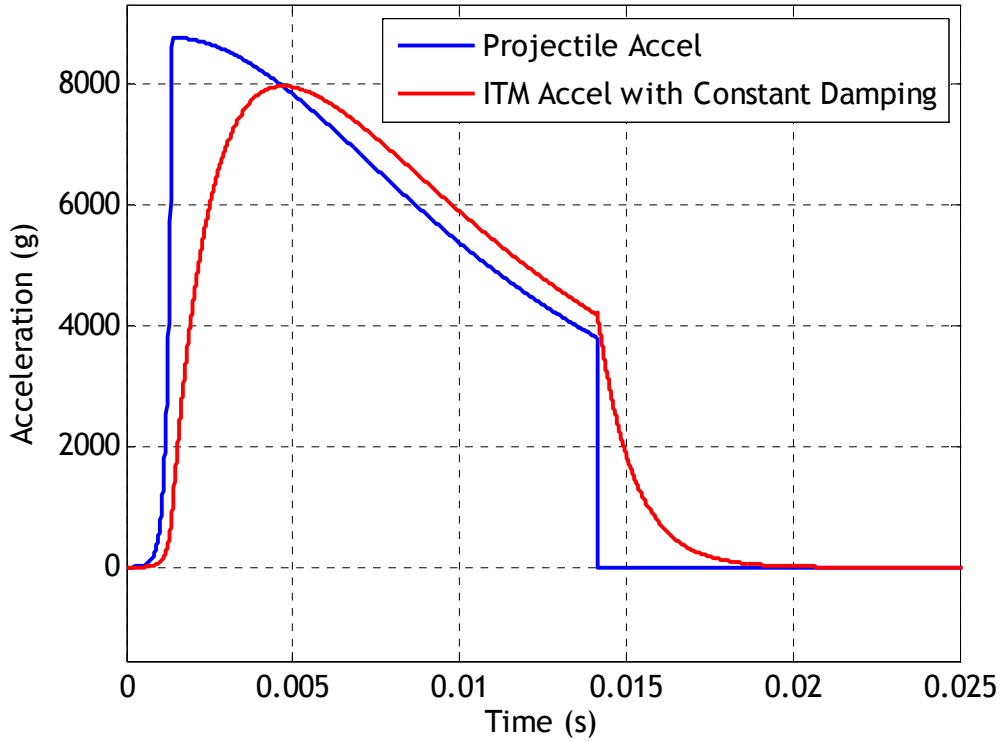

Figure 5.11: Acceleration vs Time.

It is clear from Figure 5.11 that the goal of achieving sizeable reductions in peak acceleration experienced by the sensor suite is not achieved using these example parameters and fixed cavity damping coefficients. To this end, several trade studies are conducted to explore how variation of mass size, damper coefficients, and cavity length

as well as the incorporation of active damping impact the ITM acceleration profile and peak acceleration values.

5.3 Trade Studies

Several trade studies are conducted to explore the effects of shock absorber mass size, length, and damping characteristics. Note the in all trade studies in this section, damping coefficients are assumed constant throughout the simulation. Section 5.3.1 studies the effect of varying the cavity length, while Section 5.3.2 develops the relationship between mass size, damping coefficient, and ITM acceleration response.

5.3.1 Cavity Length Trade Study

An identical interior ballistic simulation as shown in Section 5.2 was performed for cavity lengths ranging from 46 cm to 366 cm. Although the length of the projectile is only approximately 92 cm, cavity lengths in excess of this are studied simply to establish trends as well as to allow the results to be extended to longer rounds. Damping coefficients in the cavity were varied with cavity length (but held constant in each simulation) such that ITM motion with respect to the projectile ceased at the rear of the cavity (i.e., the ITM did not impact the rear of the cavity). Mass size for all simulations was 730 g, assuming that the ITM consists of three 200 g MEMS sensors and 130 g of additional packaging.[63] Table 5.2 shows damping coefficients used for each cavity length, while Figure 5.12 shows acceleration profiles of the projectile and ITM for each cavity length. Note that as cavity length increases, ITM peak acceleration decreases. This is because longer cavity lengths allow for lower damping coefficients, resulting in a longer acceleration pulse that is lower in peak magnitude. Such behavior is typical of a first-order system.

Table 5.2: Cavity Lengths and Damping Coefficients.

Cavity Length (cm)	Damping Coefficient (N/m/s)
46	1313
91	671
183	452
274	336
366	263

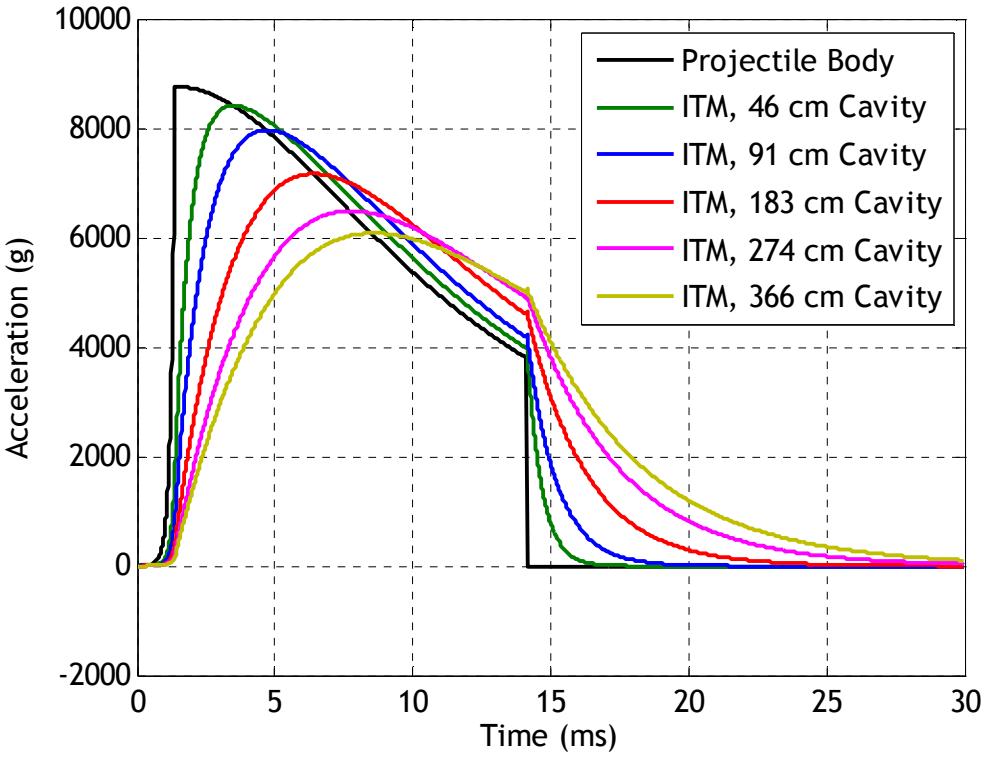

Figure 5.12: Acceleration vs Time for Various Cavity Lengths.

5.3.2 Mass Size and Damping Coefficient Trade Study

The ITM Shock Absorber is a first-order dynamic system which is excited by the acceleration impulse on the projectile body. As such, a simplified dynamic model can be studied in which ITM motion is described by

$$F(t) = m_T A(t) \tag{5.1}$$

where $F(t)$ is the force on the ITM, m_T is the ITM mass, and $A(t)$ is the acceleration profile generated by the pressure pulse within the gun. Now, the ITM Shock Absorber is simply a mass-damper system, and therefore

$$m_T \ddot{s} + c_v \dot{s} = m_T A(t) \tag{5.2}$$

where c_v is the damping coefficient within the cavity. In the Laplace domain, this equation can be written (assuming zero initial conditions)

$$p^2 S(p) + p\left(\frac{c_v}{m_T}\right) S(p) = A(p) \tag{5.3}$$

where p is used as the Laplace variable rather than s to avoid confusion with ITM displacement. Equation (5.3) can be solved to yield the transfer function of ITM displacement with respect to the acceleration impulse, yielding

$$\frac{S(p)}{A(p)} = \frac{1}{p\left(p + \frac{c_v}{m_T}\right)} \tag{5.4}$$

Therefore, the ratio c_v / m_T is the inverse of the first-order system time constant. Given a fixed cavity length and the stipulation that the ITM must come to rest before impacting the rear of the cavity, the time constant of the damper can be computed directly. Using this time constant, damping coefficients can be correlated with proper ITM mass for design purposes. A plot of damping coefficient as a function of mass size for various cavity lengths is shown in Figure 5.13.

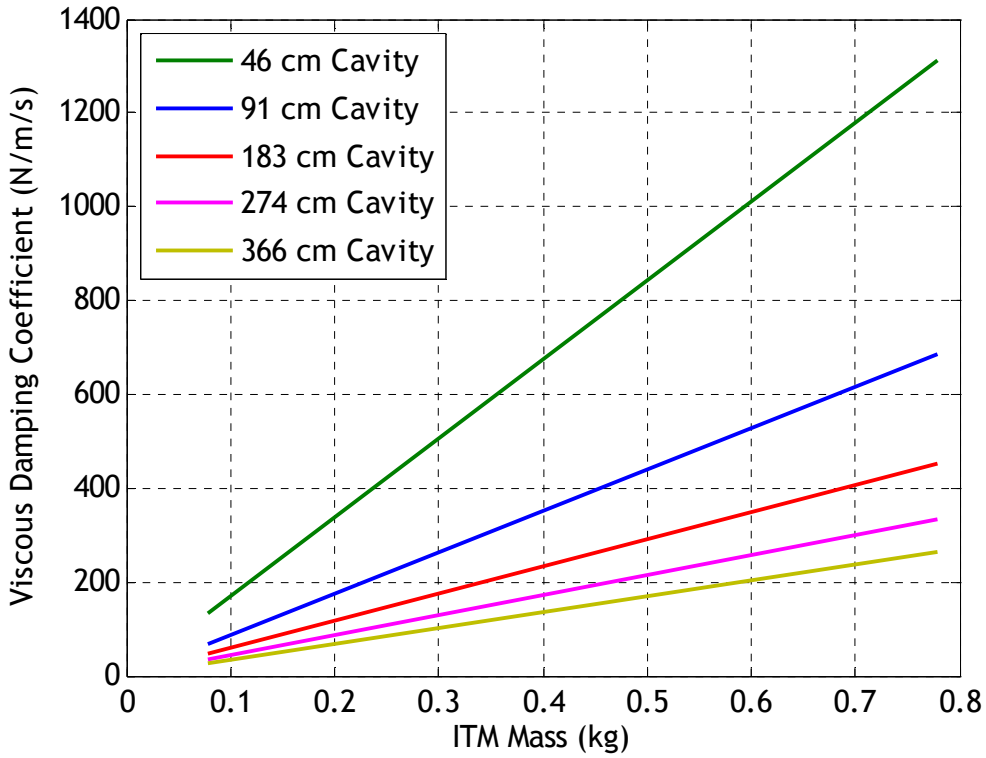

Figure 5.13: Viscous Damping Coefficient vs ITM Mass Size.

5.4 Active Damping and Minimum Peak Acceleration

It is clear from the results presented in Sections 5.2 and 5.3 that significant reductions in peak acceleration experienced by the ITM are not possible using a fixed damping coefficient within the cavity. It would, however, be beneficial to know the minimum theoretical peak acceleration experienced by the ITM if a means of variable (or

active) damping within the cavity could be implemented. This theoretical minimum value is computed as follows. First, assume that at some final time t_f relative motion between the ITM and projectile body ceases (i.e., $\dot{s} = 0$). Furthermore, at time t_f the ITM has traveled the full length of the cavity and the projectile has achieved its muzzle exit velocity of v_f. Also note that the minimum peak acceleration naturally occurs when ITM acceleration with respect to the inertial frame is a constant such that

$$\vec{a}_{T/I} \bullet \vec{I}_P = \hat{a} \tag{5.5}$$

Therefore, the acceleration-distance relation yields

$$\frac{1}{2}\hat{a}t_f^2 = x\left(t_f\right) - CL \tag{5.6}$$

where x is the position of the projectile mass center and CL is the cavity length. Furthermore, since acceleration of the ITM with respect to the inertial frame is constant,

$$\hat{a} = \frac{v_f}{t_f} \tag{5.7}$$

Equations (5.6) and (5.7) can be solved simultaneously for t_f and the minimum theoretical peak acceleration $\hat{a}$ given a specific cavity length, muzzle velocity, and distance versus time profile for the projectile. Table 5.3 provides t_f and $\hat{a}$ for the example projectile used above. Note that, predictably, t_f increases and $\hat{a}$ decreases as cavity length grows.

Table 5.3: Minimum Peak Acceleration vs Cavity Length.

Cavity Length (cm)	t_f **(ms)**	**Minimum Peak Acceleration (g)**
46	15.0	5565
91	16.2	5153
183	18.5	4503
274	20.9	3994
366	23.2	3598

Given the predicted minimum acceleration for a specific cavity length, an expression can be derived describing how cavity damping coefficient c_v must be actively changed in order to achieve the ideal flat acceleration profile. Note that, in the absence of weight and control forces, the equation of motion for the translating mass in the $\vec{I}_T$ direction can be written as,

$$\vec{I}_T \bullet m_T \vec{a}_{T/I} = -\dot{s} c_v \tag{5.8}$$

since constraint force is zero along the axis of the cavity. Substituting the expression shown in equation (5.5) yields

$$c_v = -\frac{m_T \hat{a}}{\dot{s}} \tag{5.9}$$

Active alteration of c_v according to equation (5.9) yields approximately constant ITM acceleration with respect to the inertial frame.

The adaptive damping law shown in equation (5.9) was implemented in simulation to demonstrate its effectiveness in reducing peak acceleration. Several different cavity lengths were considered. Figure 5.14 shows ITM acceleration time histories for each cavity length, while Figure 5.15 shows time histories of the adaptive damping coefficients. Note that due to physical considerations viscous damping was limited to positive values only, and was also limited to values less than 5800 N/m/s. Also note that the optimum acceleration profiles have the rectangular shape described above, but show somewhat higher peak accelerations than those listed in Table 5.3. This is due not only to the limitations placed on c_v, but also to the fact that the simulation models the mass with a certain length rather than as a point mass (as the analytical model above assumes), decreasing total useable cavity length.

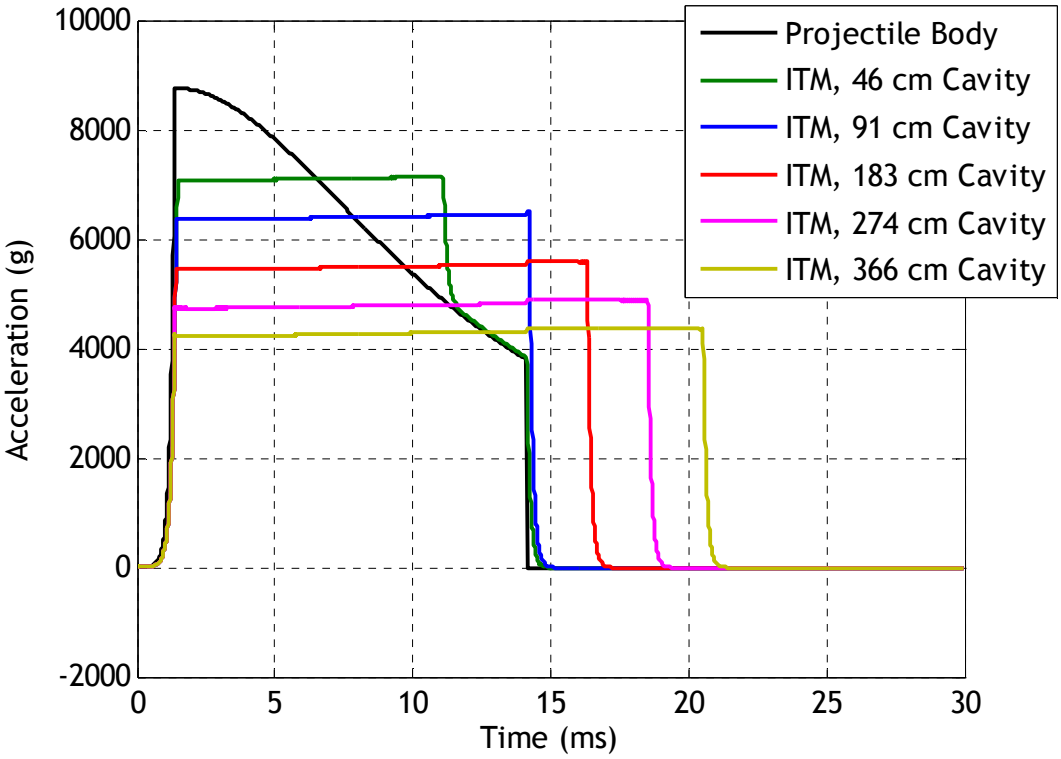

Figure 5.14: Acceleration vs Time.

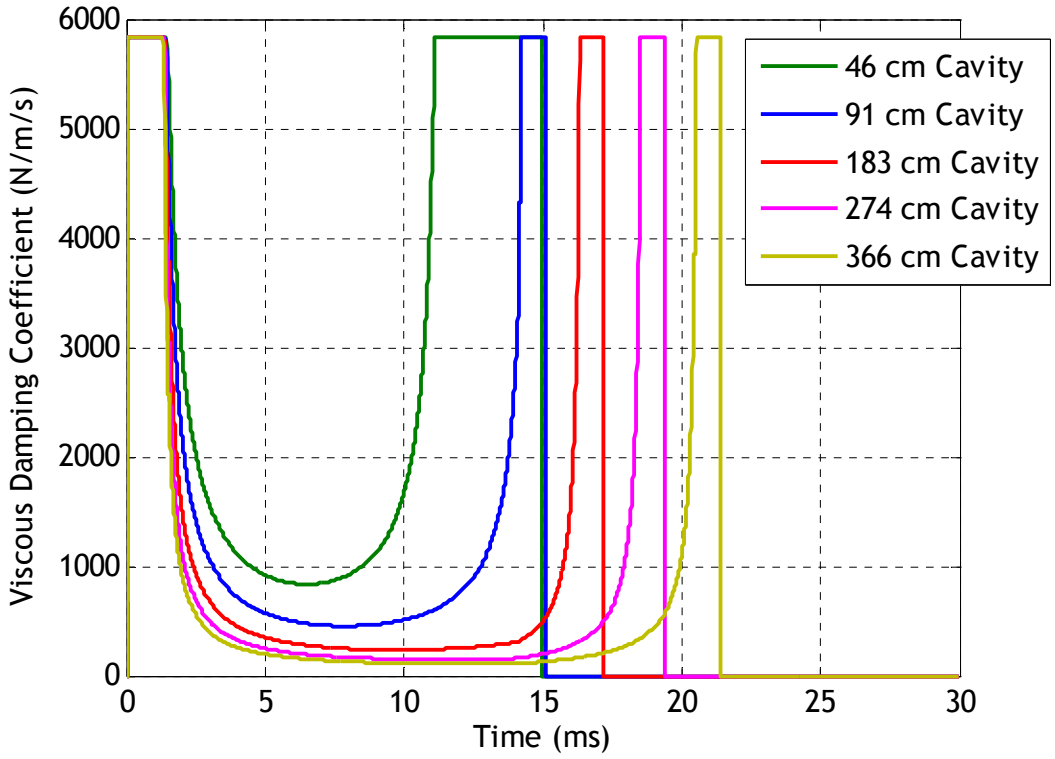

Figure 5.15: Viscous Damping Coefficient vs Time.

5.5 Simulation Using Experimental Acceleration Profile

While the pressure curve shown in Section 5.2 is useful for predicting shock absorption performance with respect to the large acceleration pulse within the gun barrel, it cannot be used to accurately simulate vibration isolation performance against high-frequency acceleration phenomena as described in Section 5.1. Recall that such phenomena typically occur due to solid rocket motor combustion or structural ringing effects just after muzzle exit. In order to accurately capture these high-frequency oscillations, experimental accelerometer data was obtained for the example 155 mm projectile and used directly to simulate shock absorber performance. Figure 5.16 shows the output of an accelerometer aligned with the axis of symmetry of the projectile. Accelerometer data was collected during an ARL flight test at Aberdeen Proving Ground, MD, using an Endevco 7270A with a data rate of 1 Megasample/sec. Note the large

amplitude, high-frequency oscillations present just after muzzle exit lasting approximately 5 ms.

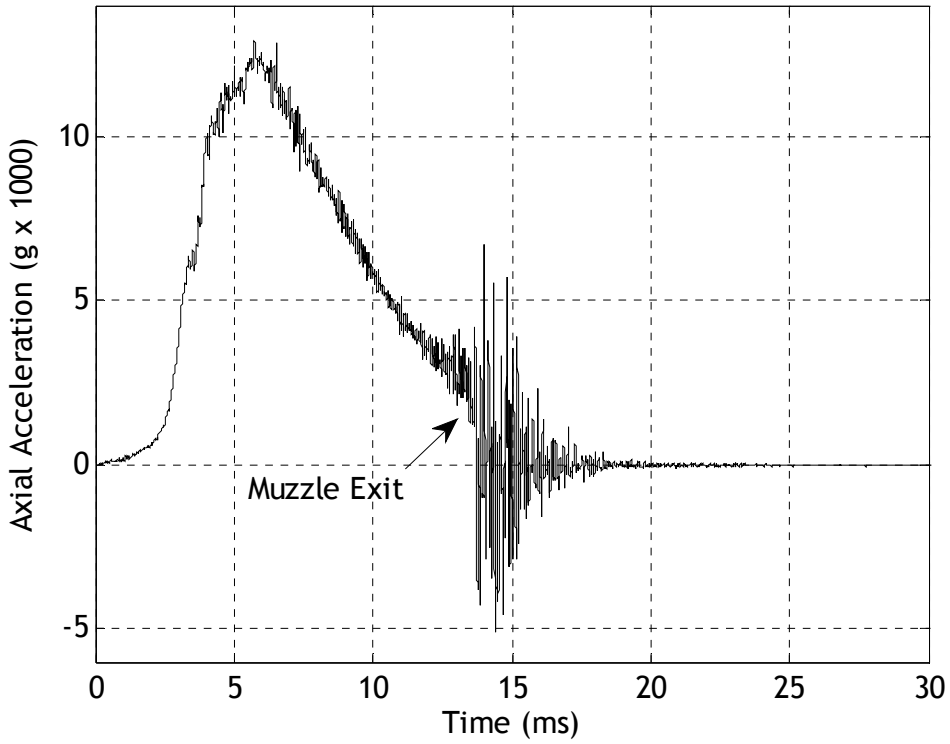

Figure 5.16: Axial Accelerometer Data for Example Projectile.

In order to simulate shock absorber isolation performance against this structural ringing effect, the axial accelerometer data was input directly into the simulation in place of the pressure-time curve described in Section 5.2. Translating mass loads were then examined for various realistic cavity lengths ranging from 7.62 cm to 91.4 cm using constant damping coefficients in each case. Figure 5.17 and the zoom view in Figure 5.18 show the acceleration loads felt by the ITM for each cavity length. Note that although the shock absorber does not significantly reduce the peak acceleration load, it is very effective at reducing high-frequency oscillations, especially for longer cavity lengths. Again, such performance is typically of a first-order damper excited at

frequencies far higher than its natural frequency. Also note that while active damping of these loads would significantly reduce acceleration oscillation even for short cavity lengths (i.e., using the technique from Section 5.4), such an active damper would require damping properties to change in tenths or hundredths of milliseconds, leading to serious physical implementation issues. Therefore, such cases are not studied here.

An interesting implication of this study is that while sensor packages can be isolated from structural ringing, accelerometers and rate sensor data would not correspond with actual projectile motion due to the mechanical decoupling of the ITM and projectile body. This may negatively affect sensor initialization and state estimation. Further studies should be conducted to examine the impact of this decoupling on overall sensor and estimation performance.

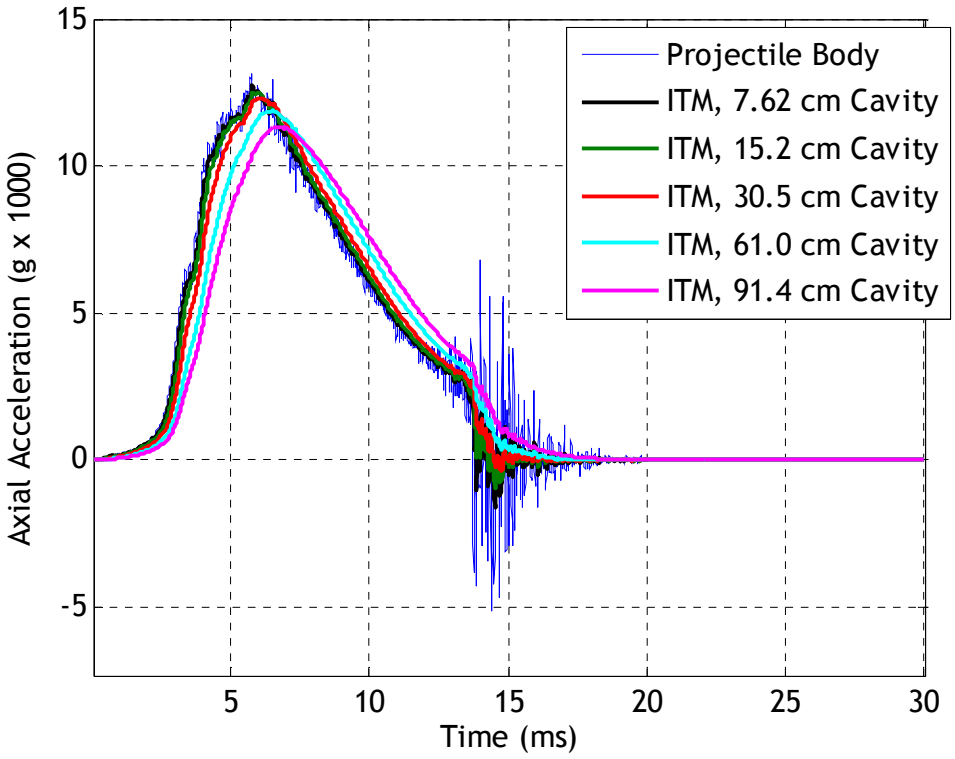

Figure 5.17: Axial Acceleration vs Time for ITM Shock Absorber.

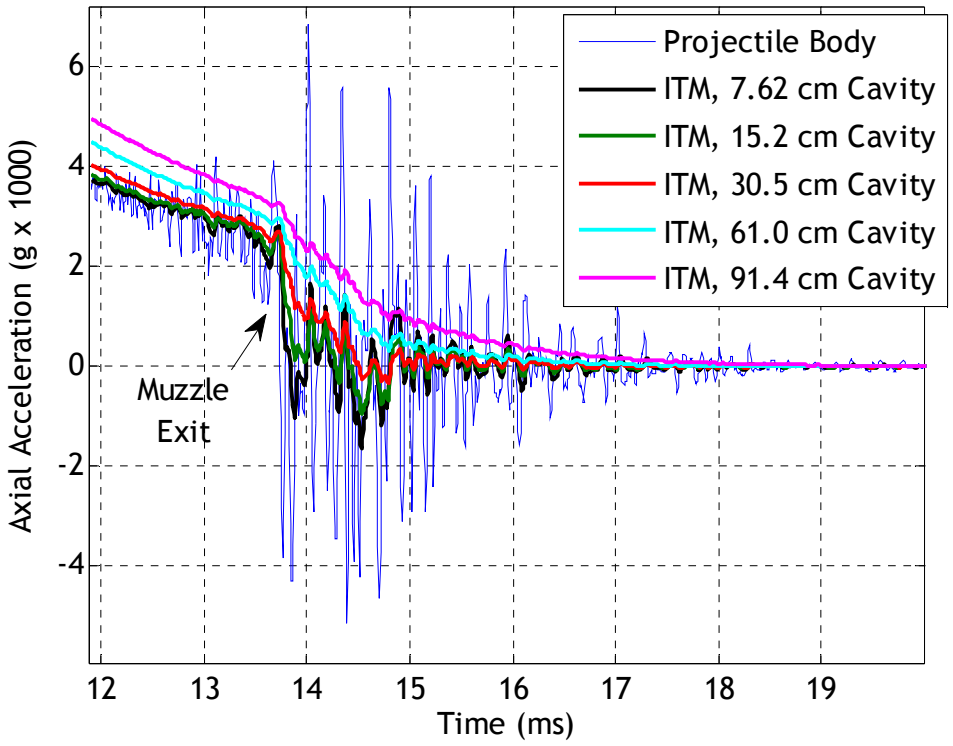

Figure 5.18: Zoom View of Axial Acceleration vs Time for ITM Shock Absorber.

5.6 Conclusion

This chapter explored shock absorber technology using an internal translating mass for projectiles containing sensitive components. First, a typical pressure-time curve was used to simulate actual acceleration loads experienced during launch. By varying mass size, shock absorber damping parameters, and shock absorber length it is shown that passive damping cannot significantly reduce peak acceleration loads felt by the internal translating mass. However, analytical results predicted theoretical minimum acceleration loads using active damping, which were verified using simulation. Finally, actual accelerometer data from the example artillery round was used to show that the ITM shock absorber is very effective at reducing high-frequency loads even with relatively small cavity sizes, on the order of centimeters. Such passive dampers provide potential solutions to the rate sensor resonance issues and other difficulties resulting from high-frequency load oscillations outlined in Section 5.1.

CHAPTER 6

ACTIVE CONTROL OF A PROJECTILE USING AN INTERNAL MOVING MASS

In this chapter, an active control system is developed to guide the internal translating mass projectile to a ground-based stationary target. Specifically, a novel sliding mode control system is derived for the ITM-Beam actuator system. In order to preserve the highest possible simulation accuracy, realistic sensor errors are included within the feedback control loop. Servo control of the internal moving mass employs a simple proportional derivative controller. In addition, flight control using both strict ITM control and combined ITM-canard control are considered. [23]

Section 6.1 provides a brief survey of previous applications of sliding mode control to smart weapons systems and other aerial vehicles. Section 6.2 describes the canard aerodynamic model, while Section 6.3 provides a complete derivation of the sliding mode control law used here as well as example cases to demonstrate control system performance. Section 6.4 provides a brief summary and final conclusions.

6.1 Sliding Mode Control of Guided Weapons

Sliding mode control (SMC) [28], the technique used to generate the control law for the internal translating mass projectile, is a switching type control law developed within the larger framework of variable structure control. Its robust nature and ability to handle highly nonlinear systems has promoted its use in a wide variety of applications, from robot manipulators to underwater vehicles and automotive transmissions. The primary benefit of SMC is that it converts an n-dimensional tracking problem into a first-order stabilization problem. Regulation of this first-order system, represented by a scalar

called the sliding variable, often proves much easier than tracking the original n variables, even in the presence of nonlinearities and uncertainties. Furthermore, by altering certain parameters within the SMC control law, a trade-off can be established between system performance and the controller's ability to remain effective in the presence of uncertainty. SMC thus proves to be a robust control framework that can handle both parametric uncertainties and unmodeled dynamics.

The mathematical foundation behind sliding mode control was developed in the Soviet Union in the 1960's and 1970's [24,25] as a specific method of variable structure control. Variable structure controllers can alter their structure instantaneously from one to another member of a set of continuous functions of the state, allowing different types of control responses in different regions of the state space. Utkin [54] developed general sliding mode control techniques in the framework of variable structure control systems. Specifically, he outlined SMC as a variable structure system (VSS) that contains a discontinuity along surfaces in the state space determined by the formulation of the sliding manifold. However, Utkin pointed out that due to the resulting discontinuity in the closed-loop dynamics of the system, the differential equations that describe resultant system dynamics no longer satisfy classical theorems on the existence and uniqueness of solutions.

While it was clear by the 1980's that SMC held great promise as a robust nonlinear control technique useful in a wide variety of applications, significant problems with its implementation remained. A particularly difficult problem is "chattering phenomenon," in which discontinuities across the sliding manifold produce high-frequency excitation within the controller. These high-frequency inputs into the system serve to both excite unwanted high-frequency system dynamics as well as place a large burden on control actuators. Slotine, Sastry, and Coetsee [19,55,56] designed techniques to mitigate this phenomenon by replacing discontinuities in the control law with smooth interpolations in regions close to the sliding surface. The region in which these

interpolations were applied, termed the "boundary layer," could be actively scaled as model uncertainty expanded or contracted. Therefore, while implementation of boundary layer techniques can be shown to degrade control performance, active scaling of the boundary layer maintains high performance in regions of low uncertainty while still eliminating high-frequency control responses.

Slotine's development of techniques to reduce control chattering facilitated the incorporation of SMC into flight vehicle control system development. Since the 1990's, use of sliding mode controllers in smart weapons has centered around guided missiles, specifically in air-to-air intercept missions. Brierley and Longchamp [57] were among the first to apply SMC to the air intercept problem. The authors first generated a sliding surface based on the missile-target line of sight angle (LOS). Then, intercept performance was compared with a standard proportional navigation guidance (PNG) law using a two-dimensional flight simulation. While in the case of no uncertainty SMC demonstrated comparable performance to PNG, the authors showed that in the case of limited uncertainty in plant dynamics SMC proved to be far more robust. In a final simulation example, the authors showed that in the case of a partial actuator failure the SMC system achieved a successful intercept where PNG did not.

More recently, Shima, Idan, Golan, and Koren [58,59,60] have explored the idea of using sliding mode control in an integrated guidance and control loop. Typically, control systems for air vehicles are designed by separating the flight control and guidance laws such that an inner-loop autopilot is constructed to follow commands of an outer-loop guidance algorithm. While separation is usually valid for most missile interception scenarios, this decoupling between guidance commands and control responses can lead to severe performance degradations during the period just before interception, when missile-target geometry changes rapidly. Therefore, the authors proposed an integrated sliding mode guidance and control loop. Initial simulation results showed the benefits of the integrated methodology, while more detailed studies [59,60] considered control of

missiles with on-off actuators or control surfaces. Interestingly, the sliding surface chosen by the authors was the zero-effort-miss distance (ZEM), defined as the miss distance if, from the current time onward, both the missile and interceptor do not apply controls.

Tournes, Shtessel, and Shkolnikov [61] have recently reported work on an SMC controlled interceptor missile that used attitude and divert thrusters. The missile utilized thrusters at the center of gravity (divert thrusters) with attitude thrusters farther forward, combining aerodynamic and thrust capabilities to increase divert performance. A higher-order sliding mode control law was derived that utilized a second-order sliding manifold. The sliding mode controller tracked commanded pitch rate and flight path angles, in contrast to Shima et al.'s use of ZEM. SMC was chosen for this application because considerable model uncertainty is created by the interaction between the airflow and thruster jets. The sliding mode controller was shown to be very robust to these uncertainties. Most recently [62], the authors reported a fully integrated guidance and control system for the same dual thrust interceptor incorporating a seeker model and missile state estimator. Once again, the sliding mode controller proved robust in the presence of significant model uncertainties, target maneuvers, time delays, and measurement noise.

Another recent application of SMC to air vehicles has been developed by Wells and Hess.[52] The authors took advantage of SMC's robust characteristics in creating an SMC design methodology for reconfigurable flight vehicles, including vehicles with significant damage to the airframe or control actuators. Incorporating an asymptotic observer into the SMC feedback loop, the authors were able to shield parasitic dynamics of the system (such as high-frequency structural modes) from high-frequency control inputs. In selecting observer eigenvalues, the authors identified a tradeoff between minimizing adverse effects of parasitic dynamics and maintaining robustness to variations in the vehicle and/or actuator dynamics. A comparison between SMC and a

classical loop-shaping controller applied to an F-18 pitch control system demonstrated that tracking and robust performance of the SMC system was far superior to that of the classical control law. Most recently, Hess and Bakhtiari-Nejad [53] have applied their reconfigurable SMC design methodology to a highly nonlinear unmanned aerial vehicle. Performance of the resulting SMC design compared favorably with that of a dynamic inversion controller.

The sliding mode controller designed here is novel in that tracking trajectory errors are used directly to generate the sliding surface. Unlike many of the missile controllers designed above using simplified two-dimensional models, the controller developed here incorporates full three-dimensional projectile motion. Furthermore, both translational and rotational body dynamics are accounted for within the control law, yielding a robust controller applicable to many classes of munitions.

6.2 Canard Aerodynamic Model

Later in this chapter, internal translating mass control is combined with canard control to simulate a system in which both types of actuators can be used efficiently at different stages throughout the trajectory to increase control performance. The aerodynamic force due to a single canard is modeled as a point force on the body exerted at the center of canard aerodynamic pressure. The orientation of the canard can be described by three body-fixed rotations. Starting from a frame aligned with the body frame P, the i^{th} canard frame C_i is first rotated about the $\vec{I}_P$ axis by the canard azimuthal angle ϕ_{C_i}. Then, the resulting frame is rotated about the resultant z axis by the canard sweep angle γ_{C_i}. Therefore, the transformation matrix from the canard frame to the projectile body frame is given by

$$T_{C_i \to P} = \begin{bmatrix} \cos(\gamma_{C_i}) & -\sin(\gamma_{C_i}) & 0 \\ \cos(\phi_{C_i})\sin(\gamma_{C_i}) & \cos(\phi_{C_i})\cos(\gamma_{C_i}) & -\sin(\phi_{C_i}) \\ \sin(\phi_{C_i})\sin(\gamma_{C_i}) & \sin(\phi_{C_i})\cos(\gamma_{C_i}) & \cos(\phi_{C_i}) \end{bmatrix} \tag{6.1}$$

Note that if all angles are zero, the canard lies in the $\vec{I}_P - \vec{J}_P$ plane. A diagram of canard angles and aerodynamic forces is shown in Figure 6.1.

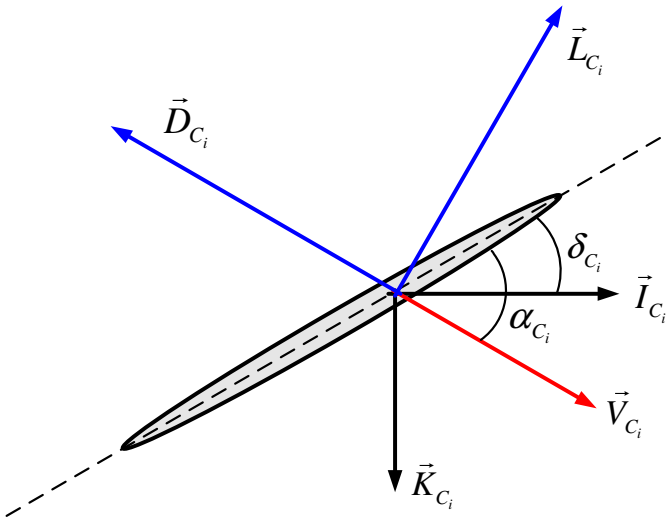

Figure 6.1: Canard Angles and Forces Diagram.

Canard lift force $\vec{L}_{C_i}$ and drag force $\vec{D}_{C_i}$ as shown in Figure 6.1 are computed using strip theory. First note that the canard aerodynamic angle of attack is computed using only the u_{C_i} and w_{C_i} components of the relative air velocity experienced at the canard computation point according to

$$\alpha_{C_i} = \tan^{-1}\left(\frac{w_{C_i}}{u_{C_i}}\right) \tag{6.2}$$

Then, canard lift and drag forces are computed according to

$$\begin{aligned}\vec{L}_{C_i} &= q_{C_i} S_{C_i} \left(-C_{L_{C_i}} \cos(\alpha_{C_i} - \delta_{C_i}) - C_{D_{C_i}} \sin(\alpha_{C_i} - \delta_{C_i})\right) \\ \vec{D}_{C_i} &= q_{C_i} S_{C_i} \left(C_{L_{C_i}} \sin(\alpha_{C_i} - \delta_{C_i}) - C_{D_{C_i}} \cos(\alpha_{C_i} - \delta_{C_i})\right)\end{aligned} \tag{6.3}$$

where q_{C_i} is the dynamic pressure at the canard computation point, S_{C_i} is the reference area of the canard lifting surface, and $C_{L_{C_i}}$ and $C_{D_{C_i}}$ are the canard lift and drag coefficients respectively. Note from Figure 6.1 that δ_{C_i} is the canard deflection angle, which is actively controlled by the smart weapon to achieve desired canard force. Lift and drag coefficients are expanded in terms of canard angle of attack according to,

$$\begin{aligned}C_{L_{C_i}} &= C_{L1}\alpha_{C_i} + C_{L3}\alpha_{C_i}^3 + C_{L5}\alpha_{C_i}^5 \\ C_{D_{C_i}} &= C_{D0} + C_{D2}\alpha_{C_i}^2 + C_I C_{L_{C_i}}^2\end{aligned} \tag{6.4}$$

and local dynamic pressure at the canard computation point is given by

$$q_{C_i} = \frac{1}{2}\rho\left(u_{C_i}^2 + v_{C_i}^2 + w_{C_i}^2\right) \tag{6.5}$$

All canard aerodynamic coefficients vary with respect to local Mach number at the canard. After lift and drag force in the canard frame is computed, canard forces are transformed into the body frame using equation (6.1) and canard moments about the projectile mass center are computed using a cross product between the distance vector

from the mass center to the canard computation point and the vector of forces exerted by the canard.

6.3 Sliding Mode Control Law Derivation

The initial step in creating a sliding mode control law is to choose an appropriate sliding variable and corresponding sliding surface. While numerous choices exist, some options produce better results than others in terms of the trade-off between model complexity and system performance. For instance, modeling of flexible body modes in flight vehicles often provides little control performance benefit while dramatically increasing model complexity.[28] Furthermore, in the case of guided projectiles, a poor choice of sliding surfaces can lead to reduced control performance, steady-state error issues, or even stability problems in some cases. Specifically, a control law that neglects translational dynamics (meaning that control is based on errors in projectile orientation and angular velocity only) is susceptible to steady-state error in high cross wind scenarios. Control laws that neglect rotational dynamics (meaning that control is based on errors in position and translation velocity only) can produce undesirable system responses in projectiles in which rotational dynamics play a large role, such as spin-stabilized munitions. Therefore, a "hybrid" rotational-translational sliding surface is proposed that captures all rigid body dynamics inherent in projectile motion.

The goal of this section is to derive a sliding mode control law that generates phase and magnitude commands for internal translating mass oscillation. The sliding mode control law accomplishes this by first solving for desired control forces in the $\vec{J}_P - \vec{K}_P$ plane. These control forces are then converted into ITM phase and magnitude commands. Finally, these phase and magnitude commands are sent to a proportional plus derivative controller that computes the required ITM control force. As in Chapter 3, this control force is exerted on the ITM-Beam through electromagnetic actuators to produce

desired ITM-Beam motion. For all cases in this chapter, proportional and derivative gains of 5×10^5 and 1000 respectively are used.

Two sliding surfaces are chosen for the sliding mode control law in order to establish projectile control in three dimensions. The lateral sliding variable S_{lat} captures error dynamics in the inertial *x-y* plane, and is given by

$$S_{lat} = w_\psi S_\psi + w_y S_y \tag{6.6}$$

where S_ψ and S_y are secondary sliding variables defined in Sections 6.3.1 and 6.3.2 respectively, and w_ψ and w_y are user-defined weighting parameters. In a similar fashion, the longitudinal sliding variable S_{long} captures error dynamics in the inertial *x-z* plane, and is given by

$$S_{long} = w_\theta S_\theta + w_z S_z \tag{6.7}$$

where S_θ and S_z are secondary sliding variables defined in Sections 6.3.1 and 6.3.2 respectively, and w_θ and w_z are user-defined weighting parameters.

6.3.1 Rotational Sliding Dynamics

The rotational sliding surfaces S_ψ and S_θ are defined such that projectile orientation tracking error decays to zero when $S_\psi = 0$ and $S_\theta = 0$. By first specifying a desired projectile trajectory, these sliding manifolds can be defined as

$$S_\theta = \dot{\theta}_e + \lambda_\theta \theta_e = \left(\dot{\theta} - \dot{\theta}_c\right) + \lambda_\theta \left(\theta - \theta_c\right) \tag{6.8}$$

$$S_\psi = \dot{\psi}_e + \lambda_\psi \psi_e = \left(\dot{\psi} - \dot{\psi}_c\right) + \lambda_\psi \left(\psi - \psi_c\right) \tag{6.9}$$

where the subscript ($_c$) denotes commanded angles and λ_θ and λ_ψ are positive user-defined gains. Note that these constants control the decay rate of the tracking error once on the sliding surface. A diagram of projectile orientation and relevant angles is shown in Figure 6.2.

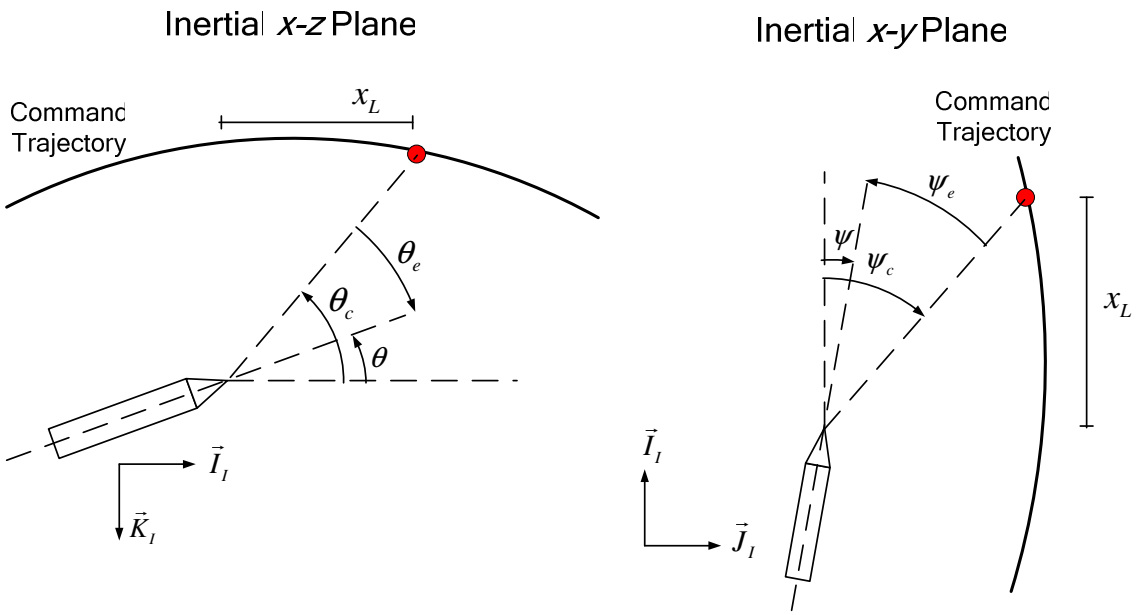

Figure 6.2: SMC Rotational Control Angle Schematic.

In order to compute the control law, expressions for commanded angles are developed as follows. The user-specified lead distance x_L is used along with an input trajectory command table (a set of points that define the commanded trajectory) to find the desired locations y_c and z_c at the current control calculation time. Then, the command angles are given by

$$\theta_c = \tan^{-1}\left(\frac{z - z_c}{x_L}\right) \tag{6.10}$$

$$\psi_c = \tan^{-1}\left(\frac{y_c - y}{x_L}\right) \tag{6.11}$$

Taking the derivative of these expressions yields,

$$\dot{\theta}_c = \frac{x_L\left(\dot{z} - \dot{z}_c\right)}{x_L^2 + \left(z - z_c\right)^2} \tag{6.12}$$

$$\dot{\psi}_c = \frac{x_L\left(\dot{y}_c - \dot{y}\right)}{x_L^2 + \left(y_c - y\right)^2} \tag{6.13}$$

Given the rotational kinematic relationships in equation (3.4) and the expressions in equations (6.12) and (6.13), the sliding surfaces in equations (6.8) and (6.9) can be rewritten as

$$S_\theta = c_\phi q - s_\phi r - \frac{x_L\left(\dot{z} - \dot{z}_c\right)}{x_L^2 + \left(z - z_c\right)^2} + \lambda_\theta \theta - \lambda_\theta \tan^{-1}\left(\frac{z - z_c}{x_L}\right) \tag{6.14}$$

$$S_\psi = \frac{s_\phi}{c_\theta} q + \frac{c_\phi}{c_\theta} r - \frac{x_L\left(\dot{y}_c - \dot{y}\right)}{x_L^2 + \left(y_c - y\right)^2} + \lambda_\psi \psi - \lambda_\psi \tan^{-1}\left(\frac{y_c - y}{x_L}\right) \tag{6.15}$$

Sliding mode control laws typically consist of an equivalent control that forces tracking error to zero when $S = 0$ and a switching control that drives tracking error dynamics to $S = 0$ when off of the sliding surface. In order to solve for the equivalent control, the time derivative of the sliding variables are set to zero. Solving these expressions for the control yields the equivalent control component of the sliding mode control law. In order to compute the derivative of equations (6.14) and (6.15), let T be the body to inertial reference frame transformation matrix given by

$$T = \begin{bmatrix} c_\theta c_\psi & s_\phi s_\theta c_\psi - c_\phi s_\psi & c_\phi s_\theta c_\psi + s_\phi s_\psi \\ c_\theta s_\psi & s_\phi s_\theta s_\psi + c_\phi c_\psi & c_\phi s_\theta s_\psi - s_\phi c_\psi \\ -s_\theta & s_\phi c_\theta & c_\phi c_\theta \end{bmatrix} \tag{6.16}$$

The derivatives of equations (6.14) and (6.15) are then given by

$$\begin{aligned} \dot{S}_\theta = D_\theta - \frac{x_L}{k_1}\frac{T_{32}}{m}F_Y^{Con} - \frac{x_L}{k_1}\frac{T_{33}}{m}F_Z^{Con} + c_\phi Q_{12}\Delta_{LR}F_Y^{Con} \\ - c_\phi Q_{14}\Delta_{LR}F_Z^{Con} - s_\phi Q_{32}\Delta_{LR}F_Y^{Con} + s_\phi Q_{34}\Delta_{LR}F_Z^{Con} \end{aligned} \tag{6.17}$$

$$\begin{aligned} \dot{S}_\psi = D_\psi + \frac{x_L}{k_2}\frac{T_{22}}{m}F_Y^{Con} + \frac{x_L}{k_2}\frac{T_{23}}{m}F_Z^{Con} + \frac{s_\phi}{c_\theta}Q_{12}\Delta_{LR}F_Y^{Con} \\ - \frac{s_\phi}{c_\theta}Q_{14}\Delta_{LR}F_Z^{Con} + \frac{c_\phi}{c_\theta}Q_{32}\Delta_{LR}F_Y^{Con} - \frac{c_\phi}{c_\theta}Q_{34}\Delta_{LR}F_Z^{Con} \end{aligned} \tag{6.18}$$

These equations involve numerous intermediate expressions which are described below. First note that the final expressions derived in Appendix B for $\dot{p}$, $\dot{q}$, and $\dot{r}$ are used to obtain equations (6.17) and (6.18). Furthermore, the matrix Q is defined as $Q = A^{-1}$, where A is the matrix used in the ITM-Beam rotational dynamics equation given in equation (3.13) (the full expression for the A matrix can be found in Appendix A). In equations (6.17) and (6.18), T and Q subscripts denote the element of the respective matrices, m denotes system mass, and F_Y^{Con} and F_Z^{Con} are control forces in the body-frame y and z directions respectively. As in Appendix B, the term Δ_{LR} is the stationline distance from the ITM-Beam hinge point L to the point of control application. Furthermore, k_1 and k_2 are given by

$$k_1 = x_L^2 + \left(z - z_c\right)^2 \tag{6.19}$$

$$k_2 = x_L^2 + \left(y_c - y \right)^2 \tag{6.20}$$

Also, the terms D_θ and D_ψ are lengthy expressions of state variables and non-control related forces. Full expressions for these quantities are provided in Appendix C. Equations (6.17) and (6.18) will be used to compute the final control law after the translational component of control has been derived in Section 6.3.2.

6.3.2 Translational Sliding Dynamics

Translational dynamics can be incorporated into the control law by defining sliding surfaces S_y and S_z given by

$$S_y = \dot{y}_e + \lambda_y y_e = \dot{y} - \dot{y}_c + \lambda_y \left(y - y_c \right) \tag{6.21}$$

$$S_z = \dot{z}_e + \lambda_z z_e = \dot{z} - \dot{z}_c + \lambda_z \left(z - z_c \right) \tag{6.22}$$

where λ_y and λ_z are positive user-defined gains. Taking the derivative of equations (6.21) and (6.22) yield, after some algebraic manipulation,

$$\dot{S}_y = D_y + \frac{T_{22}}{m} F_Y^{Con} + \frac{T_{23}}{m} F_Z^{Con} \tag{6.23}$$

$$\dot{S}_z = D_z + \frac{T_{32}}{m} F_Y^{Con} + \frac{T_{33}}{m} F_Z^{Con} \tag{6.24}$$

where

$$D_y = \lambda_y\left(T_{21}u + T_{22}v + T_{23}w\right) + \dot{T}_{21}u + \dot{T}_{22}v + \dot{T}_{23}w + T_{21}\left(\frac{F_x}{m} + rv - qw\right) + T_{22}\left(\frac{F_y}{m} - ru + pw\right) + T_{23}\left(\frac{F_z}{m} - pv + qu\right) - \ddot{y}_c - \lambda_y\dot{y}_c \tag{6.25}$$

$$D_z = \lambda_z\left(T_{31}u + T_{32}v + T_{33}w\right) + \dot{T}_{31}u + \dot{T}_{32}v + \dot{T}_{33}w + T_{31}\left(\frac{F_x}{m} + rv - qw\right) + T_{32}\left(\frac{F_y}{m} - ru + pw\right) + T_{33}\left(\frac{F_z}{m} - pv + qu\right) - \ddot{z}_c - \lambda_z\dot{z}_c \tag{6.26}$$

where F_x, F_y, and F_z consist of the sum of all non-control-related external force components expressed in the body frame (i.e., the sum of aerodynamic, weight, and Magnus forces).

6.3.3 Translational-Rotational Hybrid SMC

To obtain the translational-rotational sliding mode control law, the derivative of equations (6.6) and (6.7) are taken, yielding

$$\dot{S}_{lat} = w_\psi\dot{S}_\psi + w_y\dot{S}_y \tag{6.27}$$

$$\dot{S}_{long} = w_\theta\dot{S}_\theta + w_z\dot{S}_z \tag{6.28}$$

Using the expansions given in equations (6.17), (6.18), (6.25), and (6.26) these derivatives become

$$\dot{S}_{lat} = D_{lat} + R_1F_Y^{Con} + R_2F_Z^{Con} \tag{6.29}$$

$$\dot{S}_{long} = D_{long} + R_3F_Y^{Con} + R_4F_Z^{Con} \tag{6.30}$$

where

$$D_{lat} = w_{\psi} D_{\psi} + w_{y} D_{y} \tag{6.31}$$

$$D_{long} = w_{\theta} D_{\theta} + w_{z} D_{z} \tag{6.32}$$

and

$$R_1 = w_{\psi}\left(\frac{x_L}{k_2}\frac{T_{22}}{m} + \frac{s_{\phi}}{c_{\theta}} Q_{12}\Delta_{LR} + \frac{c_{\phi}}{c_{\theta}} Q_{32}\Delta_{LR}\right) + w_{y}\frac{T_{22}}{m} \tag{6.33}$$

$$R_2 = w_{\psi}\left(\frac{x_L}{k_2}\frac{T_{23}}{m} - \frac{s_{\phi}}{c_{\theta}} Q_{14}\Delta_{LR} - \frac{c_{\phi}}{c_{\theta}} Q_{34}\Delta_{LR}\right) + w_{y}\frac{T_{23}}{m} \tag{6.34}$$

$$R_3 = w_{\theta}\left(-\frac{x_L}{k_1}\frac{T_{32}}{m} + c_{\phi} Q_{12}\Delta_{LR} - s_{\phi} Q_{32}\Delta_{LR}\right) + w_{z}\frac{T_{32}}{m} \tag{6.35}$$

$$R_4 = w_{\theta}\left(-\frac{x_L}{k_1}\frac{T_{33}}{m} - c_{\phi} Q_{14}\Delta_{LR} + s_{\phi} Q_{34}\Delta_{LR}\right) + w_{z}\frac{T_{33}}{m} \tag{6.36}$$

In order to guarantee attraction to the sliding surface, a switching control is chosen such that

$$\dot{S}_{lat} = -\alpha_{lat}\,\mathrm{sat}\left(S_{lat}\right) \tag{6.37}$$

$$\dot{S}_{long} = -\alpha_{long}\,\mathrm{sat}\left(S_{long}\right) \tag{6.38}$$

The saturation function used in equations (6.37) and (6.38) is defined as

$$\text{sat}(y) = \begin{cases} y & if \quad |y| < 1 \\ 1 & if \quad y \geq 1 \\ -1 & if \quad y \leq -1 \end{cases} \tag{6.39}$$

Note that use of the saturation function rather than the signum function eliminates "control chattering" phenomenon typically exhibited by switching controllers. Finally, combining expressions for $\dot{S}_{lat}$ and $\dot{S}_{long}$ in equations (6.29), (6.30), (6.37), and (6.38), the following matrix equation is formed:

$$\begin{Bmatrix} F_Y^{Con} \\ F_Z^{Con} \end{Bmatrix} = \begin{bmatrix} R_1 & R_2 \\ R_3 & R_4 \end{bmatrix}^{-1} \begin{Bmatrix} -\alpha_{lat}\text{sat}(S_{lat}) - D_{lat} \\ -\alpha_{long}\text{sat}(S_{long}) - D_{long} \end{Bmatrix} \tag{6.40}$$

Equation (6.40) is used to calculate desired force commands in the body y and z directions. As a check on the derivation of the control law, closed form expressions for F_Y^{Con} and F_Z^{Con} obtained from equation (6.40) were substituted back into equations (6.23) and (6.24) to shown that: when $S_{lat} = 0$, $\dot{S}_{long} = 0$; when $S_{lat} > 0$, $\dot{S}_{lat} < 0$; and when $S_{lat} < 0$, $\dot{S}_{lat} > 0$. Identical hand calculations were performed for S_{long}.

The SMC law used here requires feedback of all 12 projectile states as well ITM-Beam angle and angular velocity (γ and $\dot{\gamma}$). Furthermore, projectile mass and all aerodynamic forces and moments are required as well. Oftentimes estimation of all of these feedback parameters involves significant error. However, the robust nature of SMC yields reasonable performance in the presence of these uncertainties. This robust nature is demonstrated using Monte Carlo simulations later in this chapter, when noise and bias errors are placed on all feedback signals.

The sliding mode control law derived above utilizes numerous user-defined gains, which are listed along with their respective purpose in Table 6.1. Of particular

importance to controller robustness are the switching gains α_{lat} and α_{long}. Theoretically, given a plant and specified bounds on uncertainty it is possible to analytically find SMC switching gains that guarantee global stability and attraction to the sliding surface. However, while in this case the plant model and uncertainty bounds are known, the extremely complicated nature of such calculations make this analytical technique practically impossible to utilize, since all types of uncertainty must be considered in all conceivable flight regimes. Instead, Monte Carlo methods may be used to determine lower bounds on switching gains by slowly decreasing them while observing controller performance over numerous controlled trajectories. Reduction of switching gains beyond the lower bound will result in noticeably reduced control performance in many cases. This empirical technique was used here to determine adequate switching gains for all cases incorporating uncertainty.

Table 6.1: Sliding Mode Controller User-Defined Parameters.

User-Defined Parameter	Name	Restrictions	Purpose
x_L	Lead Distance	> 0	Provides damping in control response
α_{lat}, α_{long}	Switching Gains	> 0	Determines rate of attraction to sliding surface
$\lambda_\theta, \lambda_\psi, \lambda_y, \lambda_z$	Sliding Gains	> 0	Determines decay rate of tracking error when $S = 0$
$w_\theta, w_\psi, w_y, w_z$	Weighting Values	$w_z \leq 0$, All others ≥ 0	Weights translational and rotational components of control law

6.3.4 Flight Control System Test Case

In order to test flight controller functionality, a step-input is applied to the control system, implemented on the example fin-stabilized projectile used in Chapter 3. Control force is exerted by a set of two canards placed on opposite ends of the body in the $\vec{I}_P - \vec{J}_P$ plane (no ITM control is used in this initial test case). Canard deflection angle can be altered by the controller between +8 deg and -8 deg. Due to the geometry of this canard configuration, the F_Z^{Con} force output from the control system is discarded (since control is not possible in the body z direction), and canard deflection angle δ_{can} is computed based on control output F_Y^{Con} according to

$$\delta_{can} = \frac{F_Y^{Con}}{\frac{1}{2}\rho V_{can}^2 C_{L_{\alpha_{can}}} S_{can}} \tag{6.41}$$

where S_{can} is the total canard area, $C_{L_{\alpha_{can}}}$ is the lift-curve slope of the canard airfoil, and V_{can} is the total velocity at the canard computation point. Initial conditions for the example step-response simulation are x = 0.0 m, y = 3.048 m, z = 3.048 m, ϕ = 0.0 deg, θ = 0.0 deg, ψ = 0.0 deg, u = 860.0 m/s, v = 0.0 m/s, w = 0.0 m/s, p = 0.0 rad/s, q = 0.0 rad/s, r = 0.0 rad/s. Gravitational forces are set to zero and the command trajectory is a straight line with y = 0 and z = 0. The initial conditions and command trajectory produce a step input into the control system. In addition, a cross wind of 24.4 m/s in the $-\vec{J}_I$ direction is introduced in order to demonstrate control performance in the presence of winds. All simulations terminate at a range of approximately 3000 m.

In addition to control law validation, this example case also serves to demonstrate the tradeoff between translational and rotational control. Three controlled simulations are run. A "translational only" case (where $w_\theta = w_\psi = 0$) demonstrates control response

when only the translational portion is included. Conversely, a "rotational only" case (where $w_y = w_z = 0$) demonstrates control response when only the rotational portion is included. A "translational plus rotational" case shows the benefits of including both components of the control law. Table 6.2 details canard and controller parameters used in this example simulation.

Table 6.2: Controller and Canard Parameters for Example Simulation.

	Parameter	Value (non-dimensional except where specified)
Translational Only	w_θ, w_ψ	0.0, 0.0
	w_y	1.0
	w_z	-1.0
	$\alpha_{lat}, \alpha_{long}$	100.0, 100.0
	λ_y, λ_z	5.0, 5.0
Rotational Only	w_θ, w_ψ	1.0, 1.0
	w_y	0.0
	w_z	0.0
	$\alpha_{lat}, \alpha_{long}$	100.0, 100.0
	$\lambda_\theta, \lambda_\psi$	5.0, 5.0
	x_L	6.1 m
Translational Plus Rotational	w_θ, w_ψ	1.0, 1.0
	w_y	0.3
	w_z	-0.3
	$\alpha_{lat}, \alpha_{long}$	100.0, 100.0
	$\lambda_\theta, \lambda_\psi$	5.0, 5.0
	λ_y, λ_z	5.0, 5.0
	x_L	6.1 m
Canard Parameters	Canard Stationline	47.24 cm
	Total Canard Area	18.58 cm^2

Figures 6.3-6.6 show trajectory, canard deflection angle, and sliding surface time histories. First, note that in each of the three cases, tracking error is nearly eliminated by the controller with reasonable rise time and damping characteristics as shown in Figures 6.3 and 6.4. However, Figure 6.3 clearly shows that the rotational only case exhibits steady-state error in the presence of cross winds. This occurs because the projectile develops a steady-state crab into the wind. Thus the sliding variables can be zero even when the projectile is not on the tracking trajectory. This is clearly demonstrated in Figure 6.5, where both sliding variables in the rotational only case are zero in the presence of steady-state error. Furthermore, while the translational only controller eliminates steady-state error issues, it does not account for rotational dynamics of the body and therefore has difficulty damping angular motion induced by control forces. This is demonstrated in the trajectory oscillations shown in Figures 6.3 and 6.4, and even more clearly in the canard deflection time history shown in Figure 6.6. Note that in the translational only case canards are fully active throughout the whole trajectory as the controller attempts to force tracking error to zero without accounting for projectile angular motion. In contrast to both of these cases, the rotational plus translational case represents an integrated control scheme in which the "inner loop," which follows angle commands, and the "outer loop," which follows position commands, are combined. As a result, the control response exhibits extremely small steady-state error without the overactive control tendencies of the translational only case. Therefore it can be seen that an effective blending of translational and rotational control leads to optimum control performance. Note that tuning of the translational and rotational weighting parameters is an empirical process; the choice of weighting parameters shown here resulted from experimentation using several different sets. The optimal weights depend on projectile

and actuator characteristics as well as control system gains, and methods for obtaining the optimal weights other than trial and error are beyond the scope of this work.

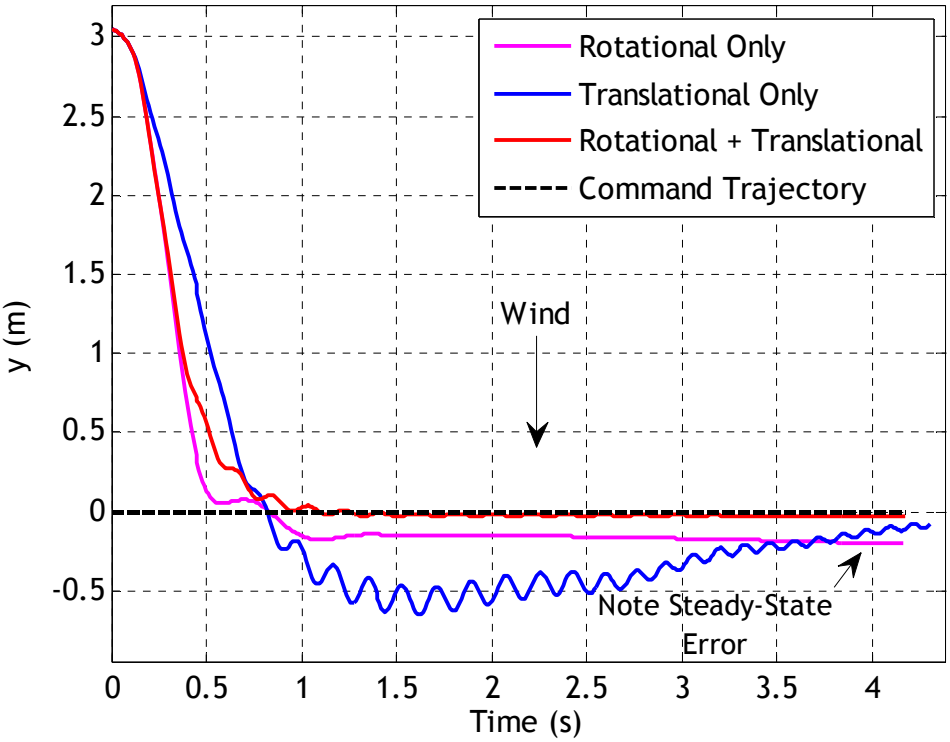

Figure 6.3: *y* vs Time for Step Input.

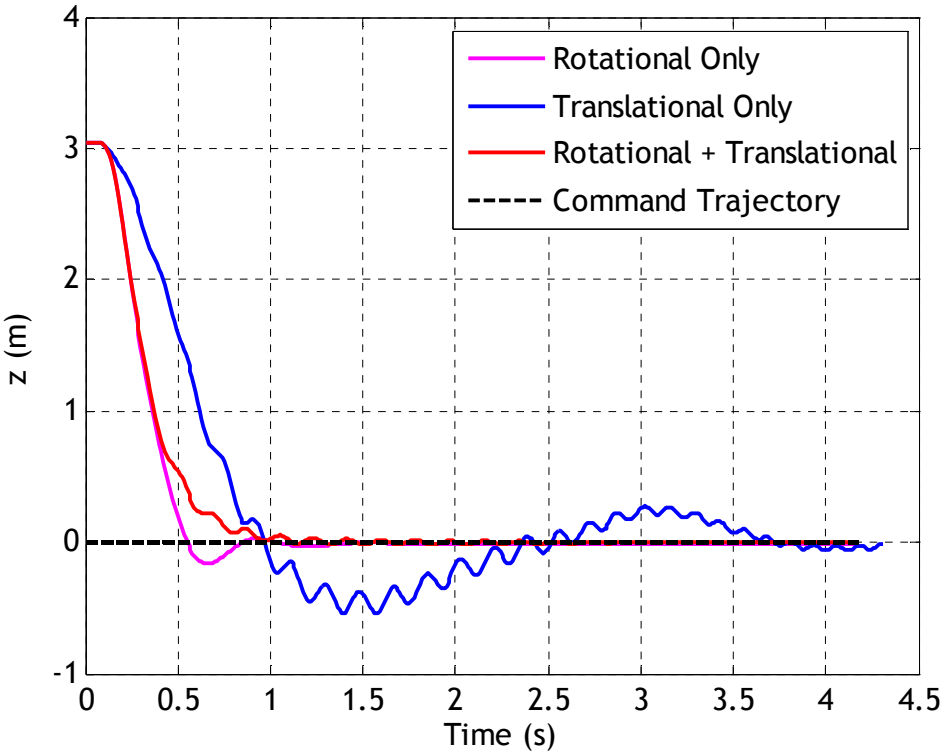

Figure 6.4: z vs Time for Step Input.

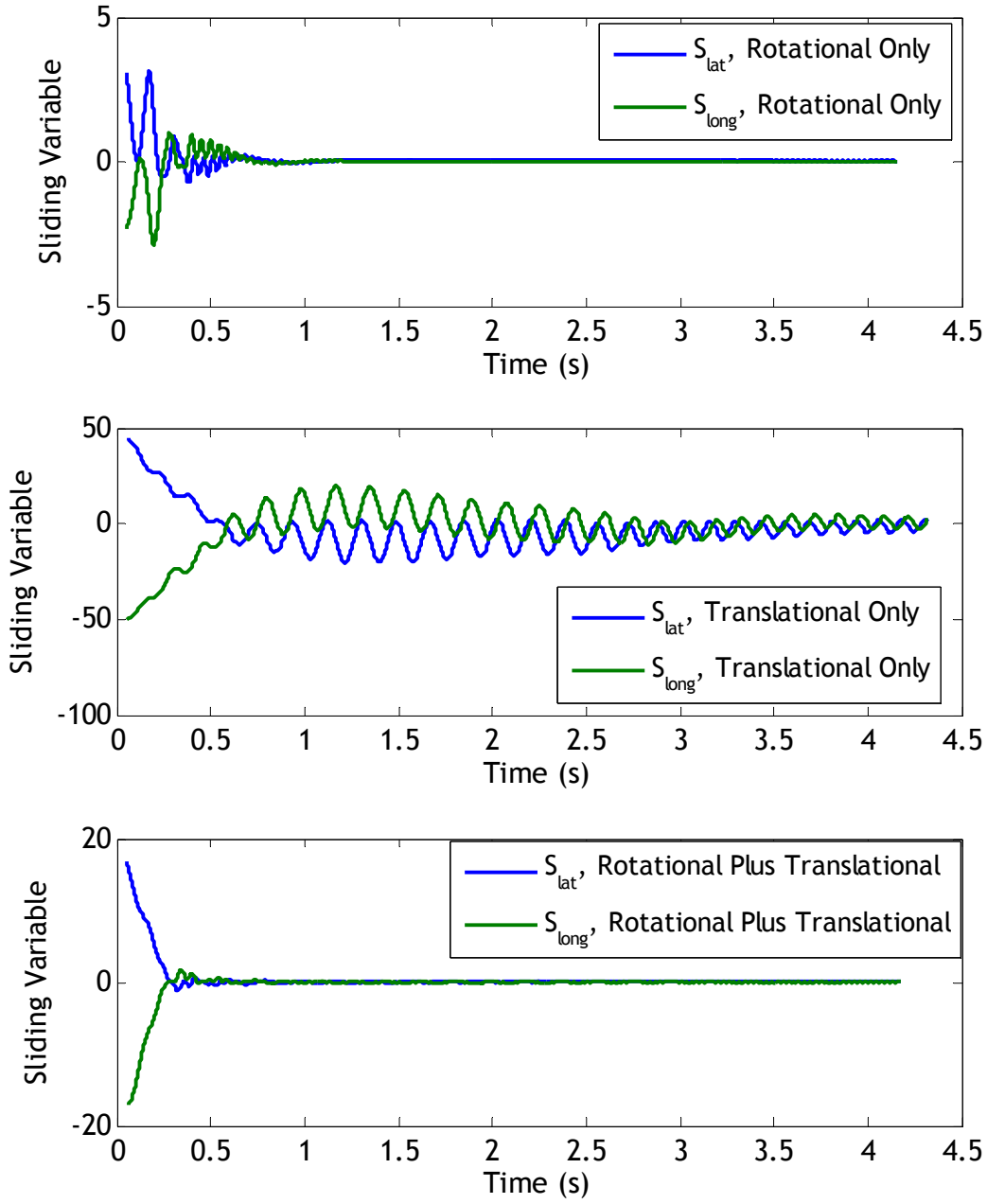

Figure 6.5: Sliding Variables vs Time for Step Input.

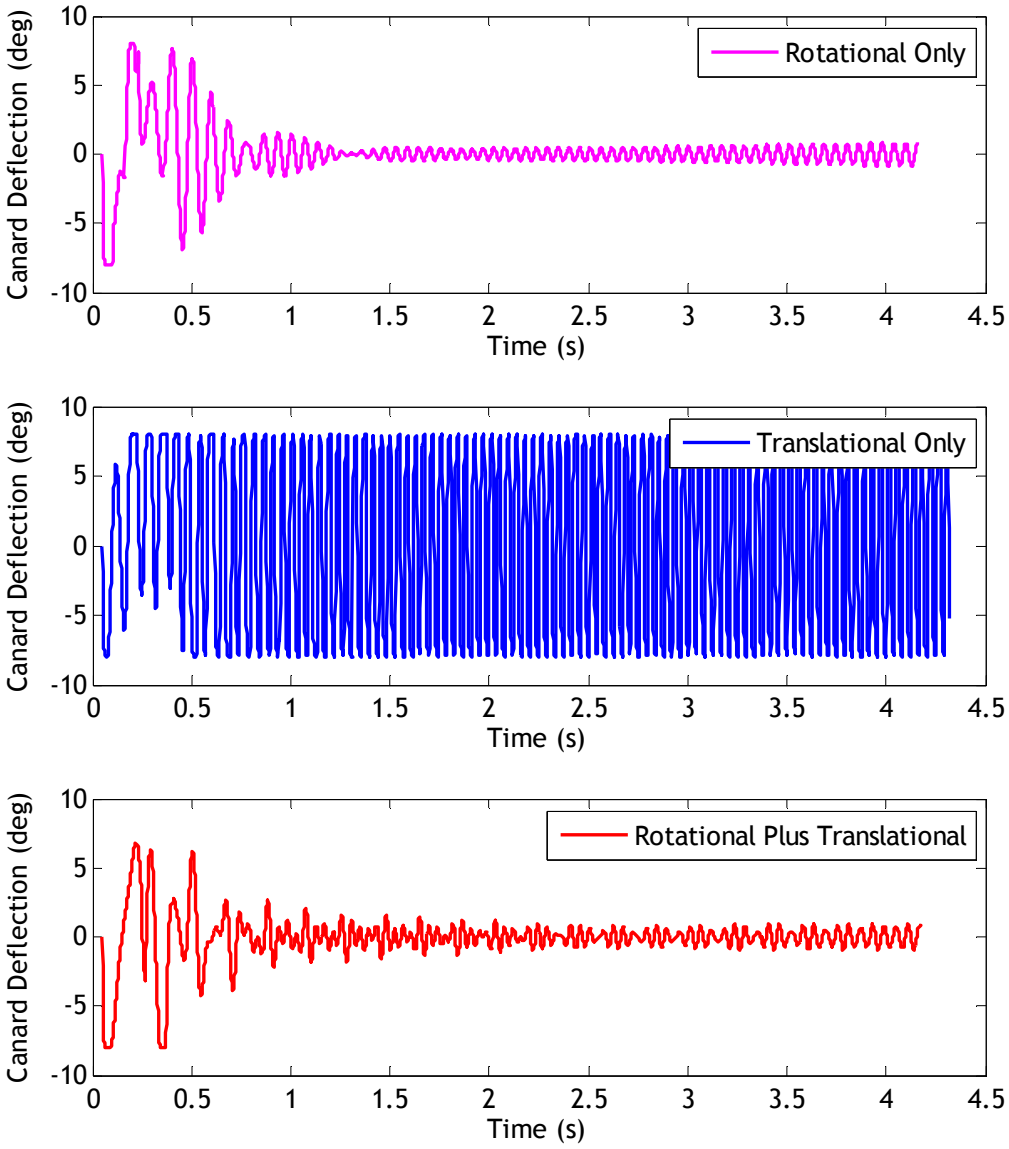

Figure 6.6: Canard Deflection vs Time for Step Input.

6.3.5 Sliding Mode Control of an Internal Translating Mass Projectile

In this section, the sliding mode control law derived above is applied to the ITM-Beam projectile described in Chapter 3 and used to generate trajectory corrections. The outputs from the sliding mode control law are force commands in the body y and z

directions, and therefore an "inner loop" control law is needed to transform these force components into internal translating mass oscillation phase angle and magnitude commands. This is accomplished as follows. First, force commands are resolved into the no-roll reference frame according to

$$F_{Y_{NR}}^{Con} = F_Y^{Con} c_\phi - F_Z^{Con} s_\phi \tag{6.42}$$

$$F_{Z_{NR}}^{Con} = F_Y^{Con} s_\phi + F_Z^{Con} c_\phi \tag{6.43}$$

The no-roll reference frame is the standard non-rolling body-fixed reference frame used in projectile flight dynamics, and can be obtained from the body frame by rotating by $-\phi$ about the $\vec{I}_P$ axis. Note that $F_{Y_{NR}}^{Con}$ and $F_{Z_{NR}}^{Con}$ are control force components in this frame. Then, the phase angle ϕ_T of ITM oscillation is obtained as

$$\phi_T = \tan^{-1}\left(\frac{-F_{Z_{NR}}^{Con}}{F_{Y_{NR}}^{Con}}\right) \tag{6.44}$$

Magnitude of ITM oscillation is calculated by

$$A_T = \begin{cases} \dfrac{1}{2}\dfrac{(L_{CAV} - L_{ITM})}{F_{LIM}}\sqrt{\left(F_Y^{Con}\right)^2 + \left(F_Z^{Con}\right)^2} & if \quad \sqrt{\left(F_Y^{Con}\right)^2 + \left(F_Z^{Con}\right)^2} < F_{LIM} \\ \dfrac{1}{2}(L_{CAV} - L_{ITM}) & if \quad \sqrt{\left(F_Y^{Con}\right)^2 + \left(F_Z^{Con}\right)^2} \geq F_{LIM} \end{cases} \tag{6.45}$$

where L_{CAV} and L_{ITM} are the lengths of the cavity and ITM respectively and F_{LIM} is a user-defined force level that sets defines saturation of the "inner loop" control system.

Note that if the total magnitude of the control force vector is greater than F_{LIM}, the entire cavity is used.

Uncertainty in plant dynamics and feedback signals is an important effect to capture in any evaluation of control performance. In this section as well as Section 6.3.6, feedback uncertainty is incorporated in the model by placing errors on nearly all feedback parameters used by the control system. At each control cycle, all body states, forces, and derivatives of body states used for both SMC and proportional derivative control calculation are corrupted by noise and bias errors. For dispersion simulations, different bias errors are used for each simulation to ensure control law robustness against these types of errors. Table 6.3 lists the standard deviations of the noise errors and the standard deviations of the biases generated for dispersion simulations. Furthermore, for demonstration purposes, Figures 6.7 and 6.8 show time histories of the *y* and drag force feedback signals corrupted by noise for the example simulation shown later in this section. Note that the feedback error levels shown in Table 6.3 represent reasonable values typical of industry-standard smart weapon state estimators.

Before outlining an example case of ITM control using the sliding mode control law, it is important to note the limited control authority inherent in this mechanism. Figure 3.5 in Chapter 3 demonstrated a maximum trajectory alteration of 25 m at 5000 m range, or approximately 5 mils, using a 4% ITM size. This control authority potential stands in stark contrast to canard-actuated systems, which can often yield one or even two orders of magnitude more control authority for reasonably-sized canards. The ITM projectile's limited control authority capability stems from several causes. First, lateral mass center offsets produced by internal translating masses on the order of a percent of the total system mass are inherently small. Secondly, projectile static stability increases as velocity decreases after launch, reducing control authority significantly throughout the flight. Furthermore, this velocity decrease causes a corresponding reduction in drag, the

source of control generation due to lateral mass center offset. These effects result in a continual decrease of control authority as flight progresses.

Table 6.3: Feedback Error Levels for Simulations with Uncertainty.

Feedback Signal	Noise Standard Deviation	Bias Standard Dev. for Dispersion Simulations
x	1.524 m	0.914 m
y	1.524 m	0.914 m
z	2.134 m	0.914 m
ϕ	300 mrad	75 mrad
θ	1 mrad	0.1 mrad
ψ	1 mrad	0.1 mrad
u	0.21 m/s	0.041 m/s
v	0.076 m/s	0.041 m/s
w	0.076 m/s	0.041 m/s
p	500 mrad/s	70 mrad/s
q	40 mrad/s	1 mrad/s
r	40 mrad/s	1 mrad/s
γ	10^{-6} rad/s	10^{-5} rad/s
$\dot{\gamma}$	10^{-5} rad/s	10^{-6} rad/s
All Forces	10% of actual value	None

An example case of ITM control applied to the fin-stabilized projectile described in Chapter 3 is shown in Figures 6.9-6.16. Several simulations are shown in order to demonstrate the capabilities of ITM control with the sliding mode control law. First, a ballistic trajectory with "nominal" initial conditions described in Table 6.4 is simulated and used as the command trajectory for all controlled simulations. Then, using perturbed initial conditions also shown in Table 6.4, a controlled simulation with no feedback uncertainty (called "Controlled, No Error") is performed, as is a controlled simulation with feedback uncertainty (called "Controlled, Error"). Also, a ballistic case using the

perturbed initial conditions (called "Ballistic") is shown for reference. Control system parameters were tuned for optimum performance, and are also shown in Table 6.4. For the controlled case including uncertainty, first-order filters are applied to the outputs ϕ_T and A_T of the inner-loop control system in order to provide smooth inputs to the ITM inner-loop controller. Time constants τ_{phase} and τ_{mag} for these filters are provided in Table 6.4.

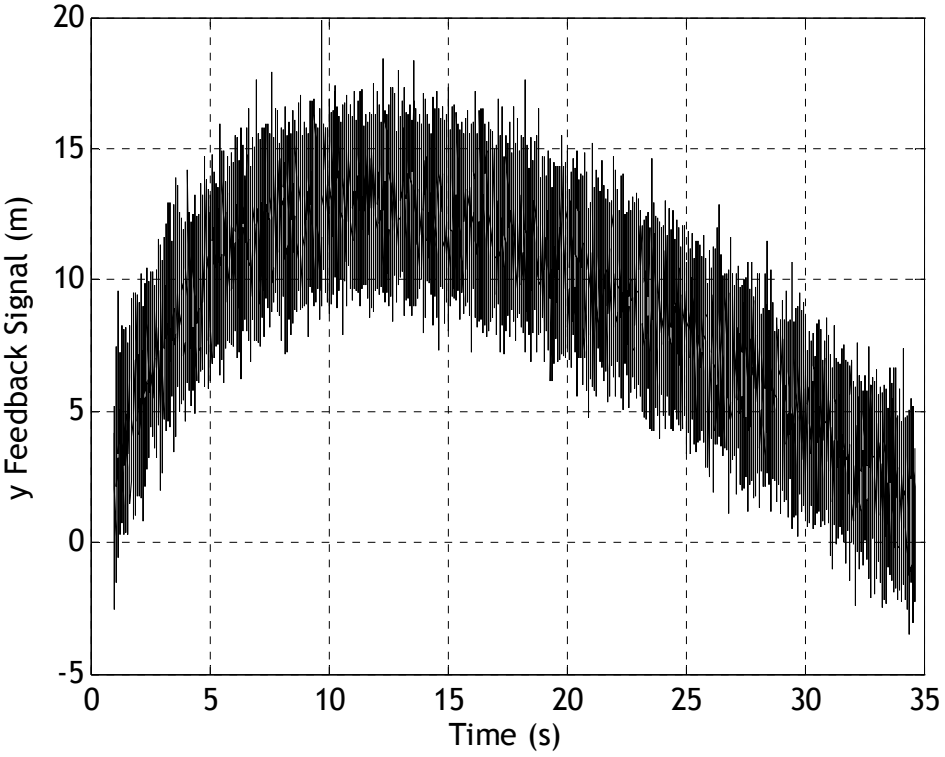

Figure 6.7: *y* Feedback Signal vs Time for Simulation with Uncertainty.

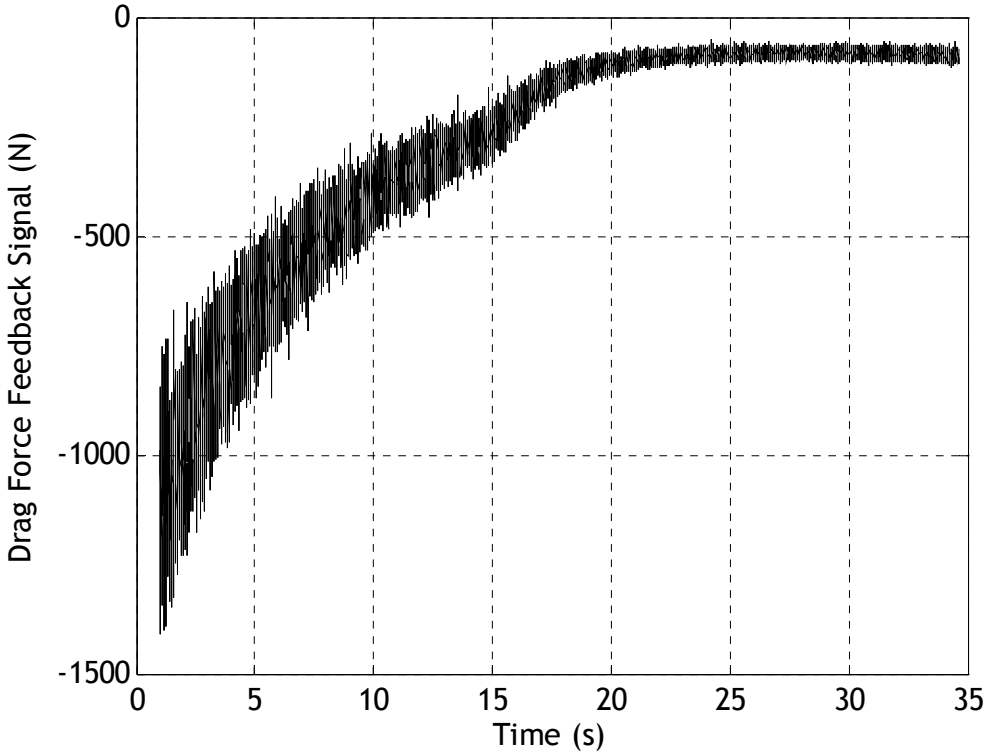

Figure 6.8: Drag Force Feedback Signal vs Time for Simulation with Uncertainty.

Table 6.4: Initial Conditions and Control Parameters for Example Case.

		Nominal	***Perturbed***
Initial Conditions	x (m)	0.0	0.0
	y (m)	0.0	0.0
	z (m)	0.0	0.0
	ϕ (deg)	0.0	0.0
	θ (deg)	17.19	17.25
	ψ (deg)	0.0	0.172
	u (m/s)	860.0	861.6
	v (m/s)	0.0	0.50
	w (m/s)	0.0	0.02
	p (rad/s)	0.0	0.357
	q (rad/s)	0.0	2.22
	r (rad/s)	0.0	0.188
	Wind Mag (m/s)	0.0	0.364
	Wind Azimuth (deg)	N/A	45.5
ITM Control Parameters	m_T (kg)	0.734	
	$\alpha_{lat}, \alpha_{long}$	280.0, 280.0	
	$\lambda_\psi, \lambda_\theta$	5.0, 5.0	
	λ_y, λ_z	40.0, 40.0	
	w_y	1.0	
	w_z	-1.0	
	w_ψ, w_θ	0.1, 0,1	
	x_L	6.1 m	
	F_{LIM}	88.96 N	
	τ_{phase}, τ_{mag}	0.11 s, 0.11 s	

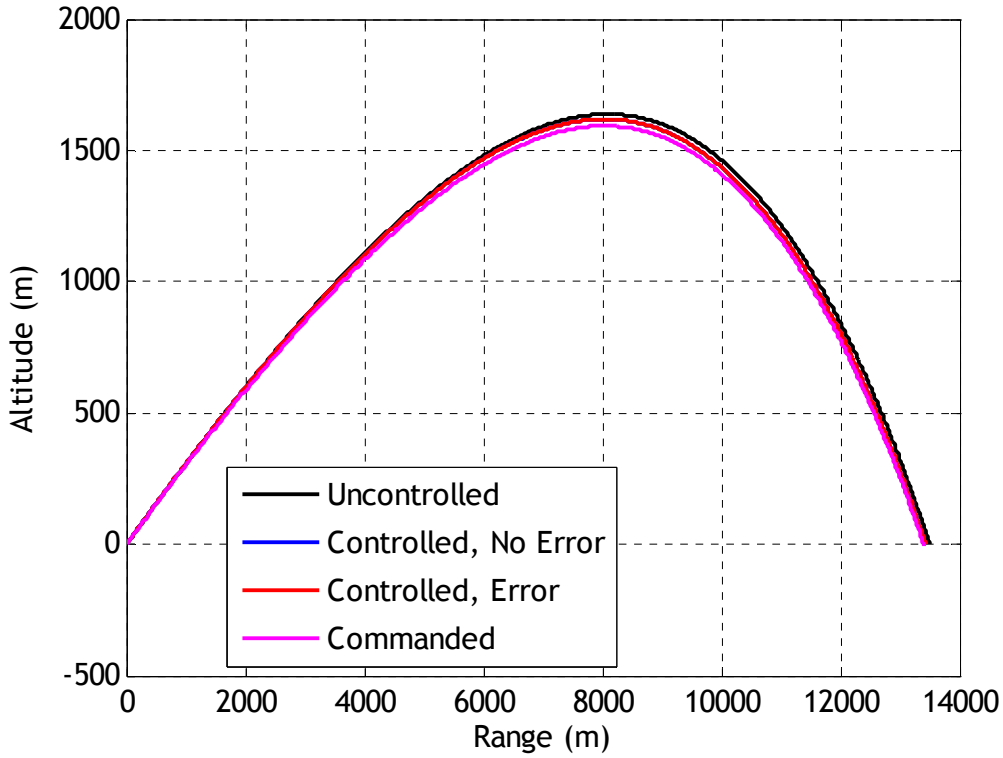

Figure 6.9: Altitude vs Range, ITM Control Example Case.

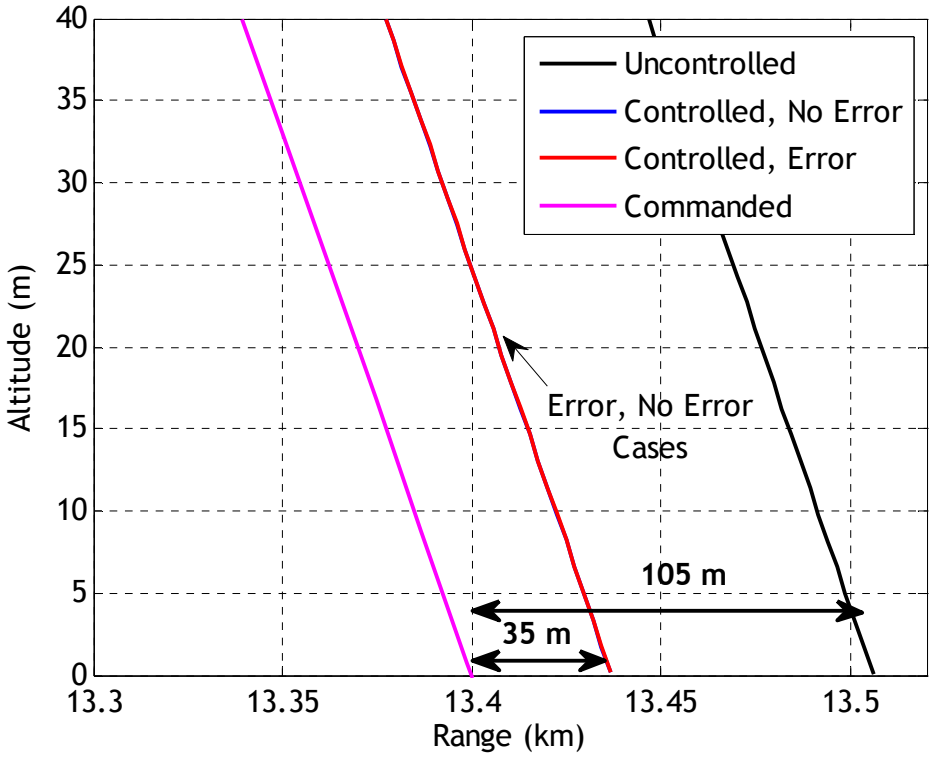

Figure 6.10: Zoom of Impact Area, Altitude vs Range, ITM Control Example Case.

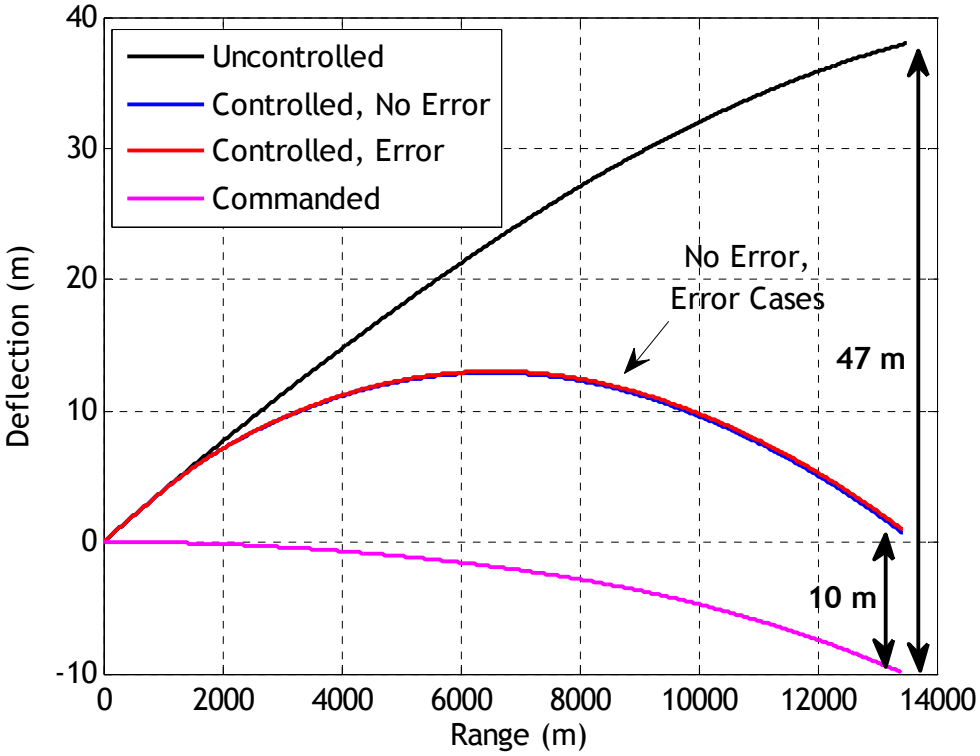

Figure 6.11: Deflection vs Range, ITM Control Example Case.

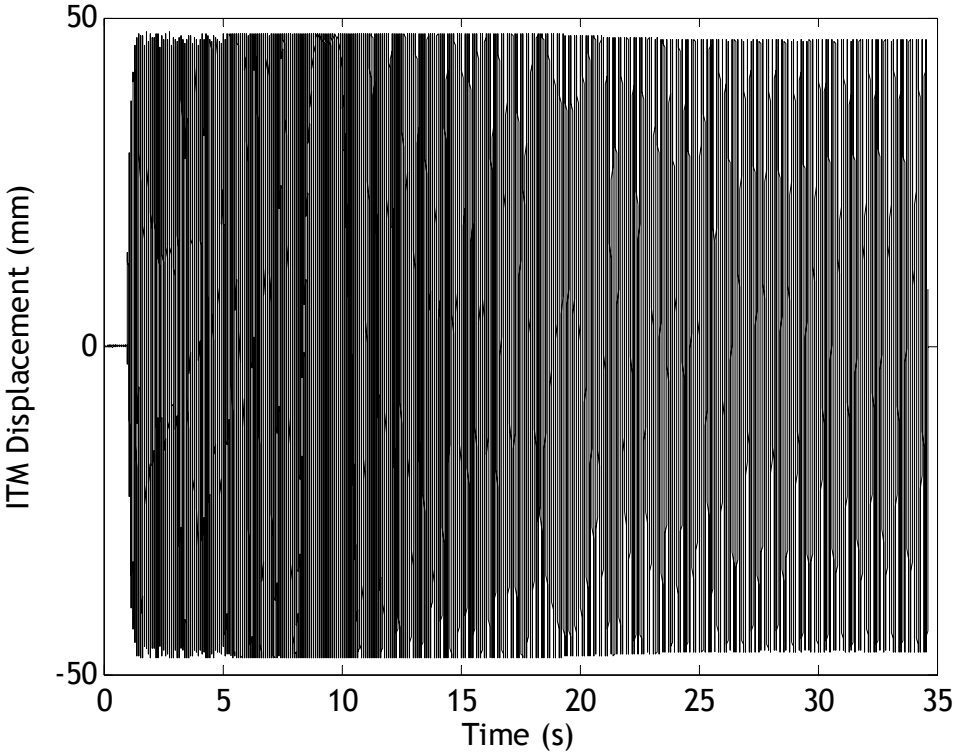

Figure 6.12: ITM Displacement vs Time, ITM Control Example Case.

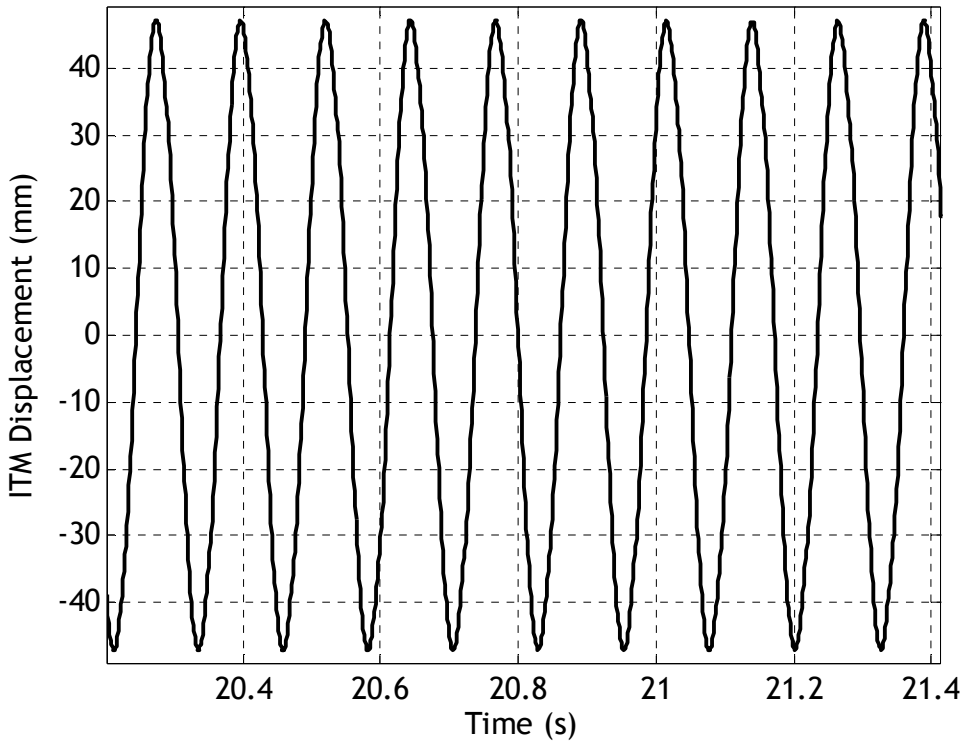

Figure 6.13: Zoom View of ITM Displacement vs Time, ITM Control Example Case.

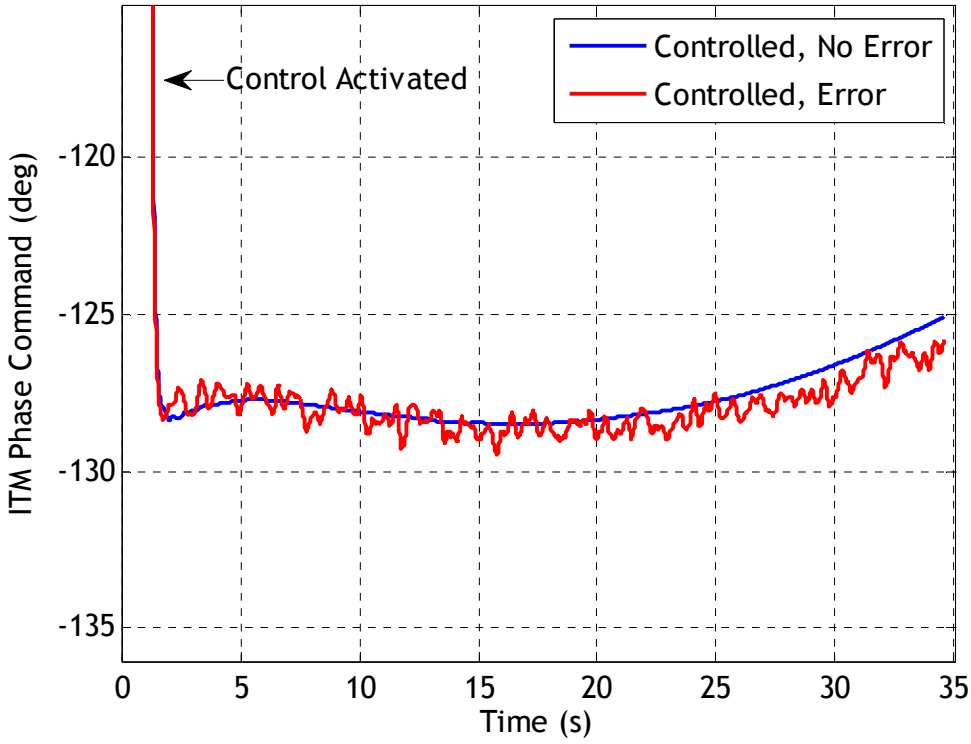

Figure 6.14: ITM Phase Command ϕ_T vs Time, ITM Control Example Case.

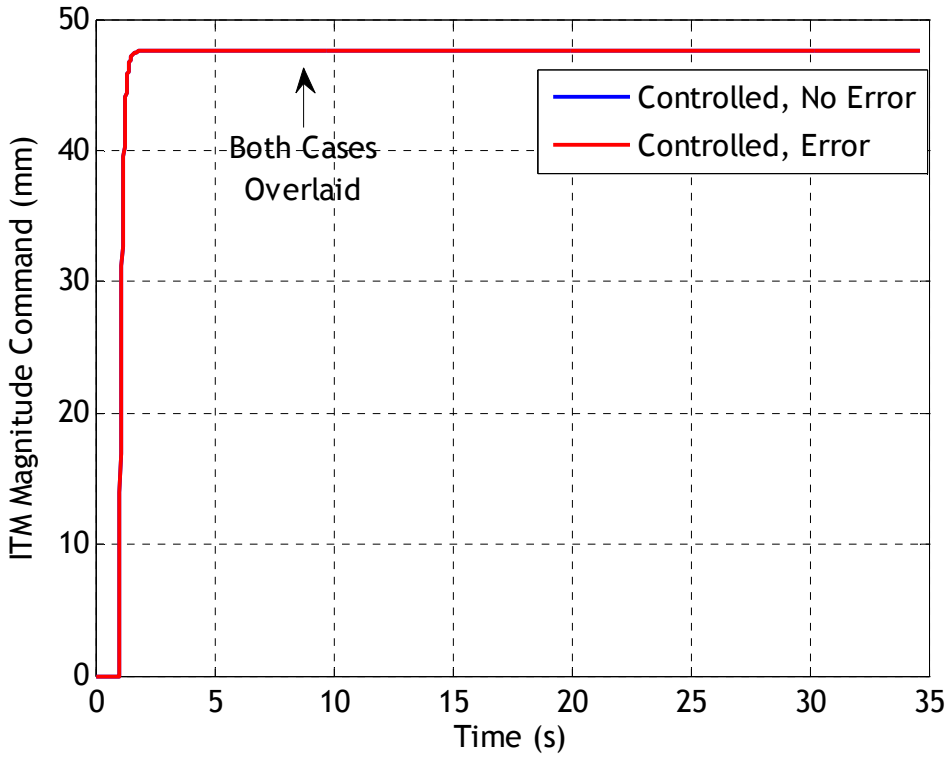

Figure 6.15: ITM Magnitude Command A_T vs Time, ITM Control Example Case.

Figures 6.9-6.16 show the results of the ITM control example case. Figures 6.9-6.11 demonstrate that the controlled impact points of both the uncertainty case and no uncertainty case lie approximately 78 m closer to the desired impact point than the perturbed ballistic trajectory impact point. Given that the range of these trajectories is approximately 13.5 km, this control authority corresponds to roughly 5 mils, which matches the control authority predictions for the same mass size in Chapter 3. Furthermore, note that the uncertainty case and no uncertainty case show nearly the same trajectory results. This is because, as seen in the magnitude command plot shown in Figure 6.15, the controller is saturated throughout the trajectory due to the mechanism's limited control authority. Furthermore, controller switching gains are set high enough that the sliding variable does not change sign due to uncertain feedback parameters, as shown in the second plot in Figure 6.16. Finally, Figure 6.14 demonstrates that the

commanded ITM phase angle is relatively steady between -125 and -130 degrees throughout the trajectory, since the direction of desired control in the no-roll frame remains fairly constant. Also note that, due to the limited nature of the mechanism's control capabilities, the sliding variables shown in Figure 6.16 never achieve zero. State time histories for body states not shown for this example case are similar to those shown in Chapter 3 and are omitted here for brevity. Finally, note from Figures 6.12 and 6.13 that the PD controller is very effective at oscillating the ITM according to the sinusoidal command.

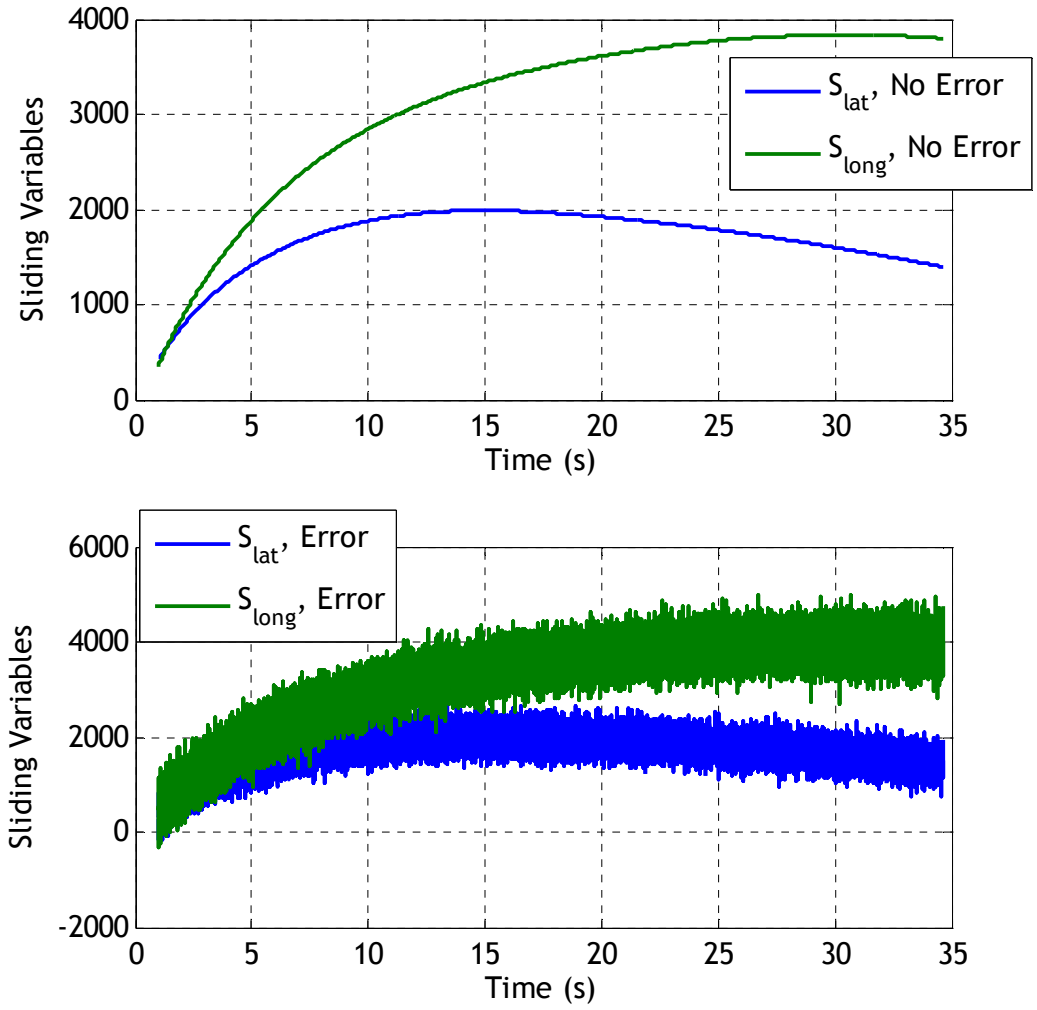

Figure 6.16: Sliding Variables vs Time, ITM Control Example Case.

Dispersion simulations of the ITM-controlled round are also performed in order to fully evaluate system performance in the presence of launch errors, plant uncertainty, sensor errors, and atmospheric winds. Several mass sizes ranging from 1% to 5% of total system mass are used in order to demonstrate that greater control authority is generated with heavier internal masses. Each dispersion simulation consists of 200 Monte Carlo simulations run with a specific mass size. Initial conditions and standard deviations used in generating dispersion results are shown in Table 6.5. Wind azimuth is a uniform random variable between 0 and 360 deg. Control parameters are similar to those given in Table 6.4 (which utilized a 4% mass), although minor tuning of the control system gains was required for different mass sizes to achieve optimum performance.

Table 6.5. Initial Conditions and Error Budget Parameters.

	Initial Cond.	**Standard Dev.**
***x* (m)**	0.0	0.0
***y* (m)**	0.0	0.0
***z* (m)**	0.0	0.0
ϕ (rad)	0.0	0.0
θ (rad)	0.30	0.0005
ψ (rad)	0.0	0.00025
***u* (m/s)**	860.0	4.57
***v* (m/s)**	0.0	1.52
***w* (m/s)**	0.0	1.52
***p* (rad/s)**	0.0	2.0
***q* (rad/s)**	0.0	1.7
***r* (rad/s)**	0.0	1.7
Wind (m/s)	0.0	3.16

Circular error probable as defined in Chapter 4 is the metric used to evaluate control system performance in this case. Feedback uncertainty is incorporated in all Monte Carlo

simulations using the error parameters outlined in Table 6.3. Also, total system mass is kept constant as ITM mass percentage changes.

In addition to examining control performance of the standard ITM-equipped round described in Chapter 3 (called "Nominal Stability"), dispersion simulations also evaluate control performance of an ITM-equipped round incorporating a variable stability mechanism as discussed in Chapter 4 (called "Variable Stability"). In order to simulate the variable stability mechanism, a one-time mass center shift of 3.11 cm is performed shortly after launch in the same manner as described in Chapter 4. This mass center shift was performed using a first-order lag in order to increase model fidelity.

Figures 6.17-6.21 show dispersion simulation results. Figure 6.17 shows example dispersion results for the ballistic and the variable stability-equipped ITM projectile using a 5% internal mass (0.91 kg). For this example case, ballistic CEP is 107 m and controlled CEP is 66 m.

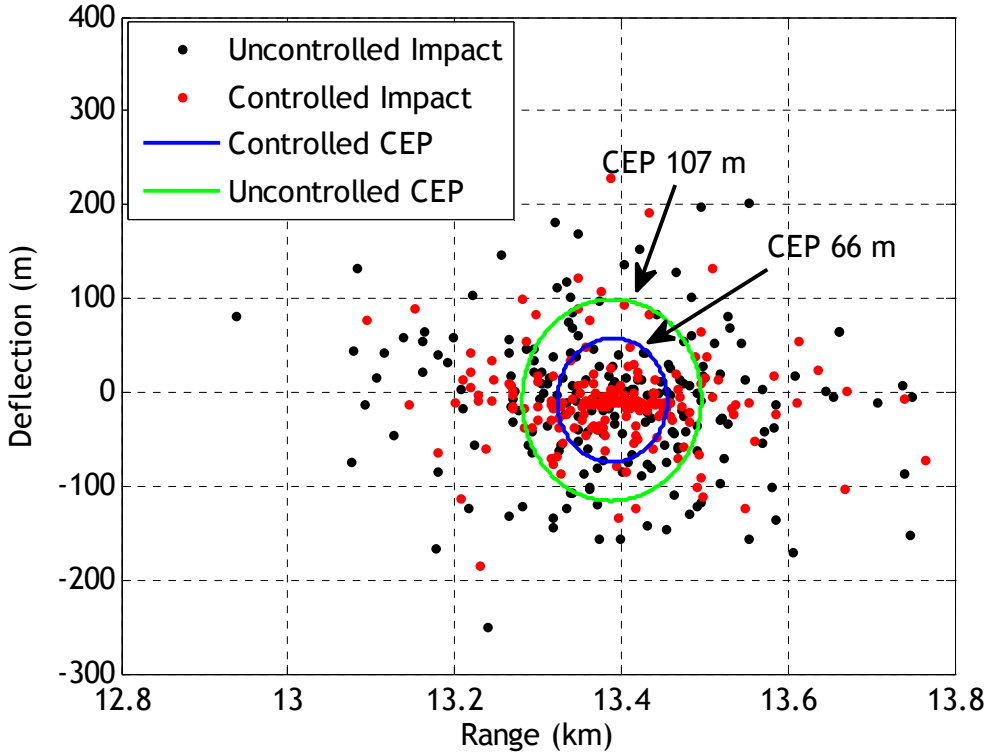

Figure 6.17: Dispersion Simulation for Ballistic and 5% ITM Variable Stability Projectile.

Figures 6.18-6.21 show the results of all dispersion simulations. In all figures, 0% ITM represents the ballistic case. First, note that as expected controlled CEP decreases as ITM percentage increases as a result of increased control authority. A maximum decrease of almost 40% in CEP is achievable using a 5% ITM as demonstrated in Figure 6.19. Figures 6.20 and 6.21 show that mean range and deflection impact points do not change significantly compared to the ballistic case, demonstrating that the control system does not introduce any undesired bias errors in the trajectory. Slight deviations in mean impact points occur due to the use of slightly different controller gains for each mass size. Finally, note that incorporation of the variable stability mechanism results in a 5-10 m reduction in CEP for all mass percentages.

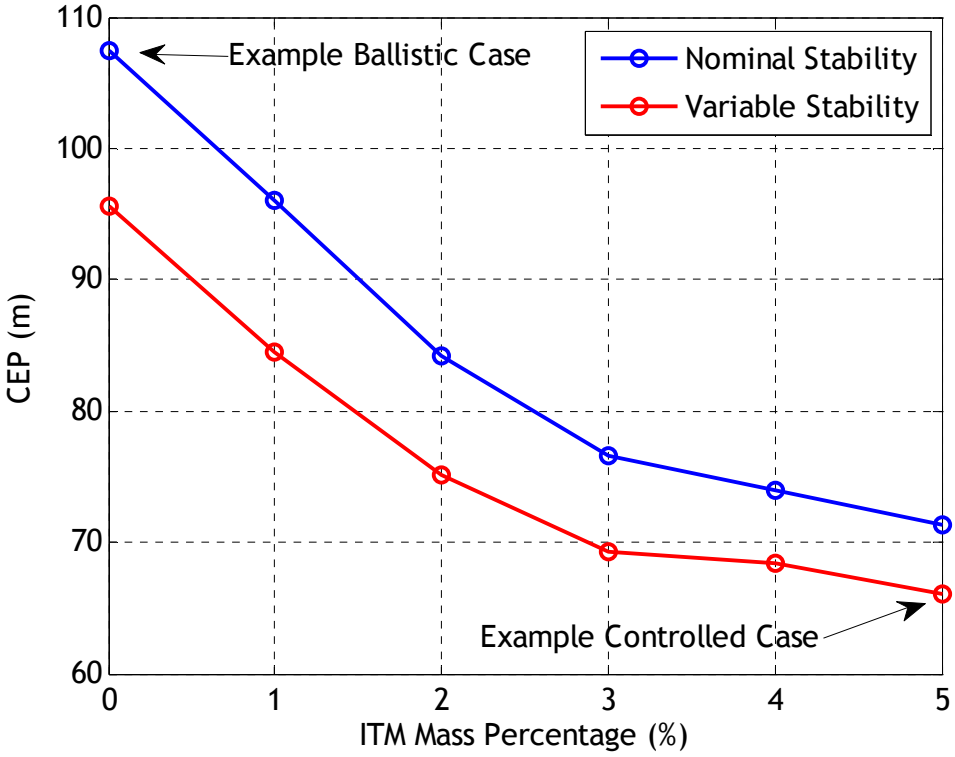

Figure 6.18: CEP vs ITM Mass Percentage.

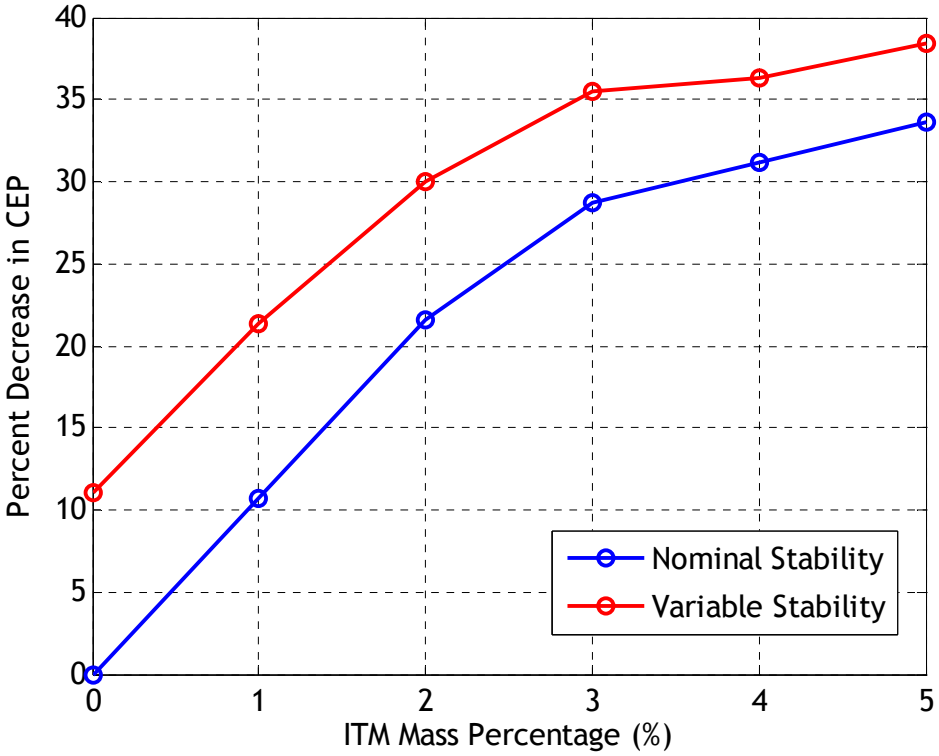

Figure 6.19: Percent Decrease in CEP vs ITM Mass Percentage.

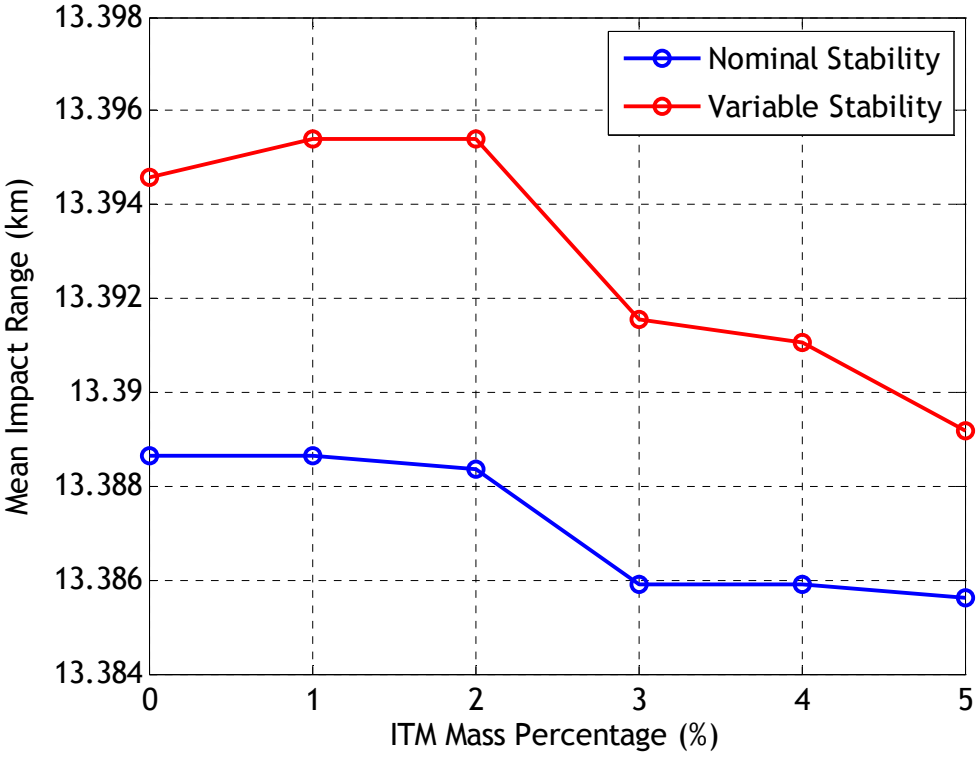

Figure 6.20: Mean Impact Range vs ITM Mass Percentage.

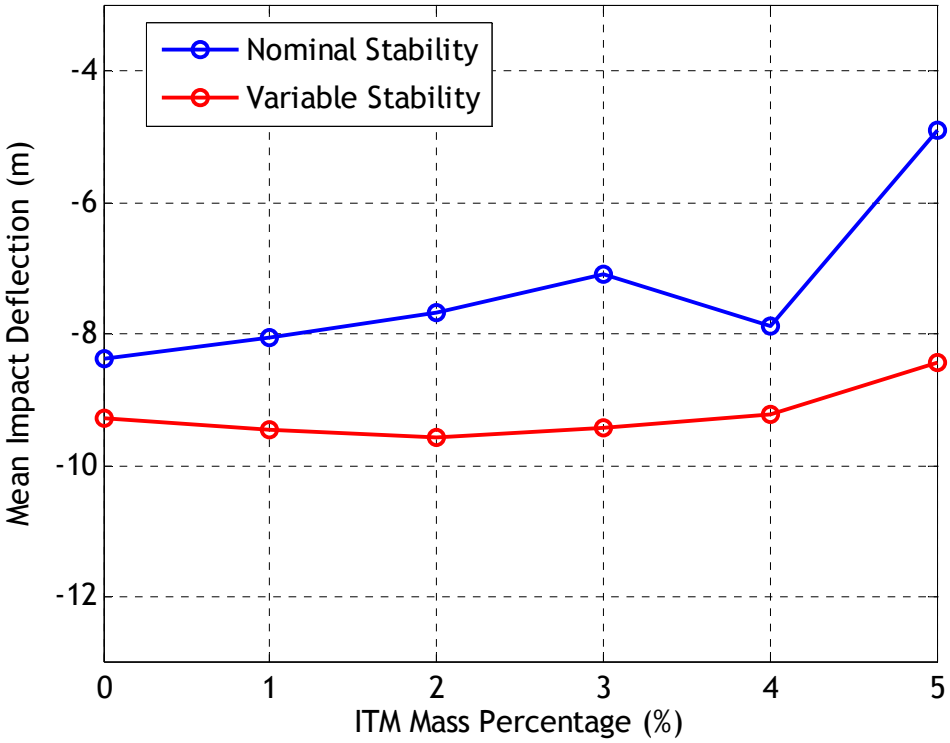

Figure 6.21: Mean Impact Deflection vs ITM Mass Percentage.

Again, Figures 6.18 and 6.19 serve to demonstrate the limited control authority of the ITM mechanism. While canard mechanisms are typically effective at reducing dispersion to the level of sensor error, the ITM mechanism lacks the control authority needed for such precision. However, as discussed previously in Chapter 1, some smart weapons applications require that the "area" nature of the weapon be maintained. In such cases, the ITM mechanism provides a means to reduce dispersion error (while not eliminating it) using a mechanism that is completely internal to the projectile. The internal nature of the ITM actuator is beneficial in that it minimizes the potential of damage during transport, and more importantly provides increased immunity to very harsh launch environments.

Another interesting feature of the dispersion results shown in Figures 6.18 and 6.19 is the diminishing payoff as ITM size increases, characterized by the decrease in the slopes of the plots as mass percentage increases. One might expect decrease in CEP per unit mass size to remain relatively constant. However, numerous example cases with larger mass sizes showed a consistent problem in overshoot resulting from large control authority at the beginning of the trajectory and severely limited control authority during the latter portions (this change in control authority throughout the trajectory was discussed in depth at the beginning of Section 6.3.5). Just after launch, the ITM control mechanism can exert significant control forces. In some trajectories, these large control inputs lead to overshoot which cannot be effectively damped later in the trajectory once control authority diminishes. Extensive tuning of controller gains was not able to substantially mitigate this overshoot tendency. This unique characteristic of ITM control leads to the conclusion that Model Predictive Control (MPC) algorithms, [64] which can account for variations in control authority as flight progresses, would be highly effective in reducing dispersion error for larger mass sizes. The potential use of MPC control laws for ITM systems is discussed in more detail in Chapter 7.

6.3.6 ITM-Canard Combined Control

Another use of internal translating mass control arises as a form of supplemental control in munitions equipped with maneuver canards. Projectiles that utilize canards for control suffer from aerodynamic drag penalties whenever these canards are deployed, and therefore often restrict control inputs to post-apogee portions of the trajectory. However, it is still desirable to provide limited control before apogee, since control during initial portions of the trajectory substantially reduces error encountered in terminal portions due to the integrated effect of many throw-off and wind errors. To this end, a control mechanism is designed combining the internal translating mass and maneuver canards. Shortly after launch, ITM control is applied to the projectile while canards remain stowed. At apogee, ITM motion ceases, canards are deployed, and a clutch mechanism links the ITM and canards. The translating mass and canards are configured such that control due to ITM movement and control due to canard deflection are in the same direction. Thereafter, ITM movement drives canard motion and the two mechanisms provide control in unison. The resulting projectile takes advantage of small, limited control inputs exerted by the ITM on the ascending portion of the trajectory with minimal drag penalties, and is able to correct any remaining errors during post-apogee portions of flight using combined ITM-canard control. A drawing of a projectile equipped with the combined ITM-canard control mechanism is shown in Figure 6.22, and a zoom view of the actuator is shown in Figure 6.23. Both drawing show the canards deployed and linked to the ITM. A diagram of applied control forces is shown in Figure 6.24.

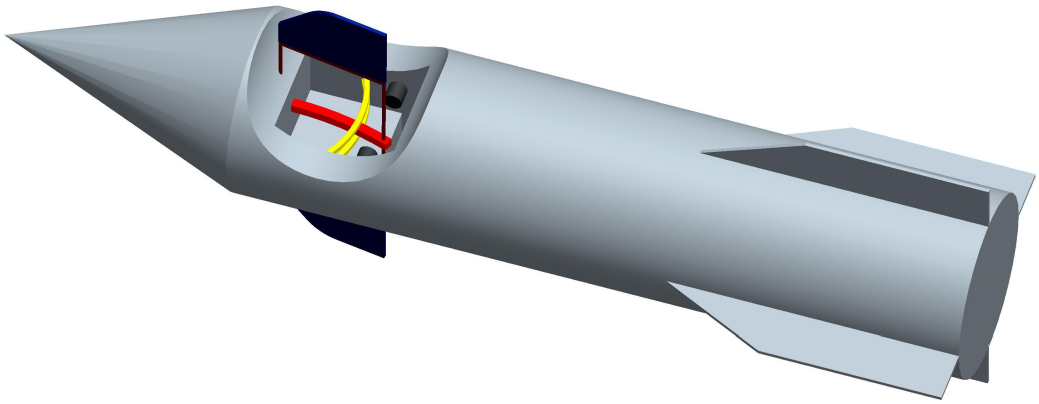

Figure 6.22: The Combined ITM-Canard Controlled Projectile.

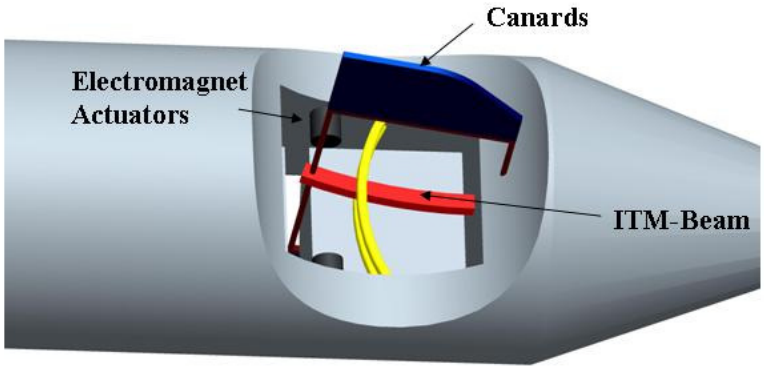

Figure 6.23: Zoom View of Combined ITM-Canard Actuator.

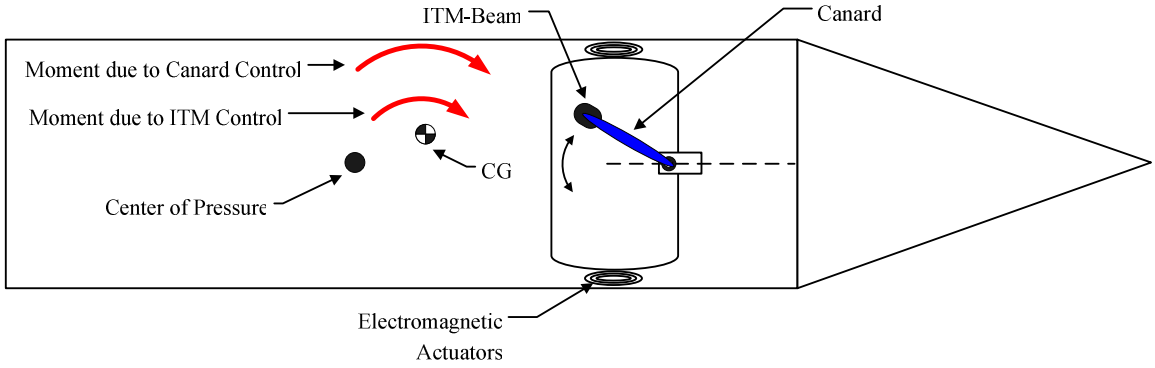

Figure 6.24: Top View and Control Moment Schematic of ITM-Canard Combined Control.

An example case of combined ITM-Canard control is shown to demonstrate both control system operation and the benefits of using this hybrid mechanism. The combined actuator is applied to the fin-stabilized example projectile used throughout this chapter and described in Chapter 3, and the methodology behind this example case is similar to that used in Section 6.3.5. A ballistic simulation using unperturbed initial conditions (called "Commanded") is used as the command trajectory. Using perturbed initial conditions, another ballistic simulation (called "Uncontrolled") is run for comparison. Two controlled cases are simulated. The first, called "Strict Post-Apogee", uses no ITM control during the ascending portion of flight and applies control using the combined mechanism only after apogee. The second controlled case, called "Preliminary ITM", uses internal mass control only during the ascending portion and combined control during post-apogee flight. Canard parameters, ITM parameters, and control system gains are described in Table 6.6. Initial conditions are identical to those used for the example case in Section 6.3.5 and are given in Table 6.4. Also, all controlled simulations incorporate feedback uncertainty, with error parameters identical to those used in Section 6.3.5 and shown in Table 6.3.

Table 6.6: Canard, ITM, and Control System Parameters for Example Simulation.

Canard Parameters	Canard Stationline Total Canard Area Maximum Canard Deflection	41.15 cm 11.15 cm^2 8 deg
ITM and Control Parameters	m_T (kg)	0.734
	$\alpha_{lat}, \alpha_{long}$	370.0, 370.0
	$\lambda_\psi, \lambda_\theta$	25.0, 25.0
	λ_y, λ_z	90.0, 90.0
	w_y	1.0
	w_z	-1.0
	w_ψ, w_θ	0.1, 0.1
	x_L	15.24 m
	F_{LIM}	889.6 N
	τ_{phase}, τ_{mag}	0.069 s, 0.22 s

Figures 6.25-6.31 show the results of the example combined ITM-canard simulation. First, note that the controlled case that uses ITM control on the ascending portion of the trajectory ("Preliminary ITM") is very effective at reducing trajectory errors to the level of sensor error. While the other controlled case that uses control over the second half of the trajectory is effective at reducing miss distance, at apogee it has significantly more error to eliminate as compared to the Preliminary ITM case, shown clearly in Figure 6.27. Figures 6.29 and 6.30 demonstrate how ITM movement occurs during the Preliminary ITM controlled case, specifically how ITM oscillation pauses near apogee to allow the canard clutch to engage. Thereafter, canard movements and ITM oscillations are synchronized to take advantage of the control inputs from both mechanisms. Finally, note that one of the benefits of this model is that by incorporating ITM dynamics, the simulation realistically models the inertial dynamics of canard actuation, since it does not assume a "massless canard" as in many industry-standard codes.

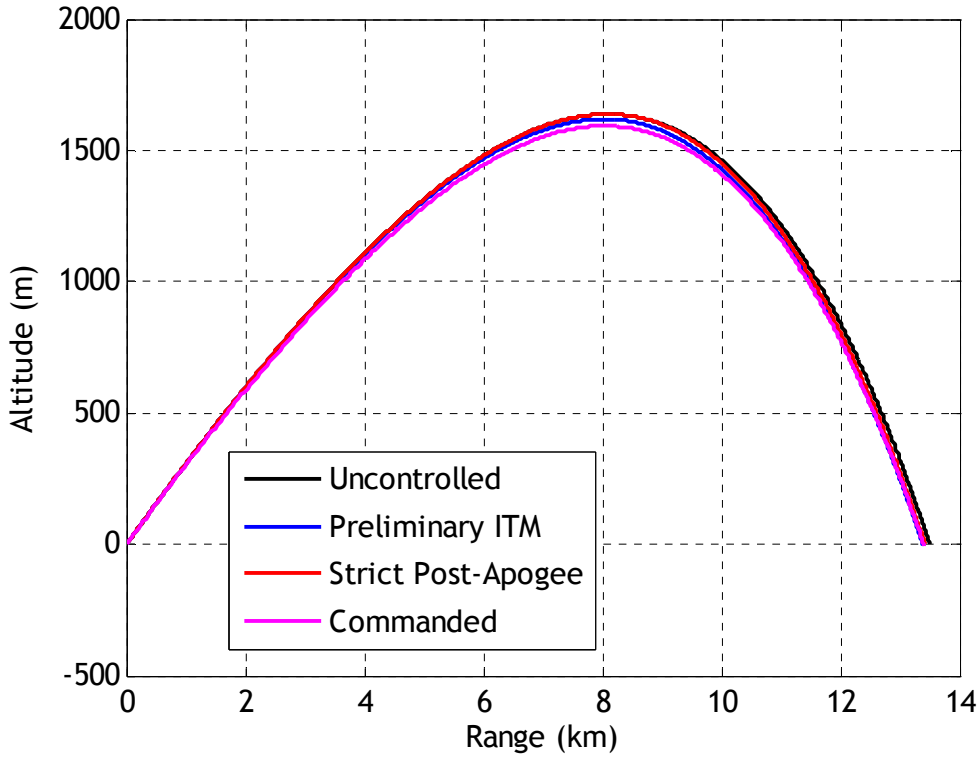

Figure 6.25: Altitude vs Range, ITM-Canard Control Example Case.

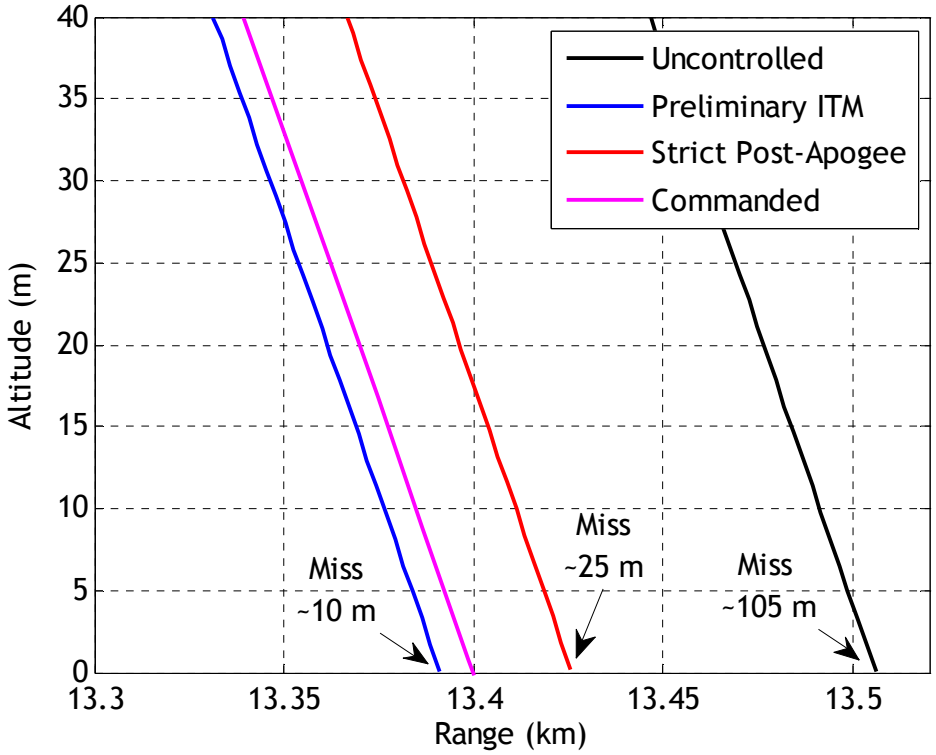

Figure 6.26: Zoom View of Target Area, ITM-Canard Control Example Case.

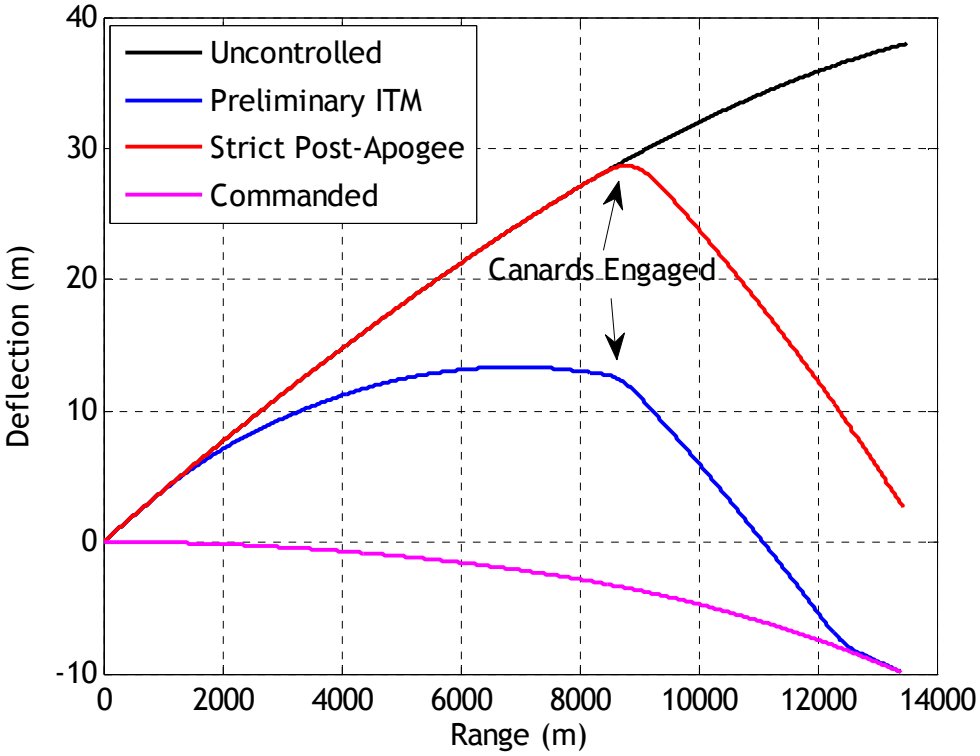

Figure 6.27: Deflection vs Range, ITM-Canard Control Example Case.

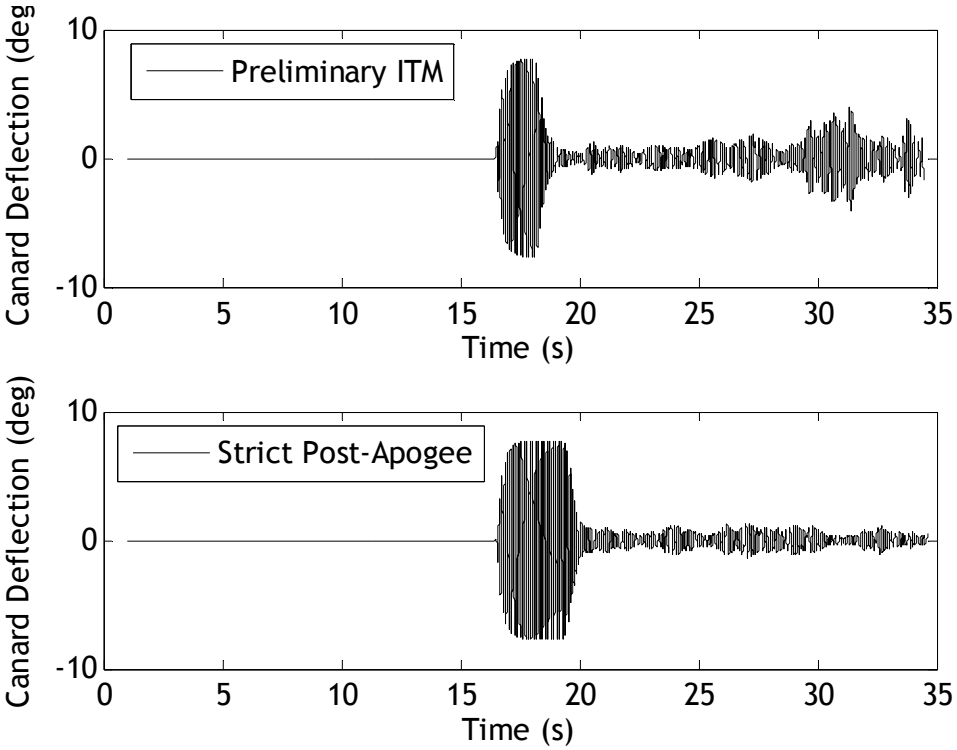

Figure 6.28: Canard Deflection vs Time for Controlled Cases.

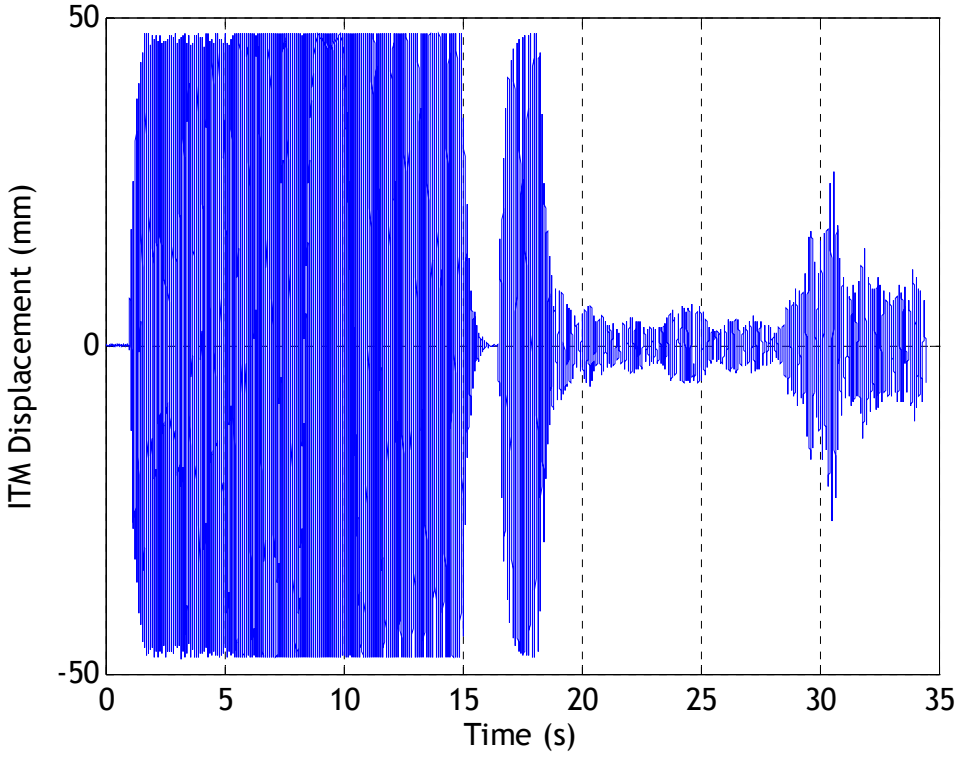

Figure 6.29: ITM Displacement vs Time for Preliminary ITM Control Case.

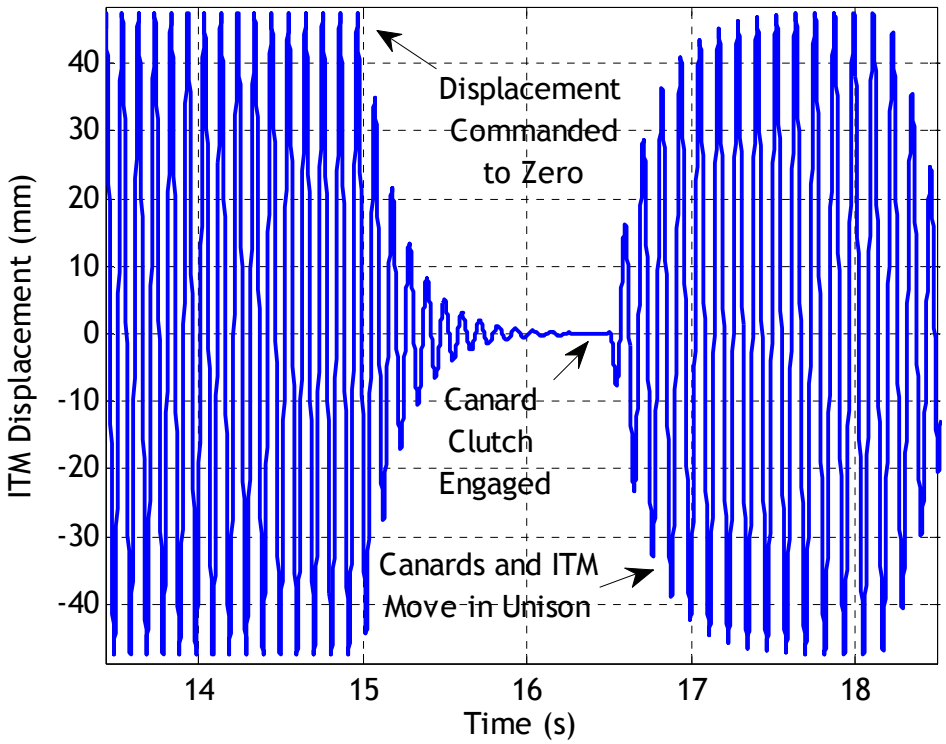

Figure 6.30: Zoom of ITM Displacement vs Time for Preliminary ITM Control Case.

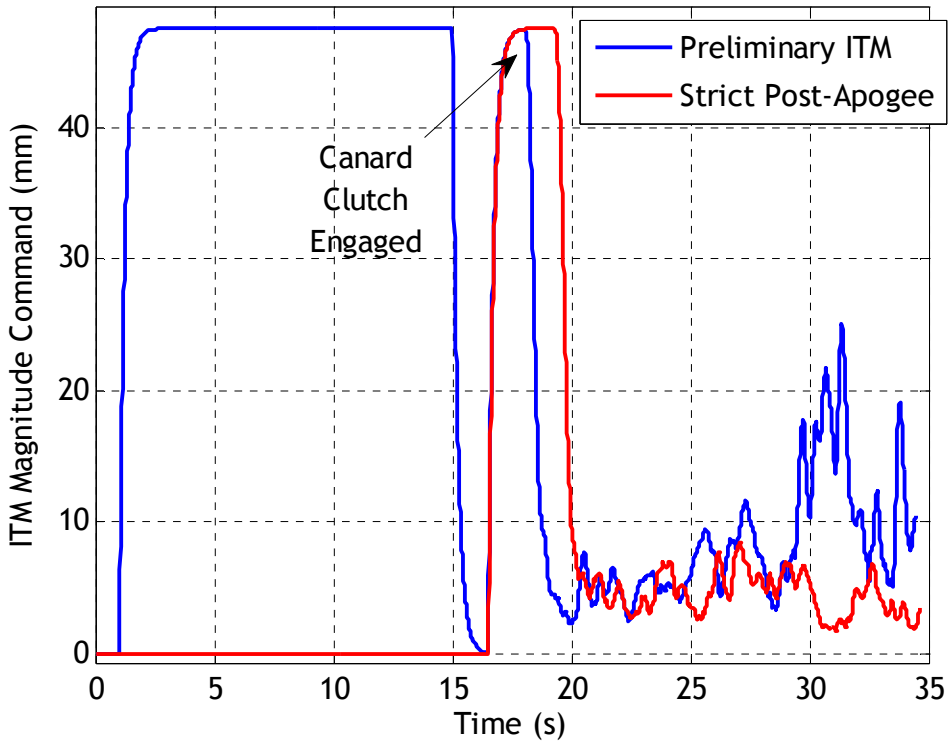

Figure 6.31: ITM Magnitude Command vs Time for Controlled Cases.

Dispersion simulations were run with the ITM-Canard combined actuator in order to examine the overall performance benefit of using the combined mechanism in the face of launch and sensor errors, model uncertainty, and atmospheric winds. This analysis was accomplished as follows. First, dispersion simulations were performed for various ITM mass percentages and terminated at apogee, yielding vertical plane dispersions that could be compared to a ballistic dispersion simulation. Then, CEP's were calculated for all cases, demonstrating that a vertical plane CEP reduction at apogee in excess of 50% is achievable with a 5% ITM. Then, each dispersion simulation is continued to ground impact to obtain impact point CEP's. These impact point dispersion simulations were repeated for several different canard sizes, demonstrating that use of larger ITM sizes allows for canard size reductions in order to achieve a certain CEP. All dispersion simulations incorporate feedback uncertainty as described in Table 6.3, and initial

condition errors and wind parameters are identical to those used in Section 6.3.5, shown in Table 6.5. Controller parameters are outlined in Table 6.7.

Table 6.7: Controller Parameters for Combined ITM-Canard Dispersion Simulations.

$\alpha_{lat}, \alpha_{long}$	370.0, 370.0
$\lambda_{\psi}, \lambda_{\theta}$	5.0, 5.0
λ_{y}, λ_{z}	40.0, 40.0
w_{y}	1.0
w_{z}	-1.0
w_{ψ}, w_{θ}	0.1, 0.1
x_{L}	15.24 m
F_{LIM}	889.6 N
τ_{phase}, τ_{mag}	0.069 s, 0.11 s

Figure 6.32 shows the results of the ballistic and 5% ITM vertical dispersion simulations to demonstrate an example of vertical-plane dispersion results, while Figures 6.33 and 6.34 show vertical-plane CEP and percent decrease in CEP as a function of ITM size respectively. Note that ballistic CEP was 34.5 m and controlled CEP for the 5% ITM case was 16.0 m, a decrease of over 50%. Also keep in mind that all vertical-plane dispersion results are considered at the apogee of flight, and that only ITM control is used to this point as described earlier. For all dispersion simulations in this section, cases using a "0% ITM" mean that no ITM control is used in the ascending portion of flight. Figures 6.33 and 6.34 demonstrate the steady and considerable decrease in vertical-plane dispersion using ITM control on the ascending portion of the trajectory. In fact, for mass sizes on the order of 5%, vertical-plane CEP approaches the level of sensor errors.

With the knowledge that use of ITM control during initial portions of the trajectory can significantly increase error at apogee, the goal is to determine possible canard area reductions as a function of internal mass size.

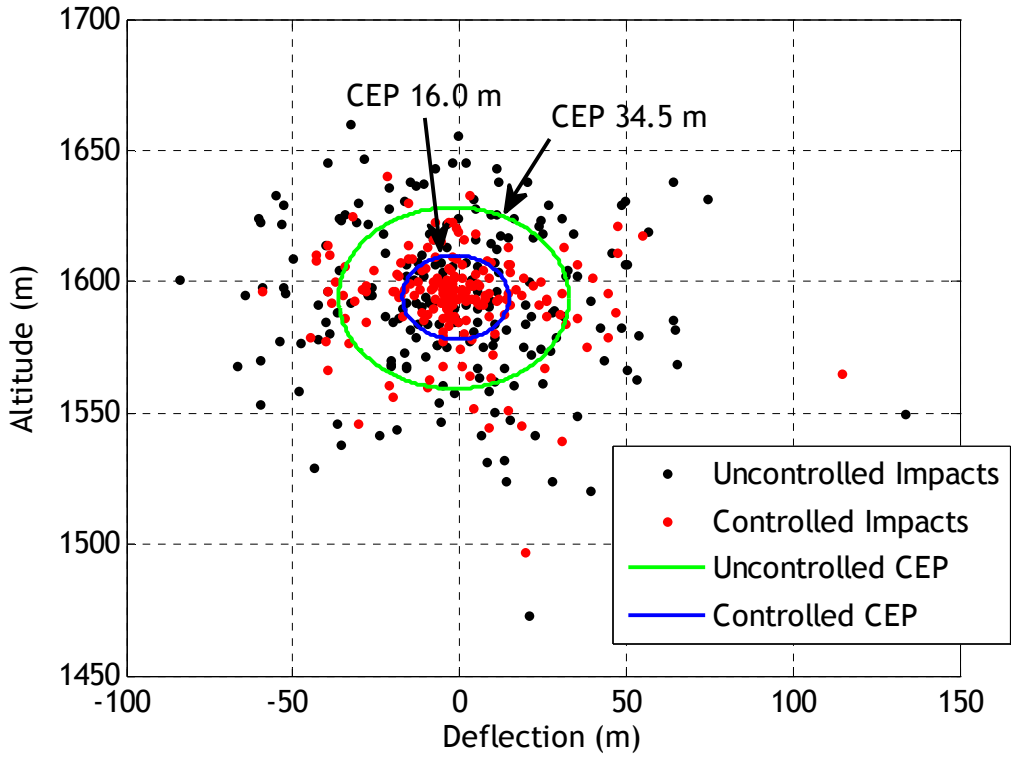

Figure 6.32: Vertical-Plane Dispersion at Apogee for Ballistic and 5% ITM Case.

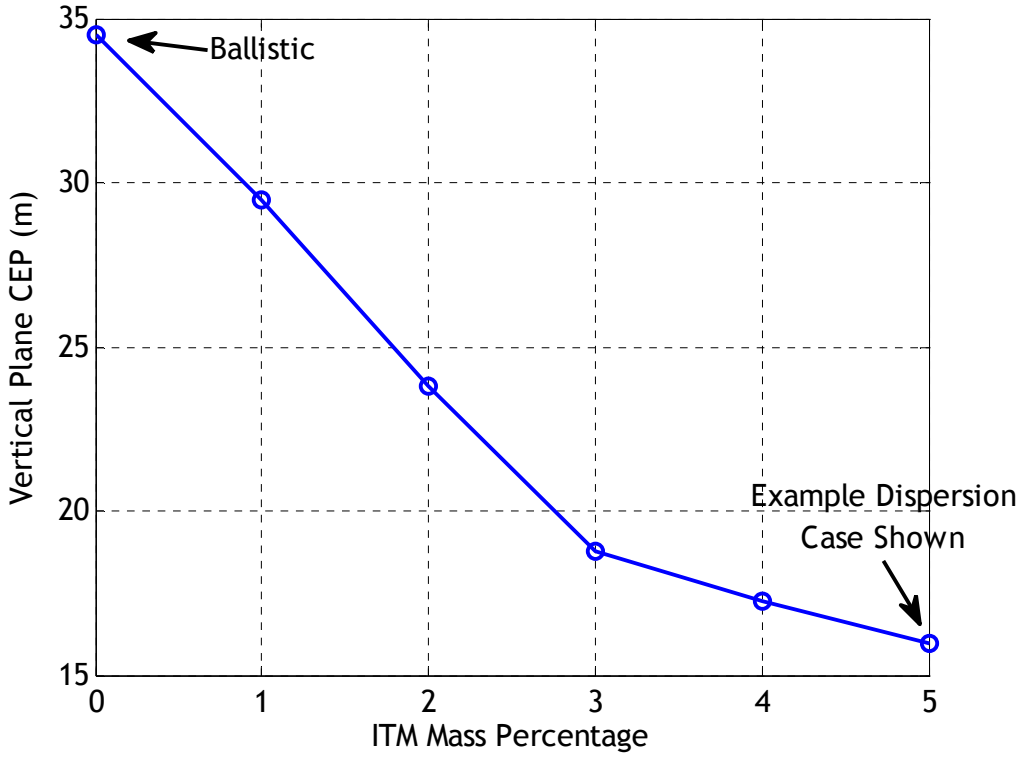

Figure 6.33: Vertical-Plane CEP vs ITM Mass Percentage.

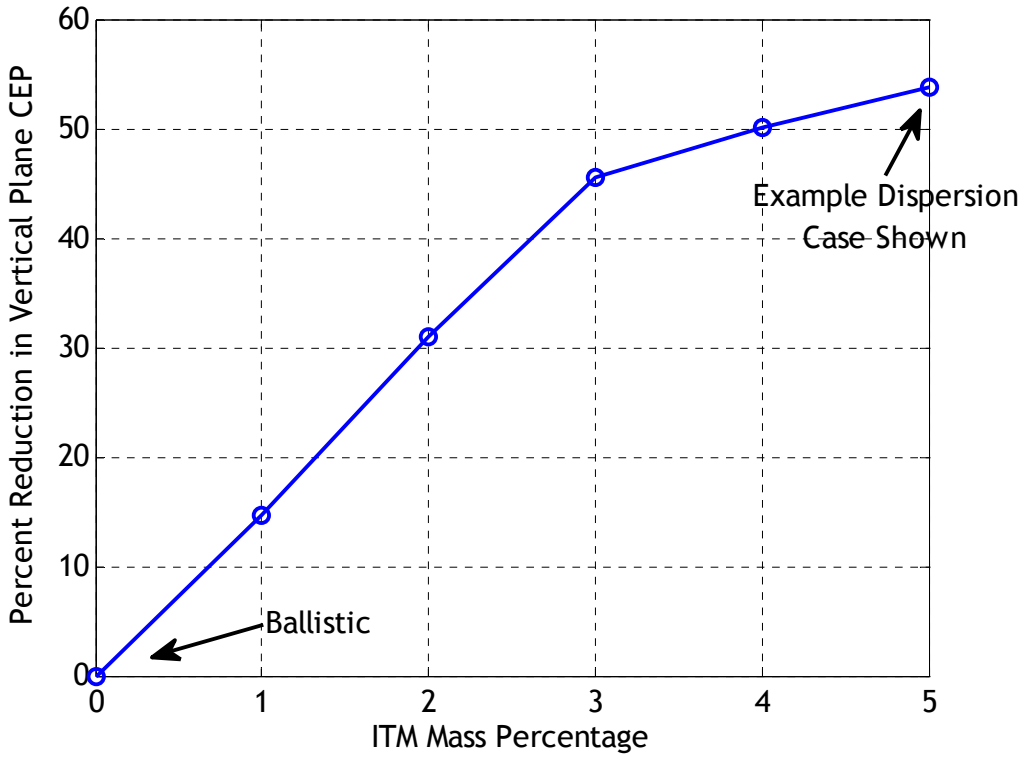

Figure 6.34: Percent Reduction in Vertical Plane CEP vs ITM Mass Percentage.

Therefore, assume that the goal is to obtain a 10 m controlled CEP with a canard stationline position of 41.15 cm and a maximum deflection angle of 8 deg. To examine required canard areas, each dispersion simulation corresponding to an ITM size was continued to ground impact. Furthermore, this process was repeated for various canard sizes, and controlled CEP's were determined. These controlled CEP's represent circular error probable for ITM-canard control along the entire trajectory as described above for an array of mass sizes and canard areas. Figure 6.35 shows CEP for various mass sizes and canard areas. Note that in this figure, "No ITM" denotes no ITM control along the ascending portion of the trajectory. It is clear that as canard size increases, CEP is reduced to the level of sensor errors. In addition, as ITM size is increased, less canard control is needed during the terminal portion of the trajectory, resulting in smaller canards required to achieve a given CEP.

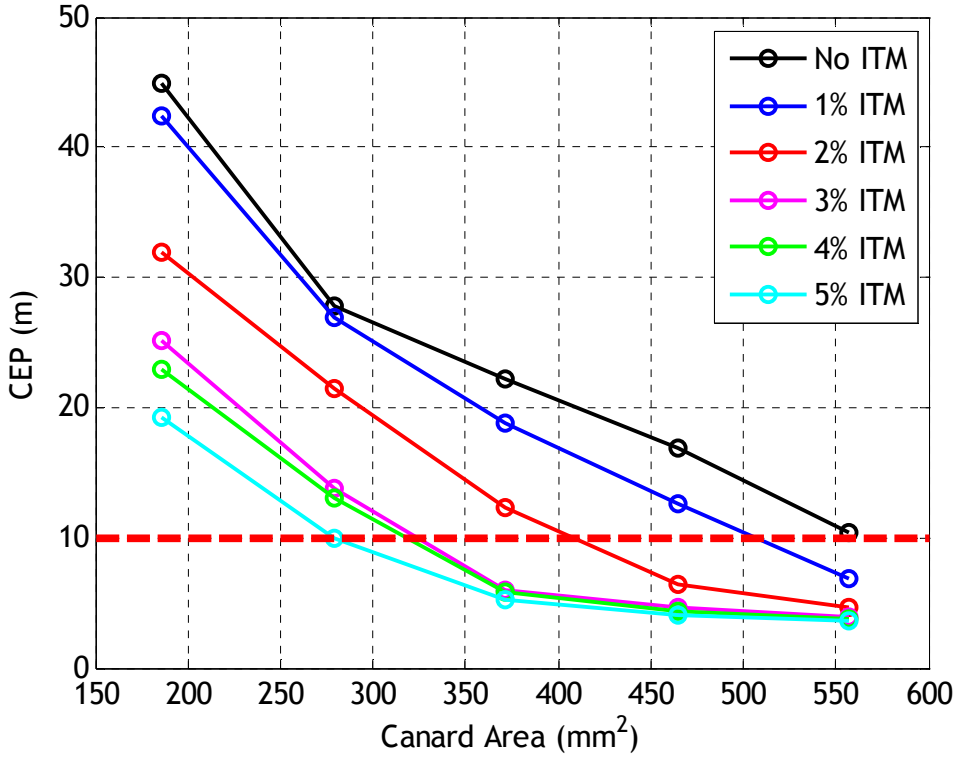

Figure 6.35: CEP vs Canard Area for Combined ITM-Canard Control.

Specifically, the canard area required to achieve a 10 m controlled CEP can be obtained by interpolating the data shown in Figure 6.35 along each ITM curve, yielding a specific canard size required for each translating mass size. Figure 6.36 shows the estimated required canard area to achieve a 10 m CEP as a function of ITM size, while Figure 6.37 shows the percent decrease of this canard size over the size needed to achieve 10 m CEP with no ITM control (i.e., the right-most point on the black curve in Figure 6.35). As expected, as ITM size increases, error at apogee is significantly reduced and smaller canards are needed to eliminate error. Clearly, significant reductions in canard area are possible as ITM size grows larger, resulting in approximately half the area required using a 5% ITM to achieve 10 m CEP.

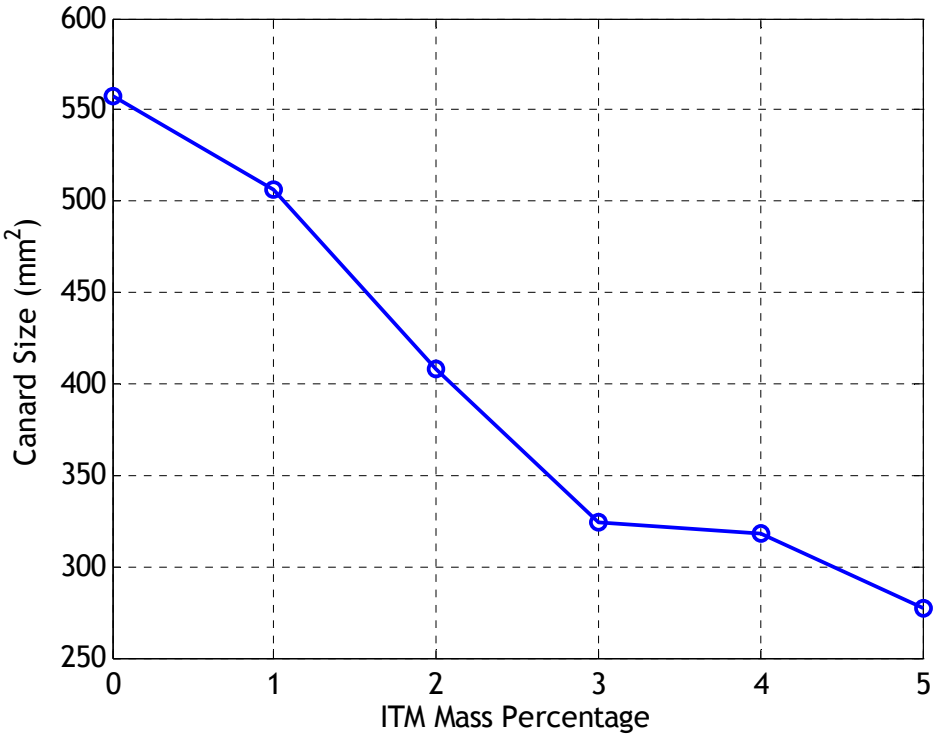

Figure 6.36: Canard Size Needed to Achieve 10 m CEP vs ITM Mass Percentage.

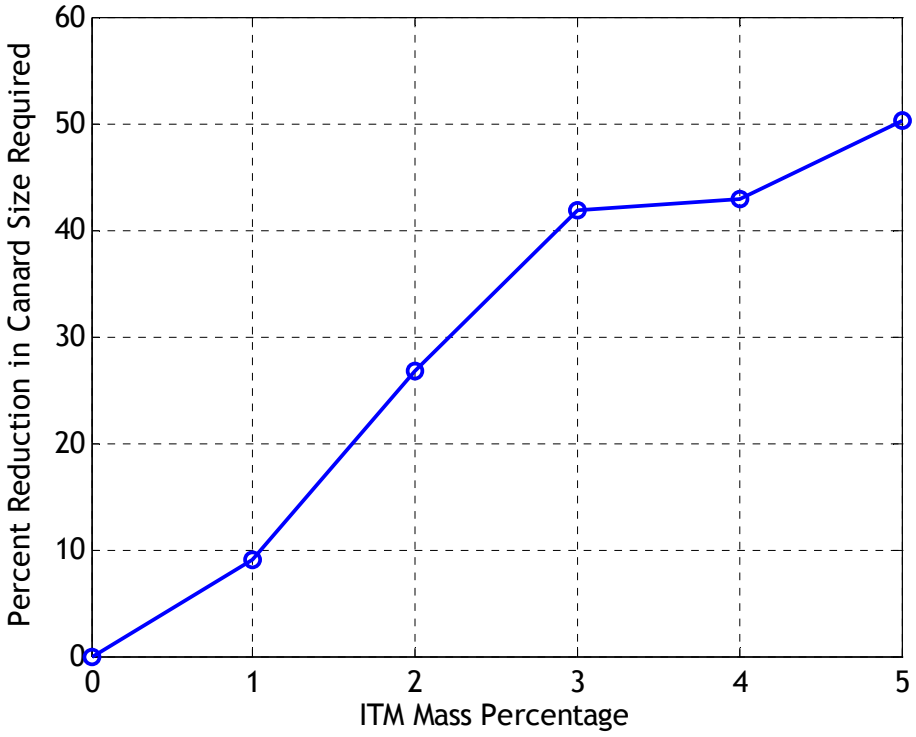

Figure 6.37: Percent Reduction in Canard Size Required as Compared to No ITM Control Case vs ITM Mass Percentage.

6.4 Conclusion

This chapter described the use of an internal translating mass in a projectile active control system. Specifically, a novel sliding mode control law was introduced and developed to provide an integrated guidance law driving ITM motion. While numerous types of control laws could have been used, sliding mode was chosen due to its robust characteristics and its effectiveness in controlling highly nonlinear systems. Then, control system performance was demonstrated using a canard-controlled projectile, validating the control law and establishing the need for both translational and rotational components of control. The control law applied to the ITM-Beam projectile showed that while control authority constraints limit trajectory correction capability with the ITM system, reasonable reductions in CEP can be achieved. However, unlike canard and thruster actuator systems, ITM systems achieve these reductions using a mechanism completely internal to the projectile. This characteristic serves to both increase transport and launch survivability and reduce the impact on gun design.

This chapter also explored the use of combined ITM-canard control actuators. Many current canard-actuated systems have some sort of translating part incorporated in the mechanism. For instance, canard deflection angle may be driven by the translation of a magnet inside a voice coil. Oftentimes, however, orientation and placement of this translating component is driven by space and simplicity considerations. This research showed that significant benefit can be obtained by configuring the translating component such that the control moment from the translating mass supplements canard control. Furthermore, use of the translating component detached from the canards during initial portions of flight can significantly reduce the dispersion error that must be eliminated by canards during terminal portions of flight.

CHAPTER 7

CONCLUSIONS AND FUTURE WORK

7.1 Conclusions

This dissertation explored the use of internal translating mass mechanisms for smart projectile flight control purposes. While several different technologies were considered in each of the five previous chapters, each fell into one of three categories. Chapters 2, 3, and 6 considered the use of internal moving masses as a direct control mechanism for a smart weapon. Chapter 4 explored the use of an internal moving mass as a supplemental mechanism that enhances overall control authority and increases the effectiveness of existing control mechanisms. Chapter 5 proposed the use of an internal moving mass as a shock absorbing device intended to isolate sensitive electronics from harsh launch environments.

The preliminary step that enabled each of these analyses was the development of the internal translating mass projectile equations of motion, as described in Chapter 2. A flight simulation was built using the resulting dynamic equations, and used to predict trajectory alteration capability by translating the mass laterally within the projectile at a frequency equal to the projectile spin frequency. Control moment was shown to be created by a lateral mass center offset. Example cases and trade studies showed that the mechanism generates reasonable but limited control authority using realistic mass sizes, and that control authority increases with mass size and oscillation amplitude, but is insensitive to cavity location along the stationline of the projectile. Further increases in control authority can be achieved with reduced projectile static stability.

In Chapter 3, a more realistic physical model of the ITM mechanism was designed (called the ITM-Beam) in order to minimize actuator force and power

requirements. The ITM-Beam consists of a flexible beam that oscillates laterally within the projectile due to an oscillatory magnetic field generated by electromagnets. ITM-Beam motion approximates internal translating mass motion for longer beam lengths. Equations of motion for this mechanism were developed, and flight simulation showed that for longer beam lengths, both the ITM-Beam and internal moving mass simulation produced nearly identical results. This correlation provided strong validation for both models. Using the new ITM-Beam dynamic simulation, force and power requirements for the ITM-Beam mechanism applied to a fin-stabilized projectile were analyzed. First, a trade study showed that longer beam lengths yield lower force and power requirements. Then, by varying beam spring and damper properties it was shown that an optimum resonance condition can be achieved that minimizes force and power requirements on the ITM actuator. Furthermore, it was shown that by actively optimizing beam vibrational properties during flight, further power reductions are possible. By integrating power requirements over a complete trajectory, it was shown that reasonable battery sizes and commercially-available electromagnetic actuators can be used to generate desired ITM-Beam motion.

Using the ITM-Beam simulation developed in Chapter 2, a sliding mode flight control law was developed to generate active control results. While many control designs could have been used, sliding mode control was chosen due to its ability to handle significant uncertainty in highly nonlinear systems. First, the control law was developed and validated using a canard-actuated fin-stabilized projectile. Then, example results were generated using a projectile equipped with the ITM-Beam control mechanism that incorporated model uncertainty and sensor error, establishing that the control law coupled with the ITM-Beam actuator can reduce impact error significantly. These results further demonstrated the control law's robustness to all types of feedback uncertainty. Dispersion simulations showed that as mass size increases, dispersion error generally decreases due to the increasing effectiveness of the ITM actuator. However, it was also

noted that control effectiveness decreases significantly throughout the trajectory due to stability and drag considerations, causing overshoot problems when ITM control is applied shortly after launch. For this reason, Model Predictive Control is proposed as a future alternative control law as described later in this chapter.

Another control scheme outlined in Chapter 6 uses ITM control to generate minor trajectory adjustments during the initial portion of flight, reducing errors before they propagate beyond the control system's corrective capabilities. Then, after apogee, internal mass control combined with canard control is used to generate large trajectory corrections. This "combined control" scheme takes advantage of all portions of flight to apply trajectory corrections while avoiding the drag penalties inherent in canard deployment early in flight. An example case demonstrated this concept, while dispersion simulations showed that by using ITM control during the initial portion of flight, the canard area required to achieve a specific controlled CEP can be reduced considerably. Smaller canards prove beneficial to designers in that they reduce space requirements, power requirements, and most importantly drag penalties. Furthermore, most canard-controlled smart weapons incorporate some manner of translating mechanism to generate canard deflection angle modulation at the projectile roll rate. This research shows that if the translating mechanism can be oriented properly and operate while disengaged from the canards, it can be used to generate control independently and reduce the burden on canard control later in flight.

In addition to the use of an internal translating mass as a direct control mechanism, use of an ITM as a supplemental device to increase control efficiency was also explored. This was accomplished in Chapter 4 by investigating the use of an ITM to actively alter projectile static stability in flight. After describing the well-known correlations between projectile static stability, dispersion error, and control authority, the concept of the variable stability mechanism was introduced. The mechanism consists of a mass that translates along the projectile's axis of symmetry during flight. The specific

concept considered here was a one-time static margin decrease shortly after launch. This one-time shift results in a projectile that is less susceptible to throw-off error at launch and more maneuverable during controlled portions of flight. An example case and trade studies showed that for a given maximum maneuver force, the variable stability-equipped projectile exhibits noticeably less dispersion error than comparable rigid rounds. Trade studies showed that the benefit of the mechanism generally increases with larger mass size, although ITM percentages larger than approximately 35% showed negligible additional benefit.

The final internal translating mass technology considered in this dissertation is the sensor suite shock absorber (Chapter 5). This device utilizes a translating mass comprised of the sensitive electronic components within the projectile sensor suite. The ITM is placed in a fluid-filled cavity along the longitudinal axis of the projectile, acting as a first-order damper. While initially the purpose of the shock absorber was to reduce the overall magnitude of the acceleration imposed on the sensor suite during launch, results showed that significant reductions are not possible using reasonable mass sizes and cavity lengths. However, through use of actual projectile launch acceleration profiles it was shown that the shock absorber is highly effective at isolating the electronics package from harmful structural high-frequency acceleration loads after launch, even using relatively small cavity lengths. These acceleration oscillations are a limiting factor in determining the time after launch that feedback control can be applied since many sensor readings prove unreliable in the presence of this vibration. Therefore, use of the proposed shock absorber could potentially allow feedback control to commence earlier in flight, leading to a more effective active control system.

Overall, it was determined that direct ITM control generates limited control authority for practical systems that can be used to reduce dispersion error but not eliminate it to sensor noise levels. Likewise, the ITM variable stability mechanism provides a limited control authority enhancement to guided projectiles starved of

adequate authority, but cannot provide large control performance improvements. Therefore, while ITM mechanisms may not be universally applicable to all smart weapon systems, they do provide a unique benefit in certain applications. Examples of potential applications include systems in which a reduced-dispersion area fire capability is desired, systems that require additional control authority without increasing direct control force, and canard-controlled projectiles that would benefit from trajectory corrections during initial portions of flight.

7.2 Recommended Future Work

The results of this dissertation have established that internal translating mass technologies prove useful for certain smart weapons applications, either as a direct control mechanism or as an enabling mechanism for other control components. Many opportunities for future work, presented below, could expand upon the findings described here and help to transition internal mass technologies to current and future smart weapons development programs.

A simple extension of the work presented here is an investigation into the use of multiple internal masses translating along orthogonal axes. One limitation of the current design of the ITM projectile is that control can only be applied along a single projectile-fixed axis (i.e., along $\vec{J}_P$ only), and thus the projectile must be in the proper roll orientation to apply control in the desired direction. Allowing two masses to translate along the $\vec{J}_P$ and $\vec{K}_P$ axes respectively would allow a control moment to be exerted in any desired direction regardless of roll orientation. Therefore, significant control authority increases are likely to be obtained. In addition, a variable stability mechanism could be implemented as a third internal mass configured to translate along $\vec{I}_P$, leading to further control authority increases. However, these control authority improvements lead

directly to increased power requirements. Furthermore, a potentially difficult consequence of implementing multiple masses is the significantly increased complexity of the dynamic equations, already complicated in their current form. This could be mitigated by use of multi-body simulation techniques.[66,67,68]

Internal moving mass control of non-rolling projectiles presents another opportunity for future research. While this concept is similar to the work done on moving mass control of missiles and reentry vehicles, [15,16] it could differ in its use of canards to roll-stabilize a standard fin-stabilized projectile. In this case, the projectile would achieve its nominal spin rate after launch. Then, when control is activated, fixed-angle reciprocating canards are extended from the body to roll-stabilize the projectile. The body roll angle could be set such that translating mass motion occurs in the desired control plane, and a constant ITM offset could be commanded to provide control moment. Such a design would likely yield significantly higher control authority than the current design, and would require considerably less power since neither the mass nor the canards would need to be oscillated at the projectile roll rate.

Another concept for future research takes advantage of the ITM projectile's reliance on drag to create control moment. A flight control system that could increase total aerodynamic drag (by, for instance, extending symmetrical speed brakes from the body) during short bursts of ITM control would likely exhibit significantly more control authority than the current design. Naturally, one of the challenges of this control technique would be the formulation of an algorithm to determine whether large drag increases would contribute error to the trajectory beyond the ITM controller's ability to eliminate it.

Model predictive control [64] of the ITM projectile is one of the most exciting future research opportunities. As described in Chapter 6, the current SMC design suffers overshoot problems using larger ITM sizes. This phenomenon is due to large initial control authority (leading to large control corrections at the beginning of the trajectory)

followed by rapidly diminishing control authority as static stability increases and drag force decreases. The large initial corrections lead to overshoot that cannot be damped as control authority is lost. A model predictive control law would likely prove very effective in taking these changes in control authority into account though control weightings. During initial portions flight control weightings could be low, while at the end of the trajectory large penalties could be placed on control. The control law would then compute control commands that would not lead to overshoot since control authority variations are modeled within the control law itself.

APPENDIX A

FULL EXPRESSIONS FOR ITM-BEAM ROTATIONAL DYNAMICS EQUATIONS

The terms of equation (3.13) are given as follows:

$$A_{11} = I_{T31} + BL\frac{m_P m_T}{m} s_\gamma r_3$$

$$A_{12} = I_{T32} - BL\frac{m_P m_T}{m} c_\gamma r_3$$

$$A_{13} = I_{T33} + BL^2\frac{m_P m_T}{m} + BL\frac{m_P m_T}{m}\left(c_\gamma r_2 - s_\gamma r_1\right)$$

$$A_{14} = I_{T33} + BL^2\frac{m_P m_T}{m}$$

$$A_{21} = I_{P31} - \frac{m_P m_T}{m} r_1 r_3$$

$$A_{22} = I_{P32} - \frac{m_P m_T}{m} r_2 r_3$$

$$A_{23} = I_{P33} + \frac{m_P m_T}{m} BL\left(r_2 c_\gamma - r_1 s_\gamma\right) + \frac{m_P m_T}{m}\left(r_1^2 + r_2^2\right)$$

$$A_{24} = \frac{m_P m_T}{m} BL\left(r_2 c_\gamma - r_1 s_\gamma\right)$$

$$A_{31} = I_{P21} + I_{T21} - \frac{m_P m_T}{m} BLr_4 c_\gamma - \frac{m_P m_T}{m} r_2 r_4$$

$$A_{32} = I_{P22} + I_{T22} - \frac{m_P m_T}{m} BLr_4 s_\gamma + \frac{m_P m_T}{m}\left(r_1 r_4 + r_3 r_6\right)$$

$$A_{33} = I_{P23} + I_{T23} - \frac{m_P m_T}{m} BLr_6 c_\gamma - \frac{m_P m_T}{m} r_2 r_6$$

$$A_{34} = I_{T23} - \frac{m_P m_T}{m} BLr_6 c_\gamma$$

$$A_{41} = I_{P11} + I_{T11} + \frac{m_P m_T}{m} BLr_5 c_\gamma + \frac{m_P m_T}{m}\left(r_2 r_5 + r_3 r_6\right)$$

$$A_{42} = I_{P12} + I_{T12} + \frac{m_P m_T}{m} BLr_5 s_\gamma - \frac{m_P m_T}{m} r_1 r_5$$

$$A_{43} = I_{P13} + I_{T13} + \frac{m_P m_T}{m} BLr_6 s_\gamma - \frac{m_P m_T}{m} r_1 r_6$$

$$A_{44} = I_{T13} + \frac{m_P m_T}{m} BLr_6 s_\gamma$$

$$\begin{aligned} B_1 = &-\vec{K}_S \bullet \mathbb{S}\left(\vec{r}_{L\to X}\right) m_T \mathbb{C}_S\left(\vec{a}_{C/I}\right) - f_{Input} BLc_\gamma - k_T \gamma - k_D \dot{\gamma} - \vec{K}_S \bullet \mathbb{S}\left(\vec{\omega}_{B/I}\right) I_T \mathbb{C}_S\left(\vec{\omega}_{T/I}\right) \\ &+ \vec{K}_S \bullet \mathbb{S}\left(\vec{r}_{L\to X}\right) \mathbb{C}_S\left(\vec{W}_T\right) - \frac{m_P m_T}{m} \vec{K}_S \bullet \mathbb{S}\left(\vec{r}_{L\to X}\right) \mathbb{S}\left(\vec{\omega}_{T/I}\right) \mathbb{S}\left(\vec{\omega}_{T/I}\right) \mathbb{C}_T\left(\vec{r}_{L\to X}\right) \\ &- \frac{m_P m_T}{m} \vec{K}_S \bullet \mathbb{S}\left(\vec{r}_{L\to X}\right) \mathbb{S}\left(\vec{\omega}_{B/I}\right) \mathbb{S}\left(\vec{\omega}_{B/I}\right) \mathbb{C}_S\left(\vec{r}_{P\to L}\right) \\ &- \frac{m_P m_T}{m} \vec{K}_S \bullet \mathbb{S}\left(\vec{r}_{L\to X}\right) \left[\mathbb{S}\left(\vec{\omega}_{B/I}\right) \times \mathbb{C}_S\left(\vec{\omega}_{T/I}\right)\right] \times \mathbb{C}_S\left(\vec{r}_{L\to X}\right) \end{aligned} \tag{A.1}$$

$$\begin{aligned} B_2 = &-\vec{K}_S \bullet m_P \mathbb{S}\left(\vec{r}_{L\to P}\right) \mathbb{C}_S\left(\vec{a}_{C/I}\right) + f_{Input} BLc_\gamma + k_T \gamma + k_D \dot{\gamma} - \vec{K}_S \bullet \mathbb{S}\left(\vec{\omega}_{B/I}\right) I_P \mathbb{C}_S\left(\vec{\omega}_{B/I}\right) \\ &+ \vec{K}_S \bullet \mathbb{C}_S\left(\sum \vec{M}_P^L\right) + \frac{m_P m_T}{m} \vec{K}_S \bullet \mathbb{S}\left(\vec{r}_{L\to P}\right) \mathbb{S}\left(\vec{\omega}_{T/I}\right) \mathbb{S}\left(\vec{\omega}_{T/I}\right) \mathbb{C}_S\left(\vec{r}_{L\to X}\right) \\ &+ \frac{m_P m_T}{m} \vec{K}_S \bullet \mathbb{S}\left(\vec{r}_{L\to P}\right) \mathbb{S}\left(\vec{\omega}_{B/I}\right) \mathbb{S}\left(\vec{\omega}_{B/I}\right) \mathbb{C}_S\left(\vec{r}_{P\to L}\right) \\ &+ \frac{m_P m_T}{m} \vec{K}_S \bullet \mathbb{S}\left(\vec{r}_{L\to P}\right) \left[\mathbb{S}\left(\vec{\omega}_{B/I}\right) \times \mathbb{C}_S\left(\vec{\omega}_{T/I}\right)\right] \times \mathbb{C}_S\left(\vec{r}_{L\to X}\right) \\ &+ \vec{K}_S \bullet \mathbb{S}\left(\vec{r}_{L\to P}\right) \mathbb{C}_S\left(\vec{W}_P\right) \end{aligned} \tag{A.2}$$

$$\begin{aligned} B_3 = &-\vec{J}_S \bullet \mathbb{S}\left(\vec{\omega}_{B/I}\right) I_P \mathbb{C}_S\left(\vec{\omega}_{B/I}\right) - \vec{J}_S \bullet \mathbb{S}\left(\vec{\omega}_{T/I}\right) I_T \mathbb{C}_S\left(\vec{\omega}_{T/I}\right) + \vec{J}_S \bullet \mathbb{S}\left(\vec{r}_{L\to X}\right) \mathbb{C}_S\left(\vec{W}_T\right) \\ &- \vec{J}_S \bullet m \mathbb{S}\left(\vec{r}_{L\to P}\right) \mathbb{C}_S\left(\vec{a}_{C/I}\right) - \vec{J}_S \bullet m_T \mathbb{S}\left(\vec{r}_{P\to X}\right) \mathbb{C}_S\left(\vec{a}_{C/I}\right) \\ &- \frac{m_P m_T}{m} \vec{J}_S \bullet \mathbb{S}\left(\vec{r}_{P\to X}\right) \mathbb{S}\left(\vec{\omega}_{T/I}\right) \mathbb{S}\left(\vec{\omega}_{T/I}\right) \mathbb{C}_S\left(\vec{r}_{L\to X}\right) \\ &- \frac{m_P m_T}{m} \vec{J}_S \bullet \mathbb{S}\left(\vec{r}_{P\to X}\right) \mathbb{S}\left(\vec{\omega}_{B/I}\right) \mathbb{S}\left(\vec{\omega}_{B/I}\right) \mathbb{C}_S\left(\vec{r}_{P\to L}\right) + \vec{J}_S \bullet \mathbb{C}_S\left(\sum \vec{M}_{system}^L\right) \\ &- \frac{m_P m_T}{m} \vec{J}_S \bullet \mathbb{S}\left(\vec{r}_{P\to X}\right) \left[\mathbb{S}\left(\vec{\omega}_{B/I}\right) \mathbb{C}_S\left(\vec{\omega}_{T/I}\right)\right] \times \mathbb{C}_S\left(\vec{r}_{L\to X}\right) \end{aligned} \tag{A.3}$$

$$
\begin{aligned}
B_4 = &-\vec{I}_S \bullet \mathbb{S}\left(\vec{\omega}_{B/I}\right) I_P \mathbb{C}_S\left(\vec{\omega}_{B/I}\right) - \vec{I}_S \bullet \mathbb{S}\left(\vec{\omega}_{T/I}\right) I_T \mathbb{C}_S\left(\vec{\omega}_{T/I}\right) + \vec{I}_S \bullet \mathbb{S}\left(\vec{r}_{L\to X}\right) \mathbb{C}_S\left(\vec{W}_T\right) \\
&- \vec{I}_S \bullet m \mathbb{S}\left(\vec{r}_{L\to P}\right) \mathbb{C}_S\left(\vec{a}_{C/I}\right) - \vec{I}_S \bullet m_T \mathbb{S}\left(\vec{r}_{P\to X}\right) \mathbb{C}_S\left(\vec{a}_{C/I}\right) \\
&- \frac{m_P m_T}{m} \vec{I}_S \bullet \mathbb{S}\left(\vec{r}_{P\to X}\right) \mathbb{S}\left(\vec{\omega}_{T/I}\right) \mathbb{S}\left(\vec{\omega}_{T/I}\right) \mathbb{C}_S\left(\vec{r}_{L\to X}\right) \\
&- \frac{m_P m_T}{m} \vec{I}_S \bullet \mathbb{S}\left(\vec{r}_{P\to X}\right) \mathbb{S}\left(\vec{\omega}_{B/I}\right) \mathbb{S}\left(\vec{\omega}_{B/I}\right) \mathbb{C}_S\left(\vec{r}_{P\to L}\right) + \vec{I}_S \bullet \mathbb{C}_S\left(\sum \vec{M}^{L}_{system}\right) \\
&- \frac{m_P m_T}{m} \vec{I}_S \bullet \mathbb{S}\left(\vec{r}_{P\to X}\right) \left[\mathbb{S}\left(\vec{\omega}_{B/I}\right) \mathbb{C}_S\left(\vec{\omega}_{T/I}\right)\right] \times \mathbb{C}_S\left(\vec{r}_{L\to X}\right)
\end{aligned}
\tag{A.4}
$$

The term B_{FLC} used in equation (3.14) is given by

$$
\begin{aligned}
B_{FLC} = &-\vec{K}_S \bullet \mathbb{S}\left(\vec{r}_{L\to X}\right) m_T \mathbb{C}_S\left(\vec{a}_{C/I}\right) - k_T \gamma - k_D \dot{\gamma} - \vec{K}_S \bullet \mathbb{S}\left(\vec{\omega}_{B/I}\right) I_T \mathbb{C}_S\left(\vec{\omega}_{T/I}\right) \\
&+ \vec{K}_S \bullet \mathbb{S}\left(\vec{r}_{L\to X}\right) \mathbb{C}_S\left(\vec{W}_T\right) - \frac{m_P m_T}{m} \vec{K}_S \bullet \mathbb{S}\left(\vec{r}_{L\to X}\right) \mathbb{S}\left(\vec{\omega}_{T/I}\right) \mathbb{S}\left(\vec{\omega}_{T/I}\right) \mathbb{C}_T\left(\vec{r}_{L\to X}\right) \\
&- \frac{m_P m_T}{m} \vec{K}_S \bullet \mathbb{S}\left(\vec{r}_{L\to X}\right) \mathbb{S}\left(\vec{\omega}_{B/I}\right) \mathbb{S}\left(\vec{\omega}_{B/I}\right) \mathbb{C}_S\left(\vec{r}_{P\to L}\right) \\
&- \frac{m_P m_T}{m} \vec{K}_S \bullet \mathbb{S}\left(\vec{r}_{L\to X}\right) \left[\mathbb{S}\left(\vec{\omega}_{B/I}\right) \times \mathbb{C}_S\left(\vec{\omega}_{T/I}\right)\right] \times \mathbb{C}_S\left(\vec{r}_{L\to X}\right)
\end{aligned}
\tag{A.5}
$$

APPENDIX B

SLIDING MODE CONTROL DERIVATION SUPPLEMENT

In order to compute the sliding mode control law developed in Section 6.3, closed-form expressions for $\dot{p}$, $\dot{q}$, and $\dot{r}$ are needed. Furthermore, these expressions must be written in control affine form such that

$$\begin{aligned} \dot{p} &= a_p + b_p F_C \\ \dot{q} &= a_q + b_q F_C \\ \dot{r} &= a_r + b_r F_C \end{aligned} \tag{B.1}$$

where the a_p, a_q, a_r, b_p, b_q, and b_r are functions of state variables and non-control related forces and moments only. In order to obtain these closed-form expressions, it is assumed that the control system is derived for the ITM-Beam system (whose equations of motion are derived in Chapter 3) and that the controller is provided full state, force, and moment feedback. Reasonable error levels are associated with all of these feedback parameters as described in Chapter 6.

The ITM-Beam dynamic model computes components of angular acceleration in the body-fixed *S* frame according to

$$\begin{bmatrix} A_{11} & A_{12} & A_{13} & A_{14} \\ A_{21} & A_{22} & A_{23} & A_{24} \\ A_{31} & A_{32} & A_{33} & A_{34} \\ A_{41} & A_{42} & A_{43} & A_{44} \end{bmatrix} \begin{Bmatrix} \dot{\tilde{p}} \\ \dot{\tilde{q}} \\ \dot{\tilde{r}} \\ \ddot{\gamma} \end{Bmatrix} = \begin{Bmatrix} B_1 \\ B_2 \\ B_3 \\ B_4 \end{Bmatrix} \tag{B.2}$$

where $\tilde{p}$, $\tilde{q}$, and $\tilde{r}$ are the components of $\vec{\omega}_{P/I}$ expressed in the *S* reference frame. Note that full expressions for the *A* matrix and $\vec{B}$ vector are provided in Appendix A. Also, for the sake of simplicity, let the transformation from the *S* frame to the *P* frame be given by

$$T_{S\to P} = \begin{bmatrix} 0 & -1 & 0 \\ 1 & 0 & 0 \\ 0 & 0 & 0 \end{bmatrix} \tag{B.3}$$

which represents a transformation of 90 deg about the $\vec{K}_P$ axis, as used for all example cases in this dissertation. The components of vector $\vec{B}$ are now divided into terms that contain control moments and those that do not. First, note from equation (A.1) that B_1 does not contain any control moments. Next, B_2 can be written as

$$B_2 = B_{2NC} + \vec{K}_S \bullet \vec{M}^L_{Con} \tag{B.4}$$

where $\vec{M}^L_{Con}$ is the control moment exerted about the hinge point *L* and

$$\begin{aligned} B_{2NC} = & -\vec{K}_S \bullet m_P \mathbb{S}\left(\vec{r}_{L\to P}\right)\mathbb{C}_S\left(\vec{a}_{C/I}\right) + f_{Input} BLc_\gamma + k_T\gamma + k_D\dot{\gamma} - \vec{K}_S \bullet \mathbb{S}\left(\vec{\omega}_{B/I}\right) I_P \mathbb{C}_S\left(\vec{\omega}_{B/I}\right) \\ & + \vec{K}_S \bullet \mathbb{C}_S\left(\sum \vec{M}^L_P\right) + \frac{m_P m_T}{m} \vec{K}_S \bullet \mathbb{S}\left(\vec{r}_{L\to P}\right)\mathbb{S}\left(\vec{\omega}_{T/I}\right)\mathbb{S}\left(\vec{\omega}_{T/I}\right)\mathbb{C}_S\left(\vec{r}_{L\to X}\right) \\ & + \frac{m_P m_T}{m} \vec{K}_S \bullet \mathbb{S}\left(\vec{r}_{L\to P}\right)\mathbb{S}\left(\vec{\omega}_{B/I}\right)\mathbb{S}\left(\vec{\omega}_{B/I}\right)\mathbb{C}_S\left(\vec{r}_{P\to L}\right) \\ & + \frac{m_P m_T}{m} \vec{K}_S \bullet \mathbb{S}\left(\vec{r}_{L\to P}\right)\left[\mathbb{S}\left(\vec{\omega}_{B/I}\right)\times\mathbb{C}_S\left(\vec{\omega}_{T/I}\right)\right]\times\mathbb{C}_S\left(\vec{r}_{L\to X}\right) \\ & + \vec{K}_S \bullet \mathbb{S}\left(\vec{r}_{L\to P}\right)\mathbb{C}_S\left(\vec{W}_P\right) \end{aligned} \tag{B.5}$$

Note that in equation (B.5) the sum of moments term can be written as

$$\sum \vec{M}_P^L = \vec{M}_{Steady}^L + \vec{M}_{Unsteady}^L + \vec{M}_{Weight}^L + \vec{M}_{Magnus}^L \tag{B.6}$$

Likewise, B_3 and B_4 can be separated such that

$$B_3 = \vec{J}_S \bullet B^* + \vec{J}_S \bullet \vec{M}_{Con}^L \tag{B.7}$$

$$B_4 = \vec{I}_S \bullet B^* + \vec{I}_S \bullet \vec{M}_{Con}^L \tag{B.8}$$

where

$$\begin{aligned} B^* = & -\mathbb{S}\left(\vec{\omega}_{B/I}\right) I_P \mathbb{C}_S\left(\vec{\omega}_{B/I}\right) - \mathbb{S}\left(\vec{\omega}_{T/I}\right) I_T \mathbb{C}_S\left(\vec{\omega}_{T/I}\right) + \mathbb{S}\left(\vec{r}_{L\to X}\right) \mathbb{C}_S\left(\vec{W}_T\right) \\ & m\mathbb{S}\left(\vec{r}_{L\to P}\right) \mathbb{C}_S\left(\vec{a}_{C/I}\right) - m_T \mathbb{S}\left(\vec{r}_{P\to X}\right) \mathbb{C}_S\left(\vec{a}_{C/I}\right) \\ & -\frac{m_P m_T}{m} \mathbb{S}\left(\vec{r}_{P\to X}\right) \mathbb{S}\left(\vec{\omega}_{T/I}\right) \mathbb{S}\left(\vec{\omega}_{T/I}\right) \mathbb{C}_S\left(\vec{r}_{L\to X}\right) \\ & -\frac{m_P m_T}{m} \mathbb{S}\left(\vec{r}_{P\to X}\right) \mathbb{S}\left(\vec{\omega}_{B/I}\right) \mathbb{S}\left(\vec{\omega}_{B/I}\right) \mathbb{C}_S\left(\vec{r}_{P\to L}\right) + \mathbb{C}_S\left(\sum \vec{M}_{system}^L\right) \\ & -\frac{m_P m_T}{m} \mathbb{S}\left(\vec{r}_{P\to X}\right) \left[\mathbb{S}\left(\vec{\omega}_{B/I}\right) \mathbb{C}_S\left(\vec{\omega}_{T/I}\right)\right] \times \mathbb{C}_S\left(\vec{r}_{L\to X}\right) \end{aligned} \tag{B.9}$$

Note that the lengthy expression in equation (B.9) is closely related to the expressions for B_3 and B_4 given in equations (A.3) and (A.4). Using the expanded expressions given in equations (B.4), (B.7), and (B.8), equation (B.2) can be separated into control-affine structure according to

$$\begin{bmatrix} A_{11} & A_{12} & A_{13} & A_{14} \\ A_{21} & A_{22} & A_{23} & A_{24} \\ A_{31} & A_{32} & A_{33} & A_{34} \\ A_{41} & A_{42} & A_{43} & A_{44} \end{bmatrix} \begin{Bmatrix} \dot{\vec{p}} \\ \dot{\vec{q}} \\ \dot{\vec{r}} \\ \ddot{\vec{\gamma}} \end{Bmatrix} = \begin{Bmatrix} B_1 \\ B_{2NC} \\ \vec{J}_S \bullet B^* \\ \vec{I}_S \bullet B^* \end{Bmatrix} + \begin{Bmatrix} 0 \\ \vec{K}_S \bullet \vec{M}_{Con}^L \\ \vec{J}_S \bullet \vec{M}_{Con}^L \\ \vec{I}_S \bullet \vec{M}_{Con}^L \end{Bmatrix} \tag{B.10}$$

Next, using the reference frame transformation given in equation (B.3) and assuming that control force can be applied only in the $\vec{J}_P$ and $\vec{K}_P$ directions, it can be shown that

$$\begin{aligned} \vec{I}_S \bullet \vec{M}_{Con}^{L} &= M_{Con_Y}^{L} \\ \vec{J}_S \bullet \vec{M}_{Con}^{L} &= 0 \\ \vec{K}_S \bullet \vec{M}_{Con}^{L} &= M_{Con_Z}^{L} \end{aligned} \tag{B.11}$$

where $M_{Con_Y}^{L}$ and $M_{Con_Z}^{L}$ are control moments about point *L* about the body *y* and *z* axes respectively. Therefore, substitution of equation (B.11) into (B.10) yields

$$\begin{bmatrix} A_{11} & A_{12} & A_{13} & A_{14} \\ A_{21} & A_{22} & A_{23} & A_{24} \\ A_{31} & A_{32} & A_{33} & A_{34} \\ A_{41} & A_{42} & A_{43} & A_{44} \end{bmatrix} \begin{Bmatrix} \dot{\tilde{p}} \\ \dot{\tilde{q}} \\ \dot{\tilde{r}} \\ \ddot{\gamma} \end{Bmatrix} = \begin{Bmatrix} B_1 \\ B_{2NC} \\ \vec{J}_S \bullet B^* \\ \vec{I}_S \bullet B^* \end{Bmatrix} + \begin{Bmatrix} 0 \\ M_{Con_Z}^{L} \\ 0 \\ M_{Con_Y}^{L} \end{Bmatrix} \tag{B.12}$$

Using the transformation in equation (B.3), it is trivial to show that

$$\begin{aligned} \dot{p} &= -\dot{\tilde{q}} \\ \dot{q} &= \dot{\tilde{p}} \\ \dot{r} &= \dot{\tilde{r}} \end{aligned} \tag{B.13}$$

Finally, let *Q* be a 4×4 matrix such that $Q = A^{-1}$ and let vector $\vec{G}$ be the product $[Q]\vec{B}_{NC}$ where $\vec{B}_{NC}$ is the first vector on the right-hand-side of equation (B.12). Using this new notation, equation (B.12) can be rewritten as

$$\begin{Bmatrix} \dot{\tilde{p}} \\ \dot{\tilde{q}} \\ \dot{\tilde{r}} \\ \ddot{\gamma} \end{Bmatrix} = \vec{G} + [Q] \begin{Bmatrix} 0 \\ M^{L}_{Con_Z} \\ 0 \\ M^{L}_{Con_Y} \end{Bmatrix} \tag{B.14}$$

Using the relations given in (B.13), equation (B.14) can be expanded to produce the following control-affine formulas for the angular acceleration components:

$$\dot{p} = -G_2 - Q_{22} M^{L}_{Con_Z} - Q_{24} M^{L}_{Con_Y} \tag{B.15}$$

$$\dot{q} = G_1 + Q_{12} M^{L}_{Con_Z} + Q_{14} M^{L}_{Con_Y} \tag{B.16}$$

$$\dot{r} = G_3 + Q_{32} M^{L}_{Con_Z} + Q_{34} M^{L}_{Con_Y} \tag{B.17}$$

where subscripts denote the appropriate component of the vector or matrix. As a final note, it is desired to obtain expressions for the angular acceleration components in terms of control forces rather than control moments. Assume that control force is exerted at some point *R* on the projectile *x* axis. Therefore, the distance vector from the hinge point to the point of control force application can be written as

$$\mathbb{C}\left(\vec{r}_{L\to R}\right) = \begin{Bmatrix} \Delta_{LR} \\ 0 \\ 0 \end{Bmatrix} \tag{B.18}$$

Therefore, control forces and control moments can be related by

$$\begin{Bmatrix} 0 \\ M^{L}_{Con_Y} \\ M^{L}_{Con_Z} \end{Bmatrix} = \begin{bmatrix} 0 & 0 & 0 \\ 0 & 0 & -\Delta_{LR} \\ 0 & \Delta_{LR} & 0 \end{bmatrix} \begin{Bmatrix} 0 \\ F^{Con}_{Y} \\ F^{Con}_{Z} \end{Bmatrix} \tag{B.19}$$

where F_Y^{Con} and F_Z^{Con} are the control force components expressed in the body frame in the body *y* and *z* directions respectively. Using the force-moment relationship in equation (B.19), the final control-affine expression relating angular acceleration components to control force components is given by

$$\dot{p} = -G_2 - Q_{22}\Delta_{LR}F_Y^{Con} + Q_{24}\Delta_{LR}F_Z^{Con} \tag{B.20}$$

$$\dot{q} = G_1 + Q_{12}\Delta_{LR}F_Y^{Con} - Q_{14}\Delta_{LR}F_Z^{Con} \tag{B.21}$$

$$\dot{r} = G_3 + Q_{32}\Delta_{LR}F_Y^{Con} - Q_{34}\Delta_{LR}F_Z^{Con} \tag{B.22}$$

APPENDIX C

ROTATIONAL SLIDING MODE CONTROL INTERMEDIATE EXPRESSIONS

In development of the rotational sliding mode control law in Section 6.3.1, the following intermediate expressions are used in equations (6.17) and (6.18).

$$\begin{aligned} D_\theta = &-\dot{\phi}s_\phi q - \dot{\phi}c_\phi r - \frac{x_L}{k_1}\left[\dot{T}_{31}u + \dot{T}_{32}v + \dot{T}_{33}w\right] + \frac{2x_L\left(\dot{z}-\dot{z}_c\right)^2\left(z-z_c\right)}{k_1^2} \\ &-\frac{x_L}{k_1}\left[T_{31}\left(\frac{F_x}{m}+rv-qw\right)+T_{32}\left(\frac{F_y}{m}-ru+pw\right)+T_{33}\left(\frac{F_z}{m}+qu-pv\right)\right] \\ &\lambda_\theta\dot{\theta} - \lambda_\theta\frac{x_L\left(\dot{z}-\dot{z}_c\right)}{k_1} + \frac{x_L}{k_1}\ddot{z}_c + c_\phi G_1 - s_\phi G_3 \end{aligned} \tag{C.1}$$

$$\begin{aligned} D_\psi = &\dot{\phi}\frac{c_\phi}{c_\theta}q - \dot{\phi}\frac{s_\phi}{c_\theta}r + \dot{\theta}\frac{s_\phi t_\theta}{c_\theta}q + \dot{\phi}\frac{c_\phi t_\theta}{c_\theta}r + \frac{x_L}{k_2}\left[\dot{T}_{21}u + \dot{T}_{22}v + \dot{T}_{23}w\right] + \frac{2x_L\left(\dot{y}_c-\dot{y}\right)^2\left(y_c-y\right)}{k_2^2} \\ &+\frac{x_L}{k_2}\left[T_{21}\left(\frac{F_x}{m}+rv-qw\right)+T_{22}\left(\frac{F_y}{m}-ru+pw\right)+T_{23}\left(\frac{F_z}{m}+qu-pv\right)\right] \\ &\lambda_\psi\dot{\psi} - \lambda_\psi\frac{x_L\left(\dot{y}_c-\dot{y}\right)}{k_2} - \frac{x_L}{k_2}\ddot{y}_c + \frac{s_\phi}{c_\theta}G_1 + \frac{c_\phi}{c_\theta}G_3 \end{aligned} \tag{C.2}$$

Note that in equations (C.1) and (C.2), matrix T is the body to inertial reference frame transformation given in equation (6.16), vector $\vec{G}$ is described in detail in Appendix B, and k_1 and k_2 are given by

$$k_1 = x_L^2 + \left(z - z_c\right)^2 \tag{C.3}$$

$$k_2 = x_L^2 + \left(y_c - y \right)^2 \tag{C.4}$$

Furthermore, body-frame force components F_x, F_y, and F_z consist of the sum of all non-control-related external force components expressed in the body frame (i.e., the sum of aerodynamic, weight, and Magnus forces).

REFERENCES

[1] Defense Science Board, Office of the Secretary of Defense for Acquisition and Technology. "Report of the Defense Science Board Task Force on Military Operations in Built-Up Areas," Washington, D.C. November 1994.

[2] Kinne, G.S., Tanzi, J.A., and Yaeger, J.W., "FA PGMs: Revolutionizing Fires for the Ground Force Commander," *Field Artillery Magazine*, May-June 2006, p. 2.

[3] Kinne, G.S., Tanzi, J.A., and Yaeger, J.W., "FA PGMs: Revolutionizing Fires for the Ground Force Commander," *Field Artillery Magazine*, May-June 2006, p. 5.

[4] Costello, M. "Range Optimization of a Fin-Stabilized Projectile," 1997 AIAA Atmospheric Flight Mechanics Conference, New Orleans, LA, paper AIAA-97-3724.

[5] Chandgadkar, S., and Costello, M. "Performance of a Smart Direct Fire Projectile Using a Ram Air Control Mechanism" *Journal of Dynamic Systems, Measurement, and Control*, Vol. 124, No. 4, December 2002.

[6] Baines, W.R., and Sumrall, C.W. "Ram Air Steering System for a Guided Missile." U.S. Patent 4522357, June 1985.

[7] Kennedy, W.B., and Mikkelsen, C. "AIT Real Gas Divert Jet Interactions; Summary of Technology," AIAA Defense and Civil Space Programs Conference and Exhibit, AIAA, Reston, VA, 1998, paper AIAA-98-5188.

[8] Frost, G., and Costello, M., "Linear Theory of a Projectile with a Rotating Internal Part in Atmospheric Flight," *Journal of Guidance, Control, and Dynamics*, Vol. 27, No. 5, 2004, pp. 898–906.

[9] Frost, G., and Costello, M., "Control Authority of a Projectile Equipped with an Internal Unbalanced Part," *Journal of Dynamic Systems, Measurement, and Control*, Vol. 128, No. 4, 2006, pp. 1005–1012.

[10] Soper, W. "Projectile Instability Produced by Internal Friction," *AIAA Journal*, Vol. 16, No. 1, 1978, pp 8-11.

[11] Murphy, C. "Influence of Moving Internal Parts on Angular Motion of Spinning Projectiles," *Journal of Guidance and Control*, Vol. 1, No. 2, 1978, pp. 117-122.

[12] D'Amico, W. "Comparison of Theory and Experiment for Moments Induced by Loose Internal Parts," *Journal of Guidance and Control*, Vol. 10, No. 1, 1987, pp. 14-19.

[13] Hodapp, A. "Passive Means for Stabilizing Projectiles with Partially Restrained Internal Members," *Journal of Guidance and Control*, Vol. 12, No. 2, 1989, pp. 135-139.

[14] Petsopoulos, T., Regan, F., and Barlow, J. "Moving Mass Roll Control System for Fixed-Trim Re-Entry Vehicle," *Journal of Spacecraft and Rockets*, Vol. 33, No. 1, 1996, pp. 54-61.

[15] Robinett, R., Sturgis, B., and Kerr, S. "Moving Mass Trim Control for Aerospace Vehicles," *Journal of Guidance, Control, and Dynamics*, Vol. 19, No. 5, 1996, pp. 1064-1071.

[16] Menon, P., Sweriduk, G., Ohlmeyer, E., and Malyevac, D. "Integrated Guidance and Control of Moving Mass Actuated Kinetic Warheads," *Journal of Guidance, Control, and Dynamics*, Vol. 27, No. 1, 2004, pp. 118-127.

[17] Rollstin, L. R., "Experimental Determination of the Artillery Shell Mass-Property/Trajectory-Drift Relationship," *Journal of Spacecraft*, Vol. 16, No. 2, 1978, pp 108-114.

[18] Rogers, J., and Costello, M, "Control Authority of a Projectile Equipped With an Internal Translating Mass," *Journal of Guidance, Control, and Dynamics*., Vol. 31. No. 5, 2008, pp. 1323–1333.

[19] Slotine, J.-J.E., Coetsee, J.A., "Adaptive Sliding Controller Synthesis for Non-Linear Systems," *International Journal of Control*, Vol. 43, Issue 6, June 1986, pp. 1631-1651

[20] Rogers, J., and Costello, M. "Cantilever Beam Design for Projectile Internal Moving Mass Systems," *Journal of Dynamic Systems, Measurement, and Control*, Vol. 131, September 2009.

[21] Rogers, J. and Costello, M. "A Variable Stability Projectile Using an Internal Translating Mass," *Journal of Aerospace Engineering*, Vol. 223, September 2009.

[22] Rogers, J., and Celmins, I., *Control Authority of a Mortar Using Internal Translating Mass Control*, ARL-TR-4857, U.S. Army Research Laboratory, Aberdeen Proving Ground, MD, June 2009.

[23] Rogers, J., and Costello, M. "Sliding Mode Control of a Projectile Using an Internal Translating Mass," *Journal of Guidance, Control, and Dynamics* (manuscript under review).

[24] Bakakin, A.V., Bermant, M.A., and Exerov, V.A. "Application of Variable Structure Systems to Stabilization of Time Varying Plants in the Presence of Restrictions on the Movement of the Controlling Device," *Automatic Remote Control*, No. 7, 1964, pp. 1016-1021.

[25] Bakakin, A.V., and Utkin, V.I. "Variable Structure Systems with Pure Delay in Switching Devices," in *Variable Structures Systems and their Application to Flight Automation* (in Russian), Nauka, Moscow, pp. 64-71, 1968.

[26] Baruh, H. *Analytical Dynamics*, McGraw Hill Company, U.S.A., ISBN 0-07-365977-0, pp. 124-127, 1999.

[27] Arrow Tech Associates, Inc. *Prodas Version 3 Documentation*, Arrow Tech Associates, Inc., 2000.

[28] Slotine, J.-J., and Li, W. *Applied Nonlinear Control*, Prentice Hall Inc., U.S.A., ISBN 0-13-040890-5, pp. 207-236, 1991.

[29] Vaughn, H.R., and Wilson, G.G. "Effect of Yaw of Repose on Ballistic Match of Similar Projectiles," *AIAA Journal*, Vol. 9. No. 6, June 1971, pp. 1208-1210.

[30] Purcell, E. *Electricity and Magnetism*, McGraw Hill Company, U.S.A., ISBN 0-07-004908-4, pp. 227, 412-138, 1985.

[31] Inman, D. *Engineering Vibration*, Prentice Hall, Inc., U.S.A., ISBN 0-13-726-142-X, p. 451, 2001.

[32] Flatau, A., Dapino, M., and Calkins, F. "High Bandwidth Tunability in a Smart Vibration Absorber," *Journal of Intelligent Material Systems and Structures*, Vol. 11, December 2000, pp. 923-929.

[33] Varga, Z., Filipcsei, G., and Zrinyi, M. "Smart Composites with Controlled Anisotropy," *Polymer*, Vol. 46, 2005, pp. 7779-7787.

[34] Varga, Z., Filipcsei, G., and Zrinyi, M. "Magnetic Field Sensitive Functional Elastomers with Tuneable Elastic Modulus," *Polymer*, Vol. 47, 2006, pp. 227-233.

[35] Davis, C., and Lesieutre, G. "An Actively Tuned Solid-State Vibration Absorber Using Capacitive Shunting of Piezoelectric Stiffness," *Journal of Sound and Vibration*, Vol. 232, No. 3, pp. 601-617.

[36] Beer, F., and Johnston, E. *Mechanics of Materials*, McGraw Hill, New York, ISBN 0-07-004284-5, 1981.

[37] Donovan, W.F. "Projectile." U.S. Patent 4241660, October 1978.

[38] Glotz, G., Becker, H., and Boeker, J. "Training Projectile." U.S. Patent 4596191, October 4, 1984.

[39] Zarchan, P. *Tactical and Strategic Missile Guidance*, American Institute of Aeronautics and Astronautics, Inc, U.S.A., ISBN 1-56347-497-2, pp. 12-15, 2002.

[40] Press, W., Teukolsky, S., and Vetterling, W. *Numerical Recipes: The Art of Scientific Computing*, Cambridge University Press, New York, ISBN 9780521880688, 2007.

[41] Paris, S., and Asma, C.O., Eds. *Experimental Determination of Dynamic Stability Parameters*, von Karman Institute for Fluid Dynamics, Rhode-St-Genese, Belgium, ISBN 978-2-930389-81-8, 2008.

[42] Davis, B., Hamilton, M., and Hepner, D. *Shock Experiment Results of the DFuze 8-Channel Inertial Sensor Suite That Contains Commercial Magnetometers and*

Accelerometers, ARL-MR-532, U.S. Army Research Laboratory, Aberdeen Proving Ground, MD, April 2002.

[43] Davis, B., Malejko, G., Dohrn, R., Owens, S., Harkins, T., and Bischer, G. "Addressing the Challenges of a Thruster-Based Precision Guided Mortar Munition With the Use of Embedded Telemetry Instrumentation," *ITEA Journal*, Vol. 30, 2009, pp. 117-125.

[44] Davis, B. "Advancements in G-Hardened Telemetry Instrumentation for the Test and Evaluation of Projectiles," *ITEA Journal*, Vol. 24, No. 2, June 2003.

[45] Brown, G., and Lovas, A. "Innovative Technologies and Techniques For In-Situ Test and Evaluation of Small Caliber Munitions," *ITEA Journal*, Vol. 29, No. 1, March 2009.

[46] Davis, B., Denison, T., and Kuang, J. "A Monolithic High-g SOI-MEMS Accelerometer for Measuring Projectile Launch and Flight Accelerations," The 3rd IEEE Conference on Sensors, Vienna, Austria, October 25-27, 2004.

[47] Jordy, D., and Younis, M. "Characterization of the Dynamical Response of a Micromachined G-Sensor to Mechanical Shock Loading," *Journal of Dynamic Systems, Measurement, and Control*, Vol. 130, July 2008.

[48] Carlucci, D., and Jacobson, S. *Ballistics*, CRC Press, Boca Raton, FL, ISBN 978-1-4200-6618-0, 2008.

[49] Perisho, C. H. "Analysis of the Stability of a Flexible Rotor Blade at High Advance Ratio," *Journal of the American Helicopter Society*, Vol. 4, No. 4, 1959.

[50] Kennedy, H. "U.S. Army Presses Ahead on Precision Guided Artillery," *National Defense*, October 2002.

[51] Brown, T.G. "Harsh Military Environments and Microelectromechanical (MEMS) Devices," *Proceeding of the IEEE, Sensors 2003*, Vol. 2, October 2003, pp. 753-760.

[52] Hess, R. A., and Wells, S. R. "Sliding-Mode Control Applied to Reconfigurable Flight Control Design," *Journal of Guidance, Control, and Dynamics*, Vol. 26, No. 3, May-June 2003, pp. 452-462.

[53] Hess, R. A., and Bakhtiari-Nejad, M. "Sliding-Mode Control of a Nonlinear Model of an Unmanned Aerial Vehicle," *Journal of Guidance, Control, and Dynamics*, Vol. 31, No. 4, July-August 2008, pp. 1163-1166.

[54] Utkin, V. I. "Variable Structure Systems with Sliding Modes," *IEEE Transactions on Automatic Control*, Vol. AC-22, No. 2, April 1977, pp. 212-222.

[55] Slotine, J.-J. E. "Sliding Controller Design for Nonlinear Systems," *International Journal of Control*, Vol. 40, Issue 2, August 1984, pp. 421-434.

[56] Slotine, J.-J. E., and Sastry, S. S. "Tracking Control of Nonlinear Systems Using Sliding Surfaces With Application to Robot Manipulators," *International Journal of Control*, Vol. 38, Issue 2, August 1983, pp. 465-492.

[57] Brierley, S. D., and Longchamp, R. "Application of Sliding Mode Control to Air-to-Air Intercept Problem," *IEEE Transactions of Aerospace and Electronic Systems*, Vol. 26, No. 2, March 1990, pp. 306-325.

[58] Shima, T., Idan, M., and Golan, O. M., "Sliding-Mode Control for Integrated Missile Autopilot Guidance," *Journal of Guidance, Control, and Dynamics*, Vol. 29, No. 2, March-April 2006, pp. 250-260.

[59] Idan, M., Shima, T., and Golan, O. M., "Integrated Sliding Mode Autopilot-Guidance for Dual Control Missiles," *Journal of Guidance, Control, and Dynamics*, Vol. 30, No. 4, July-August 2007, pp. 1081-1089.

[60] Koren, A., Idan, M., and Golan, O. M., "Integrated Sliding Mode Guidance and Control for a Missile with On-Off Actuators," *Journal of Guidance, Control, and Dynamics*, Vol. 31, No. 1, January-February 2008, pp. 204-214.

[61] Tournes, C., Shtessel, Y., and Shkolnikov, I. "Missile Controlled by Lift and Divert Thrusters Using Nonlinear Dynamic Sliding Manifolds," *Journal of Guidance, Control, and Dynamics*, Vol. 29, No. 3, May-June 2006, pp. 617-625.

[62] Shtessel, Y., and Tournes, C., "Integrated Higher-Order Sliding Mode Guidance and Autopilot for Dual-Control Missiles," *Journal of Guidance, Control, and Dynamics*, Vol. 32, No. 1, January-February 2009, pp. 79-94.

[63] Atlantic Inertial Systems. "SiIMU02 MEMS Inertial Measurement Unit." Atlantic Inertial Systems. http://www.atlanticinertial.com/index.php?/products/detail/siimu02/ (accessed 25 August 2009).

[64] Camacho, E., and Bordons, C. *Model Predictive Control*, Springer Verlag, London, ISBN 1-85233-694-3, 1999.

[65] Ollerenshaw, D., and Costello, M. "Model Predictive Control of a Direct Fire Projectile Equipped with Canards," *Journal of Dynamic Systems, Measurement, and Control*, Vol. 130, No. 6, 2008.

[66] Chiou, J. C., and Wu, S. D. "Constraint Violation Stabilization Using Input-Output Feedback Linearization in Multibody Dynamic Analysis," *Journal of Guidance, Control, and Dynamics*, Vol. 21, No. 2, March-April 1998, pp. 222-228.

[67] Udwadia, F. E. "Equations of Motion for Constrained Multibody Systems and Their Control," *Journal of Optimization Theory and Applications*, Vol. 127, No. 3, December 2005, pp. 627-638.

[68] Udwadia, F. E., and Phohomsiri, P. "Explicit Poincare Equations of Motion for General Constrained Systems, Part II: Applications to Multi-Body Dynamics and Nonlinear Control," *Proceedings of the Royal Society*, *Series A,*Vol. 463 (2082), 2007, pp. 1435-1446.

[69] Beyer, E. "Design, Testing, and Performance of a Hybrid Micro Vehicle – The Hopping Rotochute." (PhD Dissertation, Georgia Institute of Technology, 2009).

[70] Costello, M., and Agarwalla, R., "Improved Dispersion of a Fin-Stabilized Projectile Using a Passive Moveable Nose," AIAA Atmospheric Flight Mechanics Conference, Denver, CO, 14-17 Aug 2000, paper AIAA-2000-4197.

[71] Landers, M., Hall, L., Auman, L., and Vaughn Jr., M. "Deflectable Nose and Canard Controls for a Fin-Stabilized Projectile at Supersonic and Hypersonic Speeds," 21st Applied Aerodynamics Conference, Orlando, FL, 23-26 June 2003, paper AIAA-2003-3805.

[72] Wikipedia. "Weeble." Wikipedia. http://en.wikipedia.org/wiki/Weeble (accessed 18 Sept. 2009).

[73] Bundy, M. *The Regional Nature of Aerodynamic Jump*, ARL-TR-1872, U.S. Army Research Laboratory, Aberdeen Proving Ground, MD, January 1999.

VITA

JONATHAN D. ROGERS

ROGERS was born in Los Angeles, California, and grew up in Southern California and the suburbs of Washington, DC. In 2006, he received a Bachelor of Science degree from Georgetown University in Physics and History. He entered the School of Aerospace Engineering at the Georgia Institute of Technology in 2006, receiving an MS in 2007 and continuing his studies to pursue a PhD. His technical interests include control and flight dynamics of smart weapons.